



**HAL**  
open science

# Ultra-wideband and high symbol rate transmission systems for next-generation optical fiber communications

Aymeric Arnould

► **To cite this version:**

Aymeric Arnould. Ultra-wideband and high symbol rate transmission systems for next-generation optical fiber communications. Optics / Photonic. Institut Polytechnique de Paris, 2021. English. NNT: 2021IPPAS006 . tel-03738115

**HAL Id: tel-03738115**

**<https://theses.hal.science/tel-03738115>**

Submitted on 25 Jul 2022

**HAL** is a multi-disciplinary open access archive for the deposit and dissemination of scientific research documents, whether they are published or not. The documents may come from teaching and research institutions in France or abroad, or from public or private research centers.

L'archive ouverte pluridisciplinaire **HAL**, est destinée au dépôt et à la diffusion de documents scientifiques de niveau recherche, publiés ou non, émanant des établissements d'enseignement et de recherche français ou étrangers, des laboratoires publics ou privés.



INSTITUT  
POLYTECHNIQUE  
DE PARIS

NNT : 2021IPPAS006

Thèse de doctorat



**NOKIA** Bell Labs

# Ultra-Wideband and High Symbol Rate Transmission Systems for Next-Generation Optical Fiber Communications

Thèse de doctorat de l'Institut Polytechnique de Paris  
préparée à Télécom SudParis

École doctorale n°626 École doctorale de l'Institut Polytechnique de Paris (EDIPP)  
Spécialité de doctorat : Électronique et Optoélectronique

Thèse présentée et soutenue à Palaiseau, le 28 juin 2021, par

**AYMERIC ARNOULD**

Composition du Jury :

Prof. Yves Jaouen Télécom Paris, France	Président
Prof. Alberto Bononi Università degli Studi di Parma, Italie	Rapporteur
Prof. Leslie A. Rusch Université Laval, Canada	Rapporteuse
Prof. Liam Barry Dublin City University, Irlande	Examineur
Prof. Badr-Eddine Benkelfat Télécom SudParis, France	Directeur de thèse
Dr. Amirhossein Ghazisaeidi Nokia Bell Labs, France	Co-encadrant de thèse

---

# Contents

	Page
Résumé en français	7
Introduction	9
<b>1 Coherent systems for optical communications</b>	<b>13</b>
<b>1.1 Introduction to optical fiber coherent communications</b>	<b>14</b>
1.1.a) Digital communications	14
1.1.b) Optical fiber communication channel	15
1.1.c) WDM transmission systems	15
<b>1.2 Coherent transmitter</b>	<b>17</b>
1.2.a) Bit-to-symbol mapping	17
1.2.b) Transmitter digital signal processing	17
1.2.c) Electro-optical conversion	20
<b>1.3 Optical fiber propagation modeling</b>	<b>21</b>
1.3.a) Linear propagation effects	21
1.3.b) Nonlinear propagation	24
1.3.c) Dual polarization propagation model	26
1.3.d) Numerical simulations of optical fiber transmission	27
<b>1.4 Optical amplification</b>	<b>28</b>
1.4.a) Types of optical amplifiers	28
1.4.b) Noise in optical amplification	30
1.4.c) Performance characterization of optical amplifiers	31
<b>1.5 Coherent receiver and digital signal processing</b>	<b>33</b>
1.5.a) Polarization and phase diversity receiver	33
1.5.b) Digital signal processing for coherent transmissions	34
<b>1.6 Summary</b>	<b>42</b>
<b>2 Performance and capacity assessment of coherent transmission systems</b>	<b>43</b>
<b>2.1 Impact of various noise sources</b>	<b>44</b>
2.1.a) Transceiver (back-to-back) penalties	45
2.1.b) Transmission line impairments	45
2.1.c) Multi-span transmission system modeling	46
<b>2.2 Transmission errors and error correction</b>	<b>48</b>
2.2.a) Hard-decision schemes	48
2.2.b) Soft-decision and advanced FEC	49
<b>2.3 Information theory and theoretical limits</b>	<b>50</b>
2.3.a) Mutual information	50
2.3.b) Source entropy	50

2.3.c)	Capacity of the optical channel . . . . .	51
<b>2.4</b>	<b>Practical limits and capacity approaching systems . . . . .</b>	<b>52</b>
2.4.a)	Modulation constraints . . . . .	52
2.4.b)	Coding constraints . . . . .	55
2.4.c)	Achievable rates for QAM systems . . . . .	57
<b>2.5</b>	<b>Trends for high capacity links . . . . .</b>	<b>59</b>
2.5.a)	Multiplexing through the physical dimensions . . . . .	59
2.5.b)	Optimization of optical bandwidth utilization . . . . .	60
<b>3</b>	<b>High symbol rate transmitters for next-generation coherent systems . . . . .</b>	<b>63</b>
<b>3.1</b>	<b>Introduction . . . . .</b>	<b>64</b>
3.1.a)	Evolution of coherent transponder capabilities . . . . .	64
3.1.b)	Overcoming electrical and electro-optical bandwidth limitations . . . . .	64
<b>3.2</b>	<b>High symbol-rate prototype characterization . . . . .</b>	<b>66</b>
3.2.a)	Experimental setup . . . . .	66
3.2.b)	Bandwidth compensation with digital predistortion . . . . .	67
3.2.c)	Hybrid optical and digital bandwidth compensation . . . . .	68
<b>3.3</b>	<b>High capacity 800 Gb/s demonstration for regional networks . . . . .</b>	<b>70</b>
3.3.a)	Back-to-back 99.5 GBd DP-64QAM signal characterization . . . . .	70
3.3.b)	Laboratory transmission line . . . . .	71
3.3.c)	Experimental results . . . . .	72
<b>3.4</b>	<b>Ultra-long haul 300 Gb/s transmission for future transoceanic systems . . . . .</b>	<b>74</b>
3.4.a)	Performance requirements . . . . .	74
3.4.b)	Experimental setup with recirculating loop . . . . .	75
3.4.c)	Experimental results . . . . .	77
<b>3.5</b>	<b>Field trial demonstration of rate versus reach trade-off optimization . . . . .</b>	<b>79</b>
3.5.a)	Experimental setup for field trial over live commercial network . . . . .	79
3.5.b)	Experimental observation of ROADM filtering effects . . . . .	81
3.5.c)	Post SD FEC decoding using SC LDPC . . . . .	83
<b>3.6</b>	<b>Summary . . . . .</b>	<b>87</b>
<b>4</b>	<b>Equalization enhanced phase noise impact on high symbol rate transmission systems . . . . .</b>	<b>89</b>
<b>4.1</b>	<b>Introduction . . . . .</b>	<b>90</b>
4.1.a)	EEPN in dispersion unmanaged transmission systems . . . . .	90
4.1.b)	Review of prior studies . . . . .	92
<b>4.2</b>	<b>DSP-aware EEPN numerical study . . . . .</b>	<b>94</b>
4.2.a)	Equivalent system model . . . . .	94
4.2.b)	EEPN identification . . . . .	95
4.2.c)	DSP aware analysis . . . . .	98
4.2.d)	Expected penalties for high speed and transoceanic . . . . .	101
<b>4.3</b>	<b>Experimental characterization of EEPN impact on a transoceanic testbed . . . . .</b>	<b>106</b>
4.3.a)	Laser source characterization . . . . .	106
4.3.b)	Submarine transmission testbed . . . . .	107

4.3.c) Experimental results . . . . .	108
<b>4.4 Summary . . . . .</b>	<b>111</b>
<b>5 Ultra-wideband transmission systems based on semiconductor optical amplifiers . . . . .</b>	<b>113</b>
<b>5.1 Introduction . . . . .</b>	<b>114</b>
5.1.a) Limits of conventional WDM systems . . . . .	114
5.1.b) Moving towards UWB systems . . . . .	114
<b>5.2 SOA for UWB transmission . . . . .</b>	<b>116</b>
5.2.a) Overview of SOA in optical communications . . . . .	116
5.2.b) Presentation of UWB SOA module . . . . .	117
<b>5.3 Experimental characterization of UWB SOA nonlinear impairments</b>	<b>119</b>
5.3.a) High power WDM operation using SOA . . . . .	119
5.3.b) Impact of the number of WDM channels on the SOA-induced nonlinear impairments . . . . .	122
<b>5.4 100 Tb/s regional transmission for upgrade of legacy terrestrial networks . . . . .</b>	<b>126</b>
5.4.a) SRS characterization in 100 km SSMF spans . . . . .	126
5.4.b) 300 km fiber link using UWB Raman/SOA amplifiers . . . . .	128
5.4.c) Experimental results . . . . .	130
<b>5.5 Record throughput on a 257 km unrepeated fiber link . . . . .</b>	<b>132</b>
5.5.a) 257.5 km transmission experimental setup . . . . .	132
5.5.b) Adaptive modulation format for capacity maximization . . . . .	134
5.5.c) Experimental results . . . . .	135
<b>5.6 Summary . . . . .</b>	<b>138</b>
<b>Conclusions and perspectives . . . . .</b>	<b>139</b>
<b>Acknowledgements . . . . .</b>	<b>143</b>
<b>List of acronyms . . . . .</b>	<b>145</b>
<b>List of symbols . . . . .</b>	<b>147</b>
<b>Bibliography . . . . .</b>	<b>148</b>
<b>Publications . . . . .</b>	<b>159</b>



# Résumé en français

Depuis la standardisation des protocoles TCP/IP au début des années 1980, la rapide évolution d'Internet en un système mondial de télécommunications a été permise par la mise en place au cours des trois dernières décennies de systèmes de communication à fibre optique à haute capacité. Cette infrastructure globale repose sur un ensemble de câbles sous-marins et de réseaux terrestres dotés de nœuds reconfigurables permettant le routage de façon transparente de canaux optiques sur de longues distances.

## Les communications à fibre optique au cœur du réseau Internet

Le développement des liaisons optiques à haute capacité a été permis par différentes innovations technologiques, incluant entre autres l'invention des sources laser et des fibres optiques dans les années 1970, le développement des amplificateurs à fibre dopée à l'erbium dans les années 1980 à l'origine des systèmes à multiplexage de longueur d'onde (WDM), puis l'utilisation de la détection cohérente et de la modulation d'amplitude en quadrature (QAM), l'introduction de puissants codes correcteurs d'erreur et d'algorithmes de traitement numérique du signal (DSP) permettant de compenser certains effets de propagation dans le canal de communication optique.

Plus récemment, des formats de modulation à mise en forme probabiliste de constellation (PCS) ont permis à l'efficacité spectrale des systèmes de s'approcher de la limite de Shannon, et les marges d'améliorations du débit de chaque canal sont de plus en plus restreintes. Dans ce contexte, le développement d'amplificateurs optiques à très large bande (UWB) ou de techniques de multiplexage spatial, permettant d'accroître le nombre total de canaux transmis, apparaissent comme de potentielles solutions pour accroître la capacité des systèmes de transmissions. Par ailleurs, le développement continu de transmetteurs à haut débit symbole est encouragé par l'industrie afin de limiter le coût des systèmes optiques WDM, en réduisant le nombre de transmetteurs requis par fibre.

## Plan de la thèse

Dans cette thèse, nous nous intéressons à des transmetteurs à haut débit symbole ainsi qu'à des systèmes de transmissions à amplificateurs UWB pour la prochaine génération de communications à fibre optique.

Le premier chapitre est consacré à une présentation de concepts fondamentaux relatifs aux communications numériques et aux systèmes de transmissions optiques à détection cohérente. Nous nous intéressons à la description et à la modélisation du canal de communication optique, qui comprend le transmetteur assurant la conversion électro-optique, la propagation dans la fibre et le récepteur permettant la détection opto-électrique. Nous présentons alors les algorithmes DSP utilisés dans

cette thèse pour la compensation des effets de propagation.

Le second chapitre présente l'évaluation de la performance du système de communication. Nous introduisons les différentes métriques pour quantifier les dégradations affectant les symboles transmis durant la propagation du signal dans le canal de communication optique. Nous détaillons les contraintes induites par la modulation et le codage sur le débit des communications basées sur les constellations QAM et PCS-QAM, et discutons la performance de ces schémas de modulation par rapport à la limite de capacité de Shannon. Nous concluons ce chapitre en détaillant la problématique à la base des études présentées dans le reste de cette thèse.

Dans le troisième chapitre, nous présentons l'implémentation et la validation expérimentale de transmetteurs à haut débit symbole pour la prochaine génération de communications cohérentes. Nous caractérisons la performance de notre prototype à haut débit symbole pour la génération de signaux autour de 100 GBd. Nous démontrons les capacités et discutons les perspectives de transmissions à haut débit symbole allant de distances régionales à des configurations transocéaniques, ainsi que dans un essai terrain mené sur un réseau commercial.

Le quatrième chapitre est consacré à une étude sur le bruit de phase augmenté par l'égalisation (EPPN), une dégradation potentiellement dominante à haut débit symbole. À l'aide de simulations numériques et d'investigations expérimentales, nous montrons que les prédictions analytiques de l'impact de l'EPPN sur les transmissions à haut débit symbole peuvent être pessimistes. En particulier, nous nuancions certaines craintes concernant les pénalités émanant de l'implémentation de transmetteurs à haut débit symbole utilisant des sources laser avec des performances standard pour les systèmes de communications optiques.

Dans le cinquième chapitre, nous nous intéressons à des systèmes de transmissions UWB basés sur des amplificateurs optiques à semiconducteurs (SOA). Nous présentons les caractéristiques d'un module UWB SOA avec une bande passante de 100 nm, promettant une augmentation considérable de capacité par rapport aux systèmes basés sur des EDFA avec une bande passante de 35-40 nm en bande C. Durant les dernières décennies, les SOA n'ont pas été considérés comme potentiels amplificateurs de lignes dans les réseaux de transport optiques à cause de leur comportement non linéaire. Nous caractérisons donc expérimentalement l'impact des dégradations non linéaires de notre SOA et montrons que celui-ci peut permettre des transmissions WDM à puissance élevée. Nous démontrons une transmission de 100 Tb/s à 300 km dans un scénario basé sur des contraintes liées aux réseaux terrestres existants, ainsi qu'une transmission record sur un tronçon de fibre de 257 km dans une configuration de lien sans répéteur.

La dernière partie de cette thèse présente les conclusions de ce travail et le met en perspective dans le cadre du développement de la prochaine génération de systèmes de communications optiques.

# Introduction

Since the standardization of the TCP/IP protocols in the early 1980s, the Internet has evolved from a small network connecting research and military infrastructures into a world-wide system of interconnected networks. Approximately one half of humanity had access to the Internet in 2018, and this fraction is expected to grow to  $2/3$  in a 5-year period. The number of connected devices to the Internet will approach 30 billions in 2023, with a 10% compound annual growth rate (CAGR) compared to the 6% CAGR of the number of users (and 1% CAGR of global population) [1]. Nowadays the Internet offers a large number of services, well beyond the World Wide Web, electronic mail and file sharing applications. In particular voice over IP, music and video streaming grow year after year as they tend to replace traditional communication media, and other bandwidth-hungry usage such as cloud computing, online gaming, Internet of Things, augmented and virtual reality also require ever-increasing network capacity. While the global IP traffic is normally expected to triple in a 5 year time (around 25 to 30% growth per year), this considerable growth is probably underestimated as some sources have recently reported that in 2020, the traffic growth jumped to 47% due to the change of Internet consumption habits after the Covid-19 outbreak [2].

## **Optical networks at the core of the Internet communication system**

The continuous development of the Internet has been supported by the deployment over the past three decades of high capacity core networks based on optical fiber communication systems. This global infrastructure relies on a backbone composed of subsea cables and on terrestrial networks with reconfigurable nodes enabling the transparent routing of optical channels over long distances. Several technological breakthroughs led to modern-day high capacity optical links at the heart of the global communication networks [3, 4]. Pioneered in the 1970s after the introduction of laser sources and optical fibers, optical transmission systems started to replace coaxial cables in transoceanic systems in the late 1980s. The invention of erbium doped fiber amplifiers (EDFAs) indeed unlocked high capacity links using wavelength division multiplexing (WDM) with the first commercial WDM systems transporting eight 2.5 Gb/s channels in terrestrial networks and two 5 Gb/s channels over transoceanic distances in 1995. Coherent detection implementation in optical transport has been another revolution with the demonstration of 100 Gb/s channel rate using quadrature phase shift keying (QPSK) in 2008. Since then, quadrature and amplitude modulation (QAM) schemes, powerful forward error correction (FEC) techniques and digital signal processing (DSP) have enabled continuous increase of the capacity and reach of optical transport networks. Today, most of the market shares correspond to 100 Gb/s and 200 Gb/s transponders for metro to subsea applications, and most recent transoceanic cables can carry up to 20 Tb/s WDM throughput.

## Capacity-approaching solutions and future directions

The performance of optical transport systems is expressed using different metrics such as the per-channel rate, the spectral efficiency (SE) or the total system throughput. For ultra long-haul transmissions the main paradigm in subsea system design has been for years the maximization of the per-fiber WDM throughput, given the high deployment costs of such systems. On the one hand, optimized fiber links with powerful linear and nonlinear DSP have pushed the end-of-link signal to noise ratio (SNR) towards the fundamental limits set by optical amplification noise and nonlinear fiber impairments. On the other hand, the ultimate SE limit is given by the Shannon's capacity, and advanced modulation formats and powerful soft decision (SD) FEC decoding now enable capacity-approaching solutions. Thanks to these state-of-the-art techniques, a succession of throughput records has been demonstrated in lab experiments. A 34.9 Tb/s C-band WDM throughput (SE 8.3 b/s/Hz) has been reported over transatlantic distance of 6375 km with geometrically shaped 64APSK format [5]. Leveraging C+L transmission with EDFA multiplexing, a SE degradation can be tolerated as long as the bandwidth extension enables the total WDM throughput scaling: nonlinear compensation and adaptive FEC have been exploited to demonstrate 65 Tb/s net rate (SE 7.3 b/s/Hz) over 6600 km with probabilistic constellation shaping (PCS) modulation [6], or 70.4 Tb/s (7.23 b/s/Hz) over 7600 km with hybrid probabilistic and geometric constellation shaping [7]. For these capacity-approaching systems, further scaling of the cable throughput via SNR or SE improvements through DSP, signaling, modulation or coding techniques is increasingly challenging. In this context, ultra-wideband (UWB) optical amplification schemes and space-division multiplexing (SDM) appear as potential solutions to further scale the system capacity by leveraging the available physical dimensions of the optical fiber link.

Furthermore, continuous technological progress in the conversion rate of digital-to-analog converters (DAC) and analog-to-digital converters (ADC) (from 56 GS/s in first coherent products up to more than 120 GS/s in current generations [8]) have enabled the transponder symbol rate scaling, allowing an increase both in the per-transponder capacity at a given distance and in the transmission reach for a given capacity. For short transmission distances, i.e. from datacenter interconnect (DCI) up to metro transmissions, cost and integration are major design criteria and foster the scaling of the per-transponder capacity, as high symbol rate transmitters are attractive to populate the WDM bandwidth with a reduced transponder count. The standardization of 400GbE client IP rate [9] together with the specification of optical solutions with the 400ZR agreement [10] will undoubtedly increase the popularity of 400 Gb/s systems [11], and increasing the transponder symbol rate beyond the 60 GBd standard of 400ZR will enable better transmission reach. The demand for transponders operating beyond 100 GBd is real as the future standards for client rates are likely to be 800 GbE and 1.6 TbE [9], challenging the current limits of DAC technologies in terms of conversion rate and bandwidth. Furthermore, considering UWB and SDM as potential enablers for future high capacity networks, high symbol rate transmissions are appealing to limit the scaling of the required transponder number with the system bandwidth extension or optical path multiplicity.

## Thesis outline

This thesis focuses on high speed transponders and UWB transmission systems for next generation optical fiber communications.

In the first chapter, we present fundamental notions on digital communication and coherent optical communication systems. We focus on the description and modeling of the optical communication channel, which encompasses the electro-optical transmitter, the propagation in the optical fiber and the opto-electrical receiver. Based on this physical layer modeling, the useful DSP algorithms to compensate for propagation effects are presented.

The second chapter focuses on the performance assessment of the communication system. We introduce the different metrics to quantify the impairments that affect the information symbols during signal propagation in the optical communication channel. We detail the modulation and coding constraints on QAM and PCS-QAM information rate, and discuss the performance of these modulation schemes compared to Shannon's capacity limit. We conclude this chapter by reviewing the motivation of the work presented in the remaining chapters of this thesis.

In the third chapter we investigate implementation challenges and experimental validation of high symbol rate transmitters for next-generation coherent communications. We characterize the performance of our high symbol-rate prototype for 100 GBd signal generation. We demonstrate the capabilities and discuss the opportunities of high symbol rate transmissions from regional distances to ultra long-haul configurations, as well as in a field-trial over a live commercial traffic network. We show how the flexibility provided by high symbol rate transmitters suits the different transmission scenarios in the Internet core communication network, and discuss their potential limitations.

The fourth chapter presents a study of equalization enhanced phase noise (EPPN), which is a potentially dominant impairment at high symbol rates. Through numerical and experimental investigations, we show that the analytical predictions of EPPN impact on high symbol rate transmissions can be pessimistic. In particular, we temper some industry concerns regarding the penalties arising from the implementation of high symbol rate transmitters based on standard laser sources.

In the fifth chapter, we focus on UWB transmission systems based on semiconductor optical amplifiers (SOA). We review the characteristics of an UWB SOA module with 100 nm bandwidth that promises considerable capacity increase compared to systems based on C-band EDFAs with 35-40 nm bandwidth. For the past decades, SOA nonlinear behavior has prevented its use as inline amplifier in optical transport networks, so we experimentally characterize the SOA-induced nonlinear impairments, and show that the considered UWB SOA can enable WDM transmission in high power regimes. We demonstrate a 100 Tb/s transmission over 300 km in a scenario based on legacy terrestrial network constraints, as well as a record throughput over a 257 km fiber span in an unrepeated optical link configuration.

The final part of this thesis presents the conclusions of this work and discusses perspectives for next-generation optical networks.



# Chapter 1

## Coherent systems for optical communications

We present in this chapter the specificities of fiber optics coherent transmission systems in the more general context of digital communications. We first describe the generation of electrical signals and the optical carrier modulation, then we review the modeling of propagation effects in the optical fiber and the noise contribution arising from optical amplification. Finally, we present the architecture of coherent receivers and we review the key DSP blocks that enable to compensate for optical channel distortions and estimate the transmitted symbols at the receiver.

### Contents of this chapter

---

<b>1.1</b>	<b>Introduction to optical fiber coherent communications</b>	<b>14</b>
1.1.a)	Digital communications	14
1.1.b)	Optical fiber communication channel	15
1.1.c)	WDM transmission systems	15
<b>1.2</b>	<b>Coherent transmitter</b>	<b>17</b>
1.2.a)	Bit-to-symbol mapping	17
1.2.b)	Transmitter digital signal processing	17
1.2.c)	Electro-optical conversion	20
<b>1.3</b>	<b>Optical fiber propagation modeling</b>	<b>21</b>
1.3.a)	Linear propagation effects	21
1.3.b)	Nonlinear propagation	24
1.3.c)	Dual polarization propagation model	26
1.3.d)	Numerical simulations of optical fiber transmission	27
<b>1.4</b>	<b>Optical amplification</b>	<b>28</b>
1.4.a)	Types of optical amplifiers	28
1.4.b)	Noise in optical amplification	30
1.4.c)	Performance characterization of optical amplifiers	31
<b>1.5</b>	<b>Coherent receiver and digital signal processing</b>	<b>33</b>
1.5.a)	Polarization and phase diversity receiver	33
1.5.b)	Digital signal processing for coherent transmissions	34
<b>1.6</b>	<b>Summary</b>	<b>42</b>

---

## 1.1 Introduction to optical fiber coherent communications

In this section, we present a general overview of digital communication systems and present the specificities of the optical communication channel, whose physical modeling is detailed in the remaining of this chapter.

### 1.1.a) Digital communications

In digital communications, regardless of the nature of the original message (text, audio, image, video,...), the information is represented by sequences of "0"s and "1"s called binary digits (bits). The aim of the telecommunication system is to reliably transmit these information streams from a digital source to a remote destination, through a communication channel that comprises the transmitter, the propagation in a physical medium (copper wires, optical fibers, free-space,...) and the receiver. A general view of such a system is given in Fig. 1.1 and can be described as follows [12, 13].

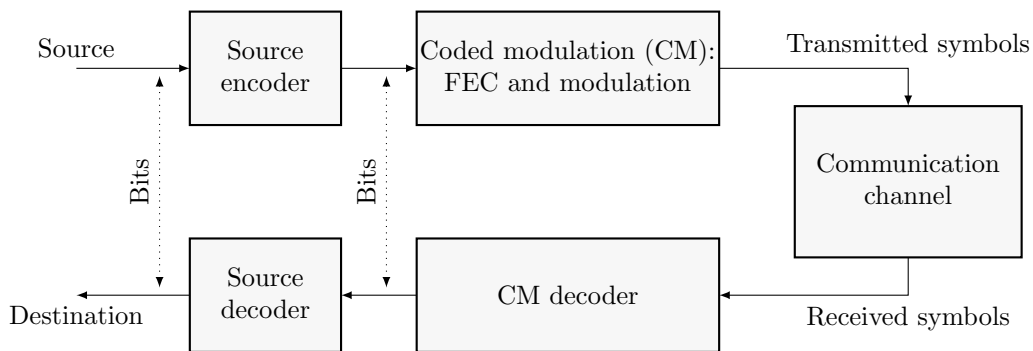


**Figure 1.1:** General view of a digital communication system

To efficiently represent the message generated by a digital source with as few bits as possible, source encoding (or data compression) is used to reduce any redundancy in the data. The coded modulation (CM) encoder consists in the combination of FEC encoding and modulation. To cope with the impact of distortions in the communication channel, FEC encoding adds redundancy in a controlled manner so that error correction can be performed at the receiver. To increase the information rate in the communication channel, multiple bits are grouped into modulation symbols, and the number of bits carried by each symbol depends on the symbol constellation choice.

The symbols are launched in the communication channel which encompasses the transmitter, that converts the digital symbols into a physical signal, the propagation in the physical medium and the receiver, that converts the physical signal back into the digital domain and compensates for the physical domain impairments.

At the output of the communication channel, the CM decoder performs demodulation and decoding, i.e. estimates the transmitted symbols and retrieves the transmitted bits after FEC decoding. The data is then decompressed by source decoding (inverse of source encoding) before reaching the remote destination.

### 1.1.b) Optical fiber communication channel

After this general view of a digital communication system, Fig. 1.2 details the specificities of the optical fiber communication channel. The symbols to be sent in the communication channel are first converted to electrical radio frequency (RF) signals through digital-to-analog (D/A) conversion. Digital signal processing (DSP) techniques can be applied to adapt the RF signals to the properties of the transceivers and the physical medium, with pulse-shaping or pre-equalization techniques. The electrical RF signals are used to modulate the light from a laser source, and the modulated optical wave propagates into the optical channel (such as fiber and network elements). At the receiver, the optical signal is converted back into electrical RF signals, before analog-to-digital (A/D) conversion. DSP is applied on the digital signals to compensate for transmission effects, and the recovered symbols are sent to the CM decoder for estimation of the transmitted bit sequences.

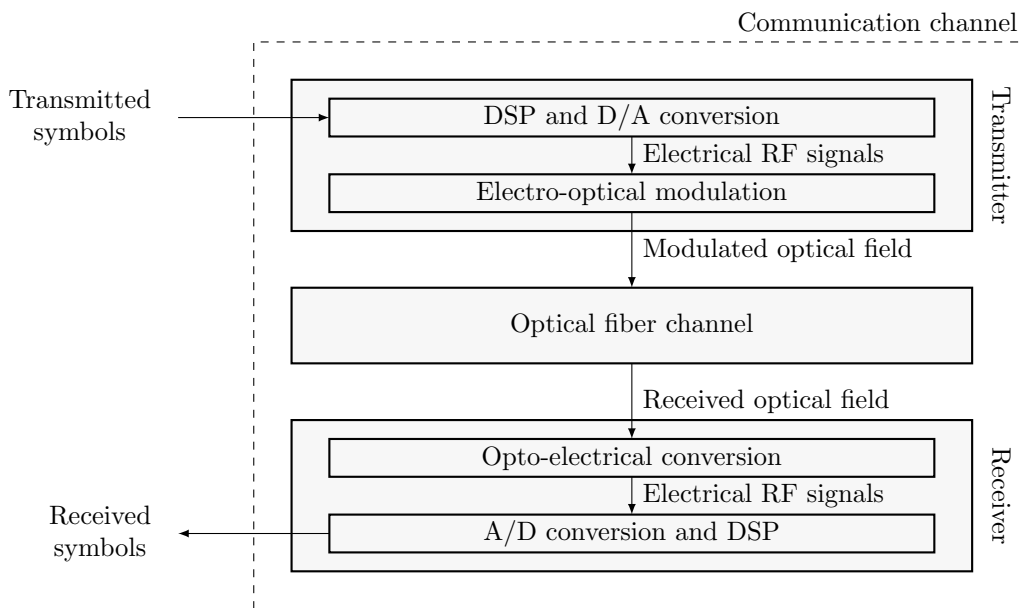


Figure 1.2: Optical fiber communication channel

The work presented in this thesis focuses on the properties of the optical fiber communication channel and on the design of efficient optical transmissions systems. This involves the modeling of the propagation in the fiber medium, the electrical and optical aspects of the transmitters and receivers, as well as the design of encoding and modulation schemes that are adapted to this communication channel. The source encoding and decoding processes are out of the scope of this work.

### 1.1.c) WDM transmission systems

A general view of a point-to-point long-haul optical fiber transmission system is given in Fig. 1.3. This WDM system consists in  $N$  parallel channels operating at different wavelengths  $\lambda_i$ , that copropagate in the same optical fiber. At the transmitter (TX) side, each information binary signal is converted into the optical domain by modulation of a laser source at carrier wavelength  $\lambda_i$ . The optical signals coming from the  $N$  transmitters are multiplexed to form the WDM signal that is sent to the optical link. In the case of a homogeneous link, the fiber link is composed of a succession of  $N_S$  identical fiber spans followed by an optical amplifier. The optical amplifier restores the signal power that is attenuated by the propagation in

the fiber before the next fiber span. At the receiver (RX) side, the WDM signal is demultiplexed and each modulated signal at carrier wavelength  $\lambda_i$  is detected by a dedicated receiver. Note that an optical link is usually composed of at least one fiber pair and each fiber corresponds to one propagation direction.

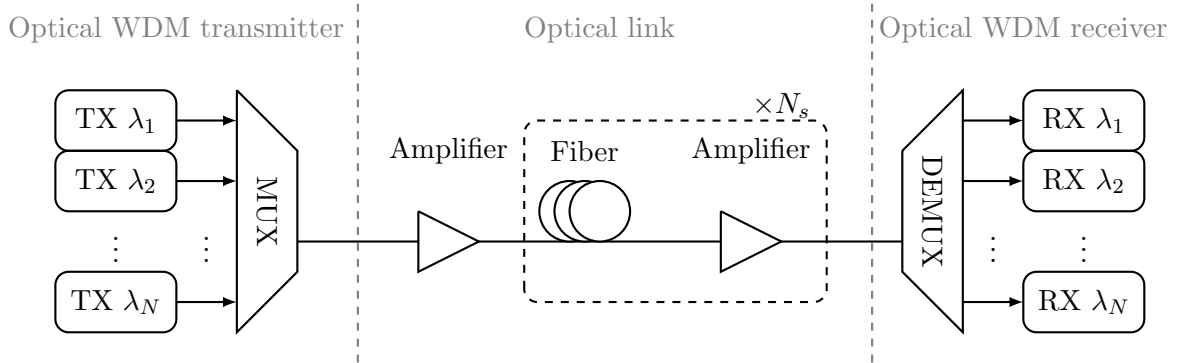


**Figure 1.3:** Long-haul WDM point-to-point transmission system

The advent of reconfigurable add/drop multiplexers (ROADMs) in the 2000s enabled the design of optical reconfigurable meshed networks, as sketched in Fig. 1.4. At each node, ROADMs are able to add or drop different channels going to or coming from different destinations, such that a given channel does not copropagate with the same channels all along its path in the network. Nowadays most optical networks are based on this meshed architecture, as the transparency of optical nodes allows considerable flexibility in network management. Point-to-point links are used only for specific purposes such as submarine communications.

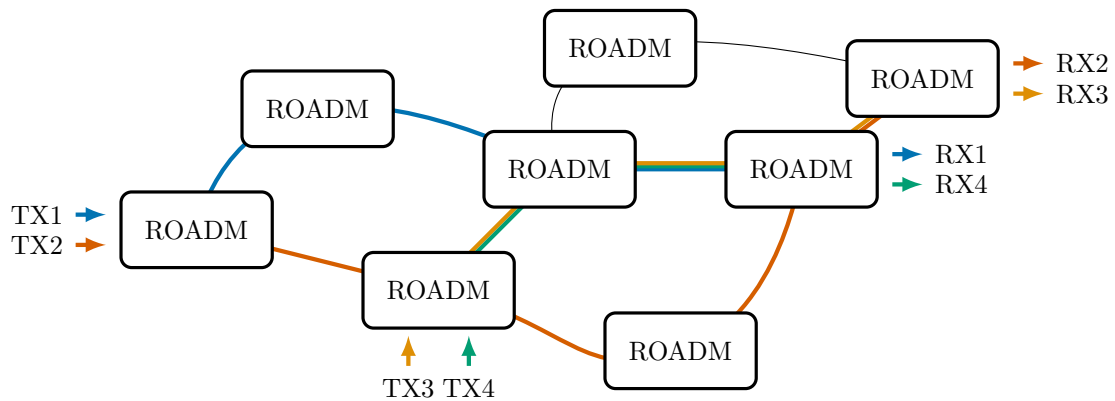


**Figure 1.4:** Optical reconfigurable meshed network

## 1.2 Coherent transmitter

The transmitter role is to convert the information from the source into a signal in the optical domain that is suitable for transmission over the optical fiber channel. This section describes how an optical fiber coherent transmitter maps bit streams to  $m$ -bit complex symbol streams, that are used to modulate a laser source with a dual polarization modulator.

### 1.2.a) Bit-to-symbol mapping

We consider for simplicity that the CM encoder can be represented by the concatenation of a binary encoder and a bit-to-symbol mapper (more details can be found in section 2.2). The output of the encoder is seen as a bit stream with independent and identically distributed "0"s and "1"s. The bit-to-symbol mapping convert groups of bits into symbols that are represented in a complex plane, as depicted in Fig. 1.5. In this thesis, only square QAM constellations are considered, i.e.  $2^m$ QAM where  $m$  is an even number. These constellations can be obtained by the product of multi-level amplitude modulation over two quadratures  $I$  and  $Q$  that contain  $2^{m/2}$  amplitude levels.

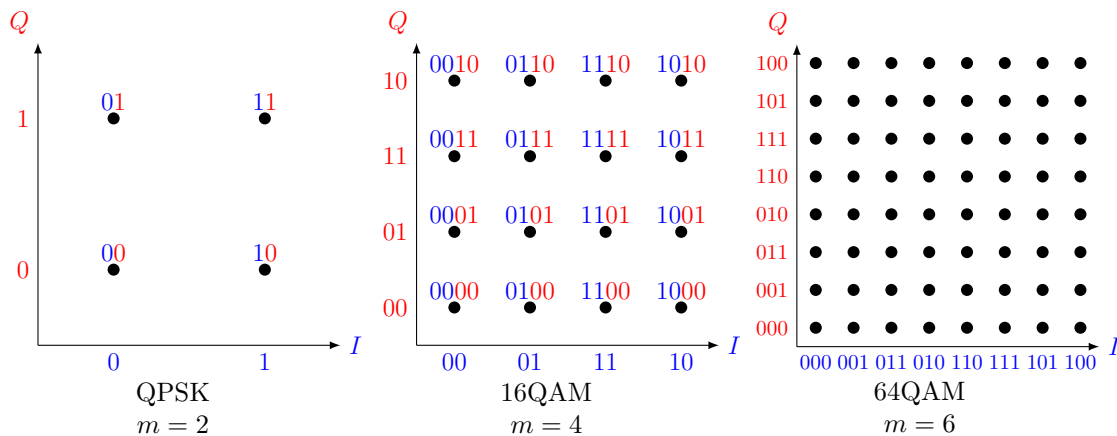


**Figure 1.5:** Regular  $2^m$ QAM constellations, for  $m = 2$  (QPSK),  $m = 4$  (16QAM) and  $m = 6$  (64QAM). The associated two-dimensional Gray mapping results from the concatenation of the Gray mappings of both quadratures.

Fig. 1.5 shows the constellations for QPSK, 16QAM and 64QAM ( $m$  is equal to 2, 4 and 6, respectively), together with an associated bit-to-symbol mapping. On each quadrature  $I$  and  $Q$ , the one-dimensional mapping of the  $m$  bits follows a Gray mapping (two adjacent codes differ by only one bit). For each complex symbol, the two-dimensional mapping is generated by the concatenation of the mapping of the quadratures. The two-dimensional mapping is therefore also a Gray mapping, which is a crucial property for the design of high performance CM schemes.

### 1.2.b) Transmitter digital signal processing

Digital filtering techniques are applied on the sequence of complex symbols generated by the bit-to-symbol mapping to generate electrical waveforms that are suitable for electro-optical modulation, propagation in the optical fiber and reception.

**(i) Pulse-shaping**

To control the frequency bandwidth of the generated signals, a pulse-shaped signal waveform is created through the multiplication of each symbol  $x_k$  by a pulse shape  $h_{ps}(t)$  centered at the symbol sample time  $kT_s$

$$x_{ps}(t) = \sum_k x_k h_{ps}(t - kT_s) \quad (1.1)$$

The pulse shape must be chosen as an acceptable compromise between

- (i) avoiding inter-symbol interference (ISI), i.e. the pulse  $h_{ps}(t - kT_s)$  is zero for all sampling instants  $t = lT_s$  except for  $k = l$ ;
- (ii) limiting the signal bandwidth  $W$  to allow channel multiplexing in the frequency domain, i.e. the frequency response  $H_{ps}(f)$  given by the Fourier transform of  $h_{ps}(t)$  must be zero for  $|f| > W/2$ .

Different pulse-shaping functions  $h_{ps}(t)$  and their frequency response  $H_{ps}(f)$  are given in Fig. 1.6 and some of their properties [13] are recalled in the following.

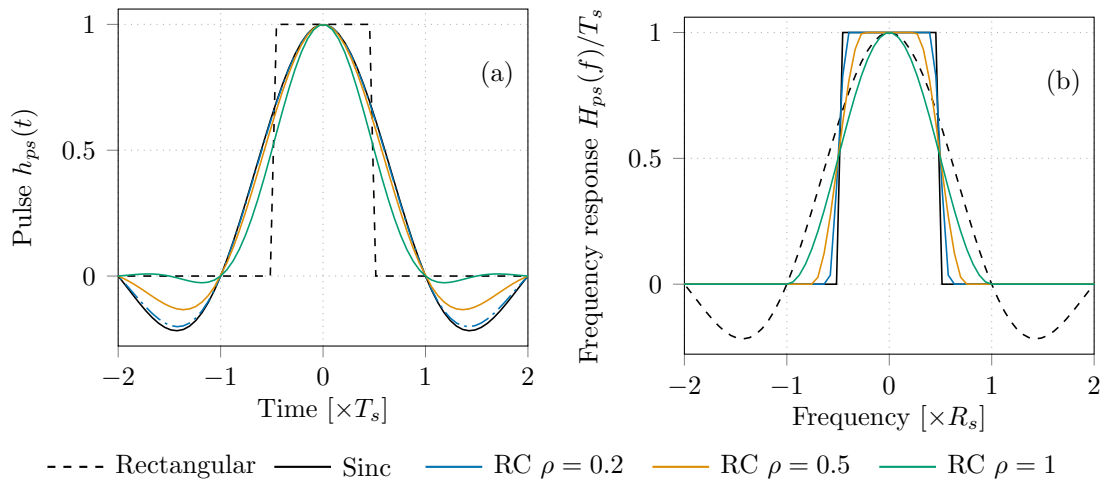


**Figure 1.6:** (a) Pulse shaping function  $h_{ps}(t)$  and (b) normalized frequency response  $H_{ps}(f)$  of different pulse shaping functions

**Rectangular pulse** The simplest way to generate a waveform from the symbol sequence is to hold the waveform at a constant unitary level during the symbol time  $T_s$ . This is equivalent to performing a pulse-shaping with rectangular pulses of width  $T_s$ . This pulse shaping however requires an infinite bandwidth, as the corresponding frequency response is

$$H_{ps}(f) = T_s \cdot \text{sinc}(fT_s) \quad (1.2)$$

where the sinc function is defined as

$$\text{sinc}(x) = \begin{cases} \frac{\sin(\pi x)}{\pi x}, & \text{if } x \neq 0 \\ 1, & \text{if } x = 0 \end{cases} \quad (1.3)$$

**Sinc pulse** For a given symbol rate  $R_s = 1/T_s$ , the pulse shape that minimizes the signal bandwidth is the sinc pulse defined by

$$h_{ps}(t) = \text{sinc}(t/T_s) \quad (1.4)$$

with a rectangular frequency spectrum  $H_{ps}(f) = T_s$  for  $|f| < 1/(2T_s)$  and the resulting bandwidth  $W = 1/T_s$ . The sinc pulse shows no ISI so perfect sampling at time samples  $kT_s$  allows recovery of each transmitted symbol without any distortion. In practical case, as the time duration of sinc pulse is infinite and the amplitude of the sinc pulse decays slowly with time, imperfect sampling can lead to significant ISI over a large number of symbols.

**Raised-cosine pulse** A commonly used pulse shape in digital communications is the raised-cosine (RC) filter, which is described in the frequency domain by

$$H_{ps}(f) = \begin{cases} T_s, & \text{if } |f| \leq \frac{1-\rho}{2T_s} \\ \frac{T_s}{2} \left( 1 + \cos \left( \frac{\pi T_s}{\rho} \left( |f| - \frac{1-\rho}{2T_s} \right) \right) \right), & \text{if } \frac{1-\rho}{2T_s} < |f| \leq \frac{1+\rho}{2T_s} \\ 0, & \text{otherwise} \end{cases} \quad (1.5)$$

and in the time domain by

$$h_{ps}(t) = \begin{cases} \frac{\pi}{4} \text{sinc} \left( \frac{1}{2\rho} \right), & \text{if } t = \pm \frac{T_s}{2\rho} \\ \text{sinc} \left( \frac{t}{T_s} \right) \frac{\cos(\pi\rho t/T_s)}{1 - 4\rho^2 t^2/T_s^2}, & \text{otherwise} \end{cases} \quad (1.6)$$

where  $\rho > 0$  is the roll-off factor. As per (1.6),  $h_{ps}(t - kT_s)$  is zero at all sampling times  $lT_s$ ,  $l \neq k$ , so the RC filter shows no ISI. The amplitude of the RC pulse decays more quickly than the sinc pulse, reducing the ISI impact in the case of imperfect sampling. The spectrum defined by (1.5) has a larger bandwidth  $W = (1 + \rho)/T_s$  than the sinc pulse, and the excess bandwidth  $\rho/T_s$  can be tuned by the roll-off parameter  $\rho$  according to the system requirements.

**Root-raised cosine pulse** For a channel with additive stochastic noise, the receiver that maximizes the signal to noise ratio (SNR) is the *matched filter*, that corresponds, for a given transmit pulse  $h_{ps}(t)$ , to the time-reversed complex conjugate  $h_{ps}^*(-t)$ . Defining the root raised cosine (RRC) filter whose spectrum is  $\sqrt{H_{ps}(f)}$ , where  $H_{ps}(f)$  is given by (1.5), the RRC is its own matched filter due to its symmetry properties. Therefore, placing a RRC filter at the transmitter and the same filter at the receiver, the overall pulse shape has the properties of the RC filter while ensuring optimal reception with matched filtering in the presence of additive noise.

## (ii) Digital equalization

The pulse shaped waveform  $x(t)$  can be further filtered by additional digital filters to compensate for transmission impairments in the communication channel, for example to cope with bandwidth limitations of the physical components acting in electrical generation, electro-optical modulation, or electrical conversion at the receiver. More details about the pre-equalization schemes are discussed in the chapter 3.

### 1.2.c) Electro-optical conversion

In the case of a coherent dual polarization transmitter, exploiting the two orthogonal polarizations  $H$  and  $V$  of the light, two waveforms  $x^H(t)$  and  $x^V(t)$  are generated from two streams of symbols  $x_k^H$  and  $x_k^V$  after pulse shaping and digital pre-equalization. Fig. 1.7 shows the schematic of a dual-polarization (DP) in-phase and quadrature (I/Q) coherent transmitter, using a single DAC per modulated dimension.

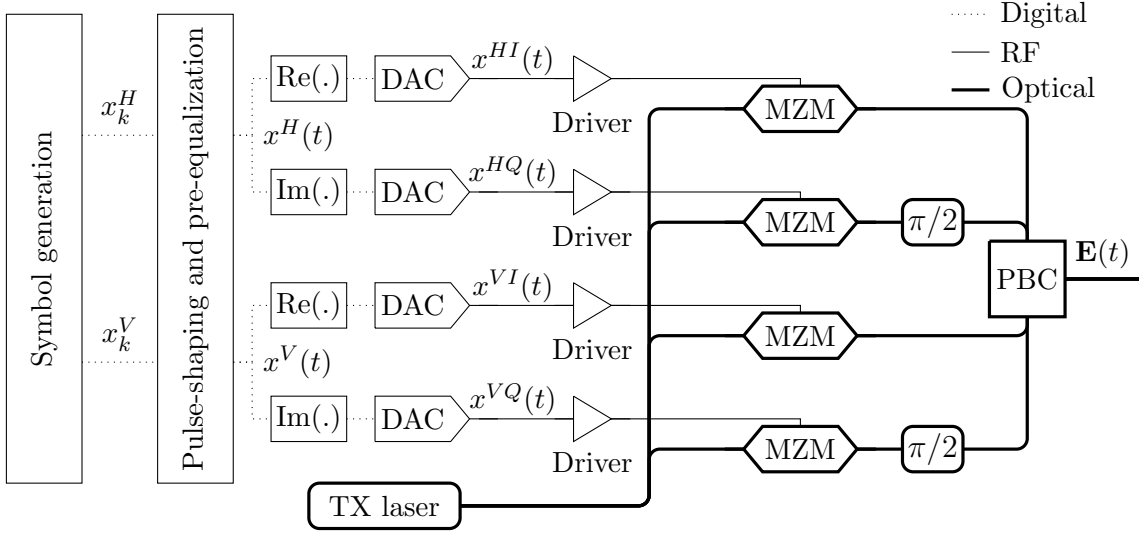


**Figure 1.7:** Dual polarization in-phase and quadrature (DP I/Q) coherent transmitter

The real and imaginary parts of each waveform  $x^{HI}(t)$ ,  $x^{HQ}(t)$ ,  $x^{VI}(t)$  and  $x^{VQ}(t)$  are sampled and quantified and after D/A conversion, the four electrical analog waveforms can be amplified with electrical amplifiers (drivers). The resulting signals are used to drive the Mach-Zehnder modulators (MZM) performing electro-optical modulation. A MZM is an interferometer that contains, in one or both arms, electro-optical cells (such as  $\text{LiNbO}_3$  crystals) that introduce phase shifts depending on the applied voltage. The phase difference between the arms results in amplitude modulation when the two signals are recombined.

A continuous wave coming from a laser with angular frequency  $\omega$  and phase  $\theta(t)$  is split to feed four MZMs (one for each quadrature  $I$  and  $Q$  of each polarization  $H$  or  $V$ ). For each polarization, a  $\pi/2$  phase shift is introduced on the output of one MZM to ensure orthogonality of the  $I$  and  $Q$  signals, before recombination through an optical coupler. Finally, the two orthogonal polarizations are combined with a polarization beam coupler (PBC). At the output of the DP I/Q transmitter, the dual-polarization modulated optical field can be expressed as

$$\mathbf{E}(t) = E^0 \begin{bmatrix} x^H(t) \\ x^V(t) \end{bmatrix} e^{j(\omega t + \theta(t))} \quad (1.7)$$

In the case of a WDM transmission with  $N_{WDM}$  DP I/Q transmitters, the  $i$ -th carrier is defined by the parameters  $E_i^0$ ,  $\omega_i$  and  $\theta_i$  of its laser source, and carries the data waveforms  $x_i^H(t)$  and  $x_i^V(t)$  such that the total field is expressed by

$$\mathbf{E}(t) = \sum_{i=1}^{N_{WDM}} E_i^0 \begin{bmatrix} x_i^H(t) \\ x_i^V(t) \end{bmatrix} e^{j(\omega_i t + \theta_i(t))} \quad (1.8)$$

## 1.3 Optical fiber propagation modeling

The most widely used optical fiber for long-haul transmissions is the single-mode fiber (SMF). As depicted by Fig. 1.8, it is composed of a central silica glass core surrounded by a cladding glass layer. One or several plastic or polymer coating layers are then used to protect the core and the cladding.

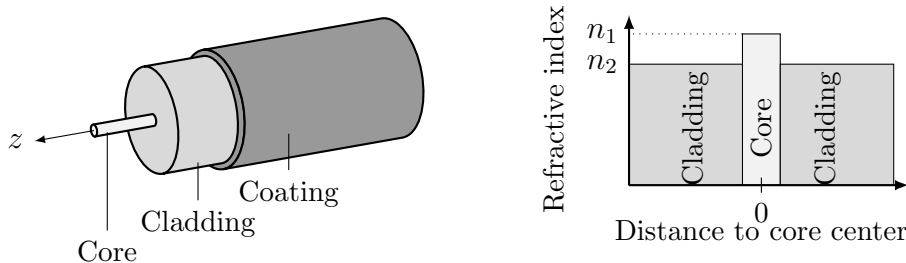


**Figure 1.8:** Single-mode fiber (SMF) schematic view and refractive index profile

The difference of refractive index between the core and the cladding enables the confinement of the light within the core thanks to total internal reflection effect. For SMF the cladding diameter is usually 125  $\mu\text{m}$  and the core radius is below 10  $\mu\text{m}$  to ensure single mode propagation in the telecommunications window around 1550 nm, as standardized in ITU-T G.652 [14] and G.654 [15] for long-haul applications. This thesis focuses only on the use of SMF, in contrast with multi-mode fibers (MMF), where several modes of propagation exist in the fiber (such as ITU-T G651.1 standard [16] for short-reach applications). MMF can be obtained by varying the fiber properties, for examples by tuning the core and cladding refractive indices, by increasing the core radius, or by a continuously-varying index (graded-index) instead of a index step between the core and the cladding.

This section provides the description of the optical field  $\mathbf{E}(z, t)$  during its propagation in the optical fiber. For simplicity, the different propagation effects are described with a scalar optical field  $E(z, t)$ , and the generalization to a dual polarization optical field is presented afterwards, together with the description of polarization-dependent impairments.

### 1.3.a) Linear propagation effects

#### (i) Power attenuation

For a scalar optical field  $E(z, t)$ , the power of the optical signal  $P(z) = \langle |E(z, t)|^2 \rangle_t$  decreases exponentially with the distance during the propagation in the optical fiber, as described by  $P(z) = P_0 \exp(-\alpha z)$ , where  $P_0$  is the fiber input power,  $z$  the distance in [km] and  $\alpha$  the attenuation coefficient [ $\text{km}^{-1}$ ], which is usually described in [dB/km]. The evolution of the optical field is then described by the equation

$$\frac{\partial E}{\partial z} = -\frac{\alpha}{2} E. \quad (1.9)$$

The loss profile of a standard SMF (SSMF) is shown in Fig. 1.9. The attenuation in optical fibers is due to scattering loss and absorption. For low wavelength, Rayleigh scattering is due to density fluctuations in the silica that appear during fiber fabrication process, causing the refractive index to fluctuate in the material and

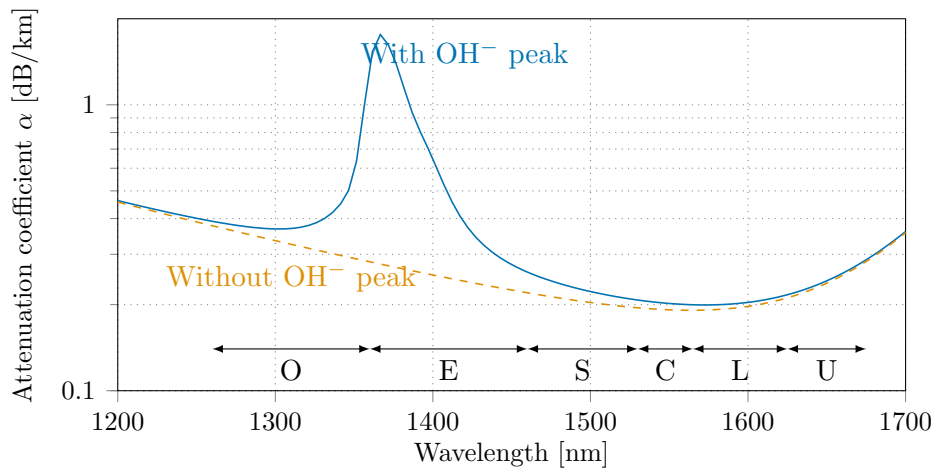


**Figure 1.9:** Attenuation profile of a SSMF (analytical fit to experimental data taken from [17])

the light to scatter in all directions. For high wavelength, loss is determined by the interaction of the light with the silica, which is called intrinsic infrared absorption. Finally, absorption peaks are also induced by the presence of impurities in the fiber, such as  $\text{OH}^-$  ions that cause a peak between 1350 and 1400 nm. Note that specific manufacturing process can ensure a very low quantity of  $\text{OH}^-$  ion in the fiber and nearly eliminate the  $\text{OH}^-$  peak for specific usages [18].

The loss profile of the SMF defined the ITU-T standard for wavelength bands for optical fiber transmissions, i.e. the O, E, S, C, L and U-band, as shown in Fig. 1.9. The C-band centered around  $\lambda_0 = 1550$  nm shows the minimum attenuation value (around 0.2 dB/km for SSMF, which can be as low as 0.15 dB/km for low-loss fibers) and is the preferred window for long-haul communications. Until the mid 1990s and the advent of optical amplifiers, 20 to 100 km spaced regenerators (each time with opto-electrical RX and electro-optical TX) were needed in most optical links [3], as the transmission reach was limited by the RX sensitivity after a single fiber span. Such regenerators were generally not flexible and WDM configurations were not possible as they would have required as many regenerators as transmitted channels. With the first demonstrations of WDM systems in 1995 using optical amplifiers with bandwidth much larger than the single channel bandwidth, it was possible to better benefit from the low-loss window of the optical fiber [4]. Section 1.4 provides a presentation of optical amplifiers for modern WDM systems and the modeling of amplified spontaneous emission (ASE) noise occurring during optical amplification.

## Chromatic Dispersion

Chromatic dispersion (CD) is due to the wavelength dependence of the fibre refractive index  $n(\omega)$ . The speed of the spectral component at angular frequency  $\omega$  is given by the phase velocity  $v_p = c/n(\omega)$ . A first consequence of CD is that channels at different wavelengths travel at different speeds, but more importantly, within a single channel, the different frequency components of a pulse have different speeds, which leads to pulse temporal broadening and ISI if uncompensated [18].

The CD effect is detailed considering the propagation constant  $\beta(\omega) = \omega/v_p$  and

its Taylor series around the reference angular frequency  $\omega_0 = 2\pi c/\lambda_0$

$$\beta(\omega) = \beta_0 + \beta_1(\omega - \omega_0) + \frac{\beta_2}{2}(\omega - \omega_0)^2 + \frac{\beta_3}{6}(\omega - \omega_0)^3 + \dots \quad (1.10)$$

where  $\beta_i$  is the  $i$ -th derivate of  $\beta(\omega)$  with respect to  $\omega$ . The propagation of the electrical field  $E(z, t)$ , when only attenuation and CD are considered, is then governed by the equation

$$\frac{\partial E}{\partial z} = -\frac{\alpha}{2}E - \beta_1 \frac{\partial E}{\partial t} - j \frac{\beta_2}{2} \frac{\partial^2 E}{\partial t^2} + \frac{\beta_3}{6} \frac{\partial^3 E}{\partial t^3} \quad (1.11)$$

or equivalently, in the retarded timeframe  $\tau = t - \beta_1 z$ ,

$$\frac{\partial E}{\partial z} = -\frac{\alpha}{2}E - j \frac{\beta_2}{2} \frac{\partial^2 E}{\partial \tau^2} + \frac{\beta_3}{6} \frac{\partial^3 E}{\partial \tau^3}. \quad (1.12)$$

$\beta_0$  [ $\text{km}^{-1}$ ], which is a constant phase shift, and the group velocity  $\beta_1$  [ps/km], which represents the speed of the envelope of the optical pulse, do not lead to any signal degradation during the propagation. The group velocity dispersion  $\beta_2$  [ $\text{ps}^2/\text{nm}$ ] corresponds to the acceleration of the spectral components and is responsible of the pulse broadening in the time domain. It is linked to the dispersion coefficient  $D(\lambda)$  expressed in [ $\text{ps}/(\text{nm}\cdot\text{km})$ ] by

$$D(\lambda) = -\frac{2\pi c}{\lambda^2} \beta_2. \quad (1.13)$$

The third order dispersion parameter  $\beta_3$  is related to  $S_0$  the linear change of the dispersion coefficient  $D(\lambda)$  around  $\lambda_0$ :

$$S_0 = \left. \frac{\partial D}{\partial \lambda} \right|_{\lambda_0} = \frac{4\pi c}{\lambda_0^3} \left( \beta_2 + \frac{\pi c}{\lambda_0} \beta_3 \right). \quad (1.14)$$

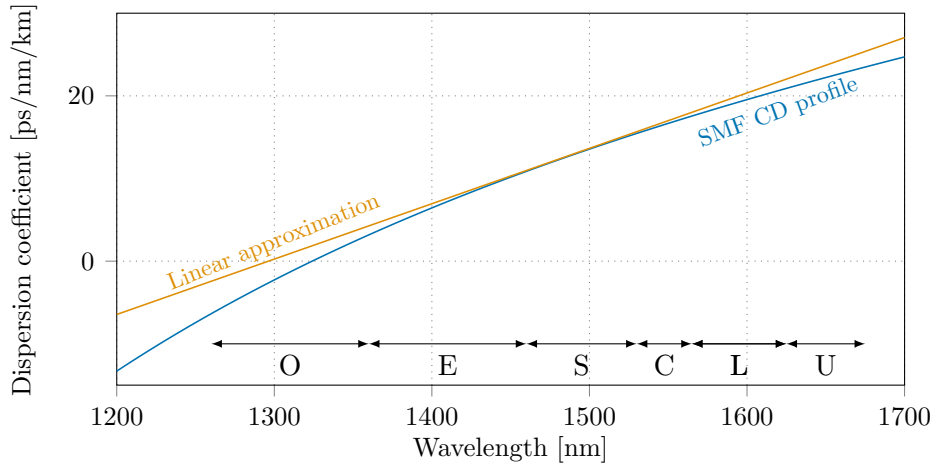


**Figure 1.10:** CD profile of a SSF (analytical expression  $D(\lambda) = \frac{S_{ZD}}{4} \lambda (1 + \frac{\lambda_{ZD}^4}{\lambda^4})$ , with  $S_{ZD} = 0.092 \text{ ps/nm}^2/\text{km}$  and  $\lambda_{ZD} = 1324 \text{ nm}$  [14]) and linear approximation with  $D_0 = 17 \text{ ps/nm/km}$  and  $S_0 = 0.092 \text{ ps/nm}^2/\text{km}$

The parameters  $S_0$  and  $D_0 = D(\lambda_0)$  are commonly used in optical communications engineering to quantify the chromatic dispersion effects. For a SMF, usual values  $D_0 = 17 \text{ ps/nm/km}$  and  $S_0 = 0.092 \text{ ps/nm}^2/\text{km}$  allow to satisfyingly approximate the CD profile over a wide wavelength range, as shown in the Fig. 1.10.

Before the advent of coherent detection and digital filtering, dispersion compensation fibers (DCF) with negative dispersion coefficient  $D$  were used in dispersion managed (DM) systems to compensate for accumulated CD in long-haul links. Dispersion compensation was performed with dispersion compensating units and/or alternation of positive and negative dispersion fiber spans to get a total CD close to 0 ps/nm/km at the end of the transmission. In modern coherent systems, the accumulated CD can be compensated at the receiver with digital filters, as presented in 1.5.b). Besides reducing nonlinear distortions compared to DM systems, electronic CD compensation allows considerable flexibility in network management, as it greatly decouples the optical path planning from the transponder design. In this work, only dispersion unmanaged (DU) systems are considered, where the CD is fully compensated at the receiver by digital filters.

### 1.3.b) Nonlinear propagation

The response of the silica fiber to light becomes nonlinear (NL) for intense electromagnetic field. The propagation of the scalar electric field  $E = E(z, t)$  is described by the nonlinear Schrödinger equation (NLSE) [18]

$$\frac{\partial E}{\partial z} = -\frac{\alpha}{2}E - j\frac{\beta_2}{2}\frac{\partial^2 E}{\partial \tau^2} + \frac{\beta_3}{6}\frac{\partial^3 E}{\partial \tau^3} + j\gamma\left(|E|^2E - T_R\frac{\partial|E|^2}{\partial \tau}E\right), \quad (1.15)$$

where  $\alpha$  is the attenuation coefficient,  $\beta_2$  is the group velocity dispersion (GVD),  $\beta_3$  is the GVD slope,  $\gamma$  is the nonlinearity coefficient,  $T_R$  is the Raman time constant and  $\tau = t - \beta_1 z$  is the retarded timeframe moving at the group velocity  $v_g = 1/\beta_1$ .

#### (i) Kerr effect

The Kerr effect corresponds to proportional variations of the refractive index  $n$  with respect to the optical field intensity. The impact of Kerr effect is described by the term  $j\gamma|E|^2E$  in the NLSE (1.15), where  $\gamma = n_2\omega/A_{eff}$  is the NL coefficient,  $n_2$  is the fiber NL Kerr refractive index and  $A_{eff}$  is the fiber effective area. For SMF, the value of  $A_{eff}$  typically ranges between 60 to 150  $\mu\text{m}^2$ , as large effective area fibers have been specially designed to show reduced NL effects [18].

The Kerr NL impairments belong to a phenomenom class called four-wave mixing (FWM). FWM can be understood by expressing the signal as the sum of different discrete spectral components. It consists in the interaction between spectral components at different frequencies  $f_1, f_2, f_3$  that results in the generation of a component at frequency  $f_0$  when  $f_0 = f_1 + f_2 - f_3$ . The strength of the component depends on system parameters, mainly the transmitted signal characteristics, the link power profile and the dispersion map.

As pictured by Fig. 1.11 representing the spectrum of a channel of interest (COI) surrounded by copropagating channels, FWM can be divided in three categories depending on the position of the interacting frequencies: (i) self-channel interference (SCI), when all interacting frequencies lie in the spectrum of the COI, (ii) cross-channel interference (XCI), when interacting frequencies belong to the COI and a single other channel and (iii) multi-channel interference (MCI), when the COI distortions arise from 2 or 3 other channels than the COI.

To quantify the NL noise power arising from Kerr effect and its impact on WDM transmission systems, a first attempt to analytically approximate the NL distortion

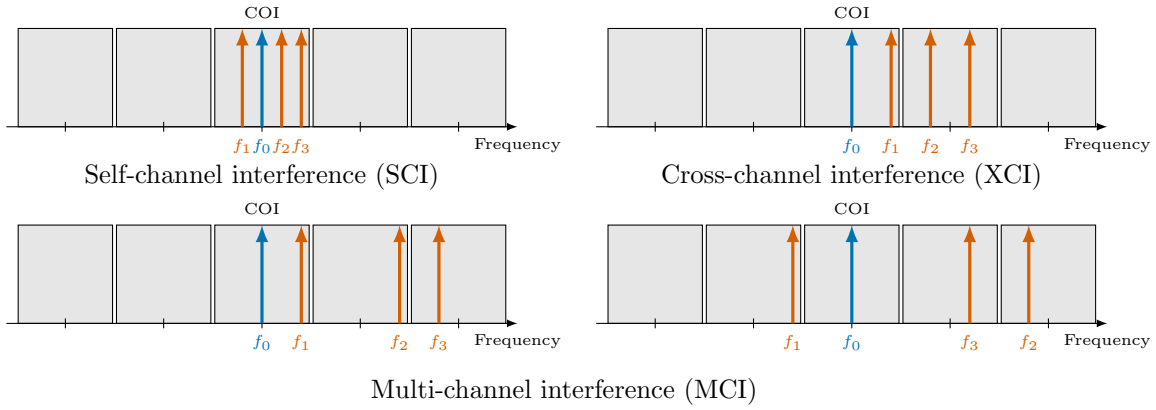


**Figure 1.11:** Schematic representation of four wave mixing (FWM) types in WDM systems depending on the position of interacting frequencies. Each filled rectangle represents a WDM channel.

spectral properties [19] used as assumption that all spectral components could be considered as Gaussian and uncorrelated. As this assumption was not correct for the DM systems used in the 1990s, with the advent of coherent detection DU systems with large accumulated CD have become practical and in this case the signal tends to behave like a stationary random process. Further work led to the Gaussian noise model (GNM) [20, 21, 22, 23], where the key assumption is that the signal, the ASE noise and the NL interferences can be considered as Gaussian signals along the propagation. The GNM provides a closed-form expression of the NL interference power as a function of the link parameters, and has been found to be a quite accurate tool to predict system performance in long-haul DU systems [24].

Another approach based on a time-domain analysis was introduced in [25], without assumption on the signal statistics. This model predicted a strong dependence of the NL variance on the modulation format, showing overestimations by the GNM, especially in the first transmission spans where the Gaussian assumptions do not generally hold [26]. The GNM was then updated in the enhanced-GNM (EGNM) to take into account the modulation format dependency, where correction terms were computed for SCI, XCI and MCI impairments [27].

Later on, the FWM interactions between the signal and the co-propagating accumulated noise coming from optical amplifiers have been included in the previous models [28, 29, 30]. NL signal noise interaction (NSNI) must indeed be taken into account to refine the prediction of uncompensated system performance in nonlinear regimes, but also to correctly estimate the expected performance of systems with NL compensation techniques presented in 1.5.b).

## (ii) Stimulated Raman Scattering

A second class of NL effects includes inelastic scattering, that implies energy exchanges between the optical field and the silica medium. Among these effects, stimulated Raman scattering (SRS) consists in the scattering of a photon of energy  $\hbar\omega_p$  by a molecule of silica, that moves to a higher-energy vibrational state, whereas a photon with lower energy  $\hbar\omega_s$  ( $\omega_s < \omega_p$ ) is generated. This generated photon enhances the optical power of the optical field around  $\omega_s$ , i.e. energy is transferred to lower frequency (higher wavelength) components. Due to the non crystalline nature of the silica, the energy level  $\hbar\omega_s$  is not unique. The Raman gain spectrum of the SMF shown in Fig. 1.12 shows a maximum transfer for a 13 THz shift, and is often

considered as linear for frequencies below this value [18, 31].

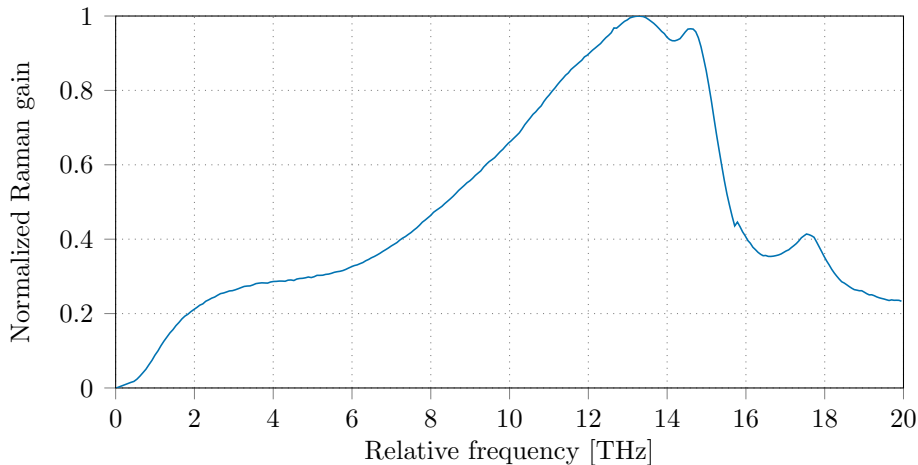


**Figure 1.12:** Example of normalized Raman gain profile for SMF

The SRS impact is in general time-dependent, since it is generated by the copropagating modulated channels. However, it has been experimentally demonstrated that for a WDM transmission using QAM modulations, the time-dependent effect of SRS crosstalk is negligible [32, 33]. The main effect of inter-channel SRS (ISRS) is the creation of a tilt of the WDM spectrum, induced by the average power transfer of high frequency (low wavelength) channels towards low frequency (high wavelength) channels. Therefore, ISRS may become detrimental due to the impact of power transfer [34]: amplified channels may experience NL distortions due to Kerr effect, and depleted channels will suffer from low power levels during amplification process. Recently, an extension of the GNM taking into account the ISRS in the propagation, called ISRS-GNM[35], has been derived to correctly predict the performance of wideband WDM systems operating in NL regimes.

As signal quality and channel capacity can be affected by ISRS, particularly in the case of wideband WDM systems, the ISRS effects are generally countered by power optimization schemes through pre-equalization methods [36]. This is discussed with more details in the chapter 5 dedicated to ultra-wideband WDM systems.

### 1.3.c) Dual polarization propagation model

When considering the dual polarization case, the two orthogonal polarizations of the optical field are described by  $\mathbf{E}(z, t) = [E^H(z, t), E^V(z, t)]^T$ .

**Polarization mode dispersion** Because of the fiber birefringence (dependence of the refractive index on the signal polarization), the polarizations travel with different group velocities. As the birefringence is due to asymmetries in the fiber stress and geometry arising from the fabrication process, the birefringence changes randomly along the fiber, and results in random coupling between the polarizations [18, 37]. This effect is referred to as polarization mode dispersion (PMD). The total PMD effect of a fiber link is commonly modeled by the transfer function

$$\mathbf{E}^{out}(z, t) = \mathbf{H}\mathbf{E}^{in}(z, t) \quad (1.16)$$

where  $\mathbf{H}$  represents the concatenation of  $N_b$  independent randomly coupled birefringent sections

$$\mathbf{H} = \prod_{i=1}^{N_b} \mathbf{R}_i \begin{bmatrix} e^{-j(\omega\tau_i+\phi_i)/2} & 0 \\ 0 & e^{j(\omega\tau_i+\phi_i)/2} \end{bmatrix} \mathbf{R}_i^{-1} \quad (1.17)$$

where  $\phi_i$  and  $\tau_i$  are respectively the phase shift and the differential group delay (DGD) between the fast and slow axes, and  $\mathbf{R}_i$  is the polarization rotation matrix relative to the orientation of the  $i$ -th section. In modern optical fibers, *PMD* coefficients are as low as 0.05 ps/ $\sqrt{\text{km}}$  [38] and due to the random orientations of the birefringent sections, the mean accumulated DGD  $\Delta\tau$  scales with the square root of the propagation distance  $L$ , i.e.  $\Delta\tau = \text{PMD}\sqrt{L}$ . The resulting DGD  $\Delta\tau$  is not detrimental for most coherent transmission systems, as it can be captured by adaptive equalizers whose task is also to track the time-varying polarization coupling at the receiver.

**Polarization dependent loss** During the propagation, polarization dependent loss (PDL), or polarization dependent gain (PDG) can be induced by discrete non-ideal optical elements such as amplifiers, ROADMs, couplers, isolators, etc. While PDL is a critical aspect in the design of optical devices, the impact of PDL accumulation in long-haul transmission is out of the scope of this thesis and is not taken into account in the propagation modeling.

**Propagation equation** It is required to rewrite the NLSE (1.15) when dual polarization signals and polarization effects are considered. The Manakov equation is commonly used to describe the coupled evolutions of  $\mathbf{E} = [E^H, E^V]^T$  in the case of random birefringence:

$$\frac{\partial \mathbf{E}}{\partial z} = -\frac{\alpha}{2} \mathbf{E} - j \frac{\beta_2}{2} \frac{\partial^2 \mathbf{E}}{\partial \tau^2} + \frac{\beta_3}{6} \frac{\partial^3 \mathbf{E}}{\partial \tau^3} + j\gamma \left( \frac{8}{9} \mathbf{E}^\dagger \mathbf{E} \mathbf{E} - T_R \frac{\partial \mathbf{E}^\dagger \mathbf{E}}{\partial \tau} \mathbf{E} \right) \quad (1.18)$$

Note that the coefficient 8/9 weighting the Kerr effect contribution comes from the averaging of PMD due to random birefringence as it is the case for propagation in SMF.

### 1.3.d) Numerical simulations of optical fiber transmission

The equations describing the single-polarization (1.15) or dual-polarization (1.18) propagation of the optical field do not generally yield analytical solutions. Therefore their approximate solutions are usually computed through numerical methods such as the split-step Fourier method (SSFM) that leverages the efficiency of fast Fourier transform (FFT) implementations in modern computers.

The SSFM consists in propagating the optical field into the fiber by small distance steps of length  $h$ . The key assumption is that in each section of length  $h$ , the linear effects (attenuation and CD) and the NL distortions (Kerr effects and inelastic scattering) can be considered to act independently. To compute the evolution of the optical field from the position  $z$  to  $z + h$ , a first operation consists in applying the linear effects in the frequency domain with efficient FFT, and the second operation corresponds to the NL distortions computation. More accurate approximation of the solution can be obtained by various computing procedures on each step, as discussed in [18].

## 1.4 Optical amplification

As pointed out in 1.3.a), single-span links would be limited to short distances without repeaters, and regenerators (with optical-electrical-optical conversion) are not suited for large-scale communication systems. As an example, for the first transatlantic optical cable TAT-8 delivered in 1988 [39], each undersea regenerator comprised of an opto-electrical receiver, an electrical amplifier and two electro-optical transmitters, one active and one spare. The transmission was limited to a single channel per fiber at 1330 nm, using 65 km spaced regenerators, without upgrade possibility for the submerged transponders.

The introduction of optical amplifiers in the early 1990s was a game changer in optical fiber communications, with the possibility of restoring the optical power after each fiber span independently of the transmitted signal properties. The length of the fiber spans is then determined by the fiber and amplifier characteristics, and usually vary between 50 and 100 km for most long-haul terrestrial and subsea links. In 1995, the first transatlantic and transpacific cables TAT-12/13 and TPC5 with optical amplifier technology were delivered [39]. The available flexibility enabled capacity upgrades as soon as 1997 on the TAT-12/13 transatlantic cable by populating the low loss window with two additional transmitters. Together with improvement of transmitter performance, WDM enabled TAT-12/13 to reach nearly 20 times the capacity of TAT-8.

### 1.4.a) Types of optical amplifiers

#### (i) Erbium doped fibre amplifier (EDFA)

Rare-earth doped fiber amplifiers, and particularly erbium doped fiber amplifiers (EDFAs), are the most common amplifiers in optical fiber communications. They were proposed in the late 1980s [40, 41] and paved the way for optical fiber networks as they enabled the first long-haul transmissions without electrical regeneration. The amplification medium is a silica fiber which has been doped with erbium ions. Laser pumps are sent in the doped fiber, together with the low-power signal to be amplified. The pumps excite the erbium ions to energy levels from which transition back to the ground level is responsible for 2 phenomena: *(i)* stimulated emission of photons of the same frequency as the incoming signal photon, enabling amplification of the signal, or *(ii)* spontaneous emission, generating noise in the same frequency band.

Using typical pump wavelength of 980 nm and 1480 nm, doped fiber lengths of few tens of meters, EDFA can typically provide gains up to 20 dB and 20 dBm output power, with noise figures around 4-5 dB. Amplification bandwidth can extend up to 40 nm, either in C or L band, and depends on the pump configuration and doped fiber length.

As the lifetime of excited erbium ions is in the order of milliseconds [42], which is order of magnitude higher than the typical symbol variations of the modulated signals (less than 0.1 ns for symbol rates higher than 10 GBd), EDFAs are insensitive to envelope variations of optical signals and their behavior is not impacted by the incoming signal, making them particularly suited for in-line amplification functions.

**(ii) Raman amplifier**

Raman amplifiers are based on the SRS effect described in 1.3.b) and use the silica fiber itself as the amplification medium. A powerful continuous wave, generated by a dedicated pump laser, is sent into the fiber together with the signal, either in the same direction (for a forward amplifier) or in the opposite direction (for a backward amplifier). A fraction of the silica molecules is therefore excited by the pump signal and if the difference between the signal and the pump frequency is within the Raman gain spectrum described in Fig. 1.12, the signal is amplified through Raman scattering. The fiber can be the transmission fiber itself (for a distributed amplifier), or a dedicated fiber with high NL behavior to shorten the amplification length (for a discrete amplifier). Furthermore, the pump itself can also be amplified with another Raman pump: such schemes are referred to as higher order Raman amplifiers.

The 3-dB Raman gain bandwidth (as the full width at half maximum (FWHM) of the peak in Fig. 1.12) is approximately 6 THz, and the amplifier bandwidth can be extended and also flattened when using multiple pumps. A huge variety of Raman amplifiers can therefore be tailored to different uses. Whereas all-Raman amplification usually combines forward and backward pumps, Raman amplification is also used in hybrid configurations using forward and/or backward pumps together with lumped amplifiers (such as EDFAs) to increase the power at the end of the span and reduce the noise generated by the lumped amplifier, as described in 1.4.b).

Although Raman amplifiers were proposed in 1972 [31] and widely researched in the 1980s, their industrial applications in transmission networks were outpaced by EDFAs until the 2000s, when the availability of compact high-power semiconductor and fiber lasers enabled easier integration of Raman amplifiers in WDM systems.

**(iii) Semiconductor optical amplifier (SOA)**

Semiconductor optical amplifiers (SOA) were proposed soon after the invention of the semiconductor laser diode in the 1960s, as the principles of these devices are close. In both cases, a Fabry-Perot cavity of semiconductor medium is electrically pumped by a driving current to obtain optical gain when incoming photons interact with the carriers in the active region through stimulated emission.

Before the advent of EDFAs, SOAs have been intensively researched for their potential applications in lightwave systems, as a compact and integrated solution for optical amplification. Their use has been ruled out due to their polarization sensitivity and their fast gain dynamics: as the carrier lifetime is in the order of magnitude of 100 ps, which is comparable with the period of the transmitted signals for  $>10$  GBd symbol rates, SOA gain varies with the envelope of the optical signal, which can lead to NL distortions. However, specific designs of SOA repeaters have recently shown to be compatible with WDM transmission requirements. More developed discussion can be found in the chapter 5, which is dedicated to the study of SOAs for ultra-wideband WDM amplification.

## 1.4.b) Noise in optical amplification

### (i) Noise figure

The noise figure (NF) concept originally comes from the RF and microwave electrical amplifier domains, where it quantifies the degradation of the SNR between the amplifier input ( $SNR^{in}$ ) and output ( $SNR^{out}$ ) [43]

$$F = \frac{SNR^{in}}{SNR^{out}}. \quad (1.19)$$

Note that the noise figure is commonly referred to its value in [dB]  $NF = 10 \log_{10} F$ .

The generalization of this definition to the optical domain is not straightforward, as the SNR is not directly measurable for optical signals. It has been shown that different approaches can lead to inconsistencies depending on the operating regimes [42, 44]. A common (but not exact) method is to evaluate the optical noise through its impact on the electrical SNR after an ideal photodetector whose performance is limited by shot noise only, leading to [42, 45]:

$$F = \frac{P_{ASE, B_{ref}}}{\hbar\omega_0 B_{ref} G} + \frac{1}{G} \quad (1.20)$$

where  $P_{ASE, B_{ref}}$  is the ASE power integrated over a reference bandwidth  $B_{ref}$ ,  $\hbar$  the reduced Planck constant,  $\omega_0$  the reference angular frequency and  $G$  the amplifier gain. The first term corresponds to the signal-spontaneous noise beating, whereas the second term corresponds to the amplification of fluctuations at the amplifier input.

This definition is compatible with the one of the RF and microwave domain [45], and the Friis formula[43] can be used to express the NF of the association of two amplifiers. For an amplifier with NF  $F_1$  and gain  $G_1$  followed by a second amplifier with NF  $F_2$  and gain  $G_2$ , the NF of the association is given by

$$F = F_1 + \frac{F_2 - 1}{G_1}. \quad (1.21)$$

### (ii) EDFA

The noise arising from ASE in optical amplification with EDFA is usually modeled as a white noise and its power spectral density (PSD) per polarization  $N_{ASE}$  is thus considered as flat. For a DP optical field, the power integrated over the reference bandwidth  $B_{ref}$  is

$$P_{ASE, B_{ref}} = 2N_{ASE}B_{ref} \quad (1.22)$$

and the per-polarization PSD of the ASE noise  $N_{ASE}$  can be described by [3]

$$N_{ASE} = (G - 1)n_{sp}\hbar\omega_0, \quad (1.23)$$

where  $n_{sp}$  is the spontaneous-emission factor of the amplifier. When considering that the term from signal-spontaneous beat noise is predominant in (1.20), and neglecting the shot noise contribution,

$$F \approx 2n_{sp} \frac{G - 1}{G} \quad (1.24)$$

so the power of the ASE contribution in the reference bandwidth around the reference wavelength can be easily expressed with the amplifier NF and gain:

$$P_{ASE,B_{ref}} = \hbar\omega_0 F G B_{ref}. \quad (1.25)$$

### (iii) Distributed Raman amplifier

For a Raman amplifier, the PSD  $N_{ASE}$  cannot be easily approximated as it results from an integration depending on the Raman gain spectrum, the fiber characteristics and the evolution of the pump power with the distance (for example, a resulting expression of the NF  $F_n$  can be found in [46, eq. (2.2.20)]).

Raman amplifiers are often characterized by their effective noise figure  $F_{eff}$ , which is defined as the NF that a fictitious discrete amplifier would need when following a passive unpumped span, to give the same NF  $F_n$  as the distributed Raman amplifier [45]. From (1.20), the NF of the unpumped span, whose gain  $G_1 = (\alpha L)^{-1}$  corresponds to the span loss, and for which the ASE noise is negligible, is simply equal to  $F_1 = 1/G_1 = \alpha L$ . From (1.21), the NF corresponding to this unpumped span followed by the fictitious lumped amplifier with NF  $F_2 = F_{eff}$  is

$$F_n = F_1 + \frac{F_2 - 1}{G_1} = \alpha L F_{eff} \quad (1.26)$$

and the effective NF is then  $F_{eff} = F_n/(\alpha L)$ . For a fixed value of the span loss  $\alpha L$ , the effective NF  $F_{eff}$  can therefore be less than 1 (negative value in [dB]).

## 1.4.c) Performance characterization of optical amplifiers

### (i) Definition

The optical signal-to-noise-ratio (OSNR) is defined as the ratio between the signal power  $P$  and the noise power in the reference bandwidth  $P_{ASE,B_{ref}}$

$$OSNR = \frac{P}{P_{ASE,B_{ref}}}. \quad (1.27)$$

Conventionally  $B_{ref}$  is equal to 12.5 GHz and is equivalently referred to as 0.1 nm for wavelength around 1550 nm.

### (ii) Single EDFA OSNR contribution

For an EDFA located after a single span, the signal power at amplifier output is

$$P = G P_{in} \exp(-\alpha L), \quad (1.28)$$

where  $P_{in}$  is the fiber span input power,  $\alpha$  the attenuation coefficient,  $L$  the fiber length and  $G$  the amplifier gain. One can therefore define the amplifier OSNR contribution  $OSNR^{amp}$  such that

$$\frac{1}{OSNR^{out}} = \frac{1}{OSNR^{in}} + \frac{1}{OSNR^{amp}} \quad (1.29)$$

and  $OSNR^{amp}$  is computed from the definition (1.27) with the output power given in (1.28) and the EDFA noise power contribution given by (1.25)

$$OSNR^{amp} = \frac{P_{in} \exp(-\alpha L)}{F \hbar\omega_0 B_{ref}} \quad (1.30)$$

A usual equation is derived by expressing (1.30) in [dB], for wavelength around 1550 nm and the reference bandwidth  $B_{ref}=12.5$  GHz,

$$OSNR^{amp}[\text{dB}] = 58[\text{dBm}] + P_{in}[\text{dBm}] - \alpha_{\text{dB}} \cdot L - NF_{\text{dB}} \quad (1.31)$$

### (iii) OSNR after multi-span link transmission

For a multi-span transmission, assuming  $N_{span}$  identical spans, with identical amplifiers after each span and considering that each amplifier independently adds a contribution whose PSD is given by  $N_{ASE}$ , the total ASE contribution is given by  $N_{span} \cdot N_{ASE}$  and the value of the OSNR at the output of the last amplifier is

$$OSNR_{link}[\text{dB}] = 58[\text{dBm}] + P_{in}[\text{dBm}] - \alpha_{\text{dB}} \cdot L - NF_{\text{dB}} - 10 \log_{10} N_{span} \quad (1.32)$$

### (iv) Benefits of distributed Raman amplification

To illustrate the advantage of hybrid amplification scheme, with a distributed Raman amplification as a preamplifier before a lumped EDFA, let's consider the case described in [42, p. 444-446], where a 50 dB loss fiber span is followed by an EDFA with  $NF_{EDFA}=5$  dB. The Raman effective NF has a minimum value  $NF_{eff} = -3.3$  dB for a Raman on/off gain  $G_{on/off,dB} = 33$  dB.

As a result, the association of this equivalent Raman amplifier with the lumped EDFA has an equivalent NF given by the Friis formula(1.21)

$$F = F_{eff} + \frac{F_{EDFA} - 1}{G_{on/off}} \quad (1.33)$$

Since  $G_{on/off,dB} = 33$  dB, the resulting NF is largely dominated by the Raman contribution  $F_{eff}$ , and the hybrid amplifier has a NF close to -3.3 dB. Using (1.31), the advantage of using distributed Raman amplification before the lumped EDFA is clear, as the link OSNR in the hybrid case is 8.3 dB higher than in the single EDFA case.

## 1.5 Coherent receiver and digital signal processing

After propagation in the optical fiber, each WDM channel is demultiplexed and sent to a dedicated coherent receiver, whose task is to convert the optical field into the electrical domain. DSP is performed on the electrical sampled waveforms to recover the transmitted symbol sequences.

### 1.5.a) Polarization and phase diversity receiver

The coherent detection consists in converting the optical modulated signal with carrier angular frequency  $\omega_{TX}$  back into four baseband electrical signals, one for each quadrature and for each polarization, thanks to the use of a local oscillator (LO), a laser with angular frequency  $\omega_{LO}$  close to the optical carrier frequency ( $\omega_{TX} \approx \omega_{LO}$ ). The four electrical signals are then sampled by ADCs. For lab experiments, high-speed oscilloscopes are usually used and data is then stored for offline DSP, whereas A/D conversion and DSP is performed with Application Specific Integrated Circuits (ASIC) in commercial systems.

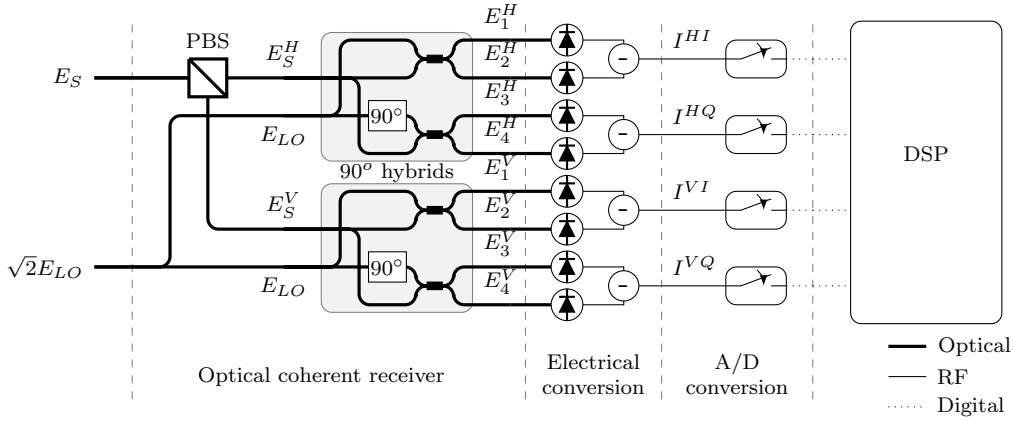


**Figure 1.13:** Schematic of coherent receiver followed by electrical conversion, sampling and offline DSP

At the input of the coherent receiver, the optical signal  $E_S$  is divided into two arbitrary but orthogonal polarization components  $E_S^V$  and  $E_S^H$  by a polarization beam splitter (PBS). Note that these components do not correspond to the original polarization components: they have been randomly coupled during propagation due to the fiber birefringence. Each component is mixed in a  $90^\circ$ -hybrid with a continuous wave  $E_{LO}$  coming from the LO. In an ideal  $90^\circ$ -hybrid, the key component is a 3 dB coupler able to add  $180^\circ$  phase shift on the signal component between the two output ports [47]. The signal is also mixed with a  $90^\circ$  phase shifted version of the LO field. As a result, the optical fields at the outputs of the two hybrid mixers are all possible combinations of the signal component  $E_S^H$  or  $E_S^V$ , its opposite generated by the  $180^\circ$  phase shift, the LO field and its quadrature. The eight resulting optical fields are given by [48]

$$\begin{bmatrix} E_1^H \\ E_2^H \\ E_3^H \\ E_4^H \end{bmatrix} = \frac{1}{\sqrt{2}} \begin{bmatrix} +E_S^H + E_{LO} \\ -E_S^H + E_{LO} \\ +E_S^H + jE_{LO} \\ -E_S^H + jE_{LO} \end{bmatrix} \quad \text{and} \quad \begin{bmatrix} E_1^V \\ E_2^V \\ E_3^V \\ E_4^V \end{bmatrix} = \frac{1}{\sqrt{2}} \begin{bmatrix} +E_S^V + E_{LO} \\ -E_S^V + E_{LO} \\ +E_S^V + jE_{LO} \\ -E_S^V + jE_{LO} \end{bmatrix}. \quad (1.34)$$

The conversion back to the electrical domain is performed with 4 balanced photodiodes. The photocurrents of each photodiode with input optical signal  $E_i$  is  $\mathcal{R}E_iE_i^*$  where  $\mathcal{R}$  is the photodiode responsivity. Balanced detection suppresses the components corresponding to direct detection, and the resulting currents are expressed by [48]

$$\begin{bmatrix} I^{HI} \\ I^{HQ} \\ I^{VI} \\ I^{VQ} \end{bmatrix} = 2\mathcal{R} \cdot \begin{bmatrix} \text{Re}(E_S^H E_{LO}^*) \\ \text{Im}(E_S^H E_{LO}^*) \\ \text{Re}(E_S^V E_{LO}^*) \\ \text{Im}(E_S^V E_{LO}^*) \end{bmatrix}. \quad (1.35)$$

As the frequency of the LO field  $E_{LO}$  is chosen to match the optical carrier frequency of  $E_S$ , the coherent detection enables to retrieve the real and imaginary parts of  $E_S^H$  and  $E_S^V$  thanks to the four photocurrents after balanced photodetection.

### 1.5.b) Digital signal processing for coherent transmissions

The single-channel DSP chain that is commonly used for the mitigation of propagation linear impairments is presented in Fig. 1.14. After A/D conversion of the outputs of the photodetectors (time sampling and quantization), the offline DSP allows to recover the symbol sequences sent over the two original polarizations of the light from the four sampled photocurrents thanks to the phase and polarization diversity described by (1.35). Such a DSP chain is able to compensate for the accumulated CD, to estimate the time-varying optical channel and mitigate PMD with an adaptive equalizer, compensate for the frequency and phase offsets between the TX and the LO lasers (carrier estimation), and equalize transmitter/receiver IQ imbalances and timing deskews with a last adaptive post-equalizer. At the end of the DSP chain, as described in Chapter 2, transmission performance is estimated from the recovered symbols  $y^H$  and  $y^V$ .

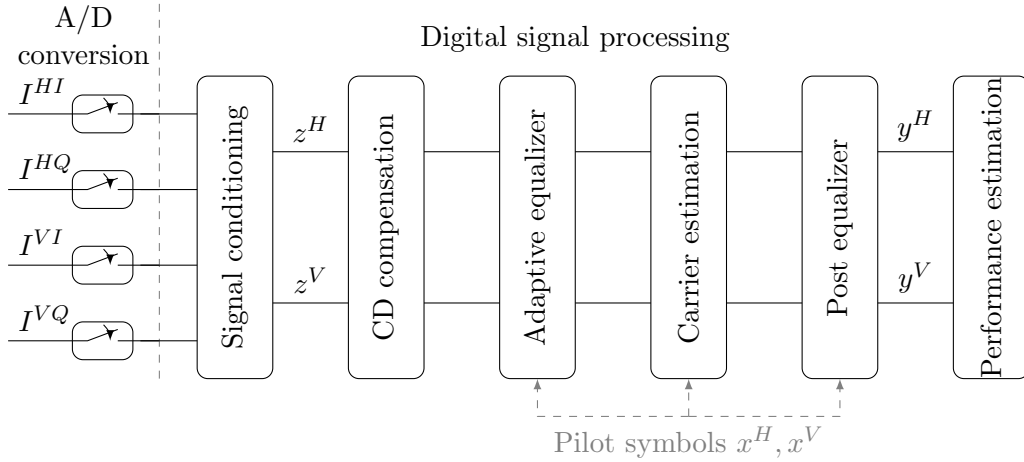


**Figure 1.14:** Single-channel coherent DSP chain for linear impairment mitigation

#### (i) Signal conditioning

After A/D conversion, the data signals are numerical waveforms, quantized with a number of levels  $2^{m_{ADC}}$  and sampled at a rate  $F_{ADC}$ , where  $m_{ADC}$  and  $F_{ADC}$  are the number of bits (resolution) and the sampling frequency of the oscilloscope. The maximum symbol rate that can be transmitted is thus theoretically limited by  $F_{ADC}/2$  to respect the Shannon-Nyquist theorem, but in practice the symbol rate

is limited by the acquisition bandwidth of the oscilloscope, that is less than the Nyquist frequency for a given sampling rate  $F_{ADC}$ .

Let's denote  $R_s$  the symbol rate of the transmitted signal. The four available waveforms are acquired with  $F_{ADC}/R_s$  samples per symbol (sps). In lab experiments, this value varies since the symbol rate of the signals is generally variable, but the sampling frequency of the oscilloscope is generally fixed. A first step is then to resample the signals at a constant value of 2 sps, the minimal value that suits the Shannon-Nyquist criterion. In practical conditions, the transmitter and the receiver do not share a common reference clock, and the exact value of  $F_{ADC}/R_s$  can slightly vary with time. However, in laboratory experiments, as the waveforms are generally short (few milliseconds), a clock tracking is not always required and the timing mismatch can, for example, be corrected by a linear compression (or dilatation) of the time axis of the receiver.

After resampling at 2 sps, the out-of-band noise can be suppressed by using a brickwall filter, i.e. an ideal bandpass filter with transfer function equal to 1 for  $|f| < f_c$ , and 0 otherwise, with  $f_c$  a frequency chosen to be slightly greater than the one-sided bandwidth  $R_s/2$ .

Finally, to suppress receiver imperfections and to simplify the DSP, any residual DC components or power imbalance on the four signals are usually corrected by mean value zeroing and power normalization.

## (ii) Chromatic dispersion compensation

In the case of a DU link, as detailed in 1.3.a), the accumulated CD during the propagation is fully compensated by a digital filter. By taking the Fourier transform of (1.12), the CD effect at the distance  $z = L$  can be represented by the transfer function

$$H^{CD}(\omega) = e^{j\omega^2(\frac{\beta_2}{2} + \frac{\beta_3}{6}\omega)L} \quad (1.36)$$

where  $\beta_2$  and  $\beta_3$  are linked to the dispersion coefficient  $D$  and slope  $S$  by (1.13) and (1.14).

In the frequency domain, the CD compensation (CDC) can be done with a filter whose transfer function is given by  $H^{CDC}(\omega) = (H^{CD}(\omega))^{-1}$ . This compensating block can also be implemented using time-domain filters designed thanks to the impulse response computed from the transfer function  $H^{CD}(\omega)$  [49]. As such a filter shows an infinite impulse response, it should be truncated with a length depending on the total accumulated dispersion. Considering modern transoceanic transmission link, with typical CD coefficient around 20.6 ps/nm/km, the dispersion induces time spread over several thousands of symbol periods. CDC with time-domain filters are not practically achievable, and frequency domain techniques such as overlap-and-save methods [50] are more efficient.

## (iii) Adaptive equalization and polarization demultiplexing

The fiber birefringence described in 1.3.c) induces polarization dependent effects during the propagation, therefore a time-varying adaptive technique is needed to

reverse the effects of polarization mixing and PMD, in order to separate the complex symbol sequences corresponding to each polarization. This is performed by an adaptive multiple-input multiple-output (MIMO) equalizer [49] as described in Fig. 1.15. In addition to polarization dependent impairments occurring during the propagation in the fiber, a multi-tap equalizer can mitigate other imperfections of the communication channel, balance the impact of temporal offset in sampling instant by distributing the response over adjacent taps, and estimate the matched filter corresponding to the pulse-shaping at the transmitter, coupled to a potential channel frequency-dependent response, as well as compensate for residual CD [51].

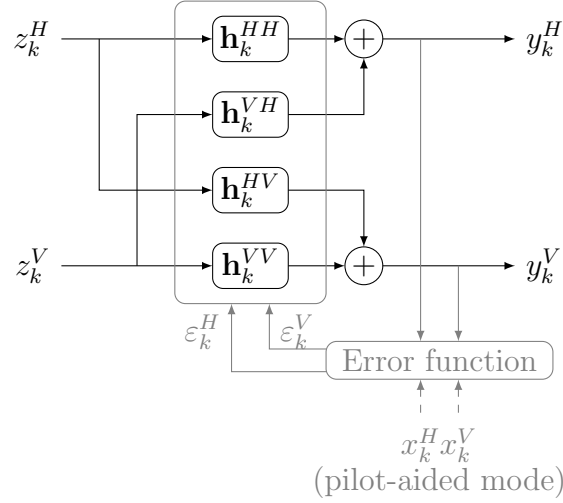


**Figure 1.15:** Adaptive equalizer with butterfly structure for time-varying channel estimation

To recover the original polarizations from the mixed components received by the polarization-diversity receiver, the outputs  $y_k^H$  and  $y_k^V$  of the butterfly structure are computed by

$$\begin{bmatrix} y_k^H \\ y_k^V \end{bmatrix} = \begin{bmatrix} (\mathbf{h}_k^{HH})^T & (\mathbf{h}_k^{VH})^T \\ (\mathbf{h}_k^{HV})^T & (\mathbf{h}_k^{VV})^T \end{bmatrix} \begin{bmatrix} \mathbf{z}_k^H \\ \mathbf{z}_k^V \end{bmatrix} \quad (1.37)$$

where  $\mathbf{z}_k^H = [z_{k-N_T}^H, \dots, z_{k+N_T}^H]^T$  and  $\mathbf{z}_k^V = [z_{k-N_T}^V, \dots, z_{k+N_T}^V]^T$  contains  $2N_T + 1$  values of the inputs centered on the  $k$ -th symbol, and  $\mathbf{h}_k^{HH}, \mathbf{h}_k^{VH}, \mathbf{h}_k^{HV}, \mathbf{h}_k^{VV}$  are vectors containing the  $2N_T + 1$  equalizer taps. The task is thus to find the time-varying equalizer filter taps as a function of the time  $k$ . Considering input signals with 2 sps, the  $2N_T + 1$  equalizer taps are updated with gradient descent method [49]

$$\begin{aligned} \mathbf{h}_{2k+2}^{HH} &:= \mathbf{h}_{2k}^{HH} + \mu \cdot \varepsilon_{2k}^H \cdot y_{2k}^H \cdot (\mathbf{z}_{2k}^H)^* \\ \mathbf{h}_{2k+2}^{VH} &:= \mathbf{h}_{2k}^{VH} + \mu \cdot \varepsilon_{2k}^H \cdot y_{2k}^H \cdot (\mathbf{z}_{2k}^V)^* \\ \mathbf{h}_{2k+2}^{HV} &:= \mathbf{h}_{2k}^{HV} + \mu \cdot \varepsilon_{2k}^V \cdot y_{2k}^V \cdot (\mathbf{z}_{2k}^H)^* \\ \mathbf{h}_{2k+2}^{VV} &:= \mathbf{h}_{2k}^{VV} + \mu \cdot \varepsilon_{2k}^V \cdot y_{2k}^V \cdot (\mathbf{z}_{2k}^V)^* \end{aligned} \quad (1.38)$$

where  $\mu$  is the parameter that is used to tune the speed of the convergence and tracking, and the costs  $\varepsilon_k^H$  and  $\varepsilon_k^V$  to be minimized are computed by an error function as described in the following.

**Constant modulus algorithm** A common algorithm known as constant modulus algorithm (CMA) [52] is used for constant amplitude signals such as QPSK, and is

based on the error function

$$\begin{aligned}\varepsilon_k^H &= C - |y_k^H|^2 \\ \varepsilon_k^V &= C - |y_k^V|^2\end{aligned}\tag{1.39}$$

where the value of the target constant amplitude  $C$  is arbitrary. The output signals  $y_k^H$  and  $y_k^V$  are usually normalized after the equalization, so that the value of  $C$  has no impact after convergence for the rest of the DSP. Even if CMA is designed for constant amplitude signals such as QPSK, it can also be used for higher-level QAM modulation formats ([49] and references herein).

**Multi-modulus algorithm** In the case of multi-modulus modulation formats, the error function can be set as

$$\begin{aligned}\varepsilon_k^H &= \hat{r}(y_k^H)^2 - |y_k^H|^2 \\ \varepsilon_k^V &= \hat{r}(y_k^V)^2 - |y_k^V|^2\end{aligned}\tag{1.40}$$

where  $\hat{r}(\cdot)$  gives for each equalized symbol  $y_k^H$  or  $y_k^V$ , the closest symbol radius in the constellation. This multi-modulus algorithm (MMA) is known as a decision-directed [53] or radius-directed equalizer.

**Pilot-aided algorithm** To ease the initial convergence of the algorithms or to improve the equalizer performance, known pilot symbols can be inserted in the sent sequences and used at the receiver. The error function is then

$$\begin{aligned}\varepsilon_k^H &= (1 - p_k^H)(\hat{r}(y_k^H)^2 - |y_k^H|^2) + p_k^H(|x_k^H|^2 - |y_k^H|^2) \\ \varepsilon_k^V &= (1 - p_k^V)(\hat{r}(y_k^V)^2 - |y_k^V|^2) + p_k^V(|x_k^V|^2 - |y_k^V|^2)\end{aligned}\tag{1.41}$$

where  $x_k^H$  and  $x_k^V$  are the  $k$ -th transmitted symbols (used as known pilots), the pilot gating functions  $p_k^H$  and  $p_k^V$  are binary functions indicating the positions of the pilot symbols in the sequences  $x_k^H$  and  $x_k^V$ .

In a pilot-aided mode, it is required to first synchronize the received signals and the transmitted sequences. A double stage adaptive equalizer can therefore be required, in particular for high-complexity constellation such as PCS modulation formats. A first CMA is used to perform a coarse polarization demultiplexing, allowing to identify synchronization patterns that have been inserted in the symbol sequences. The received signals can then be synchronized with the pilot gating functions and the transmitted sequences, so that the pilot-aided algorithm completes the polarization impairments mitigation and performs estimation of matched filter and channel frequency response.

After adaptive equalization performed with 2 sps to be able to estimate channel characteristics without spectral aliasing, the signals are usually down-sampled at 1 sps and the remaining DSP algorithms are performed at symbol time.

#### (iv) Carrier frequency and phase estimation

As mentioned in the architecture of the coherent receiver in Fig. 1.13, the LO laser must have an angular frequency  $\omega_{LO}$  close to the one of the TX laser  $\omega_{TX}$ , to convert

the modulated signal around the carrier frequency down to a baseband modulated signal. However the two different lasers have slightly different frequencies and also generate instantaneous phase noise (PN). The carrier estimation then consists in a first coarse compensation of the phase offset due to the laser angular frequency difference  $\delta\omega = \omega_{TX} - \omega_{LO}$ , followed by a fine estimation of the slowly varying phase  $\theta_k$  due to random PN arising from both TX and LO lasers.

Assuming that the previous algorithms have completely compensated for CD, DGD, PMD and performed polarization demultiplexing, the signal of one of the  $H$  or  $V$  polarizations can be written as:

$$y_k = x_k e^{j\phi_k + j\theta_k} + n_k \quad (1.42)$$

where  $x_k$  and  $y_k$  are the  $k$ -th sent and received symbols,  $\phi = \delta\omega T_S$  the discrete value of the phase due to laser frequency offset sampled at symbol time  $T_S$ ,  $\theta_k$  a discrete time-varying phase and  $n_k$  an additive complex Gaussian noise.

**Frequency estimation** In the case of QPSK symbols, with a constant phase rotation of the constellation, the possible symbols can be taken as the four roots of unity, such that  $(x_k)^4 = 1$ . This interesting property leads to

$$(y_k)^4 = (x_k e^{j\phi_k + j\theta_k} + n_k)^4 = e^{j4\phi_k + j4\theta_k} + w_k \quad (1.43)$$

where  $w_k$  is a zero-mean process containing  $n_k^4$  and all cross-products of powers of  $e^{j\phi_k + j\theta_k}$  and  $n_k$ . The random phase  $\theta_k$  being still unknown, the frequency offset is then estimated from the block-wise maximization of the periodogram [54] of  $(y_k)^4$

$$\hat{\phi}_k = \frac{1}{4} \operatorname{argmax}_{\phi} \left| \frac{1}{2N+1} \sum_{l=-N}^N (y_{k+l})^4 e^{-j\phi l} \right|^2 \quad (1.44)$$

where  $2N+1$  is the number of samples used to average the zero-mean noise  $w_k$  of (1.43).

This method can be extended by noting that  $E[(y_k)^4] \neq 0$  for any  $2^m$ QAM format, the maximization method described in (1.44) is still valid for estimation of frequency offset with  $2^m$ QAM constellations [54].

**Phase estimation** After frequency estimation, the signal of one of the  $H$  or  $V$  polarizations can be written as:

$$y_k = x_k e^{j\theta_k} + n_k \quad (1.45)$$

To estimate the phase  $\theta_k$ , the blind phase search (BPS) algorithm [55] consists in taking blocks of  $2N+1$  received symbols around  $y_k$ , and trying to find an angle  $\hat{\theta}_k$  that minimizes the sum of the squared distances between the rotated received symbols and the closest constellation symbol, i.e.

$$\hat{\theta}_k = \operatorname{argmin}_{\theta} \sum_{l=-N}^N J(y_{k+l}, \theta) \quad (1.46)$$

where the decision-aided cost function associated to one symbol is defined by

$$J(y_k, \theta) = \left| y_k e^{-j\theta} - \hat{d}(y_k e^{-j\theta}) \right|^2 \quad (1.47)$$

with  $\hat{d}(y_k e^{-j\theta})$  the estimated symbol from the rotated received symbol  $y_k e^{-j\theta}$ .

For all the QAM formats considered in this thesis, the constellation shows a rotational symmetry of order 4, meaning that the cost function is periodic and (1.46) does not show a global minimum. This algorithm therefore tests equally spaced phases between 0 and  $\pi/2$ , then removes possible phase discontinuities and the cycle slips induced by phase ambiguity are estimated and removed thanks to pilot symbols in the sequences.

When using high-complexity constellation such as PCS modulation formats, similarly to the adaptive equalizer, this algorithm can be modified to use pilot symbols in the estimation process, using pilot gating functions  $p_k$  as previously defined. The cost function is then

$$J(y_k, \theta) = (1 - p_k) \left| y_k e^{-j\theta} - \hat{d}(y_k e^{-j\theta}) \right|^2 + p_k \left| y_k e^{-j\theta} - x_k \right|^2. \quad (1.48)$$

### (v) Adaptive post-equalization

At this stage, all major impairments arising from the propagation in the optical fiber channel have been removed. However, before performance estimation a last DSP block called post-equalizer can be implemented to compensate for phase or gain mismatch between  $I$  and  $Q$  components of each polarization. Phase shift or gain imbalance can indeed arise from mismatches between the DAC outputs at the transmitters, from incorrect settings of the modulator operating point, or from differences in physical paths in the optical or electrical circuits.

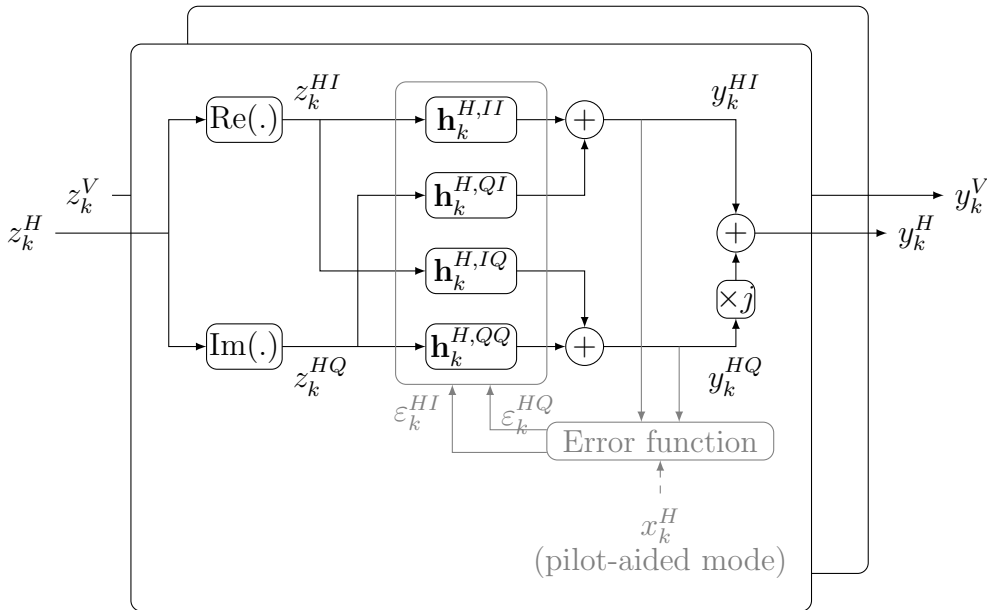


**Figure 1.16:** Adaptive post-equalizer with butterfly structure

In this thesis, the post-equalizer architecture described in Fig. 1.16 is considered. Whereas the  $2 \times 2$  MIMO adaptive equalizer presented in Fig. 1.15 for polarization

demultiplexing has two complex inputs (the two polarizations), here a  $2 \times 2$  MIMO post-equalizer is defined per polarization, and for each polarization it takes as inputs the real and imaginary values of the complex symbol, to be able to compensate  $IQ$  imbalances from the TX side. The implementation aspects are similar to the algorithms presented for polarization demultiplexing and are not detailed here.

### (vi) Nonlinear compensation techniques

As presented in 1.3.b), the NL impairments arising from intra and inter-channel FWM through SCI, XCI and MCI are deterministic and could in theory be compensated by means of DSP, provided that the link structure (dispersion map, fiber power profile evolution, etc) is perfectly known.

The most commonly used algorithm for nonlinear compensation (NLC) is the digital back propagation (DBP) [56]. This technique consists in digitally propagating at the receiver the optical field in a virtual link representing the physical fiber channel. This algorithm has been widely researched since 2008 and has enabled impressive experimental transmission reach increases compared to uncompensated transmissions. Similarly to SSFM to approximate the optical field evolution with numerical simulations (see 1.3.c), in DBP the virtual link is divided in  $N_{steps}$  elementary sections of length  $h$ , where CD and NL effects are assumed to be independent.

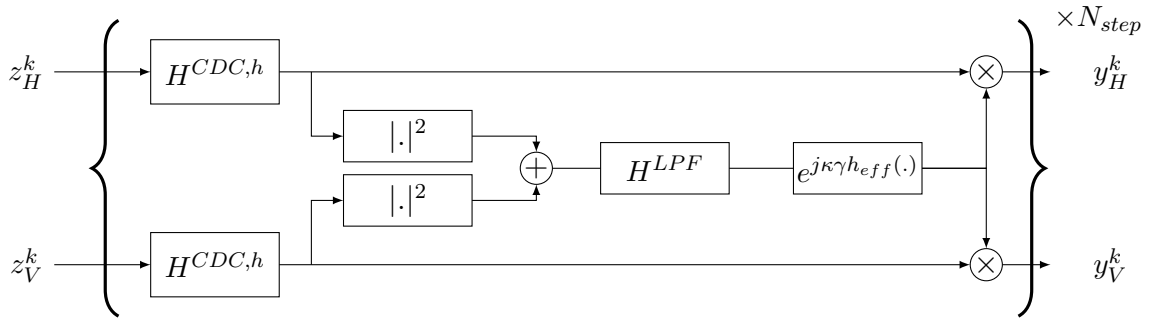


**Figure 1.17:** NL compensation (NLC) technique using digital back-propagation (DBP)

As shown in Fig. 1.17, the DBP replaces the CDC block and consists in applying through SSFM the inverse CD and NL operations given by the NLSE (1.18) on a succession of elementary sections:  $H^{CDC,h}$  is the per-section CDC, then the nonlinear section is phase shift depending on the instantaneous power, where  $\gamma$  is the NL coefficient,  $h_{eff} = (1 - e^{-\alpha h})/\alpha$  the step effective length and  $\kappa$  is a parameter to be optimized [56]. Besides, a similar technique can be applied at the transmitter side to precompensate the NL distortions, as shown in [57] or with a hybrid scheme with precompensation at the transmitter and DBP at the receiver [58].

The main drawback of DBP is its high computational complexity as it requires a huge number of FFT computations. Several approaches have been proposed to reduce its complexity. As an example, the filtered DBP (FDBP) [59] allows to increase  $h$  and reduce  $N_{steps}$  without sacrificing performance. As shown in Fig. 1.17, a low-pass filter  $H^{LPF}$  is used to smooth the optical field power after CDC.

Another approach is based on perturbation theory and called perturbative NLC (PNLC). As the time-domain analysis can be used to analytically approximate the

NL perturbations during the optical field propagation (see 1.3.b)), PNLC precalculates the distortions that affect the received samples  $z_k^V$  and  $z_k^H$  and correct them as

$$y_k^H = z_k^H - \kappa \delta z_k^H \quad (1.49)$$

$$y_k^V = z_k^V - \kappa \delta z_k^V \quad (1.50)$$

$$(1.51)$$

where the computed predistortions  $\delta z_k^H$  and  $\delta z_k^V$  are functions of the received samples  $z_k^V$  and  $z_k^H$  and coefficients depending on the power profile, the dispersion map and the pulse shape, as given in [60].

In practice, although these different approaches can be used to correct SCI impairments, XCI and MCI are often considered to be prohibitively complex for WDM commercial systems. The full-field NLC techniques are not only computationally costly, they also require the knowledge of all the co-propagating channels. In particular, they are impossible in meshed networks where neighboring WDM channels can be added or dropped at each network node, and the co-propagating channels are therefore unknown. Most NLC schemes therefore focus on intra-channel impairments, whereas inter-channel impairments are commonly considered as additive noise.

## 1.6 Summary

In this chapter, we have introduced optical coherent communications and WDM transmission system architectures that has been developed in the past three decades and that constitute the backbone of the global Internet network. We have presented the modeling of the physical layer of the optical communication channel, including the optical signal generation, the propagation in the optical fiber, the reception and opto-electrical conversion, as well as the compensation of the propagation effects by means of DSP.

We have presented the key elements to model propagation impairments, as well as the DSP tools to recover the transmitted constellation symbols. In the next chapter, we present the metrics to evaluate the transmission system performance from the received symbols and quantify the achievable information rate of the transmission system.

# Chapter 2

## Performance and capacity assessment of coherent transmission systems

In this chapter, we introduce the metrics that enable to characterize the communication system performance from the recovered symbols after transmission in the optical communication channel (transmitter, propagation, reception and DSP). We present a brief overview of FEC codes allowing high capacity optical transmissions. We review some concepts of information theory to derive the Shannon capacity, that upper bounds the information rate of the optical channel. We detail the modulation and coding constraints on  $2^m$ QAM and PCS $2^m$ QAM achievable information rate, and we conclude this chapter by stating the motivation of the work presented in the remaining chapters of this thesis.

### Contents of this chapter

---

<b>2.1</b>	<b>Impact of various noise sources</b>	<b>44</b>
2.1.a)	Transceiver (back-to-back) penalties	45
2.1.b)	Transmission line impairments	45
2.1.c)	Multi-span transmission system modeling	46
<b>2.2</b>	<b>Transmission errors and error correction</b>	<b>48</b>
2.2.a)	Hard-decision schemes	48
2.2.b)	Soft-decision and advanced FEC	49
<b>2.3</b>	<b>Information theory and theoretical limits</b>	<b>50</b>
2.3.a)	Mutual information	50
2.3.b)	Source entropy	50
2.3.c)	Capacity of the optical channel	51
<b>2.4</b>	<b>Practical limits and capacity approaching systems</b>	<b>52</b>
2.4.a)	Modulation constraints	52
2.4.b)	Coding constraints	55
2.4.c)	Achievable rates for QAM systems	57
<b>2.5</b>	<b>Trends for high capacity links</b>	<b>59</b>
2.5.a)	Multiplexing through the physical dimensions	59
2.5.b)	Optimization of optical bandwidth utilization	60

---

## 2.1 Impact of various noise sources

The optical communication channel described in Chapter 1 encompasses the transmitter (TX DSP, D/A conversion and electro-optical modulation), the propagation (in the optical fiber and network elements) and the receiver (including opto-electrical conversion, A/D sampling and RX DSP to compensate for transmission impairments). Fig. 2.1 summarizes this equivalent model. At the transmitter, the CM encoder generates the transmitted symbols  $x_k$ , and we note  $y_k$  the recovered symbols after DSP. We note with  $X$  and  $Y$  the random variables whose realizations are  $x_k$  and  $y_k$ . In this chapter, we introduce the metrics to characterize the optical communication channel, and we present the limits in terms of achievable information rate for theoretical and practical modulation and coding schemes.

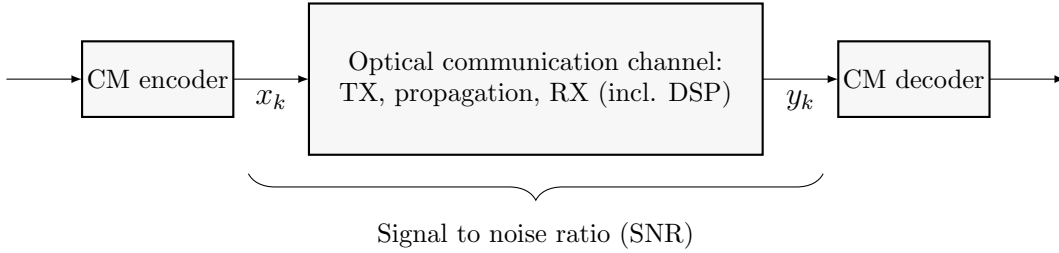


**Figure 2.1:** Optical communication channel in the digital communication system

In long-haul optical fiber systems such as the ones considered in this work, the different noise sources described in the previous chapter can be well described by Gaussian statistics, so the signal-to-noise ratio (SNR) is a suitable metric to characterize the impairments of the communication system physical layer.

Assuming the received signal is corrupted by an additive noise which is independent from the sent signals, for a sufficiently large number of samples  $N_S$ , the SNR can be computed as [61]

$$SNR = \left( \frac{|\mathbf{x}|^2 |\mathbf{y}|^2}{|\mathbf{y}^\dagger \mathbf{x}|^2} - 1 \right)^{-1} \quad (2.1)$$

where  $\mathbf{x} = [x_1, \dots, x_{N_S}]^T$  and  $\mathbf{y} = [y_1, \dots, y_{N_S}]^T$  are vectors containing the samples of the transmitted and recovered symbols, and  $\dagger$  is the conjugate transpose operation. This expression results from the least squares estimation of the signal power within the power-normalized received samples.

Assuming that all sources of impairments can be modeled as additive and uncorrelated white Gaussian noises, the total noise variance is composed of the summation of the different noise contributions and the resulting SNR is described by

$$SNR = (SNR_{TRX}^{-1} + SNR_{line}^{-1} + SNR_{extra}^{-1})^{-1} \quad (2.2)$$

where  $SNR_{TRX}$  represents the transceiver (TRX) implementation impairments,  $SNR_{line}$  accounts for the transmission line impairments and the third term  $SNR_{extra}^{-1}$  accounts for additional penalties that cannot be attributed to the TRX or the line exclusively, such as filtering penalties (see chapter 3), equalization-enhanced phase noise (see chapter 4), and other effects (crosstalk penalties, polarization impairments, residual chromatic dispersion, etc) that are not modeled in detail in this thesis.

### 2.1.a) Transceiver (back-to-back) penalties

The performance of the overall system is first limited by the impairments coming from both the TX and the RX. The conversion steps from the DAC at the TX and the ADC at the RX induce quantization and electronic noise. The signal can also be corrupted by distortions induced by finite-length, non-ideal filters used for pulse-shaping, predistortion and equalization, or bandwidth limitations from electrical and electro-optical components. Moreover, the power at the TX output is limited by the insertion and modulation power losses and the use of optical amplifiers leads to ASE noise. In this thesis, the maximum achievable SNR of the TRX is described by

$$SNR_{TRX} = \frac{1}{k_{TRX}} \quad (2.3)$$

where the normalized variance  $k_{TRX}$  accounts for all the aforementioned TRX penalties and is experimentally measured in back-to-back configuration.

### 2.1.b) Transmission line impairments

The transmission line noise contribution can be separated into a linear part  $SNR_{ASE}$  accounting for ASE noise from the amplifiers and a NL contribution  $SNR_{NL}$  corresponding to NL propagation impairments

$$SNR_{line}^{-1} = SNR_{ASE}^{-1} + SNR_{NL}^{-1} \quad (2.4)$$

when neglecting other effects such as guided acoustic Brillouin scattering (GAWBS) and signal droop.

#### (i) ASE noise from optical amplifiers

As detailed in 1.4.b), ASE occurs in the optical amplification process and degrades the OSNR according to the formula (1.32). The OSNR takes into account the noise in the reference bandwidth  $B_{ref}$ , whereas the SNR accounts for the noise variance  $\sigma_{ASE}^2$  in the signal bandwidth defined by the symbol rate  $R_s$ . Assuming a locally white noise, the corresponding SNR is computed as

$$SNR_{ASE} = \frac{P_{ch}}{\sigma_{ASE}^2} = \frac{B_{ref}}{R_s} OSNR \quad (2.5)$$

where  $P_{ch}$  is the per-channel power at the amplifier output (fiber input) and  $\sigma_{ASE}^2 = P_{ASE, B_{ref}} \cdot R_s / B_{ref}$ .

The SNR versus OSNR curve can be measured in a back-to-back configuration, by sweeping OSNR while adding variable ASE noise to the signal. Fig. 2.2 shows the back-to-back characterization of an arbitrary 49 Gbd signal, with various values of TRX impairments  $SNR_{TRX}$ . In the high OSNR region, the SNR accounting for TRX and ASE impairments saturates at the value  $SNR_{TRX}$  (three cases corresponding to values of 22.5, 20 and 17.5 dB are shown here), corresponding to the TRX intrinsic penalties. When the OSNR decreases, i.e. the ASE noise becomes dominant, the SNR is limited by the  $SNR_{ASE}$  that originates from the optical amplification process.

The SNR versus OSNR curve is a useful design tool to predict the performance of transmission systems, assuming only transceiver impairments and additive ASE

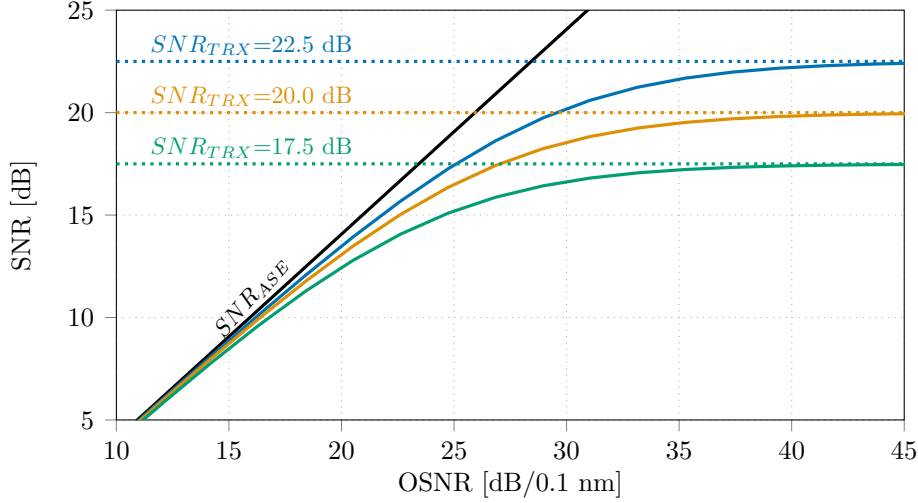


**Figure 2.2:** Typical SNR versus OSNR curve for arbitrary symbol rate of 49 GBd and different TRX impairments

noise from optical amplifiers. For a given target SNR value, the required OSNR value can be determined from this curve and specifies the optical channel requirements, i.e. the acceptable penalties from the optical line in a transmission usecase.

## (ii) Nonlinear propagation

The Kerr NL distortions described in 1.3.b) are usually modeled as an additive Gaussian noise source with variance  $\sigma_{NL}^2 = a_{NLI}P_{ch}^3$ , where the NL coefficient  $a_{NLI}$  depends on the COI channel characteristics, the WDM co-propagating channels and the fiber link properties. The strength of the NL interferences can be computed numerically by SSFM simulations, measured experimentally or predicted with analytical models such as the ones introduced in 1.3.b). The SNR accounting for the NL fiber impairments is then expressed as

$$SNR_{NL} = \frac{P_{ch}}{\sigma_{NL}^2} = \frac{1}{a_{NLI}P_{ch}^2}. \quad (2.6)$$

The NL distortions can be separated in two contributions (intra- and inter-channel)

$$a_{NLI} = a_{NLI,intra} + a_{NLI,inter} \quad (2.7)$$

where the expressions of  $a_{NLI,intra}$  and  $a_{NLI,inter}$  depend on the link characteristics and the properties of the COI and the co-propagating WDM signals, as given in [30] in the case of a WDM point-to-point link, with identical spans, same pulse-shaping and modulation formats over all co-propagating channels.

### 2.1.c) Multi-span transmission system modeling

The overall SNR of the transmission system accounting for TRX impairments, ASE amplifier noise and NL fiber distortions is then

$$SNR = \frac{P_{ch}}{\sigma_{ASE}^2 + k_{TRX}P_{ch} + a_{NLI}P_{ch}^3} \quad (2.8)$$

The SNR as a function of the channel power  $P_{ch}$  shows a maximum value, for an optimal power value  $P_{ch,NLT}$

$$P_{ch,NLT} = \left( \frac{\sigma_{ASE}^2}{2a_{NLI}} \right)^{1/3} \quad (2.9)$$

and this maximum SNR value is called the NL threshold (NLT)

$$SNR_{NLT} = \left( k_{TRX} + 3 \left( \left( \frac{\sigma_{ASE}^2}{2} \right)^2 a_{NLI} \right)^{1/3} \right)^{-1}. \quad (2.10)$$

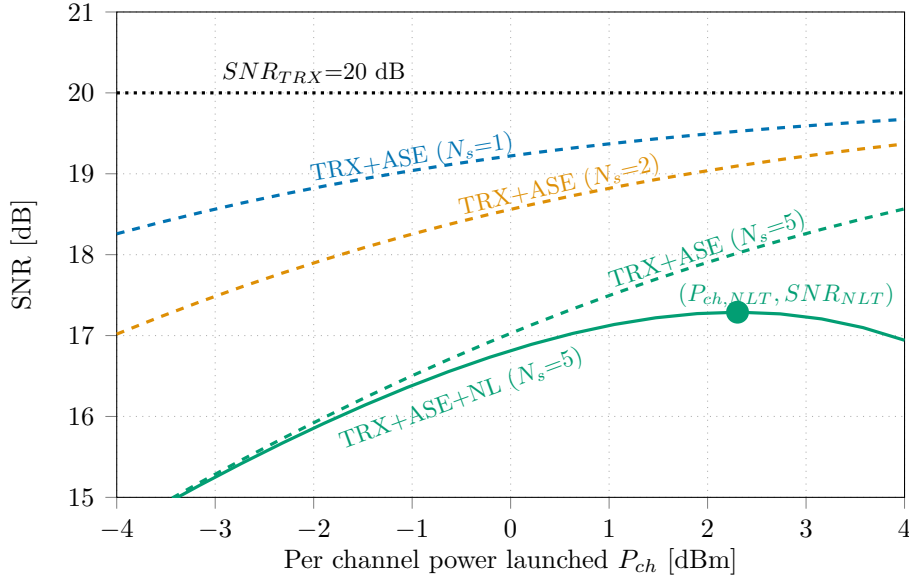


**Figure 2.3:** SNR evolution versus per-channel power  $P_{ch}$  in linear transmission case of a 49 Gbd signal (1, 2 or 5 spans of 100 km SSMF) and with arbitrary nonlinear impairments for the case of 5 spans.

Fig. 2.3 shows the evolution of the SNR as a function of the per channel power  $P_{ch}$  of a 49 Gbd signal. The SNR in dashed lines accounts for the TRX impairments (set to  $SNR_{TRX} = 20$  dB as shown by the black dotted line) and the linear ASE contribution, for a link composed of 1, 2 or 5 spans of 100 km SSMF (20 dB span loss). Each span is followed by an EDFA with a NF of 5 dB. When considering only the linear impairments, increasing the launched power enables to limit the degradation due to the ASE noise and the SNR tends towards the TRX limits. When taking into account the NL impairments, here with an arbitrary value  $a_{NLI} = 10^3 \text{ W}^{-2}$  for the 5 span case, the overall SNR (solid line) exhibits a maximal value  $SNR_{NLT}$  for an optimal power  $P_{ch}$ , that depends on the TRX characteristics and the fiber link properties through the ASE noise variance and the nonlinear coefficient  $a_{NLI}$ . The optimal performance is obtained as the best trade-off between ASE noise in the linear regime and NL impairments in high power regime.

## 2.2 Transmission errors and error correction

The previous section presented the characterization of the optical communication channel in terms of symbol distortions. The performance of the transmission system is ultimately evaluated in terms of transmission errors, and the bit error rate (BER) requirements to declare "error-free" transmission is between  $10^{-12}$  in the late 1990s to as low as  $10^{-16}$  today [48]. Without error correcting schemes, such requirements would impose prohibitively high SNR targets and low transmission distances.

To overcome these limits, FEC techniques have been introduced in optical fiber communications in the 1990s [48, 62, 63]. The idea of channel coding is to add redundancy in data at the transmitter, and exploit this redundancy at the receiver to reduce the BER through FEC decoding. To do so, FEC encoder takes blocks of  $K_c$  information bits and outputs  $N_c$  bits, adding  $N_c - K_c$  redundant bits, and we define the code rate  $r_c = K_c/N_c$  and the FEC overhead

$$OH_c = \frac{N_c - K_c}{K_c} = \frac{1}{r_c} - 1. \quad (2.11)$$

Fig. 2.4 gives the architecture of the corresponding system, and from now on we assume that the CM encoder can be represented as a binary FEC encoder followed by a memoryless bit-to-symbol mapper, and that at the receiver the CM decoder comprises of a demapper followed by a binary FEC decoder. This approach is suboptimal compared to the optimal CM scheme, but is more practical as it enables the use of widely explored binary FEC encoders and decoders [64]. We note  $x_k$  and  $y_k$  the symbols at the optical communication channel input and output, and  $b_{k,j}$  the  $j$ -th bit of the label of the  $k$ -th symbol  $x_k$ .

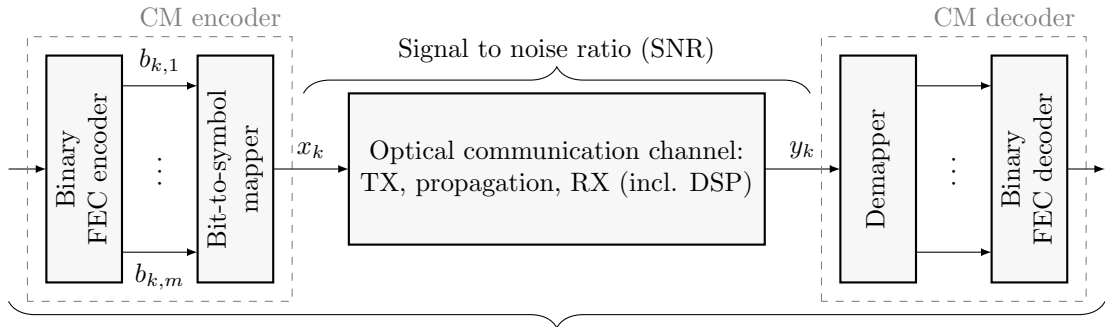


**Figure 2.4:** Optical communication channel with binary FEC encoder and decoders

### 2.2.a) Hard-decision schemes

In a hard decision (HD) scheme, for each recovered symbol  $y_k$  a symbol decision  $\hat{x}_k$  can be made among all possible symbols in the constellation  $\mathcal{A}$  using the maximization of the posterior probability  $p_{X|Y}$

$$\hat{x}_k = \underset{a \in \mathcal{A}}{\operatorname{argmax}} p_{X|Y}(a|y_k). \quad (2.12)$$

When the physical channel impairments are modeled by an equivalent additive Gaussian noise, this is equivalent to

$$\hat{x}_k = \underset{a \in \mathcal{A}}{\operatorname{argmin}} \left( |y_k - a|^2 - \frac{p_X(a)}{SNR} \right) \quad (2.13)$$

where  $p_X$  is the prior distribution of the transmitted symbols.

In this case, the bit demapper produces the output bits  $\hat{b}_{k,1}, \dots, \hat{b}_{k,m}$  from the symbol decisions  $\hat{x}_k$  by merely reversing the bit-to-symbol mapping function and the system performance can be evaluated over  $N_s$  symbols by the pre-FEC BER

$$BER_{pre} = \frac{1}{mN_s} \sum_{k=1}^{N_s} d_H(x_k, \hat{x}_k) \quad (2.14)$$

where  $d_H(x_k, \hat{x}_k) = \sum_{j=1}^m (1 - \delta(b_{k,j}, \hat{b}_{k,j}))$  is the Hamming distance between the sent symbol  $x_k$  and the symbol decision  $\hat{x}_k$ , and  $\delta(a, b)$  is the Kronecker delta function ( $\delta(a, b)$  is 1 if  $a = b$ , and 0 if  $a \neq b$ ).

In HD schemes, the FEC requirements are often described by the pre-FEC BER ( $BER_{pre}$ ), i.e. the BER at the FEC input that is required to ensure a given BER ( $BER_{post}$ ) at the FEC output. In the first generation of FEC for optical communications introduced in the mid 1990s, the Reed-Solomon RS(255,239) code (standardized by ITU-T G975 [65]) used 6.7% overhead and  $BER_{pre}$  of  $10^{-4}$  for  $BER_{post}$  of  $5 \times 10^{-15}$ . In the late 1990s, a second generation of codes, using higher complexity codes or concatenation of two low-complexity codes, enabled more powerful correction with longer code block lengths. A popular scheme is the concatenation of two Bose-Chaudhuri-Hocquenghem (BCH) codes as defined in ITU-T G975.1 [66], with a total overhead of 6.7% and  $BER_{pre}$  of  $3.1 \times 10^{-3}$  and  $BER_{post}$  of  $10^{-16}$ .

### 2.2.b) Soft-decision and advanced FEC

Whereas the first and second generation codes were based on HD schemes, the third generation introduced soft-decision (SD) to improve decoding performance, thanks to high resolution ADC, coherent detection and advanced DSP. In SD schemes, the demapper outputs soft information (e.g. bit-wise probabilities, as in section 2.4.b)) instead of HD bits, and this soft information is used by the SD FEC decoder.

Together with block Turbo codes, low density parity check (LDPC) codes have been brought to optical communications in the 2000s [67, 63]. As LDPC codes present an error floor that prevents the post-FEC BER to decrease rapidly below  $10^{-12}$ , they are often used as an inner code to decrease BER to a range of  $10^{-3}$  to  $10^{-5}$ , and an HD outer code with small overhead finally reduces the BER to the system requirement. More recently, new coding schemes such as polar codes and spatially-coupled (SC) codes have been introduced, with appealing complexity and asymptotically capacity-achieving performance. SC-LDPC enables virtually arbitrarily long codewords with simple decoder, and alleviates the error floor issue of LDPC and the need of an outer code [68]. SC-LDPC codes are potential candidates for future lightwave systems and are used in the experiments described in the following chapters of this thesis.

For SD FEC schemes, it has been shown that the pre-FEC BER is not an accurate metric to predict the post-FEC BER [69, 70]. Computing the BER at the output of the communication channel indeed implies the use of a HD demapper, whereas in a SD decoding scheme the decoder is fed with soft information. The following section introduces some information theory concepts that are required to define a suitable metric for SD-FEC performance prediction.

## 2.3 Information theory and theoretical limits

To quantify the amount of information that can be transmitted over the optical fiber channel, probabilistic models on information source and communication channel are required. These models have been introduced by C. E. Shannon in 1948 [12], well before the development of the first optical fiber transmission systems. In his work, Shannon used a mathematical model to describe a general digital communication system and derived the channel capacity, the upper bound of the information rate that can be transmitted, under the assumption of an AWGN channel.

### 2.3.a) Mutual information

As in section 2.2,  $X$  and  $Y$  are the random variables representing the channel input and output symbols. To quantify the amount of information the event  $Y = y$  provides about the event  $X = x$ , we use the mutual information of the event  $(X, Y) = (x, y)$  defined as [13]

$$I(x, y) = \log_2 \frac{p_{X|Y}(x|y)}{p_X(x)}, \quad (2.15)$$

and the average MI between  $X$  and  $Y$ , over all pairs of events, is then defined by:

$$MI(X, Y) = E_{X,Y} \left[ \log_2 \frac{p_{X|Y}(X|Y)}{p_X(X)} \right] = E_{X,Y} \left[ \log_2 \frac{p_{Y|X}(Y|X)}{p_Y(Y)} \right] \quad (2.16)$$

### 2.3.b) Source entropy

The self-information of the event  $X = x$  is derived from (2.15) as  $I(x) = -\log_2 p_X(x)$  and the average self-information of the random variable  $X$  is called entropy and is equal to

$$H(X) = E_X [-\log_2 p_X(X)]. \quad (2.17)$$

The entropy measures the amount of information on  $X$  provided by its own observation: it is the information rate of the source  $X$ . The entropy is also a measure of uncertainty in  $X$ . The uncertainty in  $X$  relative to the realizations of the random variable  $Y$  is described by the conditional entropy

$$H(X|Y) = E_{X,Y} [-\log_2 p_{X|Y}(X|Y)] \quad (2.18)$$

Note that by substituting (2.17) and (2.18) into (2.16), we can express the mutual information as an entropy difference [48]

$$MI(X, Y) = H(X) - H(X|Y). \quad (2.19)$$

In general, the mutual information  $MI(X, Y)$  quantifies the dependency between the random variables  $X$  and  $Y$ . As in our case,  $X$  and  $Y$  represent the transmitted and received signals, the average MI represents the maximum amount of information that can be transported over the channel. For the rest of this thesis, the term average is omitted and MI refers to (2.16).

As per (2.19),  $MI(X, Y)$  is upper bounded by the entropy  $H(X)$  (defined by the signal source) and is reduced by  $H(X|Y)$  (defined by the channel properties). As  $H(X|Y)$  measures the uncertainty we have in the sent signal  $X$  relatively to the observed signal  $Y$ , this quantity increases with the noise amount in the communication channel.

In an ideal transmission channel without any impairment, the knowledge of  $Y$  fully determines the state of  $X$ , i.e. for any event  $(x, y)$ ,  $p_{X|Y}(x, y) = 1$  and  $H(X|Y) = 0$  so  $MI(X, Y) = H_X$ . For a non-ideal channel, when the observation  $Y$  is corrupted by noise,  $H(X|Y) > 0$  and (2.19) imposes that  $MI(X, Y) < H_X$ .

### 2.3.c) Capacity of the optical channel

The capacity of the channel is defined as the maximum of the MI, where the maximization is performed over all the possible source distributions  $p_X(\cdot)$

$$C = \max_{p_X(\cdot)} MI(X, Y). \quad (2.20)$$

Assuming that  $X$  and  $Y$  are complex values and linked by an AWGN channel, i.e. the received signal can be expressed as  $Y = X + N$  with  $N$  a complex circular AWGN with variance  $N_0$ , which is independent from  $X$ , then the channel transition probability is

$$p_{Y|X}(y|x) = \frac{1}{\pi N_0} \exp\left(-\frac{|y-x|^2}{N_0}\right). \quad (2.21)$$

Shannon showed in [12] that  $MI(X, Y)$  is maximized when the input distribution is itself Gaussian

$$p_X^*(x) = \operatorname{argmax}_{p_X} MI(X, Y) = \frac{1}{\pi P} \exp\left(-\frac{|x|^2}{P}\right), \quad (2.22)$$

and the maximum of the mutual information (called channel capacity) is:

$$C = \max_{p_X} MI(X, Y) = \log_2(1 + SNR) \quad (2.23)$$

where  $SNR = P/N_0$  is the signal to noise ratio.

The Shannon capacity limit is then a reference that will be used throughout this thesis to benchmark the performance of optical fiber communication systems. For a given  $SNR$  value, determined by the physical model of the channel (see 2.1), an ideal modulation and coding scheme results in an information rate equal to the channel capacity  $C$ , which is therefore referred to as the channel unconstrained capacity.

## 2.4 Practical limits and capacity approaching systems

As per (2.22), optimal signaling requires a Gaussian modulation of the variable  $X$ , which means that  $X$  should take values  $x$  in an infinite and continuous alphabet. In practice this is not achievable and we present here the practical modulation schemes used in this thesis. We then review the achievable information rates corresponding to these modulation schemes, as well as the impact of practical FEC schemes. In particular, we review the definition of suitable metrics for performance prediction of transmission systems using SD-FEC schemes.

### 2.4.a) Modulation constraints

#### (i) Regular QAM formats

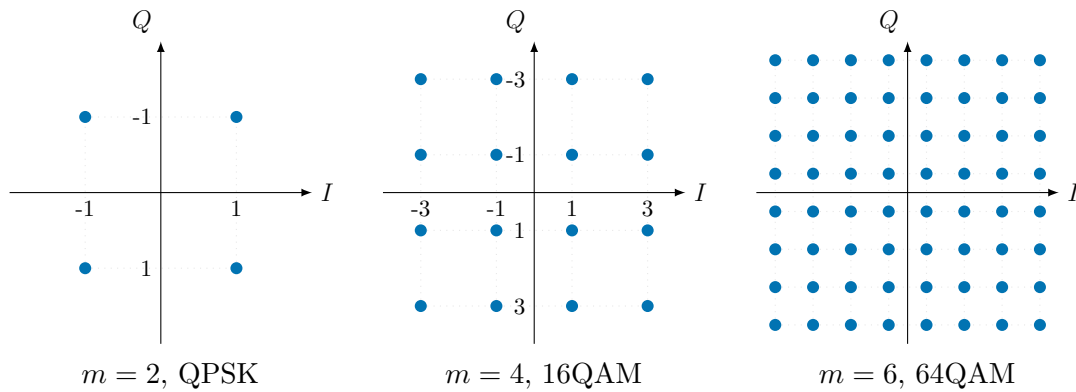


**Figure 2.5:** Regular  $2^m$ QAM constellations: QPSK, 16QAM and 64QAM

In square QAM constellations as the ones described in Fig. 2.5, the complex symbols are taken in a constellation alphabet  $\mathcal{A}$  of size  $2^m$ , where  $m$  is an even number and represents the number of bits carried by each symbol. For each quadrature, the real-value symbols are uniformly drawn from the  $2^{m/2}$  amplitude set  $\{\pm 1, \pm 3, \dots, \pm m/2 - 1\}$ . The  $2^m$ QAM constellation is then formed by taking a cartesian product of the two quadratures, thus for each complex symbol  $a \in \mathcal{A}$ ,  $p_X(a) = 2^{-m}$ , and the source constellation entropy is  $H = m$ .

#### (ii) Probabilistic constellation shaping (PCS)

As the mutual information over the Gaussian channel is in theory maximized with a Gaussian input distribution, several modulation schemes have been designed to produce more "Gaussian-like" constellations than the regular QAM formats. The generation of PCS signals is enabled by a distribution matcher, which allows to set the symbol probabilities of the symbol of a regular  $2^m$ QAM constellation according to a specific and nonuniform distribution  $p_X(a)$

$$p_X(a) = \frac{\exp(-\nu|a|^2)}{\sum_{a \in \mathcal{A}} \exp(-\nu|a|^2)}, \quad (2.24)$$

where  $\nu$  is a free parameter used to tune the Maxwell Boltzmann distribution  $p_X(a)$ . The corresponding source constellation entropy is given by

$$H = - \sum_{a \in \mathcal{A}} p_X(a) \log_2 p_X(a). \quad (2.25)$$

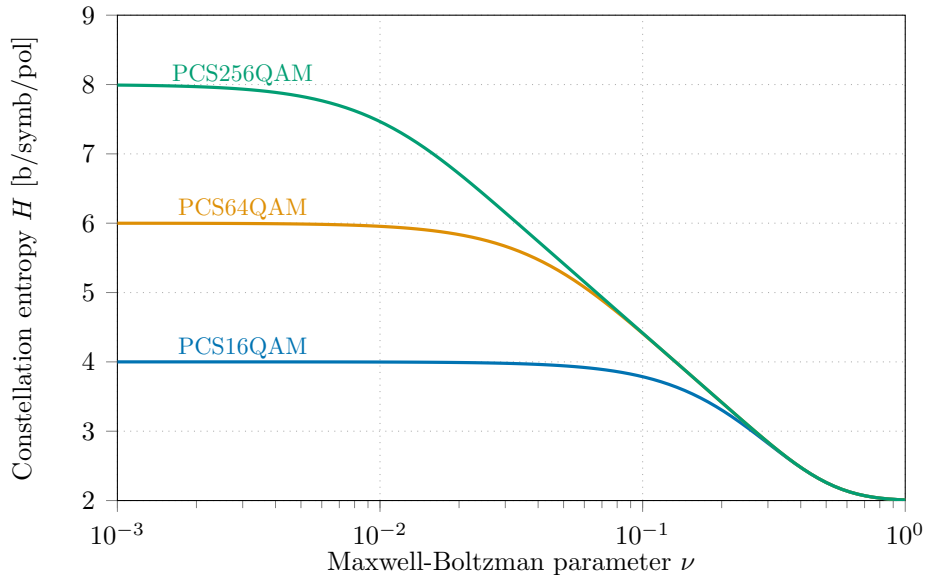


**Figure 2.6:** Constellation entropy  $H$  vs. Maxwell-Boltzmann shaping parameter  $\nu$

The evolution of the constellation entropy as a function of the shaping parameter  $\nu$  is given in the Fig. 2.6. Note that when setting  $\nu = 0$ , the PCS definition degenerates to a regular  $2^m$ QAM constellation. When  $\nu \rightarrow +\infty$ , the probability of the 4 symbols with smallest radius tends to 0.25, whereas the probability of all other symbols tends to 0, so the constellation tends towards a QPSK constellation and  $H$  tends asymptotically to 2 b/symb/pol for any PCS $2^m$ QAM scheme.

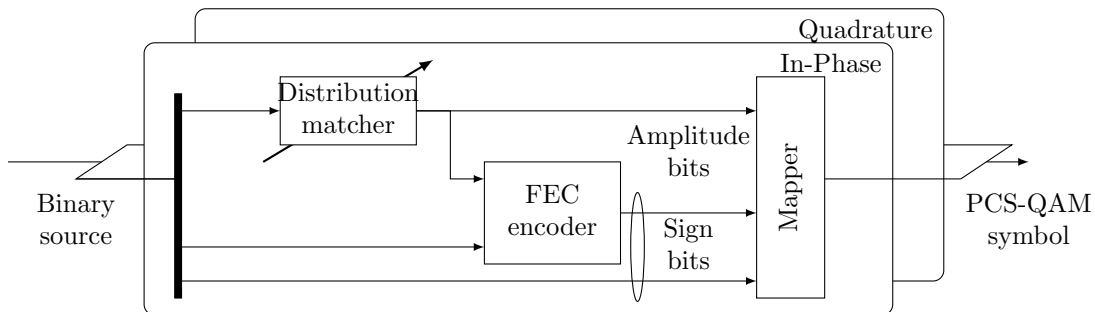


**Figure 2.7:** PAS architecture for PCS-QAM signal generation

The classical scheme formed by the concatenation of a binary FEC encoder and a bit-to-symbol mapper is not appropriate to generate PCS signals and must be replaced by the probabilistic amplitude shaping (PAS) architecture [71, 72] that enables joint coding and shaping. For each quadrature, a real symbol is drawn from the symbol set  $\mathcal{A}' = \{\pm 1, \pm 3, \dots, \pm m/2 - 1\}$  according to the non-uniform probability (2.24) with the parameter  $\nu$  chosen so that the PAS entropy is half of the desired PCS entropy. As described in Fig. 2.7, the distribution matcher generates the absolute amplitudes of the PAM constellation, and the FEC encoder generates equally distributed parity bits. Each positive amplitude is then multiplied with the sign given by the sign bits (FEC parity bits and some uncoded bits). The QAM symbol is finally obtained by taking the cartesian product of the two PAS outputs. Note that the implementation of the distribution matcher is out the scope of this thesis and in the following, the PCS sequences are obtained by generating the PCS symbols with the appropriate probability.

As detailed in [71, eq. (34)], the PAS architecture imposes an intrinsic lower limit on the FEC code rate. For  $2^m$ QAM constellations the code rate must satisfy

$$r_c \geq \frac{m-2}{m} \quad (2.26)$$

To summarize, the PAS scheme enables to generate more "Gaussian-like" PCS signals from any regular  $2^m$ QAM constellations. PCS scheme benefits from the powerful existing DSP algorithms of  $2^m$ QAM with limited required adaptation, contrary to other approaches such as geometric constellation shaping (GCS).

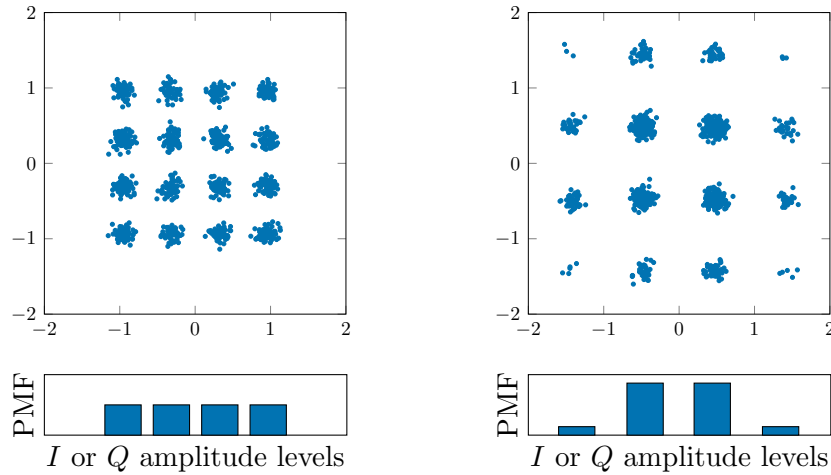


**Figure 2.8:** Constellation diagram (additive noise corresponding to 20 dB SNR) and quadrature probability mass function (PMF) of 16QAM and PCS16QAM ( $H=3.2$  b/symp/pol)

Fig. 2.8 shows examples of symbols for a 16QAM (entropy 4 b/symb/pol) and a PCS16QAM (entropy 3.2 b/symb/pol), where the transmitted constellation power has been normalized to 1 before applying a complex white Gaussian noise corresponding to a 20 dB SNR. A fundamental property of the PCS can be observed here. By reducing the probability mass function (PMF) of the outer symbols, PCS concentrates the constellation power on the inner symbols. As a result, for a normalized constellation the minimum distance between the symbols is increased: at the cost of a reduced information rate, the PCS has an improved robustness to noise.

### (iii) Modulation-constrained MI

When considering  $2^m$ QAM or PCS $2^m$ QAM modulations, as the symbol alphabet has a finite size the MI defined by (2.16) results in

$$MI(X, Y) = E_{X, Y} \left[ \log_2 \frac{p_{Y|X}(Y|X)}{\sum_{a \in \mathcal{A}} p_{Y|X}(Y|a) p_X(a)} \right] \quad (2.27)$$

which corresponds to the achievable information rate that can be transmitted, given a constellation  $\mathcal{A}$  and the channel statistics  $p_{Y|X}$ , therefore referred to as modulation-constrained MI.

## 2.4.b) Coding constraints

### (i) Soft-decision bit metric decoding

The practical scheme considered in this thesis is depicted in Fig. 2.9. As mentioned previously in section 2.2, we use binary encoder and decoder for simplicity. This differs from the HD scheme described in section 2.2 by the fact that at the receiver side the demapper outputs soft information (such as bit-wise probabilities  $p_{B_j|Y}$ , or log-likelihood ratios) that are propagated to a SD-FEC decoder [69]. In the bit-interleaved coded modulation (BICM), a bit interleaver is included between the FEC encoder and the symbol mapper. Interleaving enables to sparse possible error bursts occurring during transmission and ensures independent errors at the input of the decoder.

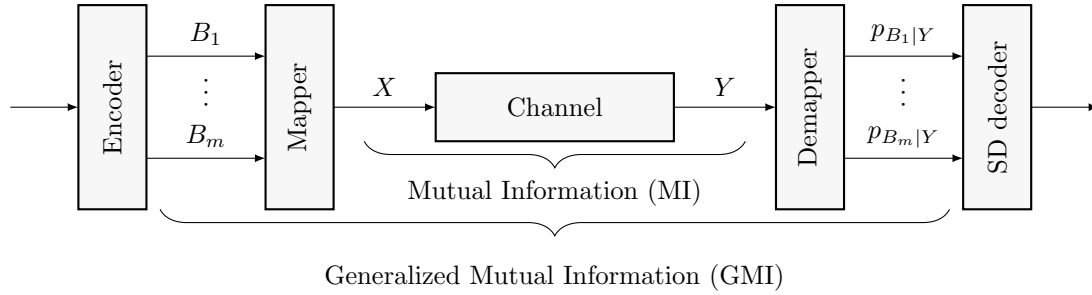


**Figure 2.9:** SD BMD system: the decoder is fed with bit-wise metrics  $p_{B_j|Y}$

In the considered SD BMD scheme, the encoder and decoder pair sees a binary-input soft-output channel. Whereas the modulation-constrained MI given by (2.27) is based on the channel metric  $p_{Y|X}$  (the symbol metric which is matched to the symbol-wise channel), one can define a BMD metric  $q_{Y|X}$  (which is matched to the bits) [72]

$$q_{Y|X}(Y|X) = \left( \prod_{j=1}^m p_{B_j|Y}(B_j|Y) \right) \frac{P_Y(Y)}{P_X(X)} \quad (2.28)$$

The BMD metric  $q_{Y|X}$  is called the mismatched decoding metric, as it is not matched to the symbol-wise channel. The BMD probabilities  $p_{B_j|Y}$  have to be computed for the  $m$  possible bits  $b_j$ , whereas the SMD metric  $p_{X|Y}$  must be computed for the  $2^m$  possible symbols  $a$ . Compared to the SMD, it induces a loss of decoding performance, that remains low when Gray mapping is used. This is particularly convenient when using the  $2^m$ QAM and PCS $2^m$ QAM described in 2.4.a), compared to other schemes such as geometric constellation shaping where the bit-mapping must be carefully optimized [72].

### (ii) Generalized mutual information

Using the BMD metric  $q_{Y|X}$  one can define the generalized mutual information (GMI) to approximate the MI for BICM scheme [72] by analogy with (2.27):

$$GMI(X, Y) = E_{X, Y} \left[ \log_2 \frac{q_{Y|X}(Y|X)}{\sum_{a \in \mathcal{A}} q_{Y|X}(Y|a) p_X(a)} \right] \quad (2.29)$$

The GMI is the reference metric for BMD schemes and represents the modulation and BMD constrained maximum information rate. Fig. 2.10 shows the evolution of

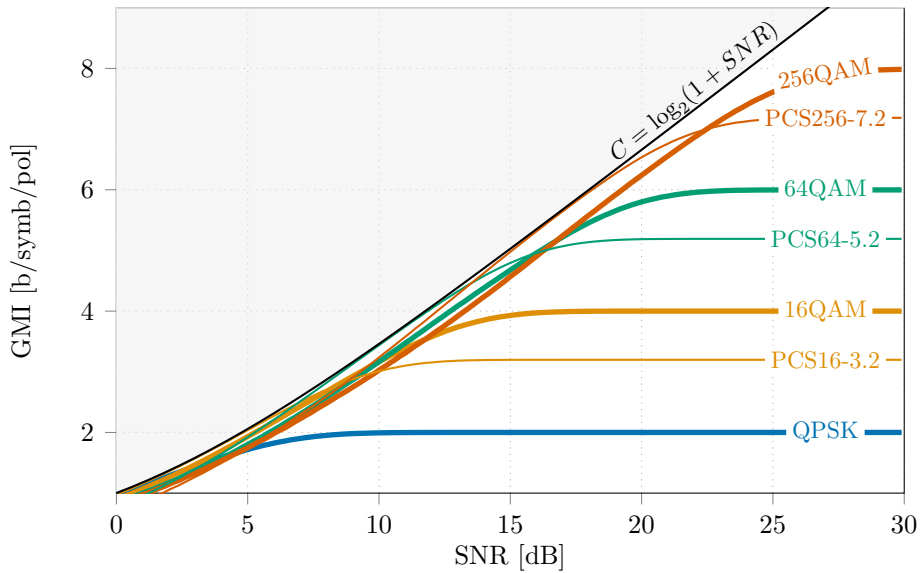


**Figure 2.10:** GMI versus SNR for regular  $2^m$ QAM and PCS $2^m$ QAM formats

the GMI versus the SNR, for different regular and PCS QAM constellations. These curves have been obtained through Monte-Carlo numerical simulations, by applying AWGN noise with variable variance (to sweep the SNR) on randomly generated symbol streams for each modulation format and each desired entropy. For high SNR values, the GMI tends asymptotically to the constellation entropy. When the SNR decreases and the noise increases, the fraction of bits required for FEC increases and the achievable information rate is reduced accordingly. This figure also illustrates the performance of the PCS modulation compared to its original constellation. For example, using an entropy of 7.2 b/symb to generate a PCS256QAM constellation reduces the maximum information rate of the constellation at high SNR, but enables to minimize the gap to Shannon capacity around a given SNR value (17 dB in this case).

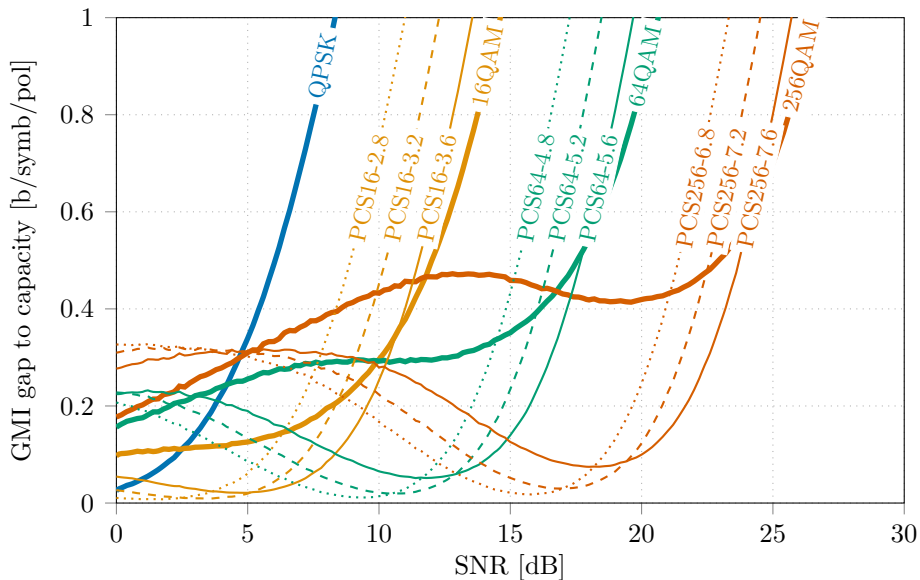


**Figure 2.11:** GMI gap to capacity versus SNR for regular  $2^m$ QAM and PCS $2^m$ QAM

Depending on the target SNR range, PCS modulation therefore provides a flexible solution for capacity-approaching systems. As depicted in Fig. 2.11, tuning the

entropy of the different PCS formats enables the GMI to approach the Shannon capacity for different values of SNR.

### 2.4.c) Achievable rates for QAM systems

The GMI offers a comparison for the modulation-constrained information rate provided by the different modulation formats. To recover the information bits after transmission over the noisy channel and decoding by the BMD scheme, the FEC uses a fraction of the transmitted bits as redundant bits to correct the errors. The post-FEC information rate (IR) of the PCS-QAM scheme is therefore given by [73, 74]

$$IR = H - (1 - r_c)m \quad (2.30)$$

in bits per symbol per polarization, where the entropy  $H$  is the maximum information rate of the PCS $2^m$ QAM scheme and  $(1 - r_c)m$  is the FEC rate loss. Note that for regular  $2^m$ QAM formats,  $H = m$  so the post-FEC IR is  $r_c m$ .

An ideal FEC scheme would allow the IR to reach the GMI, the corresponding code rate is defined as the normalized GMI (NGMI) [70, 72]

$$NGMI = 1 - \frac{H - GMI}{m}. \quad (2.31)$$

which is simply  $NGMI = GMI/m$  for regular  $2^m$ QAM formats.

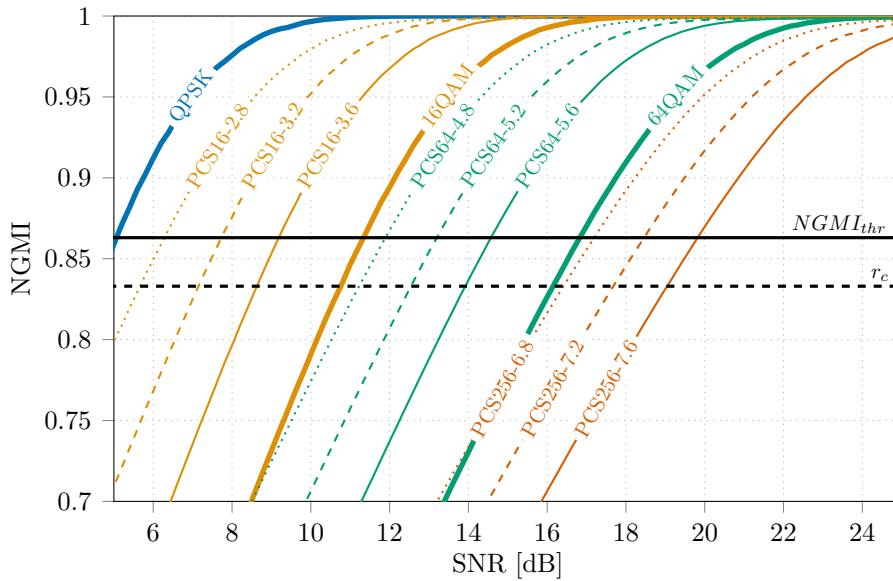


**Figure 2.12:** NGMI versus SNR for regular  $2^m$ QAM and PCS $2^m$ QAM

Fig. 2.12 shows the evolution of the NGMI as a function of the SNR, for different regular and PCS formats. These curves have been obtained from Fig. 2.10 and NGMI definition (2.31).

As the NGMI is the maximum code rate of an ideal FEC scheme, the SNR values corresponding to a given value of  $r_c$  on the NGMI vs SNR curves represent for the different modulation formats the minimum required SNR allowing the ideal FEC to provide error-free transmission. In a practical FEC implementation, the NGMI threshold is defined by  $NGMI_{thr} = r_c + \Delta$ , with  $\Delta > 0$  the implementation penalty

in terms of code rate compared to ideal FEC. Using the FEC code rate  $r_c$  and the implementation penalty  $\Delta$  to get the NGMI threshold  $NGMI_{thr}$ , these curves allow to determine the required SNR for the corresponding NGMI threshold, for the different modulation formats.

The NGMI is therefore a suitable metric in place of the pre-FEC BER to predict the post-FEC BER for SD systems using QAM or PCS-QAM constellation or to determine the system margins to the FEC limit [69, 70]. Besides, the NGMI curves in the Fig. 2.12 show the considerable flexibility allowed by PCS $2^m$ QAM: for a given SNR describing the system performance, and for a given  $NGMI_{thr}$  defined by the FEC  $r_c$  and implementation penalties, one can find with a quasi infinite granularity the PCS format with highest information rate that enables error-free transmission.

## 2.5 Trends for high capacity links

For WDM communication systems, the per-fiber capacity  $C_f$  in [b/s] is derived from the Shannon capacity (2.23) as

$$C_f = W \cdot M \cdot 2 \log_2(1 + SNR) \quad (2.32)$$

where  $W$  is the optical bandwidth in [Hz],  $M$  is the per-fiber number of optical paths (modes, cores), and  $2 \log_2(1 + SNR)$  is the unconstrained capacity for DP I/Q systems. The WDM system throughput is therefore determined on the one hand by physical dimensions (the system bandwidth  $W$  and the number of optical paths  $M$ ) and on the other hand by modulation, coding, signaling and processing limitations, as the system actual information rate is bounded away from the unconstrained capacity by modulation and coding implementation.

### 2.5.a) Multiplexing through the physical dimensions

Up to now, WDM systems operating in the C-band over SMF are the most common systems for commercial transmissions. For these systems, the bandwidth  $W$  is up to around 4.2 THz, with a single spatial path (single mode) per fiber.

In theory, as described by (2.32), the per-fiber capacity  $C_f$  scales linearly with the optical bandwidth  $W$  and the number of optical paths  $M$  (the physical dimensions), and the cable capacity scales linearly with the number of fibers  $N$  (fiber count). In practice, scaling these parameters generally reduces the overall SNR due to several constraints or impairments on multiplexing schemes, as described in the following. Research effort towards multiplexing remains appealing as long as the capacity scaling (with  $W$ ,  $M$  or  $N$ ) exceeds the penalty in the SNR log factor.

#### (i) Fiber multiplicity in optical cables

Today's cables for datacenter interconnect have fiber counts over 1000, whereas long-haul terrestrial cables can pack more than 100 SMF fibers, and subsea cables count a few dozens of fibers. In terrestrial applications, the number of fibers is mainly limited by the physical space occupied by the equipments in the network node stations. In subsea cables, the number of fiber pairs (FP) is limited by the constraints on the cable size and on the available electrical power. As the cable needs to transport the electrical power to supply the submerged amplifiers, the total power is limited and is shared between the amplifiers. Increasing the number of FP without linearly scaling the electrical power requires to decrease the power per fiber, to move back into the linear regime and to reduce the per-fiber bitrate. Today, space-division multiplexing (SDM) subsea cables have up to 12 or 24 FP, as the paradigm of maximizing the per-fiber bitrate gives way to maximizing the per-cable bitrate and cost per bit per km.

#### (ii) Multi-mode and multi-core fibers

SDM more generally refers to increasing the number  $M$  of parallel transmission paths: this can be achieved with technological evolutions in the fiber design and

integration, such as multi-mode fibers (MMF), multi-core fibers (MCF) or even MMF/MCF associations. As MCF have multiple separate cores inside the silica cladding, crosstalk between the signals propagating in the different cores can happen, depending on the core coupling arising from physical architecture. MIMO DSP can therefore be required to compensate for these impairments. Under specific design, such as appropriate tuning of core and cladding refractive index profiles, several propagation modes can coexist in MMF. Few-mode fibers (FMF) with limited number of modes are particularly appealing to reduce the receiver and DSP complexity associated to mode demultiplexing and crosstalk compensation compared to MMF [4].

### (iii) Ultra-wideband systems

The optical bandwidth  $W$  is mainly limited by two factors: the low-loss window of the silica fiber as shown in Fig. 1.9, and the availability of optical components (lasers, modulators, amplifiers, etc) able to operate in the corresponding frequency range. Commercial systems operating over the C+L band are now a reality, from terrestrial applications to subsea cables. Whereas the design of new fibers with larger low-loss window is an active research area, the development of ultra-wideband (UWB) amplification schemes also aims at exploiting the full capacity of already existing networks.

## 2.5.b) Optimization of optical bandwidth utilization

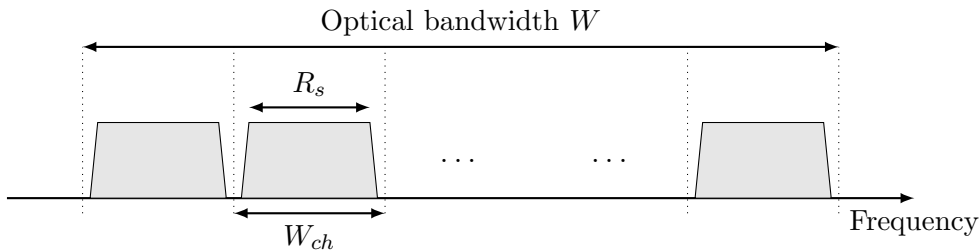


**Figure 2.13:** Typical bandwidth utilization in a WDM transmission system

Fig. 2.13 sketches a typical channel partition across the bandwidth of the optical system. Assuming  $N_{WDM}$  identical WDM channels, each channel is described by its spectral width  $W_{ch}$ , its symbol rate  $R_s$ , the SNR after transmission as modeled in section 2.1 and the post-FEC  $IR$  which depends on the modulation and coding schemes, as described in section 2.4. Each DP channel carries a net bit rate

$$R_b = 2 \cdot IR \cdot R_s \cdot r_p \quad (2.33)$$

where the pilot rate  $r_p < 1$  accounts for the rate reduction due to DSP or framing pilot insertion. Each channel can be characterized by its spectral efficiency

$$SE = \frac{R_b}{W_{ch}} \quad (2.34)$$

that quantifies the amount of information that is effectively transmitted per unit of occupied optical bandwidth. Therefore, the total aggregated throughput over the bandwidth  $W = N_{WDM} \cdot W_{ch}$

$$C_{f,WDM} = M \cdot W \cdot SE \quad (2.35)$$

is bounded away from the Shannon per-fiber WDM capacity (2.32) because for each channel, the spectral efficiency  $SE = 2.IR.(R_s/W_{ch}).r_p$  is less than the unconstrained capacity  $2 \log_2(1 + SNR)$  for several reasons:

- (i) the coding and modulation schemes impose  $IR < \log_2(1 + SNR)$
- (ii) bitrate loss is caused by pilot insertions ( $r_p < 1$ )
- (iii) pulse-shaping and spectral guardbands between adjacent channels induce a spectral loss ( $R_s/W_{ch} < 1$ ).

As explained in section 2.4, powerful FEC schemes and PCS modulation formats allow to limit the coding and modulation losses (i) to low values. The pilot overheads (excluding FEC) described by (ii) are also limited to a few percents and their impact is therefore not burdensome. Leveraging high values of the symbol rate  $R_s$ , there is room to improve the bandwidth utilization (iii), as the required guardband between channels is mostly determined by network routing elements and does not scale with the symbol rate. Besides, the number of required transceivers to populate the optical bandwidth decreases as the transceiver symbol rate increases: this is promising to reduce the transmission cost per bit, and is also a key enabler to allow UWB or SDM to be cost-efficient systems.

In this context, the chapters 3 and 4 focus on implementation challenges and experimental validation of high symbol rate transceiver utilization in long-haul coherent systems. The chapter 5 of this thesis is dedicated to the evaluation of UWB transmission systems using semiconductor optical amplifiers (SOA), with a three-fold increase in bandwidth compared to conventional C-band EDFA.



## High symbol rate transmitters for next-generation coherent systems

This chapter focuses on the implementation challenges and experimental validation of high symbol rate transceivers based on latest DAC capabilities. After summarizing the evolutions in coherent transponders over the last decade and reviewing possible directions for future developments, we present the architecture and characterization of our high symbol rate prototype and we demonstrate its capabilities with signals up to 100 GBd for high speed transmissions in configurations ranging from regional terrestrial networks to ultra long transoceanic distances.

### Contents of this chapter

---

<b>3.1 Introduction</b> . . . . .	<b>64</b>
3.1.a) Evolution of coherent transponder capabilities . . . . .	64
3.1.b) Overcoming electrical and electro-optical bandwidth limitations . . . . .	64
<b>3.2 High symbol-rate prototype characterization</b> . . . . .	<b>66</b>
3.2.a) Experimental setup . . . . .	66
3.2.b) Bandwidth compensation with digital predistortion . . . . .	67
3.2.c) Hybrid optical and digital bandwidth compensation . . . . .	68
<b>3.3 High capacity 800 Gb/s demonstration for regional networks</b> . . . . .	<b>70</b>
3.3.a) Back-to-back 99.5 GBd DP-64QAM signal characterization . . . . .	70
3.3.b) Laboratory transmission line . . . . .	71
3.3.c) Experimental results . . . . .	72
<b>3.4 Ultra-long haul 300 Gb/s transmission for future transoceanic systems</b> . . . . .	<b>74</b>
3.4.a) Performance requirements . . . . .	74
3.4.b) Experimental setup with recirculating loop . . . . .	75
3.4.c) Experimental results . . . . .	77
<b>3.5 Field trial demonstration of rate versus reach trade-off optimization</b> <b>79</b>	
3.5.a) Experimental setup for field trial over live commercial network . . . . .	79
3.5.b) Experimental observation of ROADM filtering effects . . . . .	81
3.5.c) Post SD FEC decoding using SC LDPC . . . . .	83
<b>3.6 Summary</b> . . . . .	<b>87</b>

---

## 3.1 Introduction

### 3.1.a) Evolution of coherent transponder capabilities

In the late 2000s, the introduction of coherent transponders quickly enabled availability of 40 Gb/s and 100 Gb/s single channel rates over optical networks, ruling out direct-detection solutions in high-capacity systems [4]. While 10 and 100 Gigabit Ethernet (GbE), standardized in 2002 and 2010 respectively, are widely used client rates addressed by legacy optical transponder capabilities, the new 400 GbE standard for client rates continue to drive the development of higher speed optical transponders.

Continuous increase in transponder symbol rates, modulation and signaling techniques enabled single channel rates to scale beyond the 100 Gb/s rate first enabled by DP-QPSK operating around 30 GBd [75]. 400 Gb/s products are now available, using for example DP-16QAM working at 60 GBd [10], or DP-64QAM operating with symbol rate below 50 GBd to increase SE for shorter reach applications [76]. Leveraging DP-PCS-64QAM and symbol rates around 100 GBd, 800 Gb/s up to 1.1 Tb/s have been recently demonstrated [77, 78, 79, 80]. The motivation to increase symbol rate is mainly cost and integration, as each single transponder carries more information and less transponders are needed to populate the system optical bandwidth.

The symbol rate scaling has been made possible by the increase of DAC/ADC conversion rate (from 56 GS/s in 2010 up to more than 120 GS/s in current generations) and also the improvement of CMOS electrical bandwidth, from 16 GHz in 2010 up to >30 GHz today [8]. As the noise resilience of the transmitted signal decreases with the constellation size, moving towards high cardinality constellations requires constant improvement of available DAC/ADC resolution in terms of effective number of bits (ENOB), whereas higher complexity DSP and FEC schemes require the better integration and size reduction of the technology nodes in the ASIC implementation, from 65 nm CMOS down to 5 nm FinFET in the next generations [8].

### 3.1.b) Overcoming electrical and electro-optical bandwidth limitations

Despite the possible limitations in terms of electrical bandwidth and implementation, the demand for transponders operating beyond 100 GBd is real as the future standards for client rate evolution are likely to be 800 GbE and 1.6 TbE [9]. In laboratory experiments, receivers are often based on state-of-the-art high speed oscilloscopes, whose bandwidth and conversion rate characteristics usually outreach the transmitter technology. Here we therefore focus on research effort to increase the channel rate at the transmitter side.

To overcome the limits of single channel transmitters, one approach is to generate high symbol rate signals by multiplexing lower-speed signals, reducing the constraints on the DAC sampling rate and bandwidth. Early proposals consisted in grouping adjacent WDM channels into super-channels, with several attempts to

maximize the super-channel SE while reducing as much as possible the number of required transmitters per super-channel [81, 82]. This solution can be easily scaled for future client rate requirements but does not offer perspective of cost reduction as the number of components (lasers, modulators, DAC, drivers) is not lowered. Other approaches aim at multiplexing signals inside the transmitter instead of combining different channels. Optical multiplexing techniques have been explored, either in time [83] or in frequency [84] domain. As they require massive integration of optical components, these techniques have not met industrial applications yet. Multiplexing is therefore more commonly performed in the electrical domain. These multi-DAC approaches, often referred to as super-DAC, can be realized by electrical time domain multiplexing (ETDM) [85, 86] or by frequency band multiplexing approaches thanks to digital [87] or analog [88] techniques. Electrical multiplexing methods require additional RF components but have shown impressive results in the generation of IMDD and coherent signals with symbol rates up to 200 GBd [89, 90].

To avoid the scaling of the number of required DACs and RF and optical components, the single-DAC architecture (i.e. with a single DAC per modulated dimension) remains often preferred in industrial applications. Besides, CMOS and BiCMOS technologies are particularly attractive as they enable direct interfacing with DSP ASICs and are particularly suited for large-scale production. However, increasing the symbol rate using these technologies is challenging, as state-of-the-art CMOS or BiCMOS converters operate up to 128 GS/s, whereas 220 GBd signal generation has been recently demonstrated using cutting-edge arbitrary 256 GS/s waveform generator [91]. The first demonstration of single-DAC 1 Tb/s DP-64QAM channel rate in 2017 was based on a SiGe BiCMOS DAC operating at 100 GBd [92], and the current single-DAC record channel rate is 1.61 Tb/s enabled by DP-PCS256QAM 128 GBd and powerful DSP algorithms [93].

Bearing in mind constraints of optical networks, we focus in this work on high symbol rate transmissions compatible with WDM transmission over legacy 100 GHz spacing grid, currently able to transport 800 Gb/s to 1 Tb/s thanks to high cardinality constellations [94, 95, 78, 79]. To overcome bandwidth limitations of single DAC architectures, optical and digital bandwidth compensation techniques enable us to study the transmission capabilities of next-generation high-speed transponders with improved bandwidth limitations [96, 97, 98, 99].

## Chapter outline

In this chapter, section 3.2 details the architecture of our high symbol rate transmitter, and presents the bandwidth compensation scheme we use in the generation of 80 to 100 GBd signals. Section 3.3 presents the experimental demonstration of 800 Gb/s over a transmission line of 605 km in our lab, leveraging 99.5 GBd DP-64QAM signals, compatible with networks upgrade in line with client rate evolutions. In section 3.4, we show how high symbol rate transmitters can also be used for transoceanic transmissions, demonstrating with a lab recirculating setup a record 300 Gb/s channel rate over an ultra long-haul 20570 km transoceanic distance for 41 channels in the C-band. Finally, section 3.5 presents the results of a field trial conducted over a live network traffic, to study the capabilities of high symbol rate signals while taking into account the constraints of a legacy network.

## 3.2 High symbol-rate prototype characterization

In this section, the architecture of our high symbol rate transmitter based on a single-DAC architecture is presented. The electro-optical bandwidth compensation technique is described and back-to-back characterization of this transmitter is performed. This transmitter or similar configurations will be used in the transmission experiments presented in the following sections of this chapter.

### 3.2.a) Experimental setup

The architecture of the high symbol rate prototype is described in Fig. 3.1(a). The transmitter is based on a 4 channel high-speed CMOS DAC operating at 120 GS/s. For each channel, the differential outputs are amplified with electrical driver amplifiers, and the resulting RF signals are used to drive a DP I/Q Lithium Niobate MZM. In order to compensate for the limited bandwidth of the transmitter, we use an electro-optical bandwidth compensation scheme.

Besides applying digital filtering on the channel waveforms before feeding the DAC, as shown in Fig. 3.1(a) a wavelength selective switch (WSS) with 6.25 GHz-grid-resolution is added at the output of the modulator to perform spectrum shaping in the optical domain. Independently from the attenuation profile, the WSS is set to reject the noise out of a 100 GHz band centered on the signal frequency. EDFAs are used to compensate for insertion and modulation losses in the DP I/Q modulator, as well as insertion losses and attenuation profile in the WSS. Without any compensation scheme, the generated spectrum of a 100 GBd signal with RRC pulse-shaping ( $\rho=0.01$ ) is given in Fig. 3.1(a), showing that the power degradation over the signal bandwidth exceeds 25 dB.

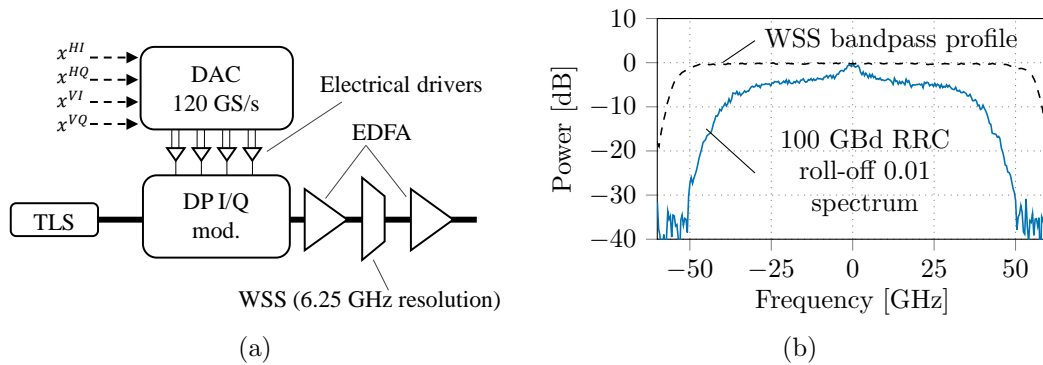


**Figure 3.1:** (a) Architecture of high symbol rate transmitter and (b) frequency response for 100 GBd RRC signal ( $\rho = 0.01$ ) in the absence of bandwidth compensation scheme.

To characterize the performance of transmitter with different bandwidth compensation schemes, we use the back-to-back setup presented in Fig. 3.2. The signal coming from the TX enters a variable noise loading stage: the optical power is swept with a VOA, so that after the following EDFA the OSNR is varied accordingly. A band-pass filter (BPF) is used to reject the noise out of a 800 GHz band centered on the test channel frequency. After a second EDFA, a fraction (typically 1 to 10%) of the optical power is sent into an optical spectrum analyzer (OSA) to measure the OSNR (in a reference bandwidth of 0.1 nm). The signal is then sent into a WSS to extract only the channel under test, which is amplified and sent into a coherent receiver, comprising a LO, a coherent mixer and balanced photodiodes with 70 GHz

bandwidth. Electrical waveforms are sampled by a 113 GHz bandwidth, 256 GS/s high-speed oscilloscope and DSP is performed offline.

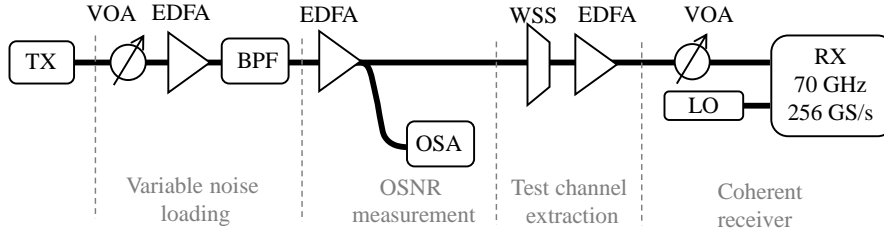


**Figure 3.2:** Experimental setup for back-to-back characterization

The DSP consists in signal conditioning (resampling at 2 sps and brickwall filtering to suppress out-of-band noise), CDC, polarization demultiplexing using CMA, carrier frequency compensation, BPS for phase estimation and a last blind LMS post-equalizer. 1% pilot symbols are used to remove cycle slips from phase ambiguity and are dropped before SNR estimation. The details of the DSP algorithms can be found in section 1.5.b).

### 3.2.b) Bandwidth compensation with digital predistortion

First, the performance of the transmitter without optical compensation is assessed. Fig. 3.3(a) shows different digital predistortions profiles: full-band DAC predistortion<sup>1</sup> resulting in a 27 dB power excursion for the digital filter, or predistortions limited to  $\pm 42$  and  $\pm 46$  GHz, that reduce the power excursion to 18 and 12 dB, respectively. The impact of the predistortion width appears clearly on Fig. 3.3(b): compensating the full-band power drop enables us to obtain a flat spectrum at the cost of an increased noise level visible at -20 dB at 50 GHz. Note that above 50 GHz, the noise is rejected by the WSS acting as a bandpass filter.

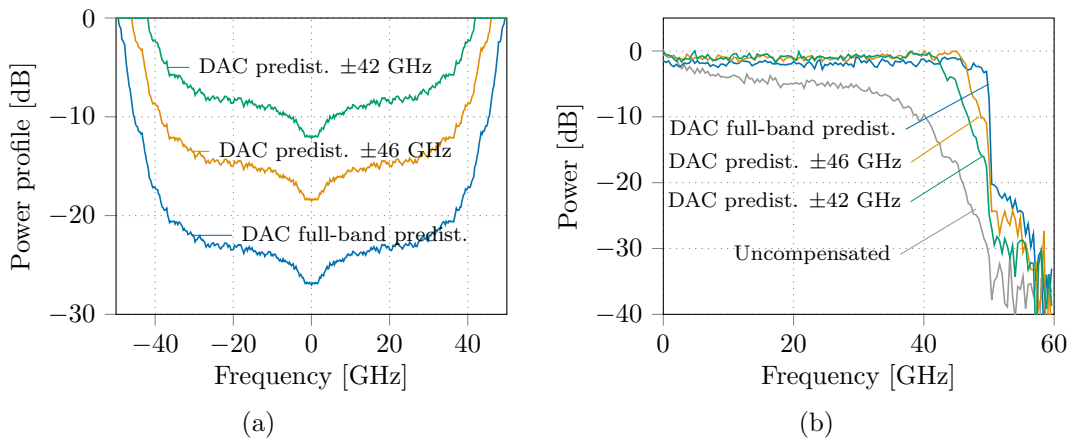


**Figure 3.3:** Digital predistortion filters (a) and optical spectrum (b) of 100 GBd DP-16QAM signal generated without optical compensation

Fig. 3.4 shows the corresponding back-to-back SNR versus OSNR curves. Without any compensation, the SNR saturates at 13.5 dB for low added optical noise (high OSNR), and in the low SNR region, the performance shows high OSNR penalty

<sup>1</sup>This corresponds to  $\pm 49.5$  GHz bandwidth to account for the RRC pulse shaping

compared to the AWGN theory. When applying a full-band DAC predistortion, the performance is improved in the low SNR region, reducing the OSNR penalty by 3 dB for SNR around 5 dB. However, using a digital filter to compensate for a  $>25$  dB power excursion considerably degrades the ENOB, the SNR plateau at high OSNR values is lowered to 12.2 dB and the OSNR penalty at a reference FEC threshold of 11.3 dB [P16] approaches 8 dB. To avoid sacrificing the ENOB and to improve the SNR performance in high OSNR region, a partial DAC predistortion is applied. When the power loss is compensated by the digital filter only up to  $\pm 46$  GHz, the maximum SNR rises around 15.2 dB, and the performance in low OSNR region is slightly improved. If we reduce the predistortion bandwidth to  $\pm 42$  GHz, the SNR plateau approaches 16 dB as we preserved the ENOB, but the performance in the low SNR region is worst than in the previous case. When considering the reference FEC threshold, the  $\pm 46$  GHz therefore appears as the best candidate with a 3.6 dB OSNR penalty compared to the pure AWGN case.

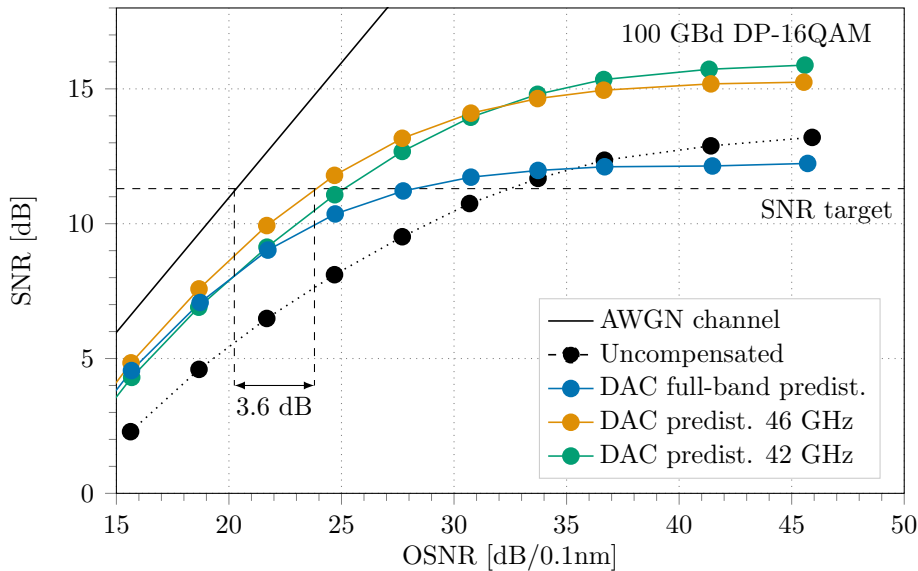


**Figure 3.4:** Back-to-back SNR versus OSNR characterization of 100 GBd DP-16QAM signal generated without optical compensation and with different digital predistortion filters

### 3.2.c) Hybrid optical and digital bandwidth compensation

To further reduce the implementation penalty at FEC threshold and to be able to study the transmission performance of future transmitters with improved bandwidth, we consider a hybrid compensation scheme, combining optical shaping with digital predistortion. As in [96, 97, 98, 99, ?], the idea is to perform a significant part of the compensation via a smooth optical attenuation profile, then finely compensate for remaining profile with the digital predistortion while limit the excursion of the digital filter and the impact of quantization noise and modulation losses.

We first apply a flat attenuation of 11 dB with the WSS on a  $\pm 30$  GHz window, enabling optical emphasis of the high frequency part of the 100 GBd spectrum. Fig. 3.5(a) shows the WSS attenuation profile and the digital predistortion filters for full-band predistortion, whose power excursion is now limited to 17 dB. Fig. 3.5(b) shows the optical spectrum of the 100 GBd signal without any compensation (as a reference) and when applying the M-shaped attenuation profile, first without digital predistortion, then with the full-band predistortion filter.

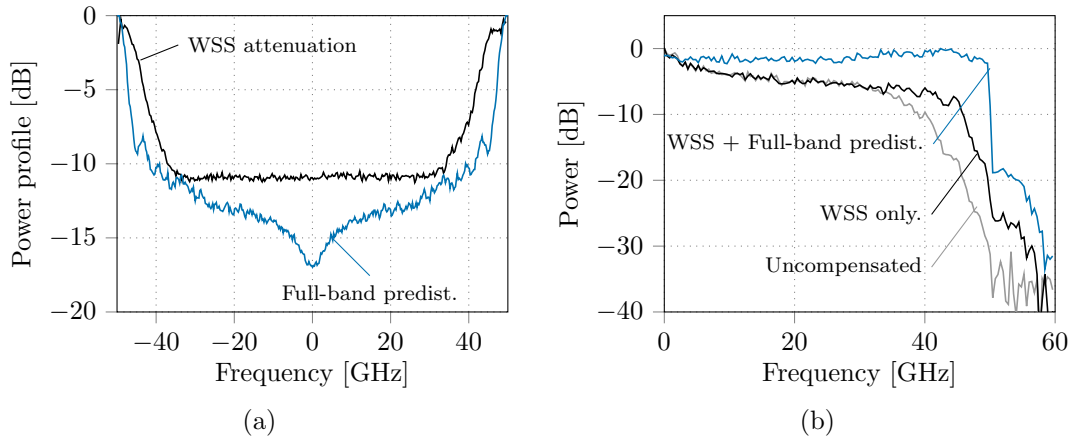


**Figure 3.5:** WSS attenuation profile and digital predistortion filter (a) and optical spectrum (b) of 100 GBd DP-16QAM signal generated with electro-optical bandwidth compensation scheme

Fig. 3.6 shows the corresponding back-to-back curves. The use of the WSS attenuation profile alone already enables to reach a SNR plateau around 15.5 dB, with around 5 dB OSNR penalty at the reference FEC threshold. When applying the full-band DAC predistortion filter, the SNR saturates above 16.4 dB. The WSS attenuation profile combined with a full-band predistortion filter shows a 2.2 dB penalty compared to the theory at the reference FEC threshold, outperforming by 1.4 dB the previous best case using only  $\pm 46$  GHz DAC predistortion.

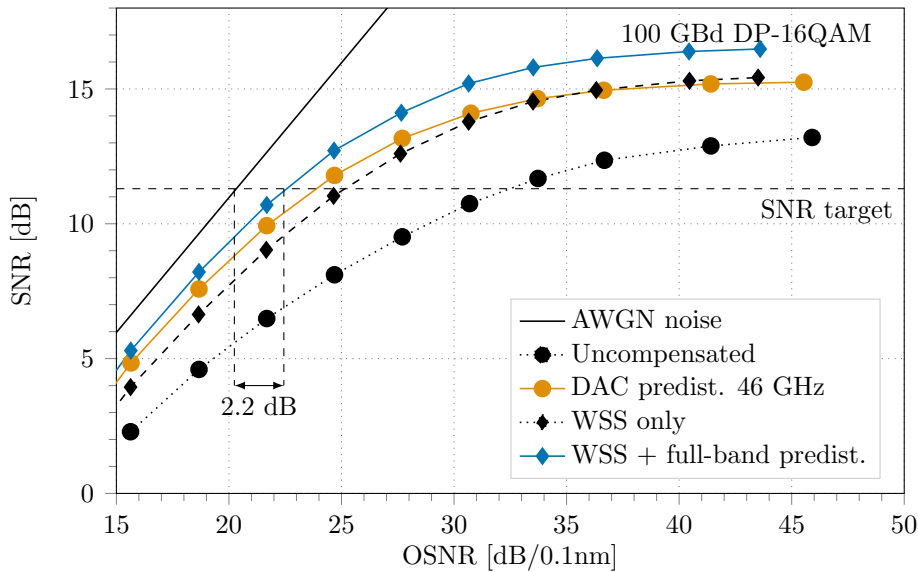


**Figure 3.6:** Back-to-back SNR versus OSNR characterization of 100 GBd DP-16QAM signal generated with M-shaped optical compensation and with different digital predistortion filters

## Conclusions on high symbol rate prototype characterization

We have presented our electro-optical compensation scheme to reduce the impact of bandwidth limitations of the association of DAC, electrical drivers and MZM. We have shown that our strategy enables us to increase the SNR saturation at high values of OSNR and reduce the OSNR penalty at FEC threshold in lower SNR regions, to be able to use the prototype for transmission over optical fiber links.

### 3.3 High capacity 800 Gb/s demonstration for regional networks

High symbol rate single-channel, single-DAC schemes are attractive as potential cost-effective solutions to provide high capacity optical services compatible with future 800 GbE. To accommodate for constraints of legacy optical networks based on 50 or 100 GHz grids, we focus on 800 Gb/s solutions with symbol rates below 100 GBd, thus ensuring SE of 8 b/s/Hz. In this context, a first 800 Gb/s net rate over 400 km was demonstrated in 2018 using 82 GBd DP-PCS-256QAM signals in a 10 WDM channel configuration [94]. Further experiments were reported in 2020 with higher symbol rates, enabling the reduction of the constellation size and the improvement of the transmission reach, such as [78, 79] operating DP-32QAM or digital multi-channel DP-PCS-64QAM with symbol rate around 96 GBd, for C-band WDM transmissions over 600 and 1000 km, respectively.

In this section based on a conference paper published at ECOC 2019 [P4], we present the demonstration of a 800 Gb/s net channel rate over 605 km of ultra low-loss fiber in a full C-band WDM configuration. We use 99.5 GBd DP-64QAM signals and demonstrate a 8 b/s/Hz spectral efficient solution compatible with legacy network constraints for regional transmissions.

#### 3.3.a) Back-to-back 99.5 GBd DP-64QAM signal characterization

The channel under test is obtained from the modulation of a tunable laser source (TLS). We load the previously described transmitter operating at 118 GS/s with randomly generated 99.5 GBd DP-64QAM sequences, with RRC pulse-shaping and roll-off 0.01. First, the WSS attenuation profile given in Fig. 3.7(a) (dashed line) is applied. Fig. 3.7(b) shows the one-sided power spectrum of the transmitter output signal. When applying only the optical compensation, the power degradation over the signal bandwidth is limited to 15 dB. The resulting spectrum is then used to design a digital filter (Fig. 3.7(a), solid line), whose frequency response is the inverse of the smoothed spectrum up to  $\pm 47$  GHz, and unity otherwise. As shown in Fig. 3.7(b), the combination of the digital predistortion and the optical attenuation profile allows to obtain a flat spectrum over the signal bandwidth.

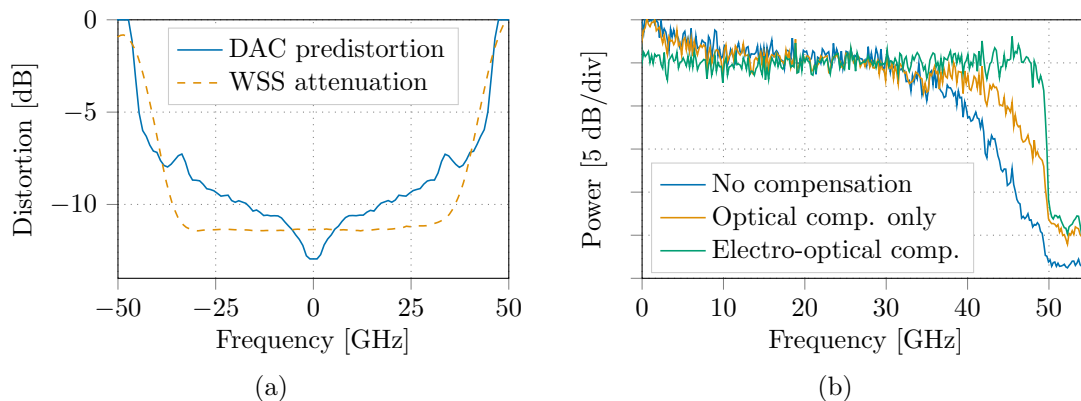


**Figure 3.7:** (a) Frequency response of DAC predistortion filter and WSS attenuation profile; (b) Power spectrum of 99.5 GBd RRC signal ( $\rho = 0.01$ ) without compensation scheme, with optical compensation only and with electro-optical compensation method.

We show in Fig. 3.8 the back-to-back performance characterization of the single 99.5 GBd DP-64QAM channel, for the raw signal without any spectrum optimization and when combining optical and digital compensation. Without any compensation, the SNR performance does not exceed 8 dB. With the use of digital pre-emphasis and optical compensation, the SNR plateau exceeds 16 dB, and the penalty compared to the theoretical curve for flat 99.5 GBd signal is approximately 5 dB for 14 dB SNR, which corresponds to the FEC requirements of the transmission experiment, as detailed in the following.

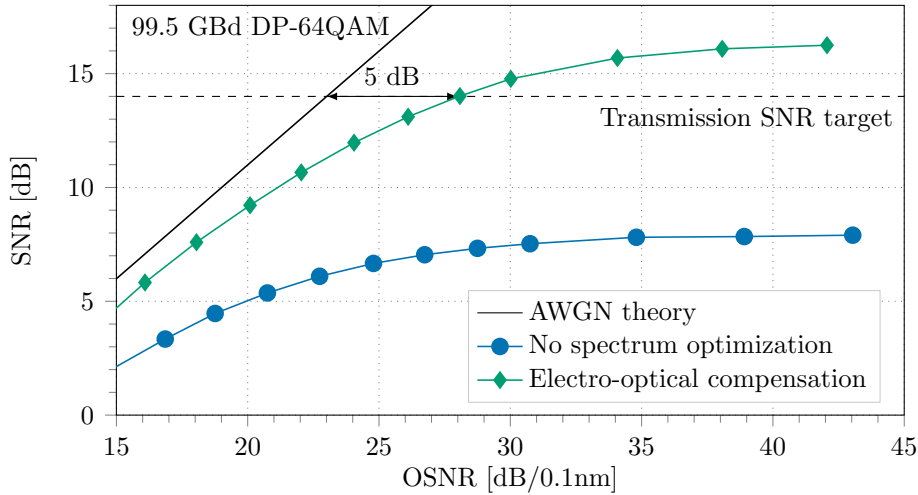


**Figure 3.8:** Back-to-back characterization of 99.5 GBd 64QAM channel without bandwidth compensation and with electro-optical compensation

### 3.3.b) Laboratory transmission line

Our experimental transmission setup is depicted in Fig. 3.9. The channel under test at 1542.34 nm occupies 100 GHz and is coupled to 86 loading channels in C-band on a 50 GHz grid. The 86 distributed feedback (DFB) sources for the loading channels are separately modulated with a DP I/Q modulator operating at 92 GS/s and fed with 49 GBd DP-64QAM sequences. After amplification, a 50 GHz-grid-resolution WSS is used to equalize the spectrum over the C-band and reject the loading signal in the 100 GHz slot of the channel under test. A polarization scrambler (PS) ensures a variable random state of polarization of the loading signal before coupling the loading channels to the channel under test. The WDM signal is then amplified by a last EDFA before being sent into the transmission line.

The transmission line is made of 11 spans of 55 km Corning EX3000 ultra low-loss (ULL) fiber (effective area  $150 \mu\text{m}^2$ ) followed by EDFA with output power ranging from 15 to 19 dBm. A gain flattening filter (GFF) is used after each EDFA to equalize the power profile over the C-band. The WDM spectrum at the line input and output, for a total launched power of 18 dBm, are shown in Fig. 3.10.

At the RX side, the channel under test is extracted with a 100 GHz-grid-resolution WSS, amplified and sent to the coherent receiver including a coherent mixer, a local oscillator, balanced photodiodes and a 70 GHz bandwidth high speed real-time scope operating at 200 GS/s. Data sets of 2 million samples are stored and offline DSP is performed (see 1.5.b)). SNR and GMI are estimated and processed signals are decoded using a family of SC-LDPC codes [68] with rates ranging from

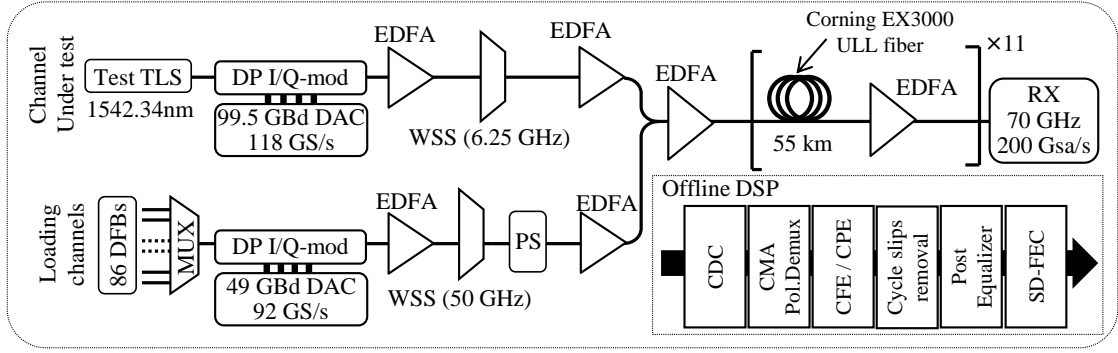


**Figure 3.9:** Experimental setup for transmission of a 99.5 GBd DP-64QAM test channel in a full C-band spectrum over a 605 km ULL fiber link

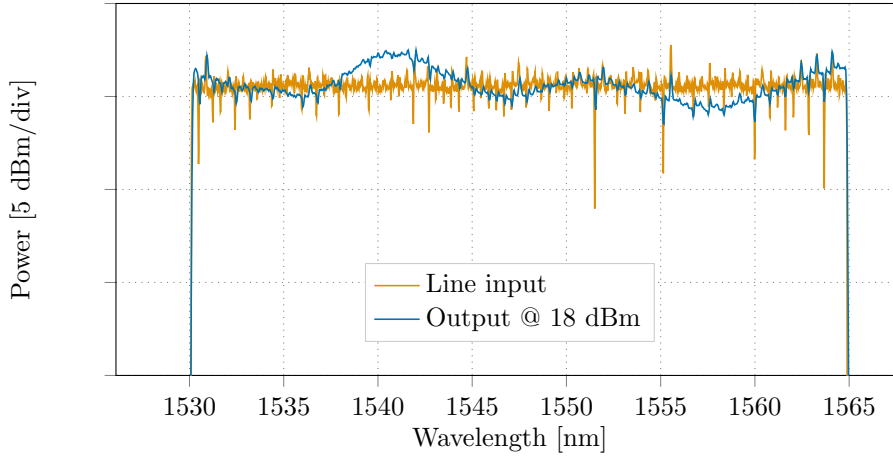


**Figure 3.10:** C-band WDM spectrum at line input and line output

0.4 to 0.91, using steps of 0.01. For each file we decoded the received waveforms by using family members and we determined the maximum code rate resulting in error-free transmission [100].

### 3.3.c) Experimental results

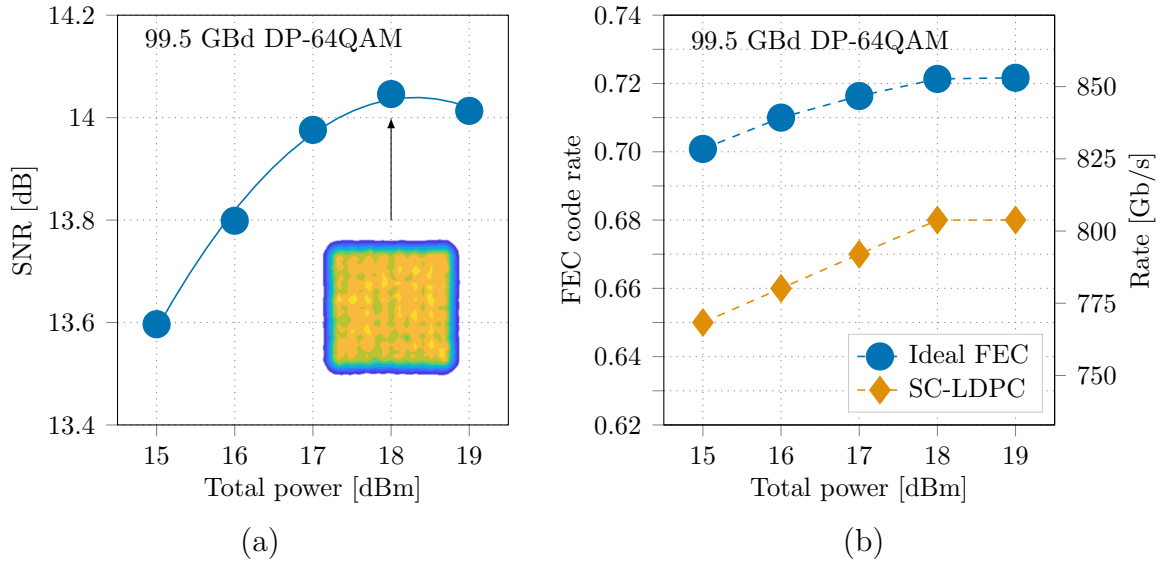
Fig. 3.11(a) shows the SNR versus total launched power after 605 km. The total launched power was varied in the transmission line from 15 to 19 dBm by changing the driving currents of all EDFAs. The non-linear threshold (NLT) in this experiment is 18 dBm, and the optimum SNR at NLT is around 14 dB.

Fig. 3.11(b) shows the highest possible code rate versus the total launched power: the ideal FEC case (circle markers) corresponds to the normalized GMI (NGMI), and for the SC-LDPC codes we select the FEC with highest rate resulting in error-free transmission, for each total launched power. For a total launched power corresponding to the NLT or (NLT+1) dBm, the highest code rate is 0.68. With 1% pilot symbols ( $r_p = 0.99$ ),  $R_s = 99.5$  GBd, the resulting net rate is

$$R_b = 2 \cdot R_s \cdot r_p \cdot 6 \text{ b/symbol} \cdot 0.68 = 804 \text{ Gb/s} \quad (3.1)$$

with a FEC implementation penalty of approximately 6% compared to the achievable information rate (AIR) in the ideal FEC case computed as

$$R_b^* = 2 \cdot R_s \cdot r_p \cdot GMI. \quad (3.2)$$



**Figure 3.11:** Evolution of SNR (a), code rate and net rate (b) as a function of the fiber total launched power, for a transmission distance of 605 km

### Conclusions on 800 Gb/s regional transmission

We demonstrated an 800 Gb/s DP-64QAM signal transmission in a full C-band WDM spectrum, over 605 km EX3000 fiber and using EDFA amplification. We generated our 99.5 GBd signal compatible with 100 GHz spacing grid using CMOS high-speed DAC, digital and optical spectrum equalization with standard WSS to overcome electro-optical bandwidth limitations, that are detrimental for high cardinality modulation formats required to transport such high capacity optical services. We demonstrated a high channel rate, spectrally efficient transmission with low complexity and commercially available DAC, compliant with cost efficiency and footprint optimization requirements for future 800 GbE standards in regional optical networks.

## 3.4 Ultra-long haul 300 Gb/s transmission for future transoceanic systems

From the first proposals of coherent fiber long-haul links in 2008, the design of submarine optical transport systems has mainly been dominated by the target of maximizing the per-fiber capacity, given the manufacturing and deployment cost of optical fiber cables extending up to 17000 km or more. Sustained research effort in advanced modulation formats and signaling techniques, powerful DSP and SD-FEC schemes, enabled the spectral efficiency of such systems to approach the Shannon's capacity in laboratory "hero-experiments" [5, 6, 7] as well as in field trials over recently deployed cables [101, 102]. In particular, such systems are ultimately limited by the fiber Kerr NL effect, and NLC techniques have been extensively explored to further increase the system throughput when operating at the NLT.

Since 2017, new paradigms for transoceanic systems architecture are emerging. Given that the delivered electrical power in submarine systems is limited by the power feeding equipment technology, the current trend is not anymore maximizing the per-fiber capacity but instead, backing off on the span input power, avoiding resource-hungry NLC and adding more submerged fiber strands, together with pump farming to share optical pump power between several amplifiers within submerged repeaters [103, 104, 105]. In this context, high symbol rate transponders appear as an attractive solution to limit the scaling of transponder count with the fiber multiplicity in future SDM systems.

In this section based on a conference paper published at OFC 2020 [P7], we demonstrate the record transmission of 300 Gb/s net channel rate over 20570 km for 41 WDM channels in the C-band, using 99 GBd DP-QPSK signals and high performance adaptive SC-LDPC codes. We examine the power transmission power efficiency evolution when halving the fiber span input power, highlighting the compatibility of our experiment with the current industry trend towards SDM systems.

### 3.4.a) Performance requirements

To achieve transmission over the 20570 km ultra long-haul distance, we modulate the test channel with 99 GBd DP-QPSK. Whereas the previous experiment uses high cardinality format to maximize the channel rate over short distances, in this case the modulation format is chosen for its resiliency to noise as required for this ultra long transmission distance.

We first show in Fig. 3.12(a) the numerical characterization of the SC-LDPC FEC code family for QPSK modulation. For each value of the SNR, with resolution of 0.25 dB, we examine all members of our SC-LDPC code family and the graph indicates the maximum code rate ensuring error-free decoding. The solid line stands for the NGMI and represents the rate for an ideal FEC decoder. For a SNR value of 4.5 dB, the maximum code rate is 0.77 and assuming 1% pilot symbols, the 99 GBd DP-QPSK is able to carry

$$R_b = 99 \text{ GBd} \cdot 2 \text{ b/symbol} \cdot 2 \cdot (1 - 0.01) \cdot 0.77 = 301.87 \text{ Gb/s} \quad (3.3)$$

with a 7.5% penalty compared to the ideal FEC case. We apply the same electro-optical scheme than in the previous experiment to compensate for the bandwidth

limitations of the 118 GS/s CMOS transmitter. Fig. 3.12(b) shows the back-to-back characterization of the 99 GBd QP-QPSK signal, with RRC pulse-shaping and roll-off 0.01. For the target operation point around 4.5 dB SNR, our transmitter shows < 1 dB implementation penalty compared to the AWGN channel.

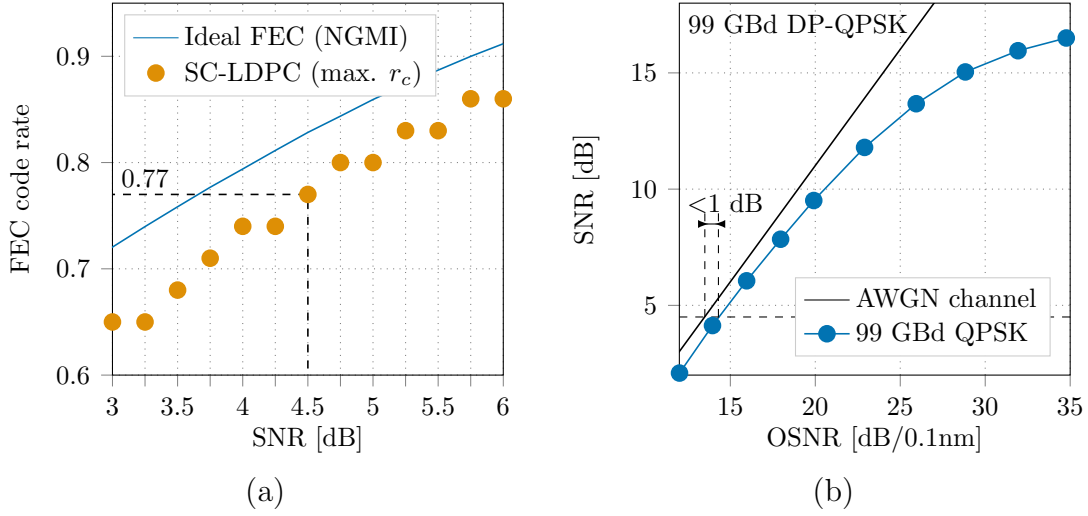


**Figure 3.12:** (a) SD-FEC code family numerical characterization for QPSK signal; (b) Back-to-back characterization of 99 GBd DP-QPSK channel with electro-optical bandwidth compensation

### 3.4.b) Experimental setup with recirculating loop

In addition to the channel under test, the test group depicted in Fig. 3.13(a) comprises two other TLS that are modulated by a distinct CMOS DAC fed with different sequences, to create two adjacent 99 GBd DP-QPSK channels. Like the test channel, a WSS is used to optically shape the adjacent channels and electronic predistortion is applied together with optical spectrum shaping. Fig. 3.13(b) shows the spectrum of the 300 GHz test group.

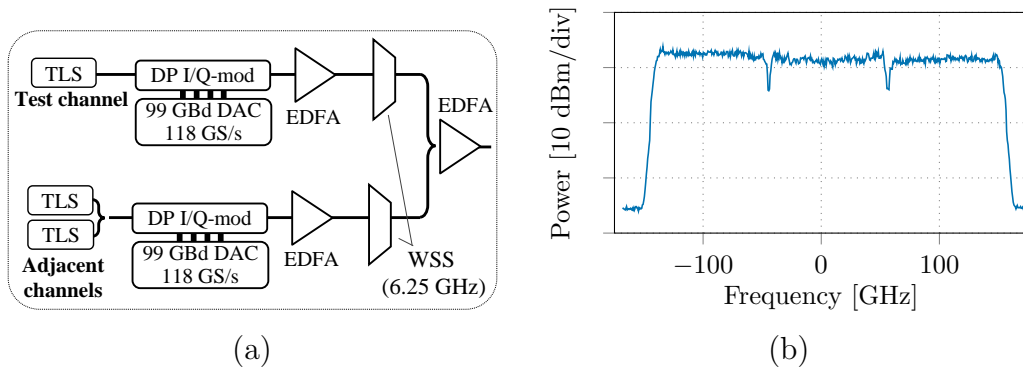


**Figure 3.13:**  $3 \times 99$  GBd DP-QPSK test group. (a) experimental setup and (b) 300 GHz spectrum

The transmission full experimental setup is given in Fig. 3.14. The test group is coupled to a C-band loading spectrum which is composed of 82 DFB on a 50 GHz grid. The DFB are modulated with a unique DP I/Q modulator, driven by a 88 GS/s DAC loaded with 49 GBd DP-QPSK sequences. After amplification, a 50 GHz-grid-resolution WSS is used to equalize the WDM spectrum over the C-band and reject the loading signal in the 300 GHz window of the test group. A 50 km fiber spool and a polarization scrambler (PS) ensures decorrelation and a variable random state

of polarization of the loading signal. The WDM signal is then amplified by a last EDFA before being sent into the recirculating loop.

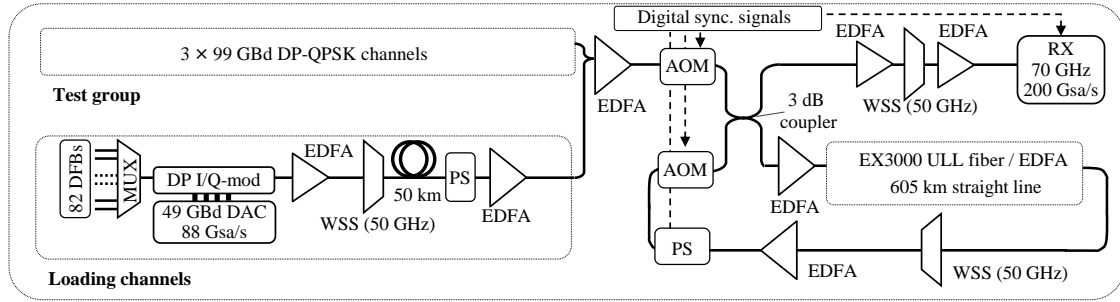


**Figure 3.14:** Experimental setup for transmission of a  $3 \times 99$  GBd DP-QPSK test group in a full C-band spectrum over transoceanic distances with a 605 km ULL fiber and EDFA recirculating loop

The recirculating loop is based on the 605 km straight line introduced in the previous experiment (section 3.3), totaling 11 spans of 55 km Corning EX3000 ULL fiber and C-band EDFA/GFF in-line amplifiers. At the output of the 11 spans, we use a 50 GHz-grid-resolution WSS for channel power equalization. A 3 dB coupler is used to couple the TX and loop outputs and acousto-optic modulators (AOMs) are used to inject into the loop light either from the TX or from the end of the loop. A loop-synchronous PS is used to randomly rotate the state of polarization after each recirculation in the loop. Fig. 3.15(a) shows the C-band spectrum at the transmitter output whereas Fig. 3.15(b) shows the optical spectrum after 34 loop circulations, totaling a distance of 20570 km. The spectrum power equalization in the loop with the WSS is highly challenging with such a high number of recirculations, as the effect of any equalization mismatch is multiplied by the number of recirculations. In particular, power equalization is inherently limited by the 0.1 dB attenuation resolution of the WSS.

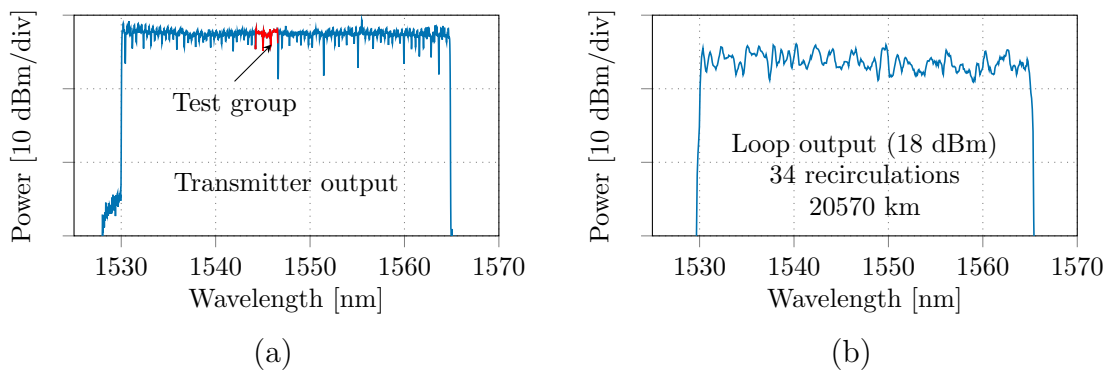


**Figure 3.15:** C-band WDM optical spectrum (a) at transmitter output and (b) at loop output after 34 recirculations

At the RX side, the test channel is extracted using a WSS, amplified and sent to the loop-synchronous coherent RX. Electrical waveforms are sampled with a 70 GHz bandwidth real-time scope operating at 200 GS/s. Data sets of 2 million samples are stored and offline DSP is performed (see 1.5.b)). As in the previous experiment, we search in the SC-LDPC code family the codes enabling error-free transmission and we select the member with the highest code rate among the appropriate codes.

### 3.4.c) Experimental results

We show in Fig. 3.16 the distributions of the SNR and in Fig. 3.16(b) the highest post SD-FEC code rate and corresponding channel rate, for all 41 channels when sweeping the test group over the whole C-band, after 20570 km and for a launched power per span ranging from 15 to 18 dBm. Each box contains 75% of the population and the horizontal bar represents the median. The horizontal ends of the whiskers correspond to the extremal values. For a launched power of 18 dBm, the measured SNR after DSP ranges from 4.54 to 5.7 dB and the code rate varies between 0.78 and 0.86 across the C-band. As all code rates are above the 0.77 code rate threshold, all our transmitted channels can transport a net bit rate greater than 300 Gb/s.

As we reduce the power to 17 or 16 dBm, the SNR is degraded, but still more than 75% of the channels are above the 4.5 dB threshold and can consequently carry 300 Gb/s net rates, whereas the worst performing channels fall to 278 and 266 Gb/s with code rate of 0.71 and 0.68, respectively. For 15 dBm, the SNR shows considerable variations even with careful optical equalization in the recirculating loop. Especially when going into the linear regime, power imbalance between channels results in high variation of the performance. As a result, adaptive selection of the best code rate for each channel is crucial to accommodate for the SNR variations, and code rates from 0.55 to 0.83 allow to reach 215 to 325 Gb/s net channel rates.

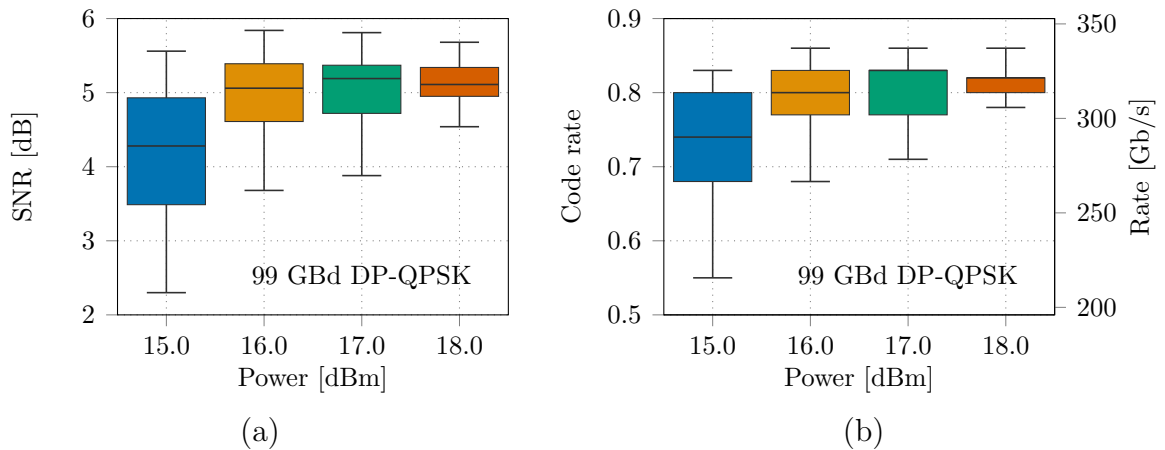


**Figure 3.16:** (a) SNR and (b) highest post SD-FEC code rate and corresponding channel rate (b), for all 41 channels in the C-band after 20570 km and for variable launched power per span

Fig. 3.17 shows the achievable throughput for each configuration (solid line, left axis). With a launched power per span of 18 dBm, the total throughput reaches 13.1 Tb/s. While 18 dBm corresponds to the NLT in this loop, we show that decreasing the total power down to 16 dBm implies a very small decrease (less than 3%) of the total throughput. Further decreasing the launch power to 15 dBm results in a higher reduction of the total throughput down to 11.5 Tb/s, corresponding to 12%, which is attributed to the fact that we enter the linear regime of fiber propagation.

In submarine links, the optical power is limited by the capacity of feeding electrical power to submerged amplifiers. The transmission power efficiency, defined as the ratio of the total throughput to the total integrated launched power, is therefore an interesting figure of merit for cost-efficient system design. This metric is represented in Fig. 3.17 (dashed line, right axis) as a function of the launched power per span. Dividing the per fiber power by two, from 18 to 15 dBm, and reduc-

ing the total throughput only by 12%, leads to increasing the transmission power efficiency by a factor  $2 \times (1 - 0.12) = 1.76$ , from 0.55 to 0.97 Gb/s/mW. Through this example we illustrate the compatibility with the current attraction in submarine industry towards SDM schemes, i.e. reducing the per-fiber throughput by sharing the available power between fibers in order to improve the transmission power efficiency.

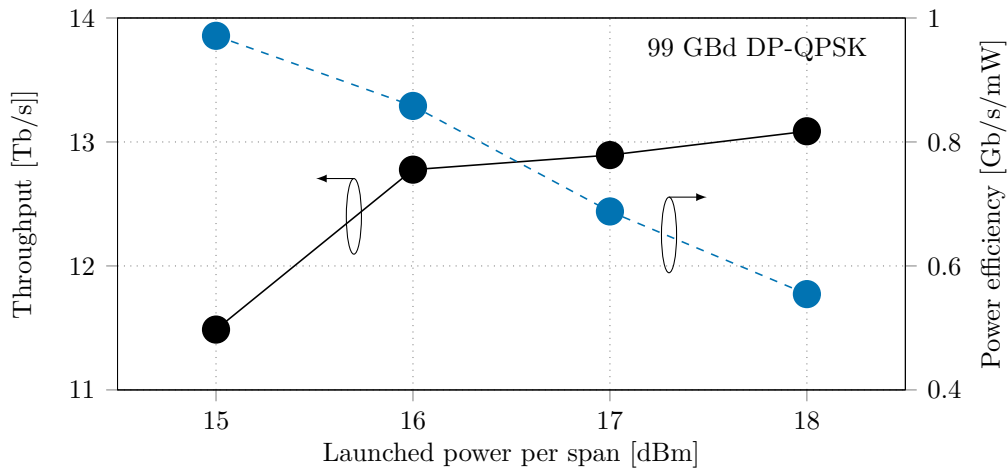


**Figure 3.17:** Total throughput (left axis) and transmission power efficiency (right axis) versus launched power per span, for 99 GBd DP-QPSK C-band WDM transmission over 20570 km

## Conclusions on ultra-long haul transmission

We demonstrate a record transmission of a per-channel net rate of 300 Gb/s for 41 WDM 100 GHz spaced channels across the full C-band, over 20570 km using EDFA amplification and avoiding nonlinear compensation. We also show that operating the system at the launched power of 3 dB below the nonlinear threshold enables us to increase the transmission power efficiency. Our demonstration is compatible with the current SDM trend of favouring the cost-per bit per cable as the main metric in power-constrained subsea systems. Within this new paradigm, as the number of fiber pairs and required transponders per submarine cable is increasing, high symbol rate transponders appear as attractive solutions to address cost-efficiency and footprint optimization in future SDM systems.

## 3.5 Field trial demonstration of rate versus reach trade-off optimization

During the last decade, 100G products have been dominating the market of coherent optics. Analysts expect in the coming years a strong popularity of 400G as a good compromise between capacity and cost for applications ranging from DCI to long-haul while waiting for the maturity of 600G and 800G commercial products [11].

The 400ZR implementation agreement [10] aims at providing interoperable and low-cost 400 Gb/s solutions for short distances, as required for example for datacenter interconnections (DCI) distances up to 120 km. 400ZR is based on DP-16QAM operating around 60 GBd, with pluggable coherent transponders enabling direct interfacing with 400 GbE client switches. Higher symbol rates (up to 90-95 GBd) are appealing to achieve 400 Gb/s services over longer distances in backbone transport networks, while keeping the spectral efficiency at 4 b/s/Hz considering insertion in 100 GHz grids of legacy optical cross-connect architecture.

In this section based on a conference paper published at ECOC 2020 [P9], we present the experimental results of a field trial using our high symbol rate prototype to generate 80 to 95 GBd DP-PCS-16QAM signals. We analyze the evolution of implementation and transmission impairments with the symbol rate, and we show that thanks to the optimization of symbol rate and constellation shaping, our solution is able to optimize the spectral efficiency versus reach tradeoff while accommodating for the constraints of legacy optical networks. 400 Gb/s to 600 Gb/s net channel rates are demonstrated over the Orange optical transport network from Paris node and using routing in points of presence in major cities in France.

### 3.5.a) Experimental setup for field trial over live commercial network

The test channel is generated from the modulation of a C-band TLS, with similar TX configuration than in the previously described experiments. As shown in Fig. 3.18, RRC pulse-shaping with roll-off 0.1 is applied to the PCS-16QAM sequences with variable symbol rate (80 to 95 GBd) and constellation entropy (2.8 to 4 b/symb/pol).

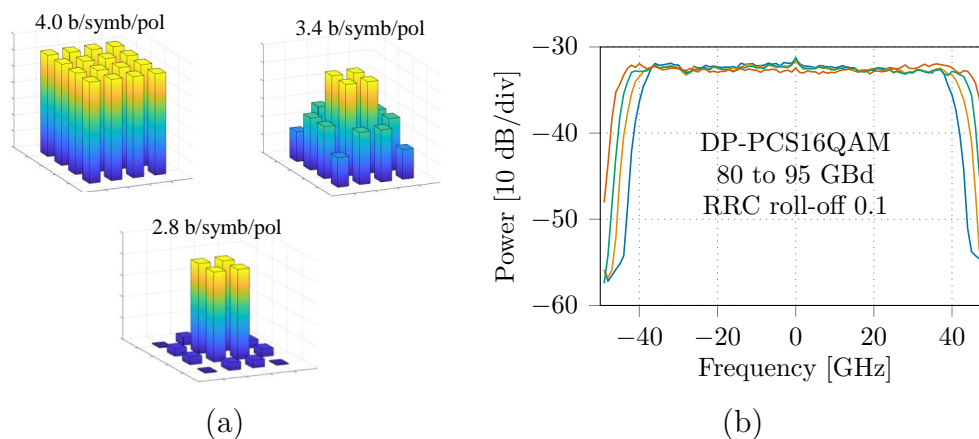


**Figure 3.18:** (a) PCS-16QAM constellation PMF with variable entropy and (b) DP-PCS-16QAM 80 to 95 GBd power spectrum (RRC roll-off 0.1)

Fig. 3.19 illustrates the experimental setup of the field trial. Using a Nokia 1830 Photonics Service Switch (1830 PSS) colorless directionless contentionless and flexgrid (CDC-F) node [106], this channel is sent to a multi-cast switch followed by an optical amplifier. The channel is then inserted into an optical cross-connect element through an add/drop (A/D) port, enabling routing to and from different directions in the Orange optical network.

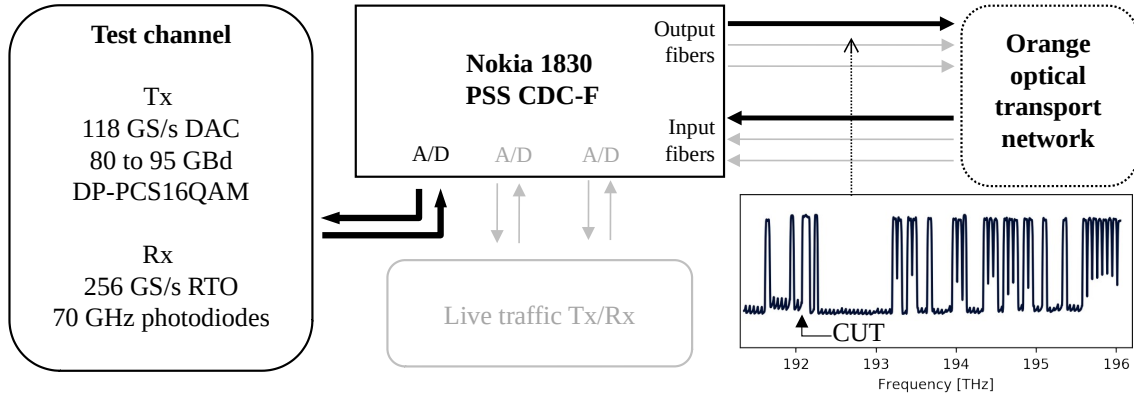
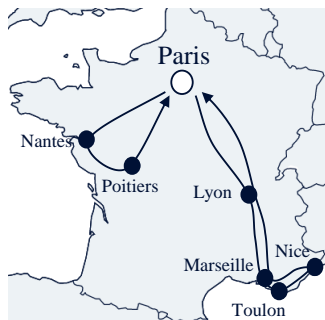


**Figure 3.19:** Experimental setup for transmission of 80 to 95 GBd DP-PCS-16QAM signals inserted in a 100 GHz slot amidst live traffic over Orange optical transport network

The channel occupies a 100 GHz slot, with central frequency varying between 191.525 and 192.125 THz for the different tests and is run alongside live commercial services with a fixed optical power set by the network control plane. Fig. 3.19 shows an example of the optical spectrum observed in the input fiber of the optical node, with our test channel centered at 192.125 THz. The test channel is surrounded by live-traffic channels over the C-band, that are either added/dropped in the Paris PoP or transparently routed to other directions through the optical cross-connect.

The different tested routes over the Orange network in France and their characteristics are listed in Fig. 3.20. Network configurations from Paris to major cities in the south of France (Lyon, Marseille, Toulon, Nice) enable us to test transmissions up to 2323 km. An additional route between Paris and Nantes allows to reach distances beyond 3000 km over legacy standard single mode fibers (SSMF). After travelling through this additional route, the test channel is only routed from one path to the other when coming back to Paris. In all the remote PoPs, routing is performed only with ROADMs, and the WSS count varies between 12 for 1100 km transmission to 37 when reaching 3446 km.



Route	Distance [km]	ROADM count	WSS count
(1): Paris - Lyon - Paris	1100	6	12
(2): Paris - Marseille - Paris	1851	9	18
(3): Paris - Toulon - Paris	2037	13	21
(4): Paris - Nice - Paris	2323	15	23
(5): Paris - Nantes - Paris + (3)	3161	20	35
(6): Paris - Nantes - Paris + (4)	3446	22	37

**Figure 3.20:** Summary of tested routes over Orange transport network in France

At the RX side, the channel is dropped, pre-amplified and sent into a coherent receiver composed of a tunable LO, a coherent mixer and 70 GHz-bandwidth

balanced photodiodes. The electrical waveforms are sampled with a 113 GHz bandwidth, 256 GS/s high speed oscilloscope and stored for offline DSP. As detailed in section 1.5.b), the DSP consists in CDC, polarization demultiplexing using pilot-aided MMA, CFE/CPE and a last blind least mean square post-equalizer. The 1% DSP pilot symbols are dropped before SNR and GMI estimation and SD-FEC decoding using SC LDPC codes [68].

### 3.5.b) Experimental observation of ROADM filtering effects

To observe the impact of the filtering caused by the cascade of ROADMs, Fig. 3.21 shows the power spectrum of the received waveforms, when transmitting in back-to-back configurations and after 1100 or 3446 km, for 80 to 95 GBd signals. While 80 and 85 GBd signals do not suffer much from the filter cascade, the narrowing of the spectrum is clearly visible for 90 and 95 Gbd, especially when going up to 3446 km.

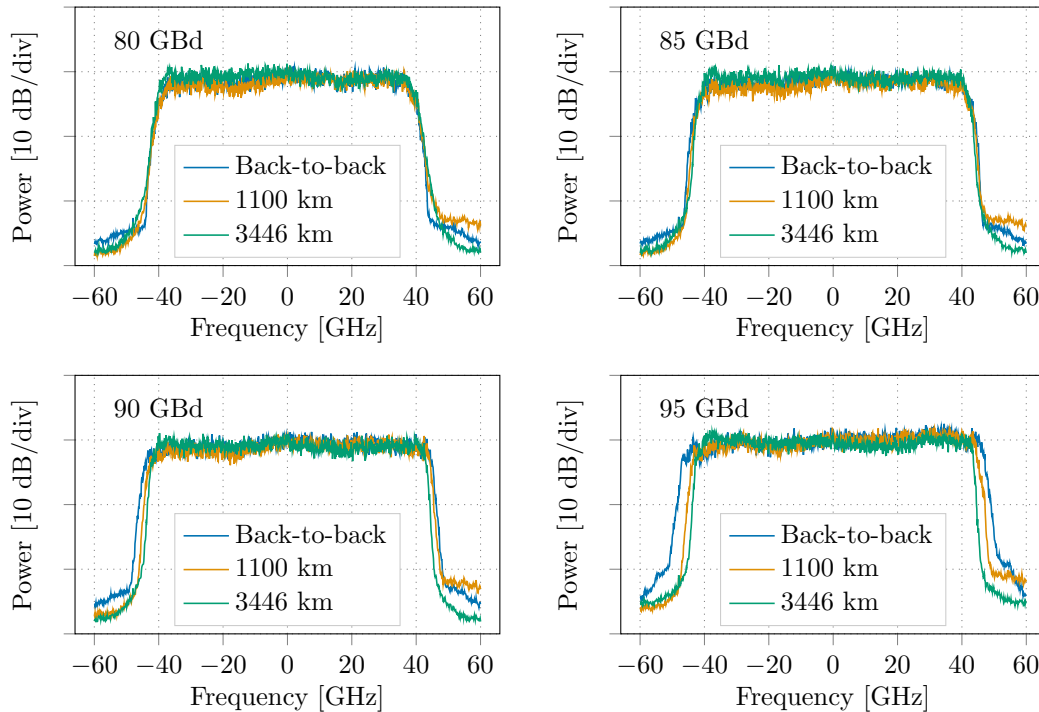


**Figure 3.21:** Filtering effects on 80 to 95 GBd signals due to ROADMs cascade

#### (i) High symbol rate implementation and transmission penalty identification

Fig. 3.22 shows the measured NGMI (circle markers) as a function of the constellation entropy, for 1100 and 3446 km transmissions and symbol rate ranging from 80 to 95 GBd. The general behaviour is that the NGMI decreases both with the symbol rate and the constellation entropy. For a given symbol rate, increasing the entropy reduces the distance between the constellation symbols, thus reducing tolerance to noise. For a given entropy, the NGMI decreases as the symbol rate increases: on the one hand, the in-band ASE noise variance grows linearly with the symbol rate and on the other hand, implementation and transmission penalties increase with the symbol rate.

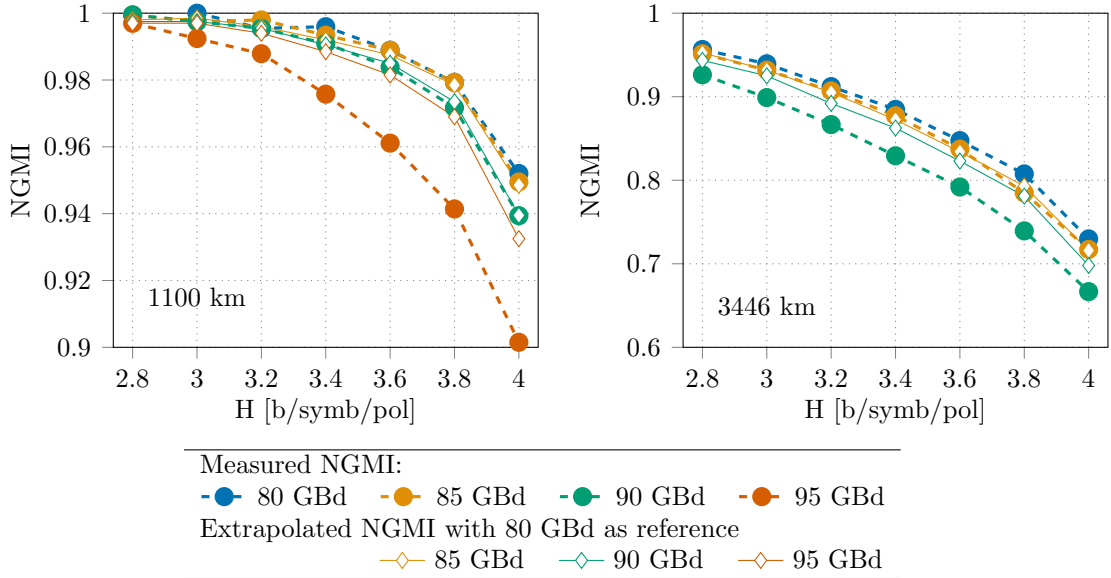


**Figure 3.22:** Evolution of NGMI as a function of constellation entropy  $H$ , for 1100 and 3446 km transmissions and symbol rate ranging from 80 to 95 GBd

To identify the role of each penalty source, we propose the following method. Taking as a reference the 80 GBd curve, we scale the corresponding ASE noise by a factor  $R/(80 \text{ GBd})$  for  $R$  equal to 85, 90 or 95 GBd, and find the corresponding NGMI (diamond markers). This *extrapolated* NGMI therefore takes into account the in-band ASE noise scaling with the symbol rate, assuming there are no extra penalties for 85, 90 and 95 GBd compared to 80 GBd. The difference between the measured NGMI and the *extrapolated* NGMI corresponds to the extra implementation and transmission penalties arising for increasing the symbol rate above 80 GBd.

We show that after 1100 km, the measured NGMI for 85 and 90 GBd signals follows the predicted trend corresponding to in-band ASE scaling, and only the 95 GBd signal appears significantly penalized by extra penalties. For 3446 km, we show the experimental results only for 80 to 90 GBd as the 95 GBd signal was too much degraded during the transmission. The 90 GBd signal now presents extra penalties compared to the extrapolated case: since the 90 GBd does not show implementation penalties at 1100 km, we attribute these extra penalties to the increased distance and particularly to the filtering effects of the 22 ROADMs (37 WSS) crossed along the route.

## (ii) Achievable rate assuming ideal SD FEC

From the NGMI values we deduce the achievable information rate (AIR) for an ideal FEC as

$$R_b^* = (H - (1 - NGMI) \cdot m) \cdot 2 \cdot R_s \cdot r_p \quad (3.4)$$

where  $H$  is the constellation entropy,  $m = 4$  the number of bits of the 16QAM constellation,  $R_s$  the symbol rate and  $r_p = 0.99$  accounts for the rate reduction due to DSP pilot insertion. The AIR computed from the measured NGMI is shown with the circle markers in Fig. 3.23, whereas the diamond markers correspond to the AIR that would be obtained from the extrapolated NGMI (with the in-band ASE scaling as the only impairment when increasing the symbol rate).

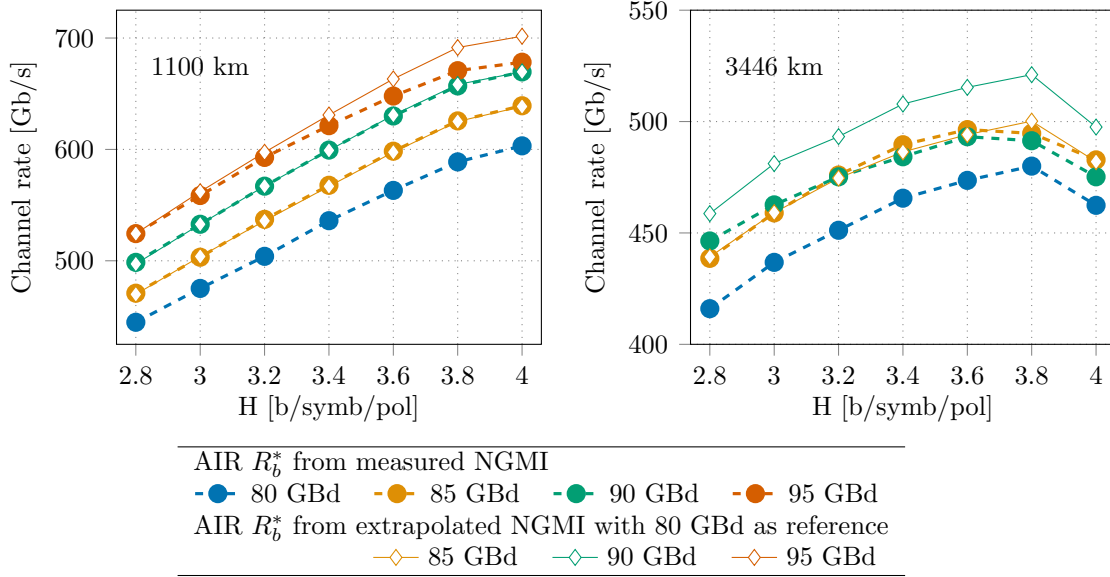


**Figure 3.23:** Evolution of the AIR (ideal FEC) as a function of constellation entropy  $H$ , for 1100 and 3446 km transmissions and symbol rate ranging from 80 to 95 GBd.

For 1100 km, for 80 to 90 GBd, the AIR increases almost linearly with the constellation entropy, except for entropy above 3.8 b/symb/pol when the NGMI drop induces an inflection in the rate growth. Besides, as the measured NGMI does not deviate from the extrapolation with the in-band ASE scaling, increasing the symbol rate from 80 to 90 Gbd enables to scale almost linearly the AIR with the symbol rate. For 95 GBd, as the measured NGMI is degraded by implementation and transmission penalties compared to the extrapolated NGMI, the AIR does not scale as expected with the symbol rate and saturates. Yet, the 95 GBd signal would allow for this 1100 km route the highest achievable rate of 678 Gb/s with an ideal FEC.

The picture changes when going to the maximum tested distance of 3446 km. 80 to 90 GBd signals show a maximum AIR (from measured NGMI) between 475 and 450 Gb/s, obtained for constellation entropies between 3.6 and 3.8 b/symb/pol. 85 and 90 GBd signals show similar performance: while the AIR is close to the extrapolated case for 85 GBd, for 90 GBd it deviates from the expectation as the signal is impaired by filtering penalties.

### 3.5.c) Post SD FEC decoding using SC LDPC

#### (i) Maximizing channel rate with adaptive SC LDPC decoding

This analysis has allowed us to identify the evolution trends of the achievable rate with ideal FEC. Now, we perform FEC decoding using a family of SC-LDPC codes [68]. The code rate ranges from 0.51 to 0.97 and we select for each waveform the highest code rate  $r_c$  allowing error-free transmission. Similarly to (3.4), the post SD-FEC net rate is computed as

$$R_b = (H - (1 - r_c) \cdot m) \cdot 2 \cdot R_s \cdot r_p. \quad (3.5)$$

Fig. 3.24 compares the AIR with ideal FEC decoding (circle markers) and the post SD-FEC net rate using the SC-LDPC codes (square markers). For the 1100 km

case, the NGMI is always above 0.9 and for the maximum entropy of 4/b/symb/pol, high performance of SC-LDPC decoding with code rate between 0.88 and 0.94 provides post SD-FEC net rate beyond 600 Gb/s for 85 to 95 GBd. For the 3446 km case, around the optimal entropy value of 3.6 b/symb/pol, the 85 GBd signal offers the highest post SD-FEC rate of 477 Gb/s with a FEC penalty of 3.9%, whereas the 90 GBd (that shows similar achievable rate with ideal FEC) is penalized by a larger 4.9% FEC penalty as the FEC penalty increases when the code rate decreases.

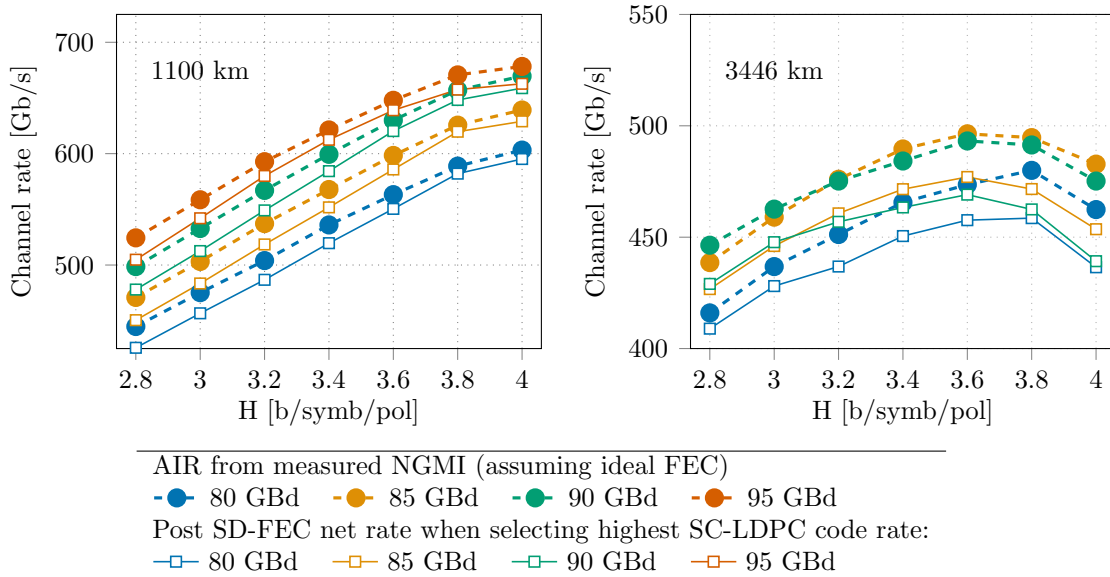


**Figure 3.24:** Evolution of the channel rate (ideal FEC and SC-LDPC) as a function of constellation entropy  $H$ , for 1100 and 3446 km transmissions and symbol rate ranging from 80 to 95 GBd.

Finally, we summarize the performance of the different symbol rates using routes from 1100 km to 3446 km. Fig. 3.25 shows the optimal net rate evolution as a function of the distance. 80 and 85 GBd transmissions show steady reductions of the net rate as the distance increases. The benefit of increasing the symbol rate is reduced as the distance and the number of ROADMs increase. 90 GBd outperforms 95 GBd for the different tested distances, except for 1100 km where the two symbol rates lead to barely the same bitrate. For distances greater than or equal to 1851 km, the performance is severely degraded by the filtering effects for the 95 GBd case. Considering 5% overhead for network protocols, 600G service is achievable at 1100 km using 90 or 95 GBd, 500G transport is possible up to 2300 km with 85 and 90 GBd, whereas 400G transmission is demonstrated up to 3400 km with 80 to 90 GBd signals.

## (ii) Adaptive PCS modulation to limit SC LDPC implementation complexity

In practice, the implementation of adaptive decoding using multiple SD FEC codes is considered as prohibitively complex. We propose to analyze the transmission results when using a single member of the SC LDPC code family to perform the SD FEC decoding. With a fixed code rate  $r_c$  and for a given symbol rate  $R_s$ , the post SD-FEC net rate given by (3.5) is a strictly increasing function of the constellation entropy  $H$ . The maximum net rate is therefore attained when maximizing the entropy, while ensuring error-free transmission with code rate  $r_c$ , i.e. ensuring NGMI above the  $r_c + \Delta$  threshold, where  $\Delta$  is the FEC implementation penalty. For this

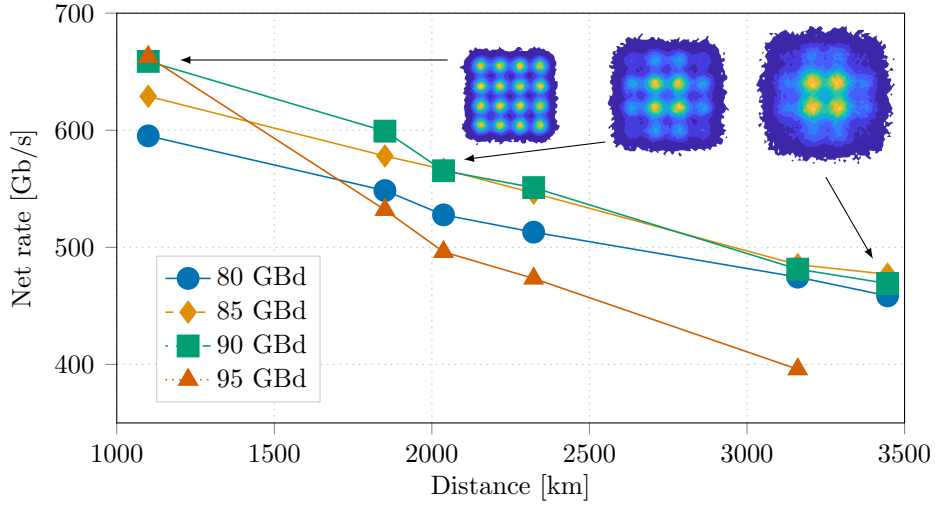


**Figure 3.25:** Optimum net channel rate versus distance when using adaptive SC LDPC decoding

study we analyze three different code rates: 0.75, 0.86 and 0.92.

For the symbol rate of 90 Gbd, Fig. 3.26(a) shows the evolution of the maximum entropy versus the transmission distance, for the selected code rates. At 1100 km, we have seen previously in Fig. 3.22 that the NGMI is above 0.94 for all entropies, so entropy of 4 b/symb/pol is achievable with the three different code rates. When increasing the distance and the transmission noise, the entropy must be decreased to keep NGMI above the NGMI threshold defined by the selected code rate, while maximizing the channel rate. The maximum entropy is then steadily reduced down to 3.6 and 3.0 b/symb/pol at 3446 km for code rate values of 0.75 and 0.86, respectively. At this maximum distance, the NGMI is 0.926 for 2.8 b/symb/pol and decoding is not achievable with 0.92 code rate.

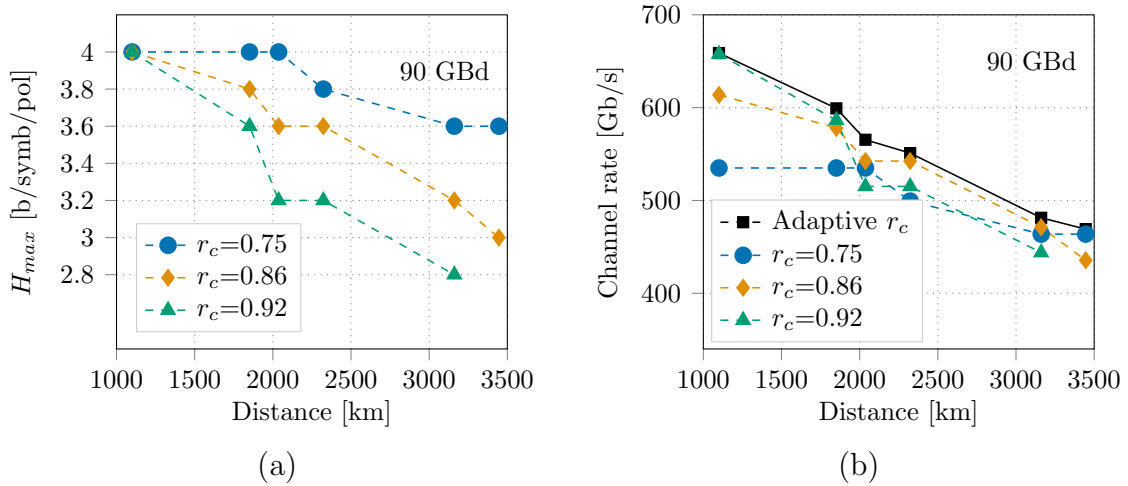


**Figure 3.26:** (a) Maximum entropy and (b) maximum channel rate evolutions with transmission distance when using a single SC LDPC code, for 90 GBd and code rates values of 0.75, 0.86 and 0.92

The post SD FEC net rate, computed with the three selected code rates and the corresponding maximal entropy values for all transmission distances, is shown in Fig. 3.26(b). The black curve represents the optimal channel rate obtained when adaptively selecting the code rate in the whole SC LDPC family as shown

in Fig. 3.25. Using the highest code rate 0.92 allows to reach the optimal 657 Gb/s net rate at 1100 km, but is detrimental when increasing the distance, as the penalty compared to the optimal case is 7.8% at 3161 km and transmission is not achievable at 3446 km. On the contrary, using the 0.75 code rate induces large 18.8% penalty at 1100 km, as below 2037 km the constellation entropy reaches its maximum at 4 b/symb/pol and the channel rate saturates at 535 Gb/s. However, the 0.75 code rate enables to approach the optimal case at 3446 km with a 3.6 b/symb/pol constellation. Finally, the channel rate using the 0.86 code rate is a satisfying trade-off between high performance at shortest reach and high noise resilience for long-haul transmission. By using this single code rate and tuning the entropy from 4 down to 3 b/symb/pol, 613 Gb/s and 435 Gb/s are achievable over 1100 km and 3446 km, respectively, and the penalty compared to the optimal case is between 1.5% (for 2323 km) and 7.1% (for 3446 km), with an average value of 4.2%.

When considering a unique code rate, optimization of the constellation entropy allowed by the PCS scheme is a crucial asset to optimize the spectral efficiency versus transmission distance trade-off while reducing the implementation complexity of SC LDPC decoding.

### **Conclusions on rate versus reach trade-off optimization**

We have demonstrated the in-field transmission of high symbol rate signals over the Orange optical network amidst commercial live-traffic. These tests highlighted how the flexibility in constellation shaping and symbol rate enables us to optimize the tradeoff between spectral efficiency and transmission reach, while taking into account the real-world network context. In particular, we have demonstrated that the implementation penalties and filtering impairments due to ROADMs cascade can be detrimental for 95 GBd transmission in legacy 100 GHz networks. We have shown that 90 GBd signals are able to transport 400G services over 3400 km, 500G over 2300 km and 600G over 1100 km thanks to adaptive SC-LDPC decoding. Finally, we have shown that adaptive constellation shaping alleviates the need of multi-FEC implementation as we have obtained >600 Gb/s transmission over 1100 km and >400 Gb/s over 3400 km when using 90 GBd with code rate 0.86, with penalties between 1.5 and 7.1% compared to the adaptive FEC scheme.

## 3.6 Summary

In this chapter, we have presented experimental demonstrations of high symbol rate (80 to 100 GBd) transmissions. The signals were generated using a DP I/Q coherent transmitter based on CMOS technology, with a single DAC per modulated dimension, compliant with industry requirements in terms of manufacturing process and integration. To cope with the bandwidth limitations of current generation DAC, electrical drivers and electro-optical modulators, we have used an electro-optical bandwidth compensation scheme allowing transmission performance assesment of next-generation high speed transmitters.

In a first transmission experiment, we have demonstrated a 800 Gb/s net channel rate over a 605 km straight line, in line with industry demands for cost-efficient and footprint optimized systems to answer future 800GbE client rates, however showing the tight requirements on line characteristics to transport an SE of 8 b/s/Hz. Then, we have demonstrated a record 300 Gb/s channel rate over a ultra-long-haul 20570 km transmission for all 41 channels in the C-band using 99 GBd DP-QPSK channels, and we have shown how high symbol rate transmitters can suit the requirements of future submarine systems, as the industry is turning towards SDM paradigm. Since the increase of fiber counts in submerged cables inevitably scales the number of required transponders to operate the cable, high symbol rate transceivers are attractive solutions for the design of cost-efficient systems. Finally, we have performed a field trial over a live traffic network to study the compatibility of 80 to 95 GBd signals with real-world network architectures, based on 100 GHz grid nodes. We have highlighted that flexibility in constellation shaping and symbol rate tuning is a major asset to take into account the constraints of legacy optical networks. We have demonstrated the successful transmission of 400 Gb/s over 3400 km ultra long-haul distance, as well as 600 Gb/s over 1100 km using 90 GBd signals.

To conclude, we have shown the capabilities of high symbol rate transmitters in a wide range of configurations, and demonstrated SE of 3 b/s/Hz over ultra-long-haul subsea distance beyond 20000 km, 4 and 6 b/s/Hz transmissions over 3400 and 1100 km distances over a live network traffic, and 8 b/s/Hz in a 600 km lab experiment. High symbol rate transmitters appear as promising candidates to answer future requirements of optical transport networks, in terms of compatibility with high client rates for short distances as well as for cost efficient designs of high capacity long-haul core systems.

Further progress in single DAC capabilities will undoubtedly demand bandwidth improvement of electrical and electro-optical components, as the tolerance to implementation penalties drops when the target SE increases. The deployment of high SE transmission with actual network constraints may also require more complex design of optical paths in reconfigurable networks. Besides the filtering penalties observed in our field trial, in a recent experiment [P16] we have characterized a potentially detrimental sensitivity of 800 Gb/s transmission based on 90 GBd 64QAM to in-band crosstalk due to imperfect channel blockings in optical cross-connects. Properly taking into account these impairments is all the more challenging as they do not arise only either from the TRX or the transmission but require a joint modeling. The next chapter is dedicated to the study of EEPN, a potentially dominant impairment for high symbol rate subsea transmissions with large CD accumulation.



# Equalization enhanced phase noise impact on high symbol rate transmission systems

This chapter focuses on the study of equalization enhanced phase noise (EEPN), that originates from the interplay of the LO phase noise (PN) with the chromatic dispersion electronic equalizer in coherent dispersion-unmanaged (DU) transmission systems. In the context of transoceanic systems, as EEPN is expected to impose tight design requirements for transmissions with large accumulated chromatic dispersion (CD) and high symbol rate transceivers, we present a detailed numerical study aiming at characterizing EEPN properties and studying the EEPN penalty when taking into account the CPE algorithm. Then, we conduct an experimental characterization campaign over a transoceanic testbed to determine EEPN impact using different LO laser sources.

## Contents of this chapter

---

<b>4.1 Introduction</b> . . . . .	<b>90</b>
4.1.a) EEPN in dispersion unmanaged transmission systems . . . . .	90
4.1.b) Review of prior studies . . . . .	92
<b>4.2 DSP-aware EEPN numerical study</b> . . . . .	<b>94</b>
4.2.a) Equivalent system model . . . . .	94
4.2.b) EEPN identification . . . . .	95
4.2.c) DSP aware analysis . . . . .	98
4.2.d) Expected penalties for high speed and transoceanic . . . . .	101
<b>4.3 Experimental characterization of EEPN impact on a transoceanic testbed</b> . . . . .	<b>106</b>
4.3.a) Laser source characterization . . . . .	106
4.3.b) Submarine transmission testbed . . . . .	107
4.3.c) Experimental results . . . . .	108
<b>4.4 Summary</b> . . . . .	<b>111</b>

---

## 4.1 Introduction

With the advent of coherent technology and DU fiber links, the design of optical transport systems has considerably evolved. CDC with electronic equalizers in flexible transponders indeed loosened the dependence between transponder technology and optical path design, and consequently allowed considerable possibilities in network management and evolution. In the domain of subsea communications, whereas optical network vendors used to specify to their clients the point-to-point system performance, they are now strongly encouraged to move to a new paradigm [107] with separate specifications for open cables and for transponder technology.

Soon after the adoption of electronic CDC, a first analytical investigation [108] highlighted that the interaction of the laser PN and the CDC electronic equalizer generates additional impairments called equalization enhanced phase noise (EEPN). This study predicted the EEPN variance to scale linearly with the accumulated CD, the signal symbol rate and the laser linewidth, imposing tight constraints on the laser sources for DU systems.

In the context of transoceanic transmissions with cables of several thousands of km, with low loss fibers showing large CD coefficients (over 20 ps/nm/km) and with next generation transponders able to operate in the 50-100 GBd range, further investigation on EEPN impact has been motivated by concerns on future systems requirements. As EEPN arises from the interaction of the transponder laser with the CDC, it intrinsically bonds the transmission line properties to the transponder characteristics. In the open cables context, this motivates a more accurate characterization for the inclusion of its impact in system performance computation.

### 4.1.a) EEPN in dispersion unmanaged transmission systems

To understand the origins of EEPN, a simplified model of a DU long-haul transmission system is given in Fig. 4.1. The signal under study is modulated by a I/Q modulator (without loss of generality, only single-polarization signals are considered here). The transmission link is composed of  $N_{span}$  identical fiber spans. Each span is followed by an EDFA to restore the optical power after fiber attenuation. At the end of the link, a LO laser and a coherent receiver are used to convert the optical signal into baseband electrical signals.

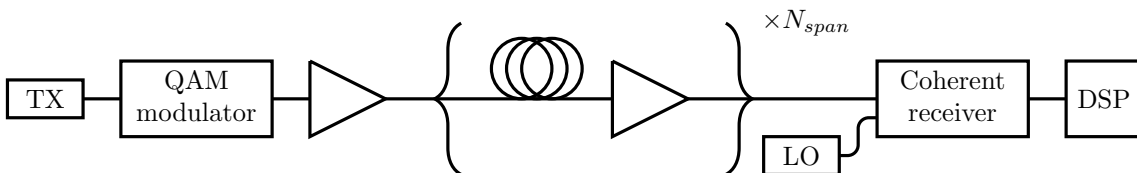


**Figure 4.1:** Simplified model of DU long-haul transmission link for EEPN study

In this model, the signal impairments are only due to fiber CD, ASE noise from optical amplification and carrier PN arising from TX and/or LO lasers. Each laser PN is modeled by a random walk (Wiener process), whose step size is proportional to the laser linewidth.

The DSP consists in matched filtering with respect to the electrical pulse shaping at the transmitter, ideal CDC in the frequency domain and CPE to estimate the

time-varying phase offset of the received constellation due to TX and LO PN, as described in section 1.5.b). CFE is not required as the frequency detuning between the lasers is set to 0 in the simulations.

As an illustrative example, Fig. 4.2 shows simulation results of the transmission of a 49 GBd QPSK signal in a 6600 km link, composed of  $N_{span} = 120$  fiber spans of 55 km PSCF (Corning EX3000) and EDFA with noise figure 5 dB. The constellations of the upper line (Fig. 4.2(a), (b) and (c)) correspond to transmissions where the CD coefficient has been set to 0, whereas for the bottom line, i.e. Fig. 4.2(d), (e) and (f), the CD coefficient value is 20.6 ps/nm/km. The simulations are performed either without PN (left column), or with a PN following a Wiener process with laser linewidth 500 kHz at the TX laser only (middle column) or at the LO only (right column).

In numerical simulations, the generated PN random walk  $\phi_k$  is perfectly known and can be used to perform CPE using genie-aided PN cancellation, such that the symbols  $\hat{x}_k$  are recovered from the symbols  $y_k$  after CDC as  $\hat{x}_k = y_k e^{-j\phi_k}$ . The grey markers indicate the signal samples after CDC and before the CPE, whereas the blue markers correspond to the signals after CPE.

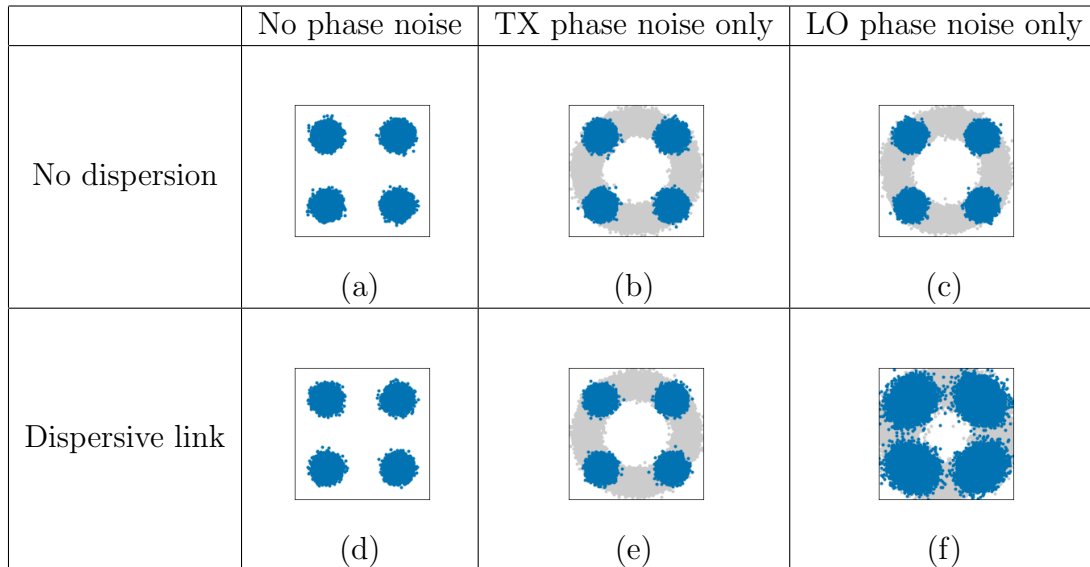


**Figure 4.2:** Constellations diagrams for 49 GBd QPSK transmission over a transoceanic link (6600 km composed of 120 spans of 55 km PSCF ( $D=20.6$  ps/nm/km,  $\alpha=0.15$  dB/km) and EDFA with noise figure 5 dB), neglecting transceiver penalties and fiber nonlinearity. The laser linewidth is 500 kHz for the TX and the LO in the middle and right column, respectively.

When the dispersion is set to 0, in the absence of PN, the constellation shown in Fig. 4.2(a) is only impaired by ASE noise: this is the reference case of this example. When PN is turned on for the TX (Fig. 4.2(b)) or the LO (Fig. 4.2(c)), the samples before CPE (grey markers) are rotated due to the random PN coming from the corresponding laser. After performing CPE with genie-aided PN cancellation, the resulting constellations (blue markers) are similar to the one in Fig. 4.2(a): in the non-dispersive case genie-aided PN cancellation allows perfect PN compensation for both TX and LO lasers.

For the case of a dispersive link, when no PN is considered (Fig. 4.2(d)), dispersion is completely mitigated by the CDC and there is no penalty compared to the reference case of Fig. 4.2(a). When only TX PN is turned on (Fig. 4.2(e)), the performance is still the same after CDC and CPE: the transmitted signal is impaired

first by the TX PN, then fiber dispersion and ASE addition. The DSP compensates first for the CD, then for the TX PN (reverse order compared to the impairments), and the resulting constellation is similar to the reference case. When LO PN is turned on, we observe that after propagation, mixing with LO, CDC and CPE, the signal is strongly degraded. Applying the CDC on the received signal impaired with LO PN results in the conversion of the pure LO PN into an enhanced noise called EEPN. EEPN results from the non-commutability of the PN and the CD, whereas the DSP performs first CDC and then CPE. Note that if CDC is performed at the transmitter side, then the roles of TX and LO lasers in EEPN generation are permuted.

### 4.1.b) Review of prior studies

The first analytical analysis of EEPN impairments used a time-domain impulse response approach to compute the variance of EEPN at CDC output with phase noise generated only by the LO laser [108]. The EEPN variance was found to scale linearly with the fiber length (through accumulated CD), the laser linewidth and the symbol rate. Whereas for a given laser linewidth, the classical PN impairments reduce with the symbol rate, EEPN impact evolves in the opposite direction, making its study crucial as the industry fosters the continuous increase of the transceiver symbol rates.

Assuming that EEPN can be modeled as an independent AWGN, the EEPN variance [108] was added to that of the ASE noise, and the EEPN system penalty was derived in terms of SNR [108] or OSNR [109]. However, the AWGN assumption, yet very useful for a coarse prediction of EEPN impact on system design, does not take into account the fundamental properties of EEPN distortions, that originates from the dispersion of the LO phase noise (a low-pass stochastic process) by the CDC equalizer.

To better capture the nature of EEPN distortions, numerical simulations have been useful to assess EEPN impact on LO linewidth constraints, as in [110], using QPSK signals and a practical  $M$ -th power method as CPE algorithm, or in [111] which highlighted tighter laser requirements for higher modulation formats such as 16QAM and 64QAM, while using a maximum likelihood estimate of the carrier phase for the CPE. It has been shown in [112] that the EEPN affecting the QPSK signal can be partially mitigated by the Viterbi-Viterbi phase recovery, so that the analytical model overestimates the EEPN impact on system design. Further on, a digital mitigation technique by a fast equalizer replacing the conventional phase recovery algorithm was also proposed in [113].

Through a frequency domain analysis with numerical simulation validation, it has been shown that the EEPN penalties can be mainly attributed to the low frequency components of the laser PN [114]. To limit the impact of EEPN on system design, hardware solutions have been proposed to partially mitigate EEPN [115], based on a hardware digital coherence enhancement (DCE) technique developed in [116] which is able to loosen the linewidth requirements at the cost of a more complex receiver architecture with an additional coherent receiver to measure the laser PN.

Based on the observations that EEPN impacts comes from the laser PN low

frequency features, and that it has been shown that CPE algorithm can influence and even mitigate EEPN impairments, we believe that further investigation of EEPN impact including CPE analysis is required, as the current industry trend is towards ever increasing symbol rates (100 GBd is now practical) and there is demand for submarine cables of 15000 km or more.

### **Chapter outline**

In this chapter, we revisit the EEPN analysis and carry out a detailed numerical characterization, taking into account the BPS [55] as the CPE algorithm. We perform Monte Carlo simulations to extract EEPN contributions, and study the EEPN penalty for PCS modulations recently proposed for transoceanic systems with large accumulated CD and high symbol rate. Then, we present an experimental characterization of the impact of EEPN arising from different laser sources in an ultra long-haul submarine configuration. In particular, we study the impact of using a standard LO laser source with 100 kHz specified linewidth on the transmission performance of a 90 GBd signal over a 10476 km transmission.

## 4.2 DSP-aware EEPN numerical study

In this section based on a journal paper [P3] published in 2019, we present the results of our numerical simulations to characterize EEPN in the context of transoceanic transmissions using high symbol rate transmitters. We first propose a system model that allows us to precisely extract EEPN distortions from the other noise contributions, and we study the temporal and statistical characteristics of EEPN. Then, we study EEPN penalty in terms of system design on modern and future transoceanic systems, based on recent transmission experiments [100, 117].

Previous studies [108, 109] have shown that for electronic CDC at the receiver the TX laser PN impacts only phase recovery but does not contribute EEPN. First, we will omit TX PN to characterize EEPN statistical and temporal characteristics. However, as we include in this analysis the influence of BPS, whose optimum performance and averaging length depend on both TX and LO PN, it will be included in the rest of the study to quantify the impact of EEPN in a realistic system after DSP.

### 4.2.a) Equivalent system model

We use the equivalent baseband model described in Fig. 4.3. A stream of symbols  $x_k$  at the symbol rate  $R_s = 1/T_s$  is passed through the equivalent transfer function  $H(f)$  modeling TX pulse shaping and fiber accumulated CD. The noise contribution  $n(t)$  is AWGN and represents the total ASE noise generated by all amplifiers during the transmission. At the receiver, the signal is multiplied by the LO field. The LO PN process  $\phi_{LO}(t)$  is a Wiener process; therefore, the continuous-wave optical field of the LO laser has a Lorentzian spectrum with FWHM  $\Delta\nu$  (cf. Fig. 4.4). The FWHM  $\Delta\nu$  is also referred to as 3 dB laser linewidth, or more simply laser linewidth.

The DSP consists of channel equalization (including matched filtering and CDC) modeled by  $H^*(f)$ , symbol-spaced sampling at the rate  $R_s = 1/T_s$ , and the CPE algorithm. Note that we focus this work on EEPN identification and CPE impact, and do not include in our simulations the role of additional DSP algorithms, such as fast adaptive equalizers that can partially mitigate EEPN, as shown in [113]. Furthermore, the frequency detuning between the TX and LO lasers is set to 0, and the impact of CFE algorithm and residual frequency offset has not been addressed in this study.

Through this study, we consider single-channel transmissions over EX3000 fiber ( $D=20.6$  ps/nm/km) with central frequency  $f_0=194$  THz, we set  $P_{in}=0$  dBm and  $P_l=10$  dBm and we neglect NL impairments.

The sampled received symbol at CPE input (output) is denoted by  $y_k$  ( $\hat{y}_k$ ). We denote the EEPN term at CPE input by  $w_k$ . It is *defined* by the following equation

$$y_k = \sqrt{P}x_k e^{j\phi_k} + n_k + w_k, \quad (4.1)$$

where  $\phi_k = \phi_{LO}(kT_s)$  is the sampled LO phase,  $n_k$  the sampled ASE noise passed through the coherent receiver and channel equalization filter  $H^*(f)$ , and  $P = 2P_l P_{in}$  the received signal electrical power after coherent detection, where  $P_l$  is the LO optical power, and  $P_{in}$  the transmitted optical signal mean power.

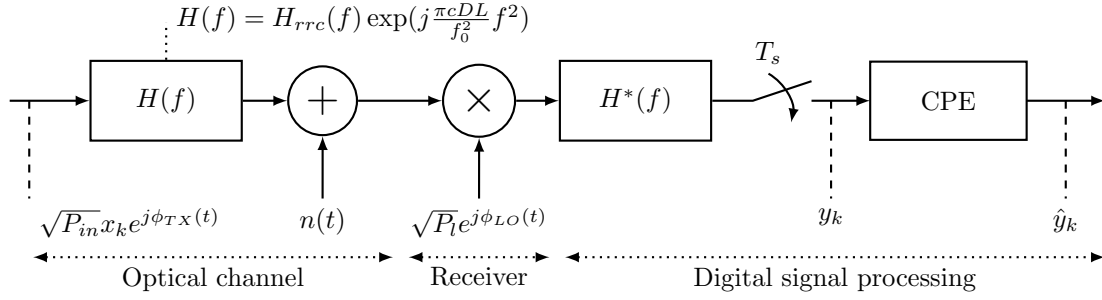


**Figure 4.3:** System baseband model with  $x_k$ : transmitted symbols,  $\phi_{TX}(t)$ : TX PN process,  $H(f)$ : channel response,  $H_{rrc}(f)$ : RRC transfer function, roll-off 0.01,  $c$ : the speed of light,  $D$ : fiber CD coefficient,  $L$ : transmission length,  $f$ : frequency,  $f_0$ : channel center frequency,  $H(0) = \sqrt{T_s}$ ,  $T_s$ : symbol duration,  $n(t)$ : ASE noise process,  $\phi_{LO}(t)$ : LO PN process,  $P_{in}$ : signal mean power,  $P_l$ : LO power,  $*$ : complex conjugation

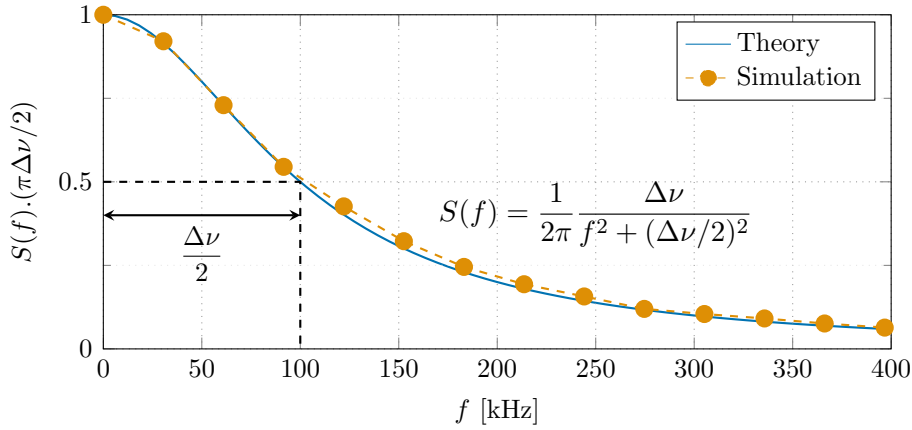


**Figure 4.4:** Normalized PSD of the LO field, for a laser linewidth  $\Delta\nu=200$  kHz.

At the receiver, the CPE gives an estimate  $\hat{\phi}_k$  of the carrier phase and rotates the received signal by this estimated phase  $\hat{\phi}_k$  such that the signal after CPE is  $\hat{y}_k = y_k e^{-j\hat{\phi}_k}$ . The total distortion, including ASE, residual PN and residual EEPN after CPE, is denoted by  $N_k$  and is obtained from

$$N_k = \hat{y}_k - \sqrt{P} x_k e^{j\hat{\phi}_k}. \quad (4.2)$$

Finally, we compute the variance  $\sigma_N^2$  of the total noise  $N_k$  and estimate the SNR of the received signal after CPE as  $SNR = P/\sigma_N^2$ .

### 4.2.b) EEPN identification

To identify the properties of EEPN, with Monte Carlo simulations we generate and save the  $x_k$ ,  $\phi_k$  and  $n_k$ , such that once  $y_k$  is produced,  $w_k$  can be extracted without ambiguity using its definition in eq. (4.1).

#### Statistical properties

We consider 6600 km transmission of a single-polarization 64QAM channel. We generate 10 sample functions of the LO PN process over a time window including  $2^{17}$  symbols, with sequence length of  $2^{13}$  symbols, and throw out 15000 symbols from each side of every simulated waveform, to avoid biasing the statistics by the numerical transients. For symbol rates of 49 and 98 GBd, Fig. 4.5 compares the evolution

with the LO linewidth  $\Delta\nu$  of the variance  $\sigma_w^2$  of the EEPN term  $w_k$  computed from the numerical simulations and the analytical variance computed in [108]:

$$\sigma_{EEP N}^2 = \frac{\pi c D L R_s \Delta\nu}{2 f_0^2}. \quad (4.3)$$

Note that (4.3) is valid for normalized transmitted symbols and therefore,  $\sigma_{EEP N}^2$  has been here multiplied by the signal power  $P$  to meet our definition of EEPN term, which does not use power normalization. We show that, before CPE, our simulations and identification of EEPN term match the analytical model in the litterature [108].

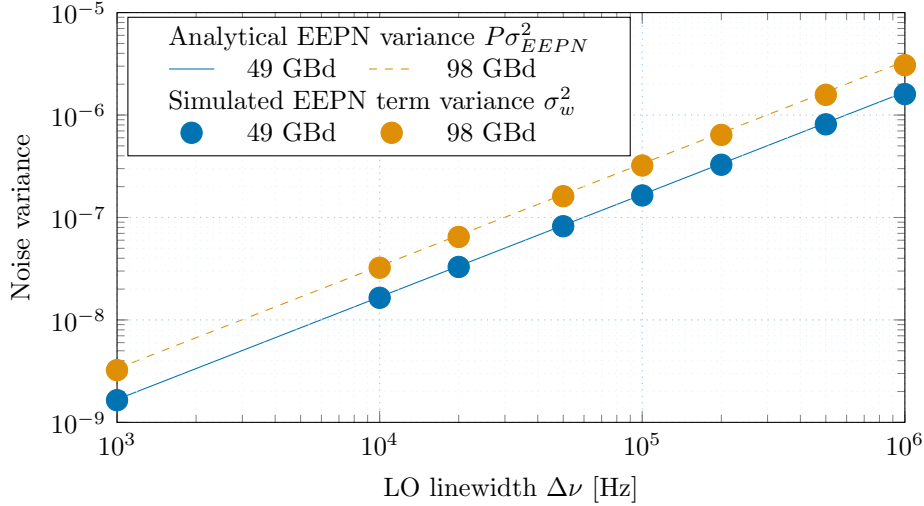


**Figure 4.5:** Analytical and numerical EEPN variance evolution as a function of LO linewidth, for 49 and 98 GBd 64QAM single-channel transmission through 6600 km EX3000, with OSNR equal to 20 dB/0.1nm

Fig. 4.6(a) shows the normalized PDF of the real part of the total noise  $n_k + w_k$  (dashed line), that fits a Gaussian shape (solid line). The total distortions accounting for ASE and EEPN can be considered as Gaussian, however we show in Fig. 4.6(b) that the real part of the EEPN term  $w_k$  at CPE input (dashed line), does not fit a Gaussian shape (solid line).

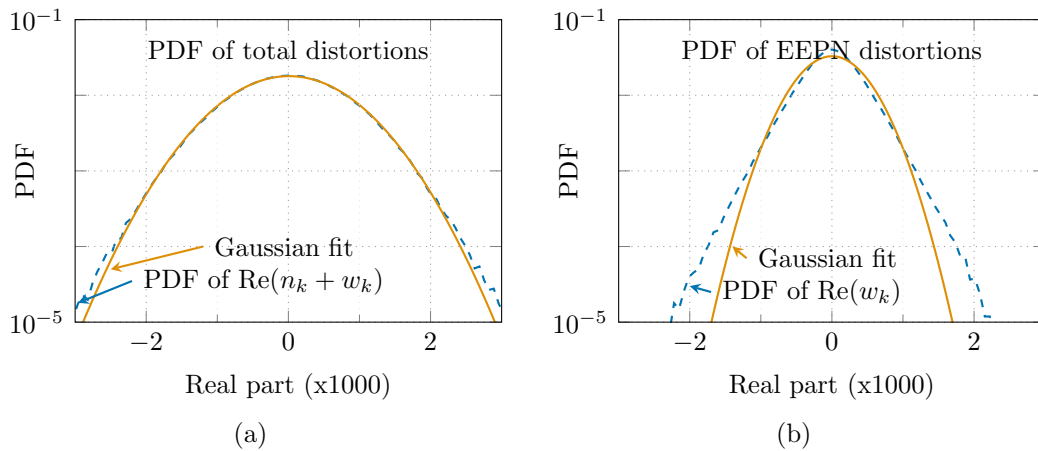


**Figure 4.6:** PDF of the real part of (a) total distortions at CPE input  $n_k + w_k$  and (b) EEPN distortions at CPE input  $w_k$ . Numerical simulations are performed for a 49 GBd 64QAM single-channel transmission through 6600 km EX3000, neglecting nonlinearity, with OSNR equal to 20 dB/0.1nm and LO linewidth set to 200 kHz

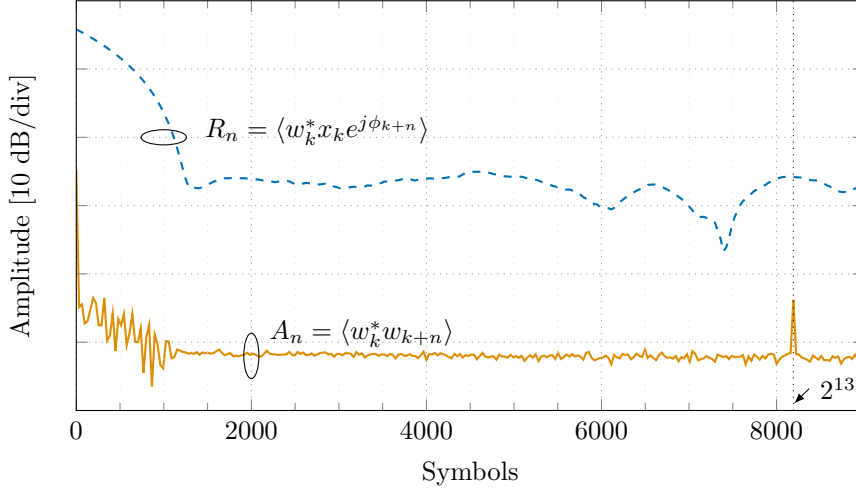


**Figure 4.7:** EEPN autocorrelation  $|A_n|$  (solid line) and signal - remodulated EEPN cross-correlation  $|R_n|$  (dashed line) for a 49 GBd 64QAM transmission through 6600 km EX3000, neglecting nonlinearity, with OSNR equal to 20 dB/0.1nm and LO linewidth set to 200 kHz.

### Temporal properties

We now study the temporal properties of the EEPN term  $w_k$ . For 49 GBd transmission over 6600 km, Fig. 4.7 shows the autocorrelation of the EEPN term defined as  $A_n = \langle w_k^* w_{k+n} \rangle$  (solid line). Averaging is performed over 500 samples of the LO PN. We observe that the autocorrelation shows a peak at  $2^{13}=8192$  symbols: its corresponds to the length of the symbol sequence and shows the dependence of EEPN term on the transmitted signal. The EEPN autocorrelation also shows low-pass features, spreading on several hundreds of symbols, highlighting the non-white nature of EEPN. We attribute these features to be caused by the dependence of the EEPN on the LO field. In [114], it has been shown that the EEPN can mainly be attributed to the low frequency components of the laser PN.

We then compute and plot the cross-correlation  $R_n$  between the LO field  $e^{j\phi_k}$  and the EEPN distortions with ideal data remodulation  $w_k x_k^*$  (hence removing dependence on the transmitted data) defined as

$$R_n = \langle (w_k x_k^*)^* e^{j\phi_{k+n}} \rangle = \langle w_k^* x_k e^{j\phi_{k+n}} \rangle \quad (4.4)$$

The cross-correlation  $R_n$  presents similar low-pass features, with more than 2 orders of magnitude higher amplitude. It shows that EEPN term, whose dependence on data has been removed, is strongly correlated to the LO field. Fig. 4.8 shows the normalized LO field-EEPN cross-correlation  $R_n$  for 6600 km or 13419 km transmission. We observe a one-sided width at half maximum of around 400 symbols for 6600 km, and 760 symbols for 13419 km.

Using numerical simulations to isolate EEPN contributions from the total noise impairments, we show that the EEPN is a non-Gaussian noise which depends on the transmitted data and the link properties. Furthermore, we show that EEPN is correlated to the LO PN. In the following, we therefore propose an analysis that takes into account the influence of the phase recovery DSP to correctly assess the impact of EEPN in transmission systems.

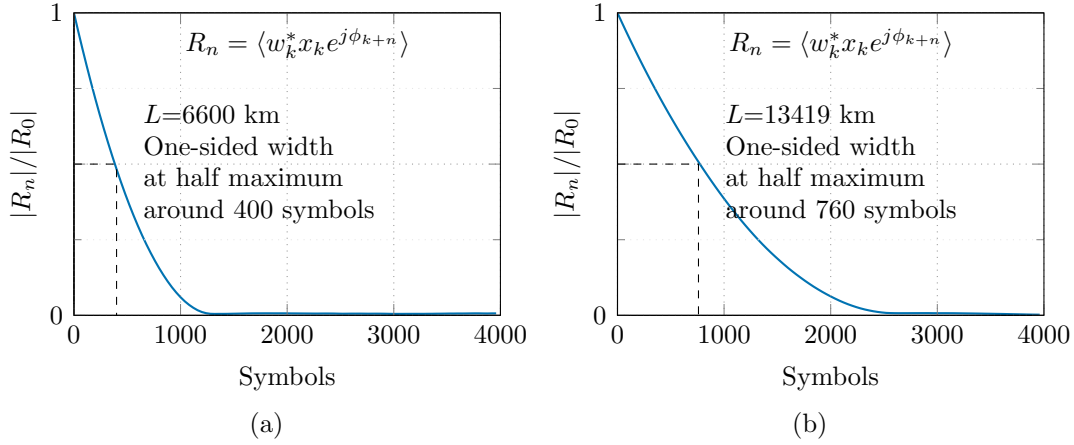


**Figure 4.8:** Signal-EEPN cross-correlation for a 49 GBd single-channel 64QAM transmission through (a) 6600 km or (b) 13419 km EX3000, neglecting nonlinearity, with OSNR equal to 20 dB/0.1nm and LO linewidth set to 200 kHz

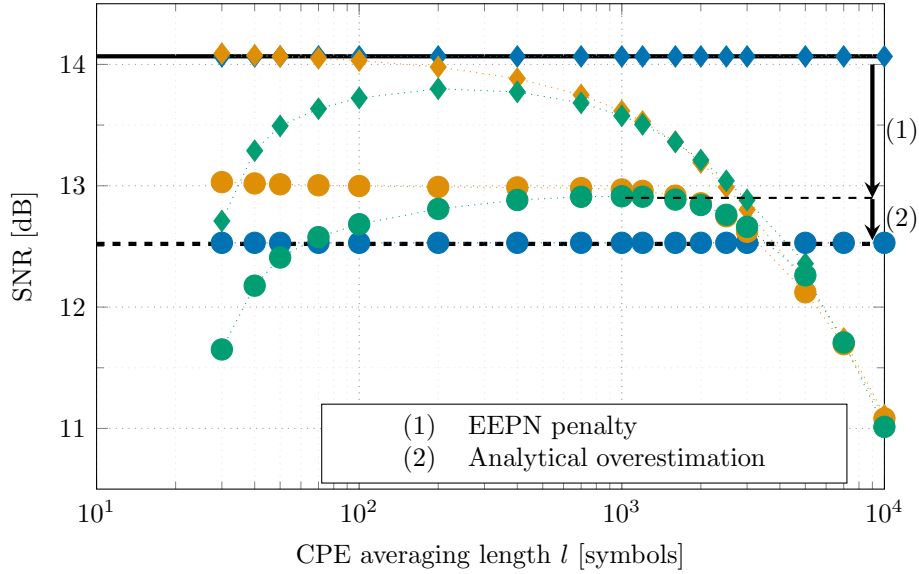
### 4.2.c) DSP aware analysis

#### CPE influence

In practical applications, CPE is performed with Viterbi-Viterbi or BPS algorithm. In numerical simulations, we have perfect knowledge of all signals and we can compare BPS to two other CPE implementations to understand the CPE behavior in the presence of EEPN: LO phase cancelation, requiring perfect knowledge of the LO random phase i.e. we assume  $\hat{\phi}_k = \phi_k$ , and ideal data remodulation (IDR), assuming perfect knowledge of the transmitted symbols and compute the estimated phase over an averaging block of length  $N = 2l + 1$  as  $\hat{\phi}_k = \angle \sum_{k=-l}^l y_k x_k^*$ . In the BPS case the estimated phase  $\hat{\phi}_k$  is computed as the output of the BPS algorithm with an averaging block of length  $N = 2l + 1$ . Note that when using BPS, in this work, all cycle slips are removed to avoid performance degradation from ambiguity coming from constellation symmetry.

Assuming the same setup as in Fig. 4.6 and with the three different CPE techniques, we compute the received signal  $\hat{y}_k$  after CPE and we plot the estimated SNR in Fig. 4.9. The solid black line is the theoretical SNR for a fixed OSNR of 20 dB/0.1nm, assuming that ASE is the only source of noise. Next, we turn on LO PN but keep dispersion to zero. Just as a numerical sanity check, LO phase cancelation (when  $\phi_k$  is used as  $\hat{\phi}_k$ ) meets the solid line of the theoretical SNR. For short CPE averaging, the IDR method reaches the theoretical performance, showing that LO PN is completely removed by data remodulation. As the block length increases, the LO PN tracking is degraded by the averaging process and the performance decreases. BPS exhibits an optimal averaging length around 200 symbols. Below this optimum, phase estimation is degraded by ASE noise which is not sufficiently averaged by the BPS process. Beyond this optimum, the averaging window is too long and does not allow to follow the LO PN, hence the BPS performance curve converges to that of the IDR curve, and both IDR and BPS performance degrade due to not following the PN Wiener process.

Next, we turn on the dispersion (hence EEPN). We observe that the phase recovery by LO phase cancelation meets the case where EEPN is modeled as an equivalent AWGN (dashed line) with the variance computed in [108] and is *not* the best strategy to perform CPE in presence of EEPN. Even if we have perfect knowledge of the

**Analytical:**

— ASE only

- - - ASE + equivalent AWGN [108]

**Simulation with ASE, without EEPN (dispersion kept to 0):**

◆ LO phase cancellation

◆ IDR

◆ BPS

**Simulation with ASE and EEPN:**

● LO phase cancellation

● IDR

● BPS

**Figure 4.9:** SNR vs. CPE averaging length, for LO phase cancellation, IDR and BPS carrier phase estimation of a 49 GBd 64QAM single-channel transmission through 6600 km EX3000, neglecting nonlinearity, with OSNR equal to 20 dB/0.1nm and LO linewidth set to 200 kHz

LO PN, as shown in [112], using LO PN as phase estimate  $\hat{\phi}_k$  is non-optimal as it ignores that the phase to be removed by the CPE is a combination of LO phase noise  $\phi_k$ , transmitted symbols  $x_k$  and CDC equalizer transfer function  $H^*(f)$ . An *ideal* phase recovery would indeed exploit the full knowledge of the PN, the transmitted symbols, the CD and the CDC. The IDR exhibits the best performance among the three considered cases in the presence of EEPN: for short averaging length, it reaches a SNR level which is 0.6 dB greater than that achieved by AWGN equivalent noise model; the performance decreases slowly when the averaging length increases (only 0.2 dB when  $l$  varies from 30 to 1000), before decreasing strongly when the averaging process does not allow to track the phase variations anymore. Finally, we show that the BPS algorithm exhibits an optimal performance which almost reaches the IDR case, outperforming the analytical prediction by 0.4 dB when the averaging block length is set to 1000. The SNR offset labeled as (1) on Fig. 4.9, shows the true EEPN penalty with optimized BPS. The SNR offset labeled as (2) is the amount by which the formula (4.3) overestimates the EEPN penalty.

We show that in the presence of EEPN, LO phase cancellation that uses full knowledge of the LO PN process is not the optimal CPE method and can be outpaced by optimized BPS. The optimal BPS performance is attained for longer averaging block length compared to PN-only case. This change of behavior of the BPS algorithm in the presence of EEPN can be considered as a signature of EEPN non-white nature, showing that the BPS must be taken into account in the study of EEPN impact.

### Impact of modulation format choice

Previous analysis was performed assuming 64QAM modulation. Now we study the influence of modulation format on BPS performance in presence of EEPN. Assuming the same setup as in Fig. 4.9, we plot in Fig. 4.10, in presence of EEPN, the SNR after BPS for QPSK, 64QAM and PCS64QAM with source entropy equal to 5.4 bits/symbol. The theoretical performance with EEPN modeled as equivalent AWGN is drawn in dashed line. Compared to 64QAM, QPSK shows better resilience to CPE averaging length variation, with a stable SNR performance of almost 13 dB with moving average filter lengths varying from 50 to 1000. For the short averaging length where the phase estimation process is limited by the ASE noise, decision errors arise more often with constellations with high cardinality and small distances between symbols. For PCS64QAM, this degradation drastically falls at low averaging lengths, indicating that PCS format imposes tighter constraints on the CPE parameter than the unshaped formats. PCS modulation indeed reduces the occurrences of outer symbols of the constellation which contribute more to the BPS cost function (see section 1.5.b)) than the inner ones. Pilot symbols can be used to improve the DSP performance for PCS format and their impact has not been considered in this study. As a matter of fact, the maximum achieved SNR for all the constellations is very similar, provided the moving average length is separately optimized for each format. The block averaging length must be optimized in each configuration and under this condition, in this example, the degradation from the advanced formats remains negligible at the optimal point of operation.

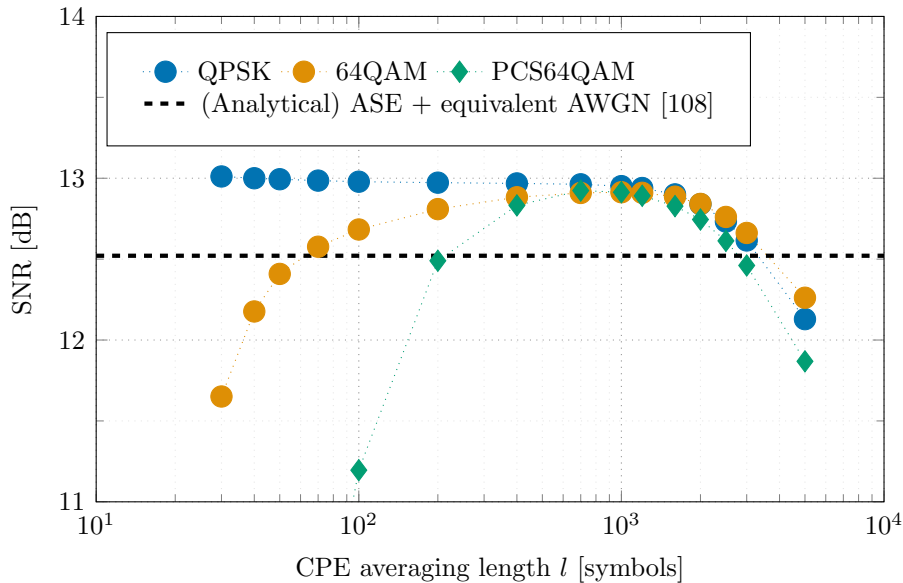


**Figure 4.10:** SNR vs. CPE averaging length, for optimized as BPS carrier phase estimation of a 49 Gbd single-channel transmission using QPSK, 64QAM or PCS64QAM, through 6600 km EX3000, neglecting nonlinearity, with OSNR equal to 20 dB/0.1nm and LO linewidth set to 200 kHz.

The optimization of the BPS averaging length, depending on parameters such as the LO linewidth, the OSNR of the transmission, the cumulated CD and the modulation format, has been shown to result in optimal averaging block length of 1000 symbols or more for the considered transoceanic transmission use cases. Such block lengths might be particularly challenging for industrial implementation using ASICs. Fig. 4.10 suggests that the sub-optimal averaging length of the CPE, due to hardware complexity constraints, may result in extra penalties, hence emphasizing

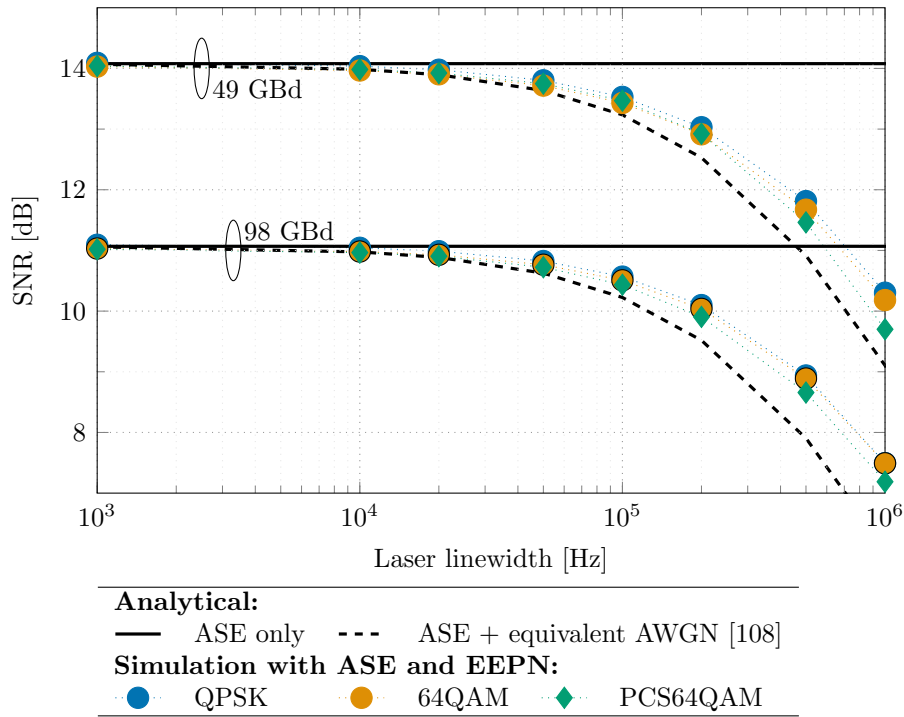


**Figure 4.11:** SNR vs. LO laser linewidth, for optimized BPS as CPR of a 49 GBd or 98 GBd single-channel transmission using QPSK, 64QAM or PCS64QAM, through 6600 km EX3000, neglecting nonlinearity, with OSNR equal to 20 dB/0.1nm.

the importance of DSP-aware analysis in studying EEPN.

To further investigate the format dependence of EEPN penalty, after selecting BPS averaging length to optimize the SNR, in Fig. 4.11 we plot the received SNR versus LO laser linewidth for a 49 GBd and a 98 Gbd transmission using QPSK, 64QAM and the PCS64QAM, after 6600 km transmission with OSNR equal to 20 dB/0.1nm. The solid line shows the theoretical performance in the absence of EEPN, whereas the dashed line indicates the analytical performance when EEPN is modeled as an equivalent AWGN using (4.3). At low linewidths, all the formats reach the theoretical SNR without EEPN, which differs by 3 dB between 49 and 98 GBd, corresponding only to a doubling of ASE noise in the channel bandwidth. Note that, for all formats, the achieved SNR with BPS is higher than what is analytically predicted with equivalent AWGN. At highest linewidth of 1 MHz, the excess EEPN penalty for PCS64QAM with respect to QPSK is inferior to 0.3 dB.

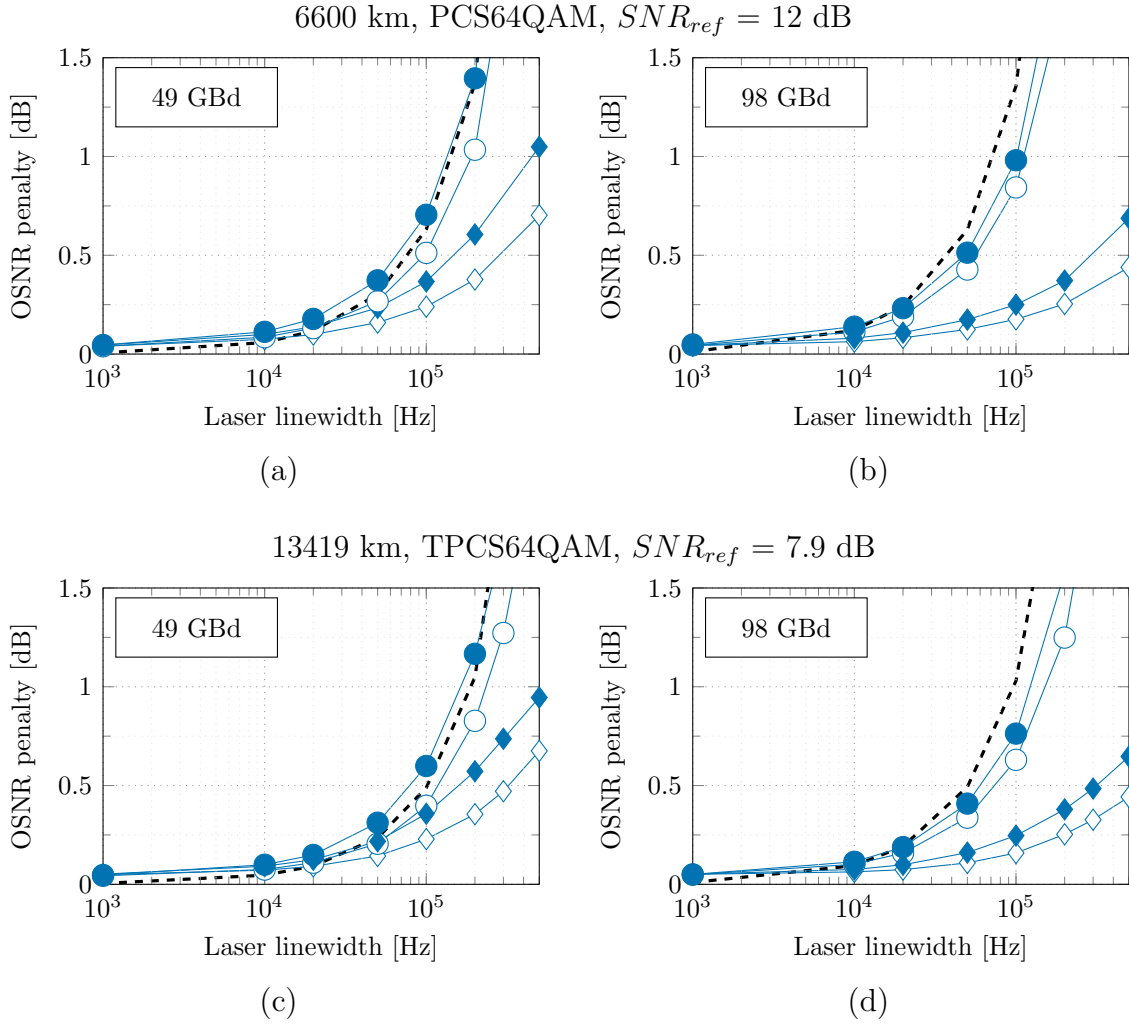
The takeaway is that according to these simulations, the EEPN penalty is only mildly format dependent, provided BPS averaging length has been optimized. In the rest of this work, we only focus on the emerging PCS formats to study EEPN penalty on long-haul transmission system design.

#### 4.2.d) Expected penalties for high speed and transoceanic

##### OSNR penalty definition

To assess the amount by which system performance could be underestimated due to simplifying assumptions, in Fig. 4.12 we plot the estimated SNR after DSP vs. OSNR curves, assuming the same numerical setup as in Fig. 4.6 and sweeping the ASE noise variance. The operative SNR at the considered configuration was set to  $SNR_{ref} = 12$  dB according to [100] and the EEPN impact is considered in terms



**Analytical:**

--- ASE + equivalent AWGN [108]

**Simulation with ASE and EEPN, phase noise generated by LO only:**

—○— Total OSNR penalty    —◇— PN penalty (no dispersion)

**Simulation with ASE and EEPN, phase noise generated by LO and TX:**

—●— Total OSNR penalty    —◆— PN penalty (no dispersion)

**Figure 4.13:** Simulation results of OSNR penalty induced by EEPN as a function of LO linewidth for a single-channel transmission through EX3000 fiber, neglecting nonlinearity. For a transatlantic 6600 km PCS64QAM transmission, OSNR penalty is given for 49 GBd (a) and 98 GBd (b). For a transpacific 13419 km TPCS64QAM transmission, (c) and (d) show OSNR penalty for 49 GBd and 98 GBd.

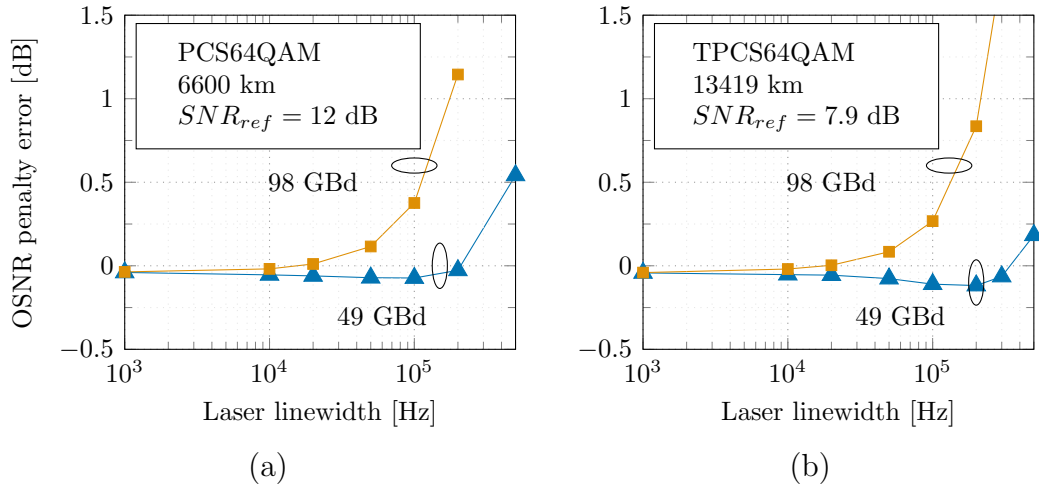
same linewidth. In this case filled circles represent the total EEPN penalty, and filled diamonds correspond to PN only penalty. For each simulation point, the BPS was separately optimized to get the maximum SNR. The dashed line represents the penalty predicted by the analytical model [108] where EEPN is modeled as an equivalent AWGN. Given this analytical model does not capture the CPE, its predictions do not depend on the linewidth of the TX laser.

Fig. 4.13(a) presents simulation results for transatlantic transmission of 49 GBd PCS64QAM over 6600 km, with a target SNR of 12 dB (parameters set according to [100]). For low linewidths, EEPN and PN penalties are similar and they are slightly

higher than the analytical prediction, due to BPS implementation penalty. As the linewidth increases, EEPN increasingly dominates PN. When TX laser linewidth is set to zero, for LO linewidths larger than 20 kHz, the total OSNR penalty (white circles) is always lower than the pessimistic analytical prediction. When TX laser linewidth is set to that of LO, even if TX laser PN does not directly contribute to EEPN generation, this additional PN impacts BPS optimum point. As a result, the PN penalty (filled diamonds) and the total penalty (filled circles) increase and to keep EEPN penalty under 1 dB of OSNR, we must limit the linewidth at 130 kHz. Since the industry trend is towards increasing the per-channel symbol rate, hence reducing transponder count and cost-per-bit, on Fig. 4.13(b), we examine the OSNR vs. linewidth penalty of 98 GBd PCS64QAM on the same link as in Fig. 4.13(a). In the analytical model, EEPN variance scales linearly with the symbol rate: as a result, OSNR penalty increases as we double the symbol rate. To keep EEPN penalty under 1 dB of OSNR, the analytical model gives a linewidth constraint on LO and TX of 70 kHz. When TX linewidth is set to 0, the total OSNR penalty is smaller than the analytical model. Besides, increasing the symbol rate reduces the share of PN penalty in the total OSNR penalty. As a result, when both TX and LO linewidths are nonzero, the linewidth constraint on both lasers to keep OSNR penalty under 1 dB is loosened to 100 kHz.

As the EEPN penalty scales up with total transmission distance, we also study a transpacific transmission of TPCS64QAM over 13419 km EX3000. In order to meet transmission experiment parameters from [117], the target SNR is set to 7.9 dB, hence both EEPN and ASE increase. In Fig. 4.13(c), we show simulation results from 49 GBd transmission. The PN penalty (white diamonds: TX source linewidth set to zero, filled diamonds: TX laser linewidth equal to LO linewidth) is comparable to that of 6600 km transmission of Fig. 4.13(a). To keep EEPN penalty under 1 dB of OSNR, we must limit TX and laser to 150 kHz. The 98 GBd transpacific results are plotted in Fig. 4.13(d). In order to keep EEPN OSNR penalty under 1 dB, the TX and LO linewidth should be kept below 120 kHz.

Finally, we plot the OSNR penalty discrepancy between the analytical model and our DSP-aware simulations for the case where TX laser linewidth equals LO linewidth. Fig. 4.14(a) shows the results for transatlantic 6600 km transmission. At 49 GBd (triangle markers), the analytical model overestimates by 0.5 dB the OSNR penalty at 500 kHz linewidth. At 98 GBd (square markers), the PN penalty is reduced. As a result, the OSNR penalty in presence of EEPN is overestimated by more than 1 dB for linewidth over 200 kHz. We plot the OSNR penalty discrepancy for transpacific 13419 km transmission in Fig. 4.14(b). For 49 GBd transmission (triangle markers), the overestimation by the analytical model remains under 0.3 dB for both LO and TX linewidths smaller than 500 kHz. However, for 98 GBd transmission (square markers), we observe more than 1 dB penalty overestimation for linewidth over 220 kHz.



**Figure 4.14:** OSNR penalty error between simulations and analytical model for 6600 km PCS64QAM (a) and 13419km TPCS64QAM (b) transoceanic transmission through EX3000 fiber, neglecting nonlinearity, versus laser linewidth (LO and TX lasers have identical linewidth).

### Conclusions on EEPN numerical study

Using numerical simulations, we have studied the statistical and temporal properties of EEPN and showed that they impose to take into account the CPE process in the analysis to assess EEPN impact on coherent transmissions. We showed the influence of EEPN on the behavior of this CPE process, and quantified EEPN penalty as a function of LO linewidth for emerging transoceanic systems with PCS constellations, highlighting the importance of DSP-aware performance analysis. Not taking into account the EEPN characteristics and the BPS effect on OSNR penalty can lead to overestimate its impact on system design. As both TX and LO play a role in the CPR algorithm, even if TX does not generate EEPN, both of them must be included in the simulations to estimate the full PN impact, which accounts for BPS residual error and EEPN.

For high baud rate transmission, EEPN penalty becomes dominant and the overestimation is significant for current laser source performance. These penalty curves might serve as guidelines for specifications of the laser sources for high baud rate coherent systems in future. Please note that the revised assessment of EEPN, is not only useful for setting requirements on laser specifications, but also to separate the extra penalty due to EEPN from other sources of penalty in advanced characterizations of submarine systems.

### 4.3 Experimental characterization of EEPN impact on a transoceanic testbed

In the context of open subsea cables that aims at separating the transmission line optimization from the transponder technology, accurate subsystem characterizations are required to predict the point-to-point system performance. The overall SNR can be expressed by [107]

$$SNR = (GSNR^{-1} + SNR_{TRX}^{-1} + SNR_{extra}^{-1})^{-1} \quad (4.5)$$

where the generalized SNR (GSNR) is used to express the line impairments (including ASE noise, fiber nonlinearities, GAWBS, signal droop),  $SNR_{TRX}$  accounts for the back-to-back TRX penalties and  $SNR_{extra}$  represents the noise coming from the transceiver due to propagation effects (such as residual chromatic dispersion, polarization effects, EEPN, crosstalk or filtering penalties, etc). Whereas the first and second term aim at separating the line and transceivers characteristics, the third term requires a joint analysis of the link properties and the transceiver characteristics.

In the EEPN case, it has been shown in the previous study that the interaction between LO phase noise, CDC and CPE algorithm adds complexity to the prediction of EEPN noise variance, and that simplifying assumptions may lead to overestimation of EEPN impact. As the accumulated CD scales linearly with the cable length, and the industry favours high symbol rate transmitters for cost-efficiency, an accurate estimation of EEPN impact is vital for the design of future transoceanic systems.

In this section based on a conference paper [P12], co-authored with Alcatel Submarine Networks (ASN) and published at ECOC 2019, an experimental characterization campaign is presented to estimate the EEPN contribution for transoceanic configurations, when using as LO a commercially available external cavity laser (ECL) as well as an ultra-low phase noise source (ULPNS) to serve as a reference. In particular, we show that for an ECL with laser linewidth specification of 100 kHz (a standard product for optical communications), the observed penalty is negligible up to 90 Gbd for a transmission distance of 10476 km over ASN straight line testbed.

#### 4.3.a) Laser source characterization

We first characterized the different laser sources that are used as LO in the rest of the study: a DFB laser source with linewidth less than 5 MHz according to its specification, a TLS with specified linewidth below 100 kHz and an ULPNS designed for fiber sensing applications, with a sub-kHz linewidth specification. The measurement method is not described here and can be found in [P12] and references herein. The characterization enabled us to determine the measured linewidths reported in Table 4.1, where the linewidth corresponds to the FWHM of the optical field PSD, as previously defined in Fig. 4.4.

For the ULPNS, the measured linewidth is 0.8 kHz, in line with the laser specification. For the TLS, the measured linewidth is 17 kHz when operating the TLS at its maximum output power of 14.5 dBm, and is degraded to 25 kHz when decreasing the power to 10 dBm, to operate the receiver in the same configuration than with the ULPNS. For the DFB, we find a measured linewidth of 1 MHz when operating

the laser at 14.5 dBm output power, and to avoid further degrading the linewidth when decreasing the power, we use a VOA at the output of the DFB to operate the receiver with 10 dBm LO power. It is interesting to note that for the TLS and DFB, the linewidth are found to be approximately 5 times lower than their specified values, showing that the supplier specifications are very conservative.

The worst-case expected SNR penalty due to EEPN is computed using the analytical model [108] and is then given by  $SNR_{extra} = (\pi c(2f_0^2)^{-1} DLR_s \Delta\nu)^{-1}$  for  $R_s=90$  GBd,  $D=19.6$  ps/nm/km,  $f_0=191.5$  THz, a transmission distance  $L=10476$  km and a reference SNR accounting for  $(GSNR^{-1} + SNR_{TRX}^{-1})^{-1}=8.3$  dB (maximum performance observed at 10476 km with 90 GBd DP-QPSK signals). Thanks to its very low linewidth, the ULPNS serves as a reference as its expected penalty, below 0.01 dB, is negligible. For the TLS with output power of 10 dBm, the worst-case penalty expected from the specification is 0.6 dB, whereas it is only 0.2 dB according to our characterization of the laser. For the DFB, the expected penalty according to the measured linewidth is 4.1 dB, whereas it would be  $>9$  dB with the specified 5 MHz linewidth and would prevent any effective transmission.

Laser source	Specified laser linewidth	Worst-case SNR penalty	Measured laser linewidth	Worst-case SNR penalty
ULPNS (10 dBm)	< 1 kHz	<0.01 dB	0.8 kHz	< 0.01 dB
TLS (14.5 dBm)	< 100 kHz	< 0.6 dB	17 kHz	0.1 dB
TLS (10 dBm)	< 100 kHz	< 0.6 dB	25 kHz	0.2 dB
DFB (14.5 dBm)	< 5 MHz	-	1 MHz	4.1 dB

**Table 4.1:** Specifications and experimental characterization of laser linewidth, and worst-case EEPN penalty using the literature analytical model [108]

### 4.3.b) Submarine transmission testbed

The transmission setup is described in Fig. 4.15. The test channel is a TLS (as the TX transmitter is not responsible for EEPN, the TX laser remains unchanged) modulated with a DP I/Q modulator driven by a high-speed DAC operating at 120 GS/s and loaded with  $2^{15}$ -long de Bruijn DP-QPSK sequences. The symbol rate is either 45 or 90 GBd.

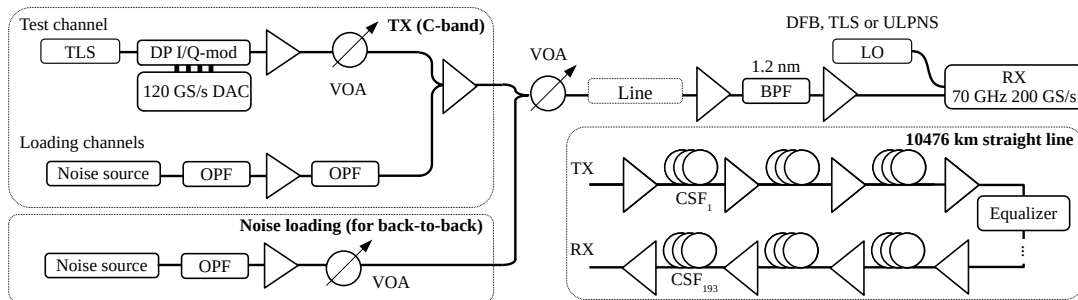


**Figure 4.15:** Experimental setup for 45 and 90 GBd DP-QPSK transmission in a C-band noise loaded spectrum: back-to-back and 10476 km straight line

To emulate WDM co-propagating channels, a spectrum comb is created with a 34 nm noise source and an optical programmable filter (OPF), with channel spacing

of 50 or 100 GHz. A second optical programmable filter is used to filter again the emulated loading channels, and equalize the power over the WDM spectrum. It is also in charge of filtering out the noise channel at the wavelength of the test channel. Finally, all the channels are coupled together and amplified.

For back-to-back measurements, a second noise source is used to degrade the OSNR of the WDM channels. It is equalized with an OPF and its power can be tuned with a VOA or filtered out for transmissions experiments. The transmission straight line is composed of 193 spans of 110  $\mu\text{m}^2$  coherent submarine fiber (CSF) with 54 km average span length, totaling a distance of 10476 km. After each span, 34 nm wide C-band EDFAs with 15.8 dBm average output power are used to operate the transmission line approximately 1 dB below the NLT. Some spans are equipped with shape equalizers to flatten the gain shape. A VOA is used to apply -4 dB to 4 dB power pre-emphasis to the test channel and vary the OSNR value at the end of the line, without changing the WDM line configuration. This allows us to observe the channel performance under different conditions of ASE noise and fiber nonlinearities.

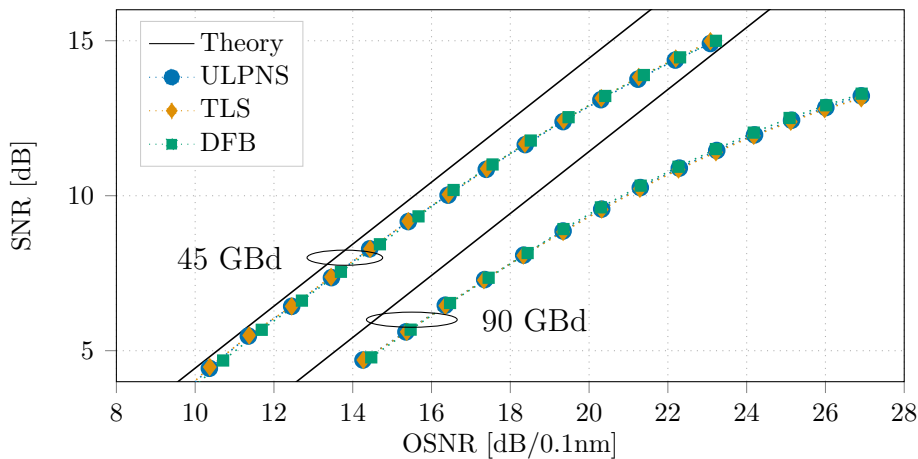
At the RX side, the signal is mixed with the LO (which is the DFB, TLS or ULPNS described previously) and the outputs of the coherent receiver are sampled with a 200 GS/s real-time scope with 70 GHz bandwidth. The offline DSP consists in signal conditioning, CDC, CMA as adaptive channel equalizer, CFE and CPE before a symbol-spaced least mean square adaptive post-equalizer, as described in section 1.5.b). BPS algorithm is used for CPE and the block length was optimized for all cases.

### 4.3.c) Experimental results

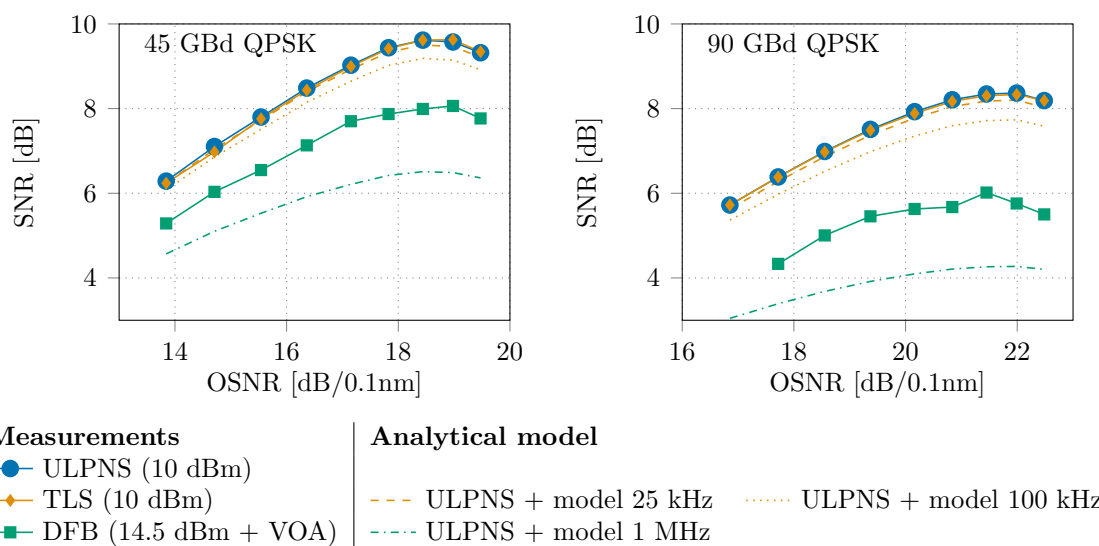
First we perform back-to-back measurements to assess the performance of using the different laser sources as LO, in the absence of EEPN. Fig. 4.16 shows the measured SNR versus OSNR curves, for 45 and 90 GBd signals. The theory for an AWGN channel is shown in black solid line, and the measurements with ULPNS, TLS and DFB are shown in circle, diamond and square markers, respectively. We do not observe a significative penalty coming from TLS and DFB compared to the ULPNS. As a result, any possible extra penalty measured in transmission configuration between the different laser sources as LO should be attributed to EEPN.

Fig. 4.17 shows the measured SNR versus OSNR, for both 45 GBd and 90 GBd signals, using as LO the ULPNS (circle markers), the TLS (diamond markers) or the DFB (square markers). We also plot the expected penalty, when adding to the ULPNS SNR curve (serving as  $(GSNR^{-1} + SNR_{TRX}^{-1})^{-1}$  reference) the penalty from the litterature analytical model [108], for LO linewidth of 25 kHz, 100 kHz and 1 MHz.

In both 45 and 90 GBd cases, there is no clear difference between the ULPNS and the TLS, as expected by the analytical model predicting a <0.2 dB penalty according to the 25 kHz measured linewidth (dashed line). However, it is clear that the penalty is negligible compared to the prediction according to the 100 kHz specified linewidth (dotted line). For the DFB, the degradation is significant compared to the reference ULPNS: the penalty reaches 1.6 dB and 2.4 dB at the NLT for 45 and 90 GBd, respectively. The penalty caused by the DFB is important and prevents its use



**Figure 4.16:** Back-to-back results for 45 and 90 GBd QPSK transmission using three different laser sources



**Figure 4.17:** Transmission results for 45 and 90 Gbd QPSK transmission over 10476 km CSF with three different laser sources and analytical expected penalties, computed with 25 kHz, 100 kHz and 1 MHz linewidth and using the ULPNS results as reference

as a LO for transoceanic transmissions, but the takeaway is that the penalty is considerably reduced compared to the analytical model (dash-dotted line), which predicted a 4.1 dB penalty at the NLT for 90 GBd. Further study is thus required to determine whether this discrepancy can be attributed to a partial mitigation of EEPN by the DSP as highlighted in our numerical simulations. Another possibility is that the actual behavior of the laser PN process is not correctly captured by the Wiener process model, and subsequently the analytical modeling of EEPN leading to the penalty computations does not hold.

### Conclusions on EEPN experimental study

We have conducted an experimental characterization of EEPN impact on the performance of modern transoceanic transmission systems. On the one hand, we have shown that commercial laser specifications are pessimistic compared to the actual linewidth according to our characterization, reducing the expected EEPN penalty when considering the analytical model in the literature. On the other hand, after conducting transmission experiments over a 10476 km testbed, we observed reduced

penalties compared to the analytical prediction, even when considering the actual laser linewidth values from our characterizations. Further investigation is required to confirm whether or not these discrepancies can be attributed to the partial mitigation of EEPN we observed in our previous numerical simulations. Concerning this experimental characterization, a key takeaway is that standard ECL sources with 100 kHz linewidth specification can be used in this transoceanic configuration for high symbol rate transmissions. Whereas a 0.6 dB penalty for 90 GBd transmission was expected from the analytical model and the laser specification, no significant penalty was observed in our experiment, compared to a sub-kHz linewidth ultra low-phase noise source.

## 4.4 Summary

In this chapter, we have investigated the impact of EEPN in the context of future ultra long transoceanic transmission systems using high symbol rate transceivers, a crucial impairment in system design as the impact of EEPN grows with the transmission distance and the signal symbol rate.

In a first part, we proposed a detailed study using numerical simulations to highlight EEPN statistical and temporal characteristics, and we provided numerical results to quantify constraints on laser linewidth on  $>6000$  and  $>13000$  km transoceanic configurations with large accumulated CD, employing high symbol rate and advanced modulation formats. We showed that taking into account the CPE in the analysis is a must as the BPS algorithm, which is usually used in practice to recover the carrier phase, can partially mitigate the EEPN and loosen the requirements on laser linewidth in system design.

As the industry of subsea communications turns towards the paradigm of open cables, separate assessment of fiber link performance and transponder capabilities are now required from optical network vendors to predict the point-to-point system performance. As EEPN results from the interaction of the CDC (where the accumulated CD is defined by the optical path), the LO phase noise (depending on the transponder requirements) and the CPE, its integration in the performance prediction is complex and requires deeper investigation. Owing to the lack of satisfying model, we conducted an experimental characterization campaign of EEPN influence on 45 and 90 GBd transmissions over a 10476 km straight line testbed, in order to analyze the overall impact of the LO laser source characteristics. When using a standard ECL source as LO, EEPN impact was negligible on our ultra long-haul transmissions even with symbol rate up to 90 GBd.

To conclude, we have presented numerical and experimental characterizations of EEPN impact on high symbol-rate transmissions. Through numerical simulations, we have highlighted the need of taking into account the CPE in EEPN characterization, as simplifying assumptions in analytical derivations can lead to EEPN impact pessimistic predictions. The EEPN impact can be all the more overestimated by using too conservative laser linewidths, as we found during our experimental investigations. We recently conducted an experimental study on the comparison of single carrier versus digital multi carrier (DMC) signaling for 120 GBd transmission up to 10980 km [P17]. DMC has indeed attracted attention as a potential scheme to address EEPN impact concerns [79]. Though we found the single carrier scheme to be more sensitive to EEPN than DMC, we highlighted that commercial integrable tunable laser assembly (ITLA) sources provide low enough linewidth to consider 100 GBd class single carrier transmissions for future transoceanic systems.



## Ultra-wideband transmission systems based on semiconductor optical amplifiers

In this chapter, we focus on solutions aiming at upgrading the capacity of WDM systems by better exploiting the fiber low-loss attenuation window thanks to UWB amplification schemes. We present the characteristics of an SOA with UWB 100 nm bandwidth, promising considerable capacity increase compared to systems based on C-band EDFAs with 35 to 40 nm bandwidth. We experimentally show that this UWB SOA is well suited for WDM operations in high power regimes, and we demonstrate a 100 Tb/s transmission in a scenario based on legacy terrestrial network constraints as well as a record throughput over a 257 km unrepeated fiber span.

### Contents of this chapter

---

<b>5.1 Introduction</b>	<b>114</b>
5.1.a) Limits of conventional WDM systems	114
5.1.b) Moving towards UWB systems	114
<b>5.2 SOA for UWB transmission</b>	<b>116</b>
5.2.a) Overview of SOA in optical communications	116
5.2.b) Presentation of UWB SOA module	117
<b>5.3 Experimental characterization of UWB SOA nonlinear impairments</b>	<b>119</b>
5.3.a) High power WDM operation using SOA	119
5.3.b) Impact of the number of WDM channels on the SOA-induced nonlinear impairments	122
<b>5.4 100 Tb/s regional transmission for upgrade of legacy terrestrial networks</b>	<b>126</b>
5.4.a) SRS characterization in 100 km SSMF spans	126
5.4.b) 300 km fiber link using UWB Raman/SOA amplifiers	128
5.4.c) Experimental results	130
<b>5.5 Record throughput on a 257 km unrepeated fiber link</b>	<b>132</b>
5.5.a) 257.5 km transmission experimental setup	132
5.5.b) Adaptive modulation format for capacity maximization	134
5.5.c) Experimental results	135
<b>5.6 Summary</b>	<b>138</b>

---

## 5.1 Introduction

### 5.1.a) Limits of conventional WDM systems

As pointed out in chapter 1, the introduction of C-band EDFAs in the late 1980s [40, 41] and their implementation in commercial optical transport systems as soon as 1995 allowed a considerable capacity growth by moving from single-channel fiber links to WDM transmission systems. At the beginning of the 2000s, systems were already using the full available bandwidth of C-band EDFAs (roughly between 1530 and 1565 nm), typically able to carry 400 Gb/s WDM throughput using 40 wavelengths at 10 Gb/s based on IMDD transceivers [4].

To answer the foreseen capacity saturation of C-band systems, extension of the optical amplification bandwidth has started to be considered as a potential solution to answer the traffic demand. In particular, the development of L-band EDFAs, with 1570-1605 nm bandwidth, promised appealing upgrade possibilities of optical links with C+L band multiplexing schemes. In the meantime, the upgrade of transceiver capabilities, first using differentially encoded modulation formats and later with coherent detection, was able to scale the SE and set aside the urgent need of bandwidth scaling.

Since then, extensive research effort in advanced modulation and coding schemes, as well as DSP to mitigate linear and nonlinear transmission effects, has enabled to scale the C-band WDM throughput up to 50 Tb/s [118] for C-band DCI transmission, and 70 Tb/s for transoceanic demonstrations using C+L amplification based on EDFA multiplexing [7].

### 5.1.b) Moving towards UWB systems

Further improvement of SE via DSP and channel coding innovations is increasingly challenging and comes with diminishing returns. As described in chapter 2, the SE is ultimately upper bounded by  $2 \log_2(1 + SNR)$  which scales logarithmically with the SNR. As the system WDM throughput is given by  $M \cdot W \cdot SE$ , where  $M$  is the number of per-fiber optical paths (modes, cores) and  $W$  the optical system bandwidth, leveraging the physical dimensions  $M$  and  $W$  is a promising way to scale the throughput of optical transport systems.

Several approaches have been proposed to extend the optical bandwidth  $W$  beyond the C and C+L conventional schemes based on EDFAs. Whereas various technologies have been proposed for amplification in O, E, S, C or L bands, we focus here in amplification schemes operating in S to L bands, as SMF attenuation out of this band is prohibitively high to address high performance applications such as metro or long-haul transmissions.

Using distributed Raman amplification on 240 km of low loss fiber, a 102 Tb/s net throughput has been obtained with a 11.2 THz bandwidth [119]. All-Raman amplification provides a flexible amplification window, that can be tuned with the wavelength and power of the Raman pumps, but has major drawbacks; mainly it cannot provide lumped amplifications, required in optical networks with add/drop nodes. Hybrid amplification schemes combining EDFAs and distributed Raman pumping have then been proposed. 120 Tb/s throughput over 630 km and 74.38 Tb/s over 6300 km low-loss fiber has been achieved with 11.1 THz continuous-band amplifica-

tion [120, 121]. Using separate amplification of S, C and L bands by multiplexing doped fiber amplifiers (DFA), a 155 Tb/s per-core throughput (0.61 Pb/s for a 4-core MCF) has been demonstrated over 54 km with amplification from 1490 nm to 1610 nm. In [122], a 115 Tb/s transmission has been reported, using for the first time SOA technology able to provide lumped and 100 nm continuous band amplification. A field trial was then conducted to demonstrate the feasibility of UWB transmission based on SOA in DCI transmissions over legacy SSMF architectures with worse performance in terms of span loss and nonlinear effects compared to the previously mentioned low-loss fibers [123].

## Chapter outline

In this chapter, section 5.2 reviews the characteristics of the SOA module for UWB WDM transmission. In particular, we present static characteristics in terms of gain, noise figure and output power. In section 5.3, an experimental characterization of the SOA-induced nonlinear impairments in high-power WDM regime is presented. Section 5.4 presents the results of a transmission experiment, achieving  $>100$  Tb/s WDM throughput over 300 km with 254 high performance 49 GBd DP-PCS64QAM channels. This experiment uses 100 km SSMF spans, compatible with architecture of legacy terrestrial networks. In section 5.5, we apply our UWB solution to unrepeated systems, a particular usecase of a transmission link without inline amplifiers. We demonstrate a record throughput of 81.2 Tb/s and a record capacity-distance product of 20.9 Pb/s·km leveraging 100 nm seamless amplification thanks to a hybrid Raman/SOA amplification scheme.

## 5.2 SOA for UWB transmission

In this section based on a paper reviewing recent advances on UWB SOAs [P14] published in 2020, we present elements motivating the renewed interest for considering SOAs as inline amplifiers in optical networks, and present some characteristics of our in-house SOA module.

### 5.2.a) Overview of SOA in optical communications

Similarly to semiconductor laser diodes, the optical gain of SOAs is obtained in an electrically pumped Fabry-Perot cavity of semiconductor medium. Whereas in a laser diode large feedback is required, in a SOA the facets of the active region are designed to limit their reflectivity so that signals travel in the forward direction only. The facet reflectivity is reduced with techniques such as antireflection coatings and/or by tilting the active region from the facet normal to separate the reflected beam from the forward beam.

In general, the SOA amplification is polarization-dependent and the gain characteristics depend on the geometry of the active region. Whereas several attempts tried to reduce the SOA polarization sensitivity by tuning the active region geometry, other approaches have been proposed to provide polarization-insensitive SOA devices, such as the association of single-polarization SOAs in series or parallel configuration, or the use of a single SOA in a double-pass configuration [3].

As the active region is typically few-millimeter long, SOA can provide optical amplification with cost-effective and integrated device, a considerable advantage compare to the typical EDFAs. SOAs provide lumped gain and can therefore compensate for lumped losses from transmitters and optical add-drop nodes, contrary to distributed Raman amplifiers. SOA devices are therefore potential candidates as in-line amplifiers, boosters and pre-amplifiers in multi-span optical transmission systems. The amplification bandwidth of SOAs is more flexible than for EDFAs, and under custom design SOAs with high output power and bandwidth up to 120 nm have been demonstrated [124].

During the past decades, the use of SOA as in-line amplifiers has been ruled out of WDM deployments for several reasons. Whereas typical NF of modern EDFAs is 4-5 dB, commercial SOAs exhibit NF around 7 dB or higher. Besides, the necessity of integrating and coupling optical components to resolve the polarization dependence of the amplification has been considered as prohibitively complex compared to the intrinsic polarization-independence of EDFA amplification. Finally, the main drawback of SOA is associated to the fundamental characteristics of light amplification in the semiconductor medium: due to the short lifetime of injected carriers (several hundreds of ps, comparable with the symbol period of >10 Gbd signals), the SOA gain fluctuates with the input signal variations and induces NL signal distortions.

For the aforementioned reasons, SOAs have mostly been exploited for their non-linear behavior in applications such as optical signal processing functions, wavelength conversion, photonic switching, etc. However, this paradigm can now be questioned as the capacity of C-band single-mode EDFA-based systems is limited by their 5 THz bandwidth and SOA wavelength flexibility and large bandwidth promise capacity upgrade by taking better advantage of the low-loss window of the

optical fiber.

### 5.2.b) Presentation of UWB SOA module

The work presented in this thesis is based on the outcome of the project CALIPSO, that aimed at the design of high gain, high output power and UWB SOA for optical fiber communications. The architecture of the UWB SOA module is given in Fig. 5.1. It uses two single-polarization SOAs in a parallel configuration, and free-space optics is used to split the two polarizations, couple the light to the SOA chips, then recombine after amplification. This enables the use of two optimized SOAs for one polarization only, which greatly relaxes the constraints on the active region design.

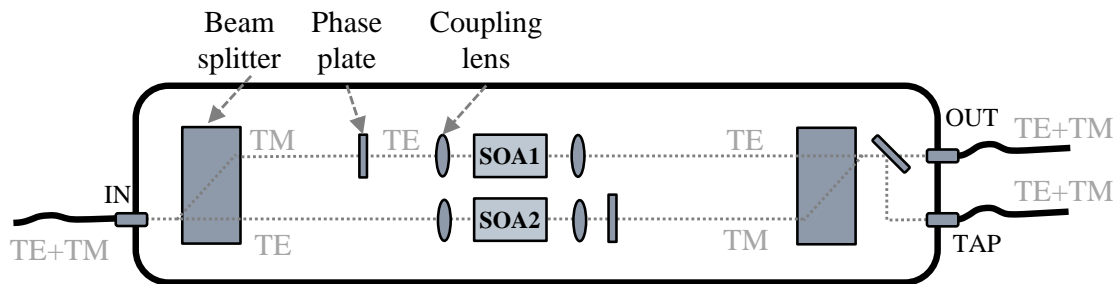


**Figure 5.1:** Schematic description of the UWB SOA module with polarization diversity architecture

More precisely, the input light from the fiber is split into transverse electric (TE) and transverse magnetic (TM) polarization modes using a birefringent material. The TM mode is then passed through a waveplate and rotated to the TE mode. Therefore, the beam light on each optical path at the input of the SOA is aligned on TE mode. The stripes are tilted to reduce facet reflection, and these facets have been anti-reflection coated. Light coupling at input and output of the SOAs is done with micro-lenses. Finally, the light on the first path is passed through a waveplate and rotated to the TM mode before being recombined with the TE mode of the second path. Optical isolation realized in free space optics has also been added on input and output paths of the proposed amplifier modules. Each SOA can be driven independently, and a sensor was inserted in between the SOAs for thermal cooling with a Peltier thermoelectric cooler. The package dimensions are 100 mm  $\times$  50 mm  $\times$  15 mm.

Fig. 5.2 shows typical performance of our UWB SOA module. The characterization is performed by injecting into the module a polarized signal composed of continuous wavelengths coming from laser sources with wavelengths between 1510 and 1615 nm. We turn on the driving current for one SOA chip at a time, and align the polarization state of the input signal with a polarization controller to maximize the power at the module output. Note that the characterization method is very sensitive to polarization alignment with the SOA chips, and that considerable precautions must be taken to maintain at best the polarization orientation during the measurements.

For an input power of 4.2 dBm, the SOA shows a 103 nm 3-dB bandwidth, with 15.6 dB gain and 20.3 dBm output power per polarization. The driving currents are 1.42 and 1.50 A and have been optimized to minimize the gain imbalance between the polarizations, which shows a maximal value of 0.5 dB around 1540 nm. In this

flat gain regime, the NF varies between 6 and 8 dB, a worse performance compared to 4-5 dB NF of EDFA, but remarkable value compared to typical NF of 10 dB of commercial C-band SOA [125].

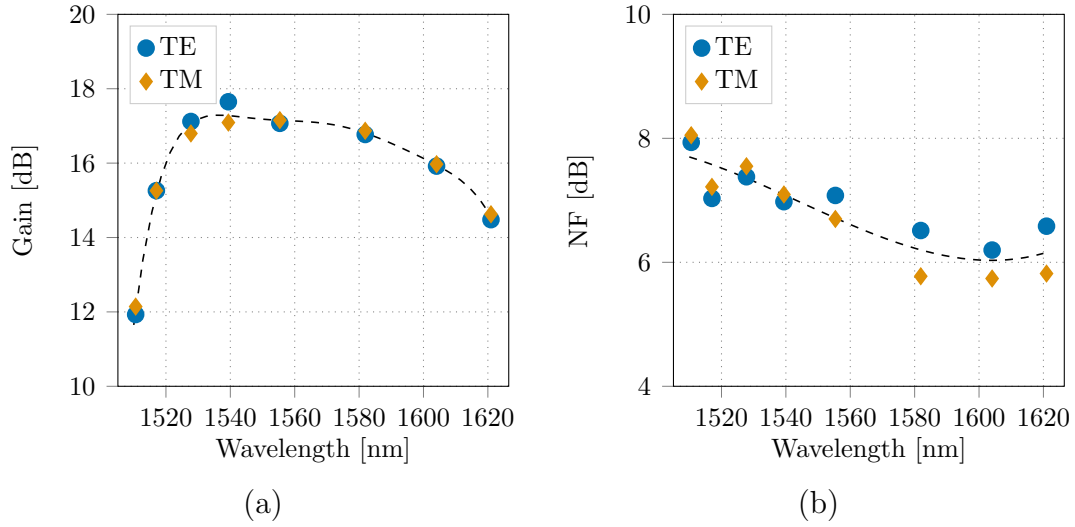


**Figure 5.2:** Characterization of UWB SOA module: gain (a) and NF (b) versus wavelength, for 4.2 dBm input power and  $1.46 \pm 0.04$  A driving currents

Note that given the difficulties of polarization alignments and NF measurements, the performance of our SOA module will be ultimately characterized through its system impact in transmission experiments. As both NF and gain are degraded for short wavelengths, we do not operate the SOA below 1515 nm to avoid severe degradation of performance by increased ASE noise.

## 5.3 Experimental characterization of UWB SOA nonlinear impairments

We have introduced the characteristics of our UWB SOA in terms of gain and NF and we now focus on NL impairments induced by SOAs in WDM regime. For the past decades SOA NL behaviour has indeed been a major hindrance to their application as inline amplifiers. Using the reservoir model [126], a time-domain first-order regular perturbation theory has been detailed in [127] to derive SOA noise variance in multi-span WDM systems using SOAs as in-line amplifiers. In [128], numerical simulations show that WDM regimes favours reduction of NL impairments, in line with experimental observations using commercial C-band SOA. As the NL behaviour arise from the gain dynamic variations to the incoming optical field, an intuitive explanation is that in WDM operation the summation of the numerous channel contributions to the optical field reduces the total optical signal intensity fluctuations at the SOA input, hence reducing the NL impairments during amplification.

In this section, based on a conference paper [P1] at OFC 2019 and extended in a journal paper [P6] published in 2020, we propose an experimental characterization of NL impairments induced by our UWB SOA. We first study the NL behavior differences between single channel and WDM amplification, for an off-the-shelf C-band SOA and for our UWB SOA. Next, we investigate the impact of increasing the channel count of a WDM signal onto the NL behavior of an UWB-SOA based device.

### 5.3.a) High power WDM operation using SOA

To highlight the impact of spreading the total power over many optical channels, we consider the experimental setup described in Fig. 5.3.

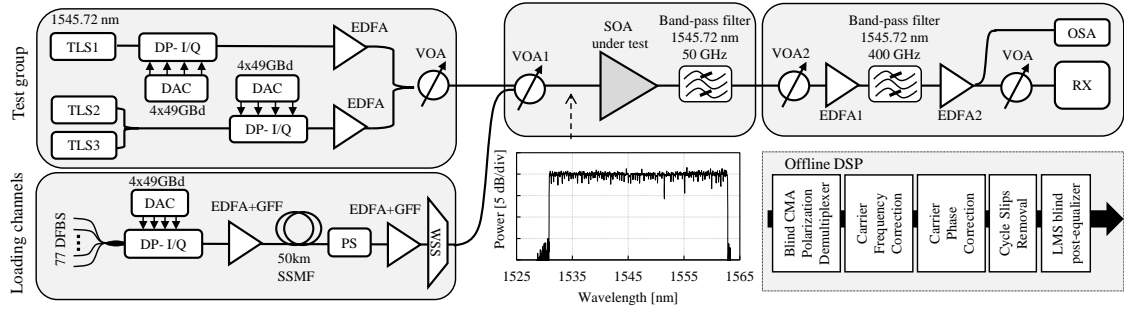


**Figure 5.3:** Experimental setup for characterization of SOA-induced impairments for off-the-shelf C-band SOA and UWB SOA module

The WDM transmitter is made of a test group of three TLS and a loading set of 77 DFB. Within the test group, the central channel is the actual channel under test whereas the two adjacent channels are separately modulated. The channels of the test group are modulated using two DP I/Q modulators, driven by two DAC loaded with different randomly generated sequences. The 77 loading channel sources are multiplexed and modulated with a third DP I/Q modulator loaded with different sequences. All channels are modulated at 49 GBd using DP-16QAM format and pulse shaping is performed using RRC pulses with roll-off 0.01. The loading channels are decorrelated by a 50 km SSMF fiber spool and a polarization scrambler (PS)

ensures a random state of polarization of the loading set. We use EDFA and GFF before and after the fiber spool and the PS to compensate for insertion and span losses. Before coupling to the set of the three TLS containing the channel under test, a WSS is used to obtain a flat WDM spectrum over the C-band as shown in the inset of Fig. 5.3, and to reject the ASE noise in the test group bandwidth. The whole WDM spectrum is sent to the SOA under test and the input power is tuned with a VOA labeled VOA1. At the SOA output, we use a fixed 50 GHz bandwidth band-pass filter to isolate the channel under test, before we sent it to the receiver.

We vary the input power in the receiver with the VOA2 to load ASE noise with the EDFA labeled EDFA1. A band-pass filter is used to suppress noise out of the 400 GHz band around the channel under test. We use the EDFA2 to compensate for the filter losses and measure with an OSA the OSNR of the signal, which is sent to the coherent RX, including a LO, a coherent mixer, balanced photodiodes and a 33 GHz bandwidth real-time scope operating at 80 GS/s. Data sets of 2 million samples are stored and DSP is performed offline, as described in section 1.5.b). The SNR of the received signal is then estimated from the sent and received symbols as described in section 2.1. Note that this estimation of the SNR is valid assuming that the distortions are considered as AWGN, neglecting the signal dependence of the NL distortions.

We compare in this study a commercial off-the-shelf (COTS) C-band device [125] and our UWB SOA module. The devices are operated at 20°C and we set driving currents to provide 17 dB saturated gain at high power regime. As described in Table 5.1, the input power for the C-band SOA is set to -5 dBm, close to the limit beyond which the 17 dB gain cannot be obtained. The UWB SOA, which is specially designed for high power regime above 20 dBm, can provide this 17 dB gain with input power of 0 dBm. The gain of 17 dB corresponds to a practical case of around 100 km of low-loss PSCF, or 80 km of legacy SSMF.

	COTS C-band SOA	Our UWB SOA module
Gain	17 dB	17 dB
Input power	-5 dBm	0 dBm
Output power	12 dBm	17 dBm
NF @1545 nm	10 dB (see [125])	6 to 7 dB (see [129] or section 5.2.b))

**Table 5.1:** Operation parameters of SOAs under test (80 WDM channels, temperature: 20°C)

We measure the SNR performance as a function of the OSNR of the channel under test in three different configurations for each SOA: single channel at low input power  $P_0$ , single channel with  $P_0+19$  dB input power, and 80 channels with total power of  $P_0+19$  dB, corresponding to a power per channel equal to  $P_0$ . Fig. 5.4 shows the experimental results. First, we consider the C-band SOA. We send a single channel in the SOA with an input power  $P_0$  equal to -24 dBm, ensuring that the SOA works in linear regime. The SNR performance reaches 15 dB for high OSNR: the noise floor is due to the sum of the TRX impairments and the ASE noise of the SOA. Next, we show the performance of a single channel at  $P_0+19$  dB = -5 dBm, and the performance is limited to 9 dB, due to a higher noise floor corresponding to the addition of SOA-induced NL distortions. The constellation in the inset (1) clearly highlights the NL nature of the noise in this case. Finally, we observe that when using 80 channels with total power equal to  $P_0+19$  dB = -5 dBm, that is to

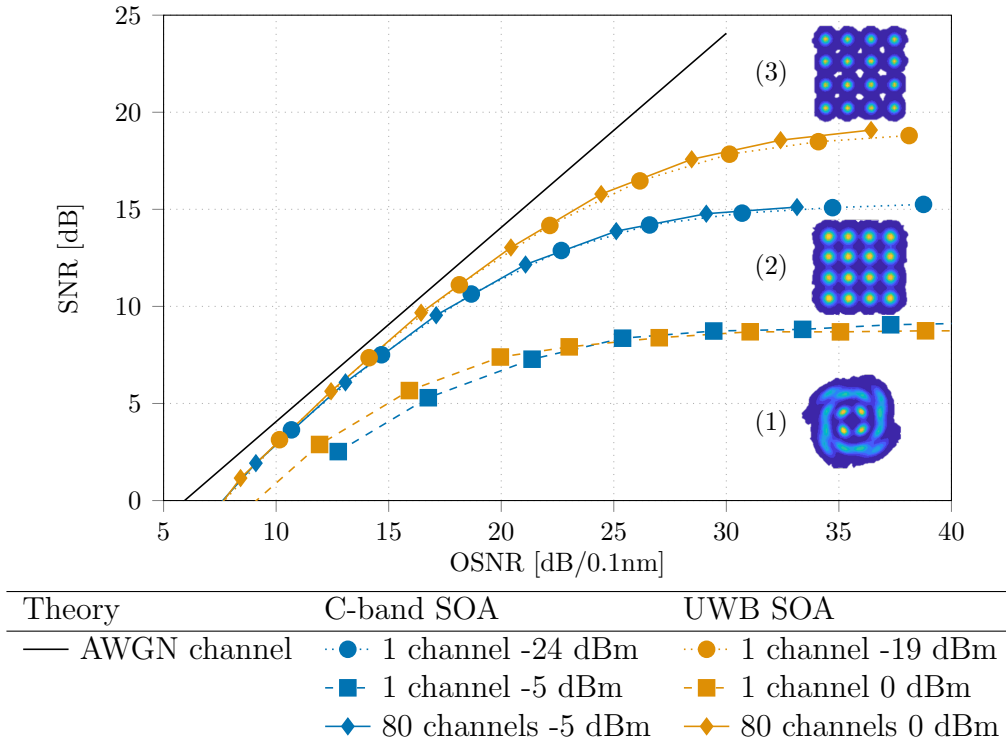


**Figure 5.4:** Single-channel and 80 channel experimental characterization of SOA-induced impairments for COTS C-band SOA and UWB SOA. Insets: constellation diagrams with NL impairments (1) and in linear regime (2) (3)

say a power per channel equal to  $P_0 = -24$  dBm, the performance coincides with the case of single channel in linear regime, as depicted by the constellation in the inset (2). Whereas single channel at  $-5$  dBm suffers from NL distortions, no NL impairment occurs when the total optical power of  $-5$  dBm is spread over 80 WDM channels. The same SNR performance is reached for the same per-channel input power: the performance is determined by TRX impairments and linear ASE noise which depends only on the per-channel input power.

Then, we show the results of a similar experiment for our UWB SOA. With a single channel at  $P_0$  equal to  $-19$  dBm, we observe a linear regime of the SOA reaching an SNR equal to 19 dB, showing that the UWB SOA presents a significantly better noise figure than the C-band SOA in this high-power regime. Similarly to the C-band SOA, when we consider a single channel at  $P_0 + 19$  dB = 0 dBm, the performance of the UWB SOA is limited by NL impairments and the SNR does not exceed 9 dB in this case. When using 80 channels with a total power  $P_0 + 19$  dB = 0 dBm, hence a power per channel  $P_0 = -19$  dBm, the performance coincides with the single channel performance in the linear regime.

For both the SOAs, when we spread the power of the optical field over a wide number of WDM channels, the performance is not degraded by SOA NL impairments. Besides, we show that our UWB SOA is particularly suited for high power WDM operation, showing better performance than the C-band SOA, with at least 5 dB higher operation power regime.

### 5.3.b) Impact of the number of WDM channels on the SOA-induced nonlinear impairments

We aim at characterizing the NL distortions induced by the UWB SOA for high WDM count and high-power regime. Our experimental setup is depicted in Fig. 5.5. The goal is to operate the UWB SOA with variable input power and channel count and to identify the noise contribution of the SOA corresponding to the different regimes.

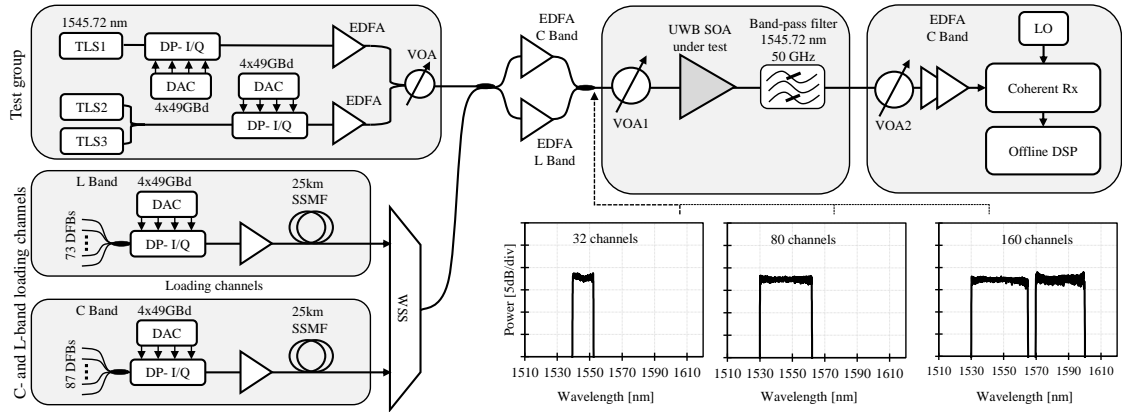


**Figure 5.5:** Experimental characterization of channel count impact on UWB SOA induced NL distortions

The TX is made of a test group of three channels including the channel under test (as described in the previous setup), and two sets of loading channels in C and L bands. For the loading channels, 87 and 73 laser sources separated by 50 GHz are separately modulated with two distinct DP-I/Q modulators, each modulator being driven by a dedicated DAC loaded with different randomly-generated DP-16QAM sequences providing both phase and amplitude variations of the optical field. These channels are amplified through C and L band amplifiers to compensate for modulation insertion losses. Fiber spools of 25 km are used to decorrelate loading channels. The channel under test is modulated with 49 GBd DP-QPSK, the QPSK format is deliberately chosen for the test channel to minimize TRX impairments in the evaluation of performance. An UWB WSS [130] with a spacing grid of 50 GHz is used to multiplex the C+L spectrum and to obtain a flat power profile over the C+L loading channels. The WDM spectrum is amplified by separate C and L EDFAs and VOA1 is used to vary the power of the total optical field at the SOA input. We show in the insets of Fig. 5.5 the equalized spectra of WDM signals with 32, 80 and 160 channels. At the SOA output, a fixed 50 GHz bandwidth band-pass filter isolates the channel under test before we send the signal to the RX. Contrary to the previous case, we do not want to sweep the ASE noise power loaded at the RX side. Here, we use the VOA2 to keep the RX input power at a constant value, ensuring that the amount of ASE noise power added by the RX remains constant, independently of the SOA noise contribution.

First, we characterize the performance of our experimental setup in the absence of UWB SOA. Fig. 5.6 shows the measured SNR versus RX input power into the C-band preamplifier. At the chosen RX input power of -21 dBm, the SNR is 18.7 dB. This accounts for the noise contribution of our TRX. When we place the UWB SOA under test in the test bench, the TRX noise remains independent of the SOA

contribution so keeping the RX input power at the constant value of -21 dBm in the following ensures that the observed performance variations are attributable to the SOA.

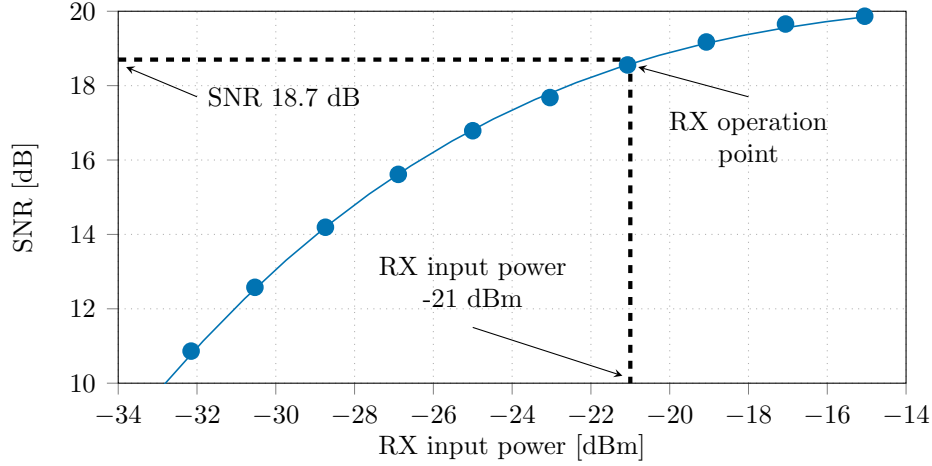


**Figure 5.6:** SNR versus RX input power (without SOA) characterization corresponding to TRX impairments. We choose the -21 dBm Rx input power operation point to keep TRX impairments at the constant value of SNR=18.7 dB

Then we launch the WDM optical spectrum into the UWB SOA with 32, 50, 80, 126 and 160 channels. In each case we vary the total input power by steps of 2 dB and measure the performance of the channel under test. Fig. 5.7 shows the measured SNR as a function of the input power into the UWB SOA for various WDM configurations. As a sanity check, we observe in the linear regime that increasing the total input power by 7.3 dB is required to reach the arbitrary value of 16 dB SNR when moving from 32 to 160 channels (i.e. a 7 dB increase in the channel count). The same optimum SNR around 18.2 dB, limited by TRX contributions for a -21 dBm RX input power, is reached for all configurations but for various input powers ranging from -4 to 5 dBm for 32 and 160 channels respectively.

Fig. 5.8 shows the SNR versus SOA input power per channel, for the different WDM combs with 32 to 160 channels. Using this representation, at low channel input power the SNR is identical whatever the channel count in the WDM signal: this corresponds to the linear regime, as observed above. We plot in black solid lines the SNR contribution of the TRX impairments  $SNR_{TRX}=18.7$  dB as well as the contribution of a linear amplifier as given by (1.31), with a NF of 7 dB (in line with the previous characterization). The dashed line represents the summation of the TRX and linear ASE contributions

$$SNR_{ASE+TRX} = (SNR_{TRX}^{-1} + SNR_{ASE}^{-1})^{-1} \quad (5.1)$$

and offers a good qualitative description of the experimental observations in linear regime. In NL regime, when we increase the number of channels the NL noise contribution is reduced, and the optimal input power per channel increases by 2.5 dB from 32 to 160 channels. This demonstrates that the increase of WDM channels in the comb enables us to operate the SOA device with better NL tolerance even at higher total input power.

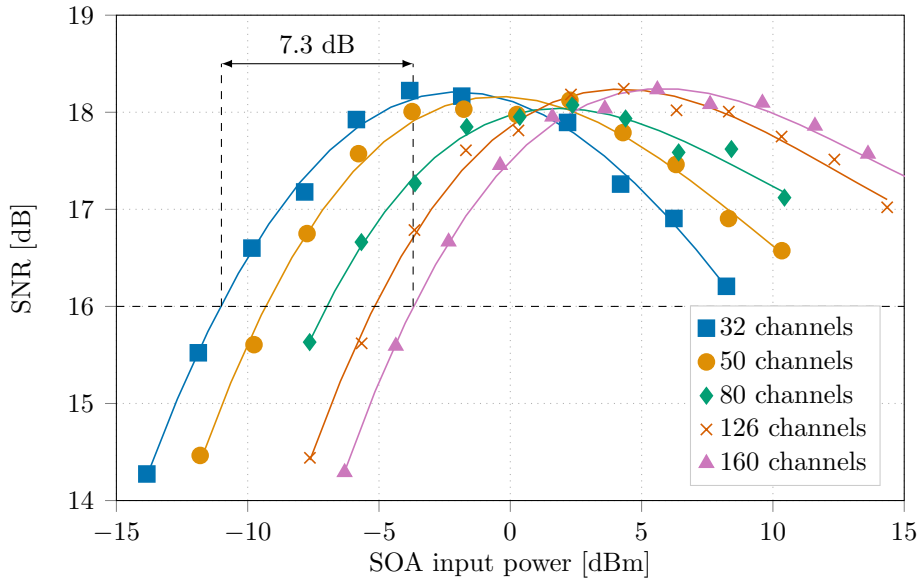


**Figure 5.7:** Measured SNR of the channel under test versus SOA input power for various WDM channel counts in C and L bands (SOA driving current: 3 A)

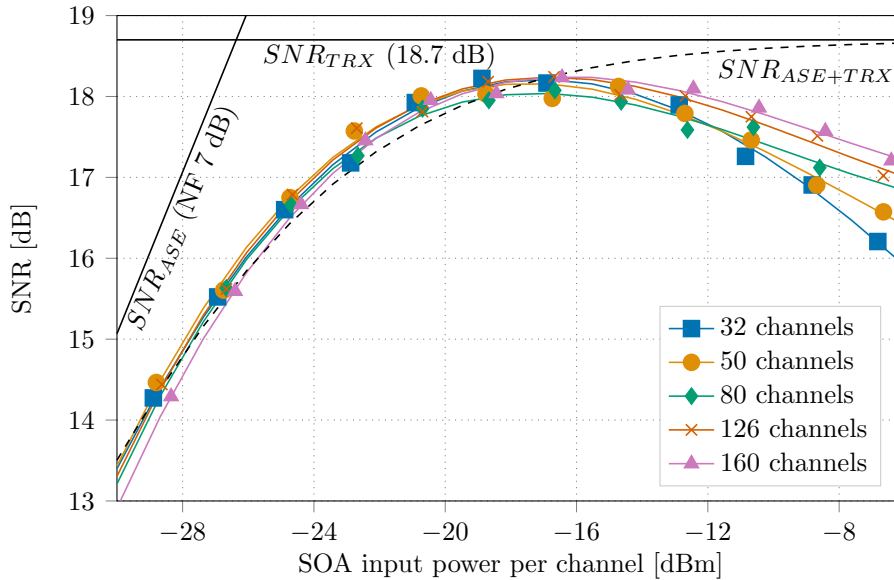


**Figure 5.8:** Measured SNR of the channel under test versus SOA input power per channel (SOA driving current: 3 A)

We eventually measured the SNR for 80 channels configuration while varying the driving current from 2 to 3 A. Fig. 5.9 shows that we can increase the optimal SOA output power by around 3 dB, up to 20 dBm, when increasing the driving current by 1.76 dB from 2 to 3 A, with less than 0.5 dB SNR decrease. This indicates that higher driving current can be used to reach higher gain in high power regime, with limited SNR penalty due to the NL contribution of the UWB SOA device.

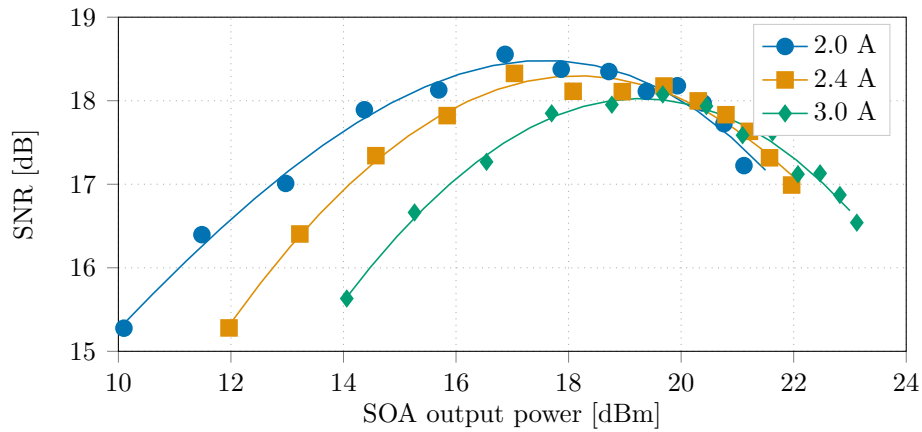


**Figure 5.9:** Measured SNR of the channel under test versus SOA output power for 80 channels and various driving currents (80 channels)

### Conclusions on UWB SOA module

We reported on the use of SOAs for amplification in WDM regime. We show that our UWB SOA can be operated at high power regime, enabling the use as inline amplifier for practical transmission use case, with better performance than the commercially available C-band SOA. We studied the influence of WDM channel number on NL distortions for the UWB SOA. Our experiment confirmed that the increase of WDM channels tends to reduce the noise variance beyond the NL threshold. Finally, we showed that increasing the SOA driving current enables to increase the SOA output power with only small NL penalty. This makes the SOA well suited for transmission systems working at high power regime and with wideband WDM signals.

## 5.4 100 Tb/s regional transmission for upgrade of legacy terrestrial networks

In this section based on a conference paper [P10] co-authored for OFC 2019 and extended in a journal paper [P5] published in 2020, we show the results of a UWB WDM transmission over  $3 \times 100$  km of SSMF, with a total throughput of 107 Tb/s. Contrary to most of recent record experiments using large effective area, low loss fibers and short span, we deliberately choose SSMF to meet with the constraints of legacy terrestrial systems and we demonstrate a 100 Tb/s class experiment compliant with legacy metropolitan networks. The excess span loss compared to PSCF can be as large as 5 dB, and the effective area is reduced by a factor of almost 2, thus increasing the power of Kerr nonlinearities, as well as enhancing the SRS tilt at each span.

### 5.4.a) SRS characterization in 100 km SSMF spans

For such a wide optical spectrum and for high power regime, nonlinear interactions caused by SRS must be considered. It has been shown that the nonlinear interchannel dynamic crosstalk in WDM transmission induced by SRS can be neglected [32, 33]. However, uncompensated power transition from short wavelengths to the longest ones is impractical in multi-span WDM transmission, since on the one hand attenuated channels corresponding to short wavelengths would suffer severe degradation when amplified several times by the UWB SOAs, and on the other hand it has been shown that the impact of SRS on the nonlinear Kerr impairments is significant in UWB systems [35]. Therefore, we conducted a characterization of our 100 km SSMF span in UWB and high-power operation.

We generate a 100 nm continuous noise spectrum by combining ASE from different noise sources with an UWB WSS [130]. We pass this optical signal through a VOA and enter the 100 km SSMF span with launched power ranging from 8.6 to 22.6 dBm. An optical spectrum analyzer is used to measure optical signal spectrum before and after the fiber span.

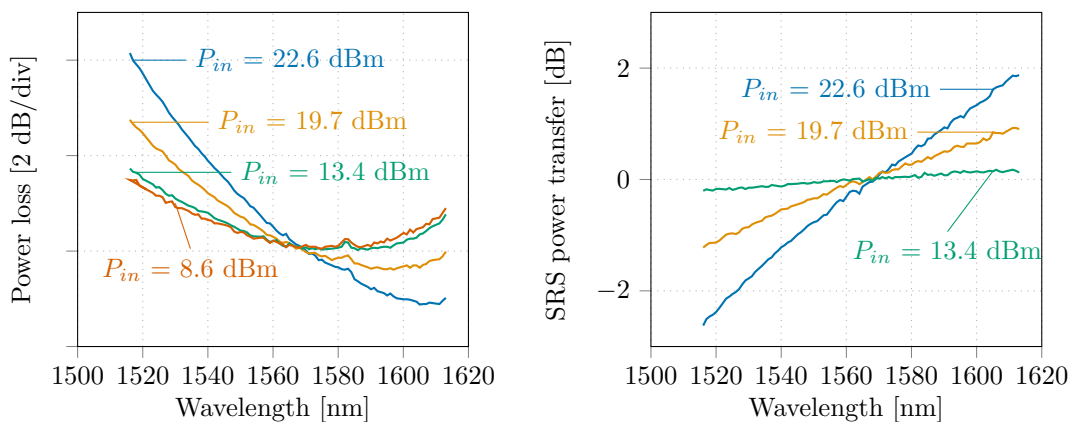


**Figure 5.10:** Power loss (a) and SRS power transfer (b) experienced by an UWB continuous signal launched at different input powers  $P_{in}$  in a 100 km SSMF span

Fig. 5.10(a) shows the power loss experienced by the UWB signal, as a function of the wavelength, and for several input powers. For lowest input powers (8.6

and 13.4 dBm), the power loss roughly corresponds to the fiber attenuation profile. When the launched power increases, short wavelengths undergo larger losses (up to 2.5 dB extra losses for 1515 nm at the maximum input power), and the power is transferred to long wavelengths whose effective loss is reduced by 1.9 dB for 1613 nm at maximum input power. We can deduce from the power loss profiles the shape of the SRS power transfer. Assuming the loss measured for the input power of 8.6 dBm is equivalent to the fiber attenuation profile in linear regime, it can be subtracted from the three other curves to obtain the SRS power transfer versus wavelength as shown in Fig. 5.10(b). We obtain a dB-scale linear SRS power transition evolution as a function of the wavelength. For the low input power of 13.4 dBm, the SRS impact is less than 0.4 dB over the 100 nm bandwidth and remains negligible. When the launched power is increased, the SRS impact rises up to 2.2 dB over the UWB spectrum for an input power of 19.7 dBm. At the highest input power of 22.6 dBm, corresponding to the operation regime of our  $3 \times 100$  km transmission experiment, the SRS power transition reaches 4.5 dB over the 100 nm bandwidth.

To curb the impact of the SRS power transition, we aim at tilting the UWB spectrum to compensate for SRS power transition. We operate the SOA to increase power at short wavelengths and decrease power at long wavelengths. The three spectra shown in Fig. 5.11(a) correspond to three different power spectral densities with the same total power of 22.6 dBm. From the spectrum #1 (solid line) to the spectrum #3 (dash-dot line), the power of the shortest wavelength has been increased by 3 dB, whereas the power of the longest wavelength has been decreased by 2 dB, to assess the influence of the input spectrum tilt on the SRS power transfer. The spectrum #2 (dashed line) corresponds to an intermediate tilted spectrum.

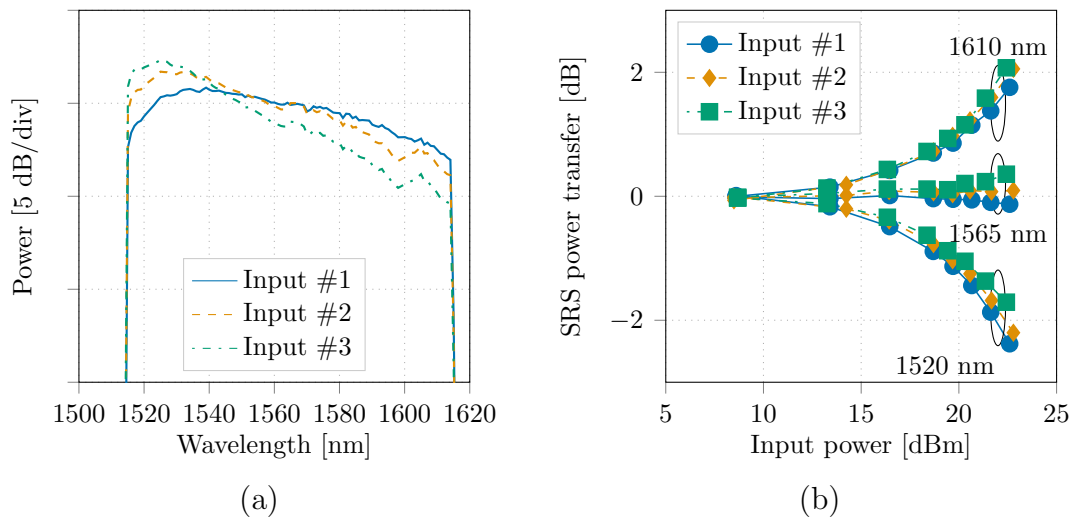


**Figure 5.11:** (a) Fiber input spectra and (b) SRS power transfer evolution versus input power, for 1520, 1565 and 1610 nm.

Then, we vary the total launched power for each case and plot in Fig. 5.11(b) the SRS power transfer at three different wavelengths (1520 nm in S-band, 1565 nm in C-band and 1610 nm in L-band). We observe that for all three input spectra, the maximum SRS power transfer of each wavelength does not change by more than 0.5 dB, around -2.1 dB for 1520 nm, 0.1 dB at 1565 nm and around 1.9 dB for 1610 nm. We show here that the input spectrum shape does not affect the SRS power transfer, which is predominantly determined by the total input power. For a given total input power, this allows us to pre-emphasize the UWB spectrum to

counter the SRS power transition impact.

### 5.4.b) 300 km fiber link using UWB Raman/SOA amplifiers

The experimental transmission setup is shown in Fig. 5.12. At the transmitter side, a 103 nm wide optical spectrum ranging from 1515 to 1618 nm is generated by combining ASE noise sources and modulated laser channels. In C and L bands, 88 and 92 laser sources separated by 50 GHz are separately modulated with two distinct DP I/Q modulators, each modulator being driven by a dedicated DAC, loaded with different randomly-generated sequences, operating at 88 GS/s, and amplified through C and L band amplifiers respectively to compensate for modulation insertion losses. Fiber spools of 25 km are used to decorrelate loading channels. Owing to the lack of laser sources outside C and L bands, we combined ASE noise to the sets of C and L band channels through different input ports of an UWB WSS [130] labeled UWB WSS #1, with a spacing grid of 50 GHz. The generated 103 nm wide optical spectrum is then coupled to a set of three channels. This set contains one central channel made of a TLS modulated with a DP I/Q modulator driven by a dedicated DAC, plus two surrounding channels modulated with a distinct DP I/Q modulator driven by another DAC. Each DAC is fed with randomly-generated sequences of 49 GBd DP-PCS64QAM, with source entropy of 5.4 b/symb/pol. Pulse shaping is performed using RRC pulses with roll-off 0.01. The optical signal ranging from 1515 to 1618 nm, covering 254 slots of 50 GHz, is then sent into an SOA-based UWB amplifier before being launched into the optical link. The total power of the optical signal is 22.5 dBm. At the end of the link, an UWB WSS#3 is used to filter out the channel under test. This signal is then pre-amplified before being sent to the coherent receiver, including a coherent mixer, a tunable LO, balanced photodiodes and a 33 GHz bandwidth real-time scope operating at 80 GS/s. Data sets are stored and offline DSP is then performed to compute SNR of the received signal, as described in sections 1.5.b) and 2.1. Finally, adaptive SD-FEC decoding is performed on the received symbols using a family of SC-LDPC codes [68].

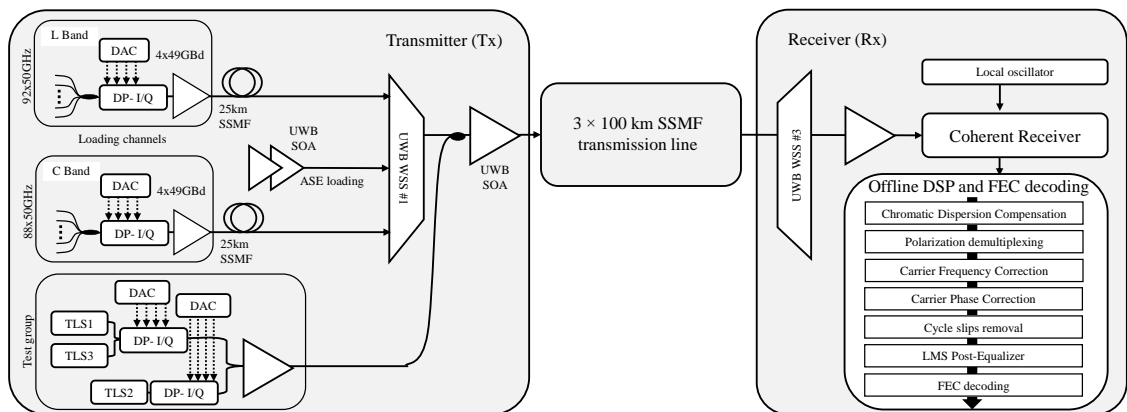


**Figure 5.12:** TX and RX experimental setup for 103 nm UWB transmission over  $3 \times 100$  km SSMF

We first characterize the 300 km transmission link. It is composed of 3 spans of 100 km of SSMF with an average loss of 20 dB at 1550 nm. At the end of each span, a combination of UWB backward Raman pumping and SOA module is used to compensate for span losses. Raman pumping is composed of 5 pumps at 1410, 1435, 1455, 1485 and 1510 nm to provide additional average 9 dB gain at the input

of an UWB SOA, to accommodate for high span losses in 100 km SSMF spans. After span 1 and 3, a static GFF is introduced to handle UWB SOA gain flatness. After span 2, an UWB WSS #2 is introduced to provide dynamic gain equalization compensating for backward Raman gain profile.

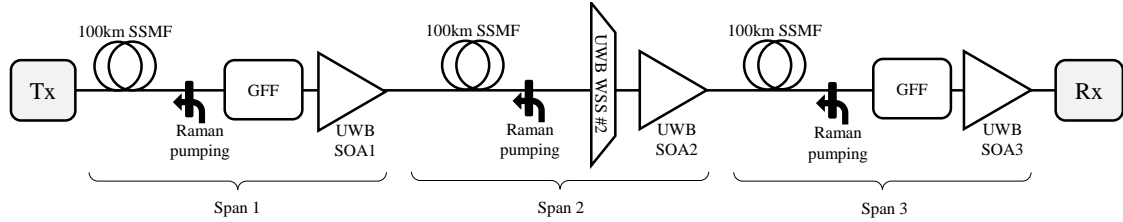


**Figure 5.13:** Description of 300 km transmission line comprising of 3 spans of 100 km SSMF followed by hybrid Raman/SOA amplifiers

Considering the SRS impairments discussed previously, we generate and launch a 103 nm UWB spectrum and operate the SOAs to provide the tilted spectrum as shown in Fig. 5.14 (solid line, left axis), with 6 dB higher power level on shortest wavelengths. We show the measured OSNR at the output of the transmission line (diamond markers, right axis) and demonstrate that our power spectrum engineering strategy enables us to limit the OSNR difference between shortest and highest wavelengths of the systems to less than 3.5 dB. The overall OSNR variation depends on the variation of the NF of the SOA over the bandwidth, but also on the power profile at SOA input resulting from the propagation and the Raman distributed amplification.

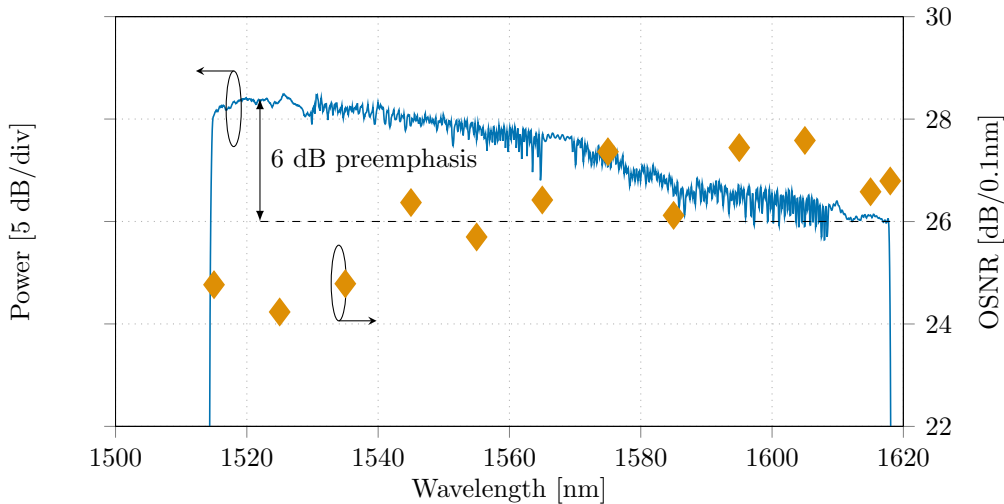


**Figure 5.14:** 103 nm optical spectrum launched into SSMF spans with 6 dB linear tilt (left axis) and measured output OSNR (right axis)

To check how the pre-emphasis strategy impacts the performance of the different channels, we measured the output SNR of the  $3 \times 100$  km transmission system at 1520 and 1610 nm by varying the power of the channel under test and its surrounding neighbors around their nominal power. Although this method does not truly represent the impact of the pre-emphasis of the whole spectrum, it offers a simple way to characterize potential NL impairments on the channel around its nominal power, without changing the settings of all amplifiers. Fig. 5.15 shows the SNR performance versus channel power pre-emphasis. At the nominal power, the SNR

performance between the 1520 and 1610 nm channels differ by approximately 4 dB, which is predominantly governed by the OSNR variation described in Fig. 5.14. This figure also indicates that the channel at 1610 nm operates a few dB below its NLT at nominal power (0 dB pre-emphasis) whereas the channel at 1520 nm operates at its NLT. We show that increasing the preemphasis tilt beyond the current setting (i.e. increasing the power in S-band and reducing the power in L-band) would not result in a performance improvement, as the 1520 nm channel performance would be penalized by NL effects, whereas the 1610 nm channel performance would be reduced by going back in the linear regime.

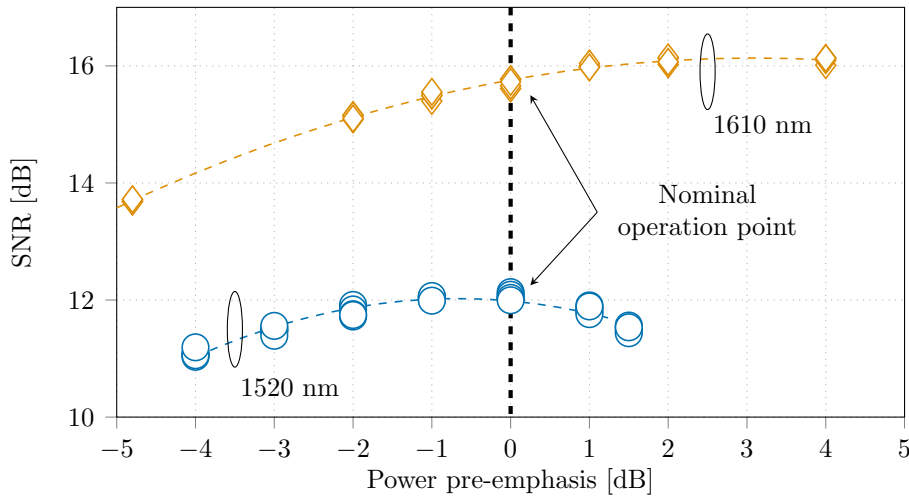


**Figure 5.15:** Measured SNR versus power pre-emphasis for DP-PCS64QAM 49 GBd signals

In such a system, the end of transmission performance is governed by linear and NL impairments that emanate from the interplay among the fiber Kerr effect, the SRS and the SOA gain dynamics, the analysis of which is particularly complex due to the wavelength dependence of fiber loss, noise figure and fiber effective area, and the fact that optical power spectrum continuously evolves along the direction of propagation.

### 5.4.c) Experimental results

We measured the performance of all the 254 WDM channels by sweeping the set of three channels including the channel under test over the whole optical bandwidth. As shown in Fig. 5.16(a), we measured SNR ranging from 11.3 dB up to 15.9 dB over the whole bandwidth. The SNR variation in the bandwidth is dominated by the OSNR evolution in the bandwidth, with additional penalties at the spectrum edges coming from bandwidth limitations of the UWB components.

Finally, for each wavelength the maximum code rate resulting in error-free FEC decoding was adaptively found among the 26 members of the SC-LDPC code family with code rate ranging from 0.67 to 0.91. Fig. 5.16(b) shows the maximum net throughput for each of the 254 channels, ranging from 343 to 469 Gb/s, leading to a total throughput of 107 Tb/s.

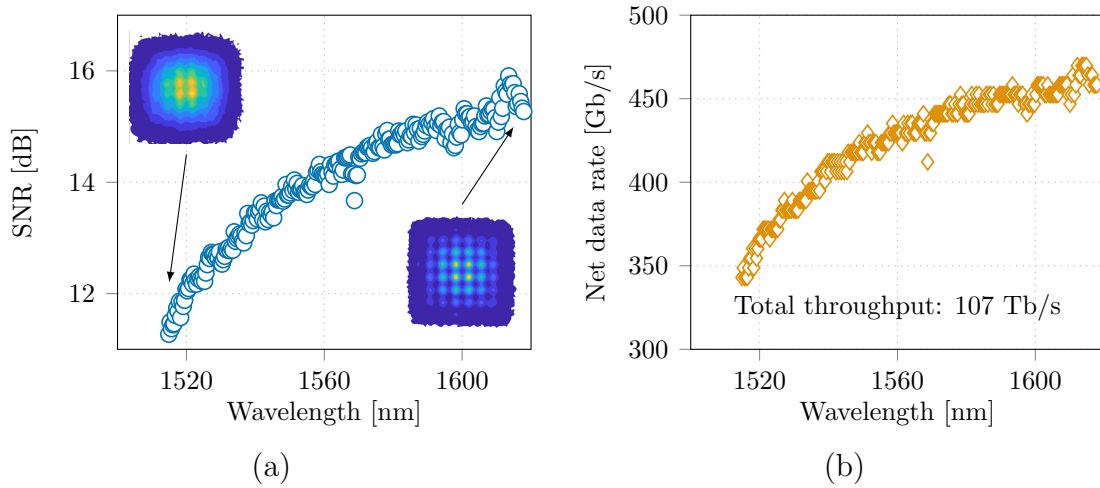


**Figure 5.16:** Measured SNR (a) and corresponding post SD-FEC net data rate (b) versus wavelength, for all 254 DP-PCS64QAM 49 GBd channels

## Conclusions on UWB regional transmission

We reported on UWB continuous amplification over S, C and L bands using hybrid Raman/SOA amplifiers. We characterized the stimulated Raman scattering effect occurring in a 100 km SSMF span for such a wide optical spectrum and high power regime. We showed that the span input spectrum shape does not affect the signal power transition from short wavelengths to longer ones. Using an appropriate power spectrum preemphasis strategy, high performance PCS-64QAM modulated channels at 49 GBd and hybrid Raman/SOA amplification, we successfully transmitted 254 channels spaced by 50 GHz over a  $3 \times 100$  km long fiber link of SSMF with a continuous optical bandwidth of 103 nm. We demonstrated a total capacity of 107 Tb/s, showing the potential of SOA technology for capacity upgrades of metropolitan networks.

More recently, we have demonstrated in [P13] a machine-learning method for Raman gain prediction and multi-pump broadband amplifier design. We have showed that the mapping between Raman pump currents and UWB loss profile can be learned by artificial neural networks based on experimental characterization of the distributed multi-pump Raman amplifier. This method can be useful to ease transmission link design tasks, such as the optimization of Raman amplifiers for multi-span UWB transmission systems, that depends on a complex interplay between Raman pumping, SRS occurring for high power regimes and wavelength-dependent fiber loss profile and SOA characteristics.

## 5.5 Record throughput on a 257 km unrepeated fiber link

Unrepeated transmission systems are economically viable solutions to provide connectivity to optical networks in areas for which the installation and future repairs of in-line amplifiers are considered to be prohibitive. Such systems consist of a single fiber span, that can extend over multiple hundreds of km, with gain provided from either or both span ends. They are particularly attractive with submerged festoon configurations to connect remote islands, as well as between coastal locations to avoid deploying terrestrial fibers and stations in highly inaccessible areas (i.e. mountain shores, tropical forests, deserts, etc). In submarine links, the absence of in-line active components also removes the need to include conductive material within the cable structure, thus further reducing the cost of the system and simplifying its design. Unrepeated spans can also be used to serve as endings of long-distance repeated systems to secondary landing points.

To increase both the throughput and the transmission distance, a multitude of techniques have been applied: low-loss high-effective area fibers, forward- and backward-propagating Raman pumps, mid-span remote optically pumped amplifiers (ROPAs), high-power booster at the transmitter, etc. ROPAs consist in a piece of doped fibre with a pump remotely located at a link end. They enable ultra-long reach, but do not operate over an ultra-wide optical bandwidth. Transmission in S-, C- and L-bands for unrepeated systems has been proposed as early as 2001 [131] as a solution to overcome the C-band capacity exhaustion, before progress in transceiver SE and the advent of coherent detection set aside the urgent need of extending the optical bandwidth. Since then, only extension to L-band has been considered, such as in [132].

In this section based on a conference paper [P15] co-authored with ASN and published at ECOC 2020, we present the potential of UWB SOAs coupled with distributed Raman amplification to upgrade the capacity of unrepeated links, leveraging seamless S+C+L WDM transmission. We demonstrate a throughput record over a 257.5 km single-span, with transmission of  $247 \times 49$  Gbd channels thanks to 100 nm continuous amplification provided by UWB SOAs and distributed backward Raman pumping.

### 5.5.a) 257.5 km transmission experimental setup

The transmission setup of the 100 nm wide optical spectrum over the 257.5 km unrepeated link is shown in Fig. 5.17. At the transmitter side, ASE noise sources are coupled through an UWB WSS [130] to generate a 100 nm wide optical spectrum, ranging from 1514.8 nm to 1615.3 nm and covering 247 slots on a 50 GHz grid. The UWB spectrum is then coupled to a test group composed of three modulated channels. The WSS allows to perform power equalization on the loading spectrum and to filter out the noise in the frequency slots corresponding to the test group. The test group contains one central channel made of a TLS modulated with a DP I/Q modulator driven by a dedicated DAC, plus two surrounding channels modulated with a distinct DP I/Q modulator driven by a dedicated DAC. Each DAC operates at 88 GS/s and is loaded with a randomly generated sequence at a symbol rate of 49 Gbd, with RRC pulse shaping and roll-off 0.01 to fit the 50 GHz channel slot.

As detailed in the following, the modulation format of the transmitted sequence is chosen between dual-polarization 16QAM (with entropy of 4 b/symb/pol) and PCS-64QAM (with entropies of 4.6 or 5.4 b/symb/pol) to maximize the information rate. The test group is swept across the UWB spectrum to measure the performance of the 247 WDM channels.

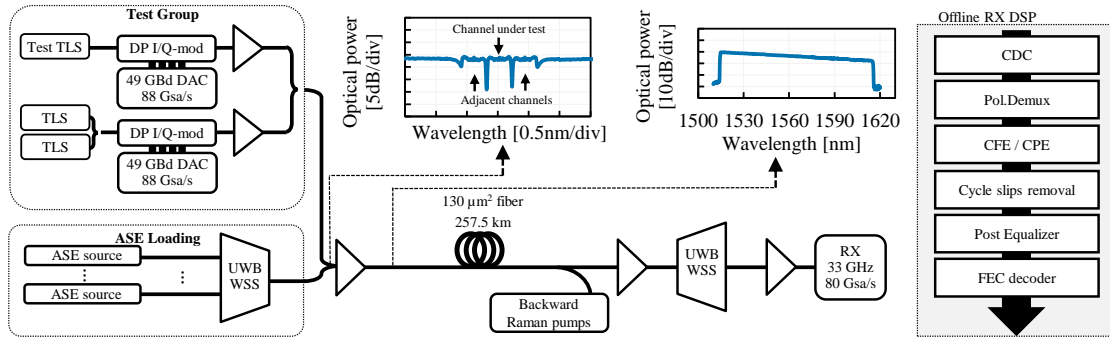


**Figure 5.17:** Experimental setup comprising a test group with three modulated channels multiplexed with UWB ASE noise spectrum, boosting SOA at the transmitter and 257.5 km of ULL PSCF with backward Raman pumping.

The optical signal is then sent to an SOA-based UWB boosting amplifier with output power of 21 dBm. The transmission line is a 257.5 km long span of Sumitomo ultra-low loss (ULL) PSCF with  $130 \mu\text{m}^2$  effective area, totaling an average span loss of 39.2 dB at 1550 nm. In the absence of Raman pumping, we determined the fiber loss profile (dotted line in Fig. 5.18) by launching the signal at a low power (7 dBm) in the fiber. As shown in Fig. 5.18, the power loss experienced by the spectrum ranges from 38.5 dB to 42 dB. When launching the optical signal at 21 dBm, the power loss profile (dashed line) is impacted by SRS effect occurring on such a wide optical signal in high power regime. Subtracting the fiber losses from the total power losses of the span, we find that the SRS gain in Fig. 5.18 (right axis) is approximately 2.5 dB between the extreme ends of the spectrum.

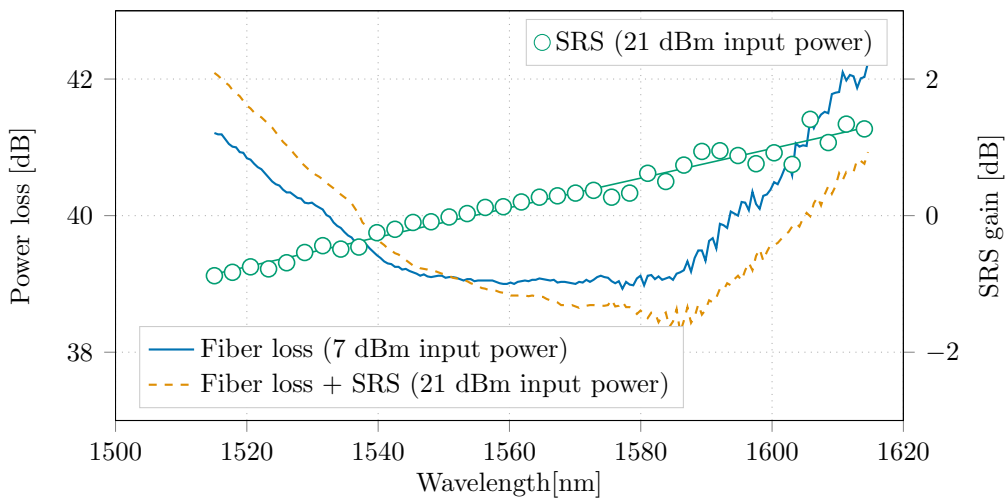


**Figure 5.18:** Span power loss (left axis) for a launched power of 7 dBm (solid line) and 21 dBm (dashed line), and corresponding SRS (right axis) for a launched power of 21 dBm, in the absence of Raman pumping.

To provide distributed Raman amplification, four Raman pumps at 1365 nm,

1425 nm, 1455 nm and 1494 nm are multiplexed at the end of the link and backward propagated into the fiber. This is a second order pumping scheme where the 1365 nm pump amplifies the other pumps over the line. The power provided by the pumps into the line are 2.1 W, 0.6 W, 0.15 W and 0.2 W respectively. Fig. 5.19 shows the measured Raman On/Off gain at the output of the line. The provided average gain is approximately 28 dB.

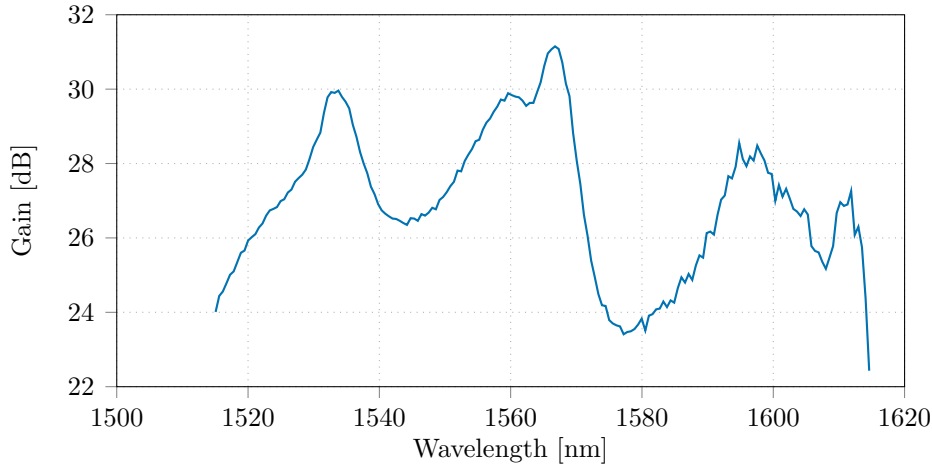


**Figure 5.19:** Raman On/Off optical gain of backward Raman pumping

At the end of the link, the channel under test is filtered out and pre-amplified before being sent to the coherent receiver, including a coherent mixer, a tunable local oscillator, balanced photodiodes and a 33 GHz bandwidth high speed real-time scope. DSP is then performed offline as described in section 1.5.b). Codes from a SC-LDPC family are adaptively selected to implement the SD-FEC decoding [68]. The code rate ranges from 0.4 (0.67 for PCS64QAM) to 0.97 with a variable granularity, from 0.0025 to 0.01 depending on the range, in order to minimize the decoding rate loss.

### 5.5.b) Adaptive modulation format for capacity maximization

To accommodate for the variations of SNR in the UWB spectrum, we have considered in this experiment three different modulation formats: 16QAM (entropy of 4 b/symb/pol) and PCS64QAM with source entropies of 4.6 and 5.4 b/symb/pol. In the following, these PCS64QAM formats are referred to as PCS64QAM-4.6 and PCS64QAM-5.4, respectively. By construction, PCS64QAM modulation is compatible only with FEC code rates larger than or equal to  $2/3$ , therefore there exists a lower SNR limit below which PCS64QAM cannot be used. In Fig. 5.20, we show the GMI evolution versus SNR for the considered PCS64QAM formats.

As the NGMI corresponds to the ideal FEC code rate, only SNR values ensuring NGMI above the  $2/3$  threshold are considered. This corresponds to GMI values above 2.6 and 3.4 b/symb/pol for source entropies of 4.6 and 5.4 b/symb/pol, respectively. As shown in Fig. 5.20, the minimum required SNR is 7.2 for PCS64QAM-4.6 and 10.0 dB for PCS64QAM-5.4, as indicated by the diamond markers.

In practice, the SC-LDPC FEC implementation induces an SNR penalty, and the circle markers represent the practical SD-FEC lower limit as observed in our experiments, i.e. 8.2 dB for PCS64QAM-4.6 and 10.8 dB for PCS64QAM-5.4. The modulation format allocation strategy in the range of SNR values from 5 to 15 dB can therefore be described as follows. For SNR values below 8.2 dB, PCS64QAM

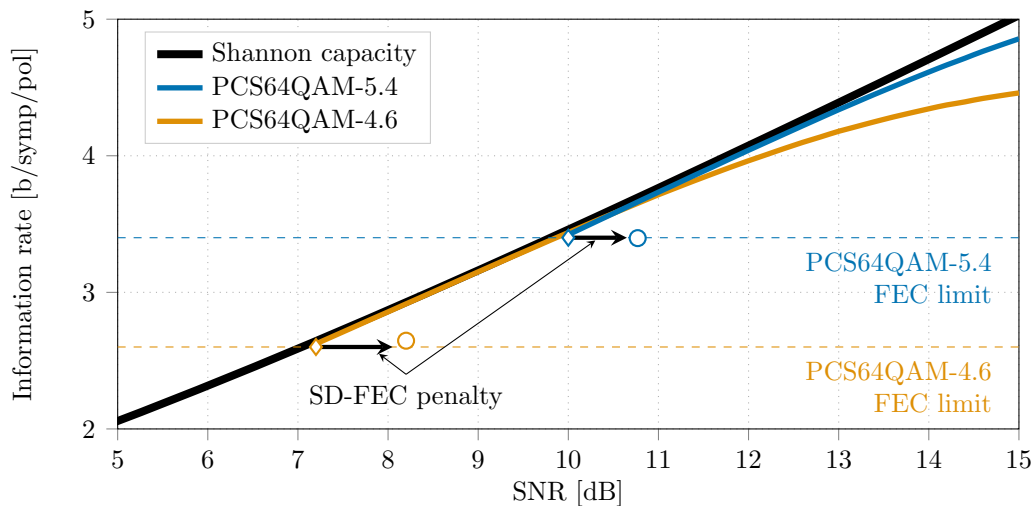


**Figure 5.20:** GMI versus SNR for PCS64QAM with entropies of 4.6 or 5.4 b/symb/pol. Circle markers represent the practical SD-FEC lower limit as observed in our experiments

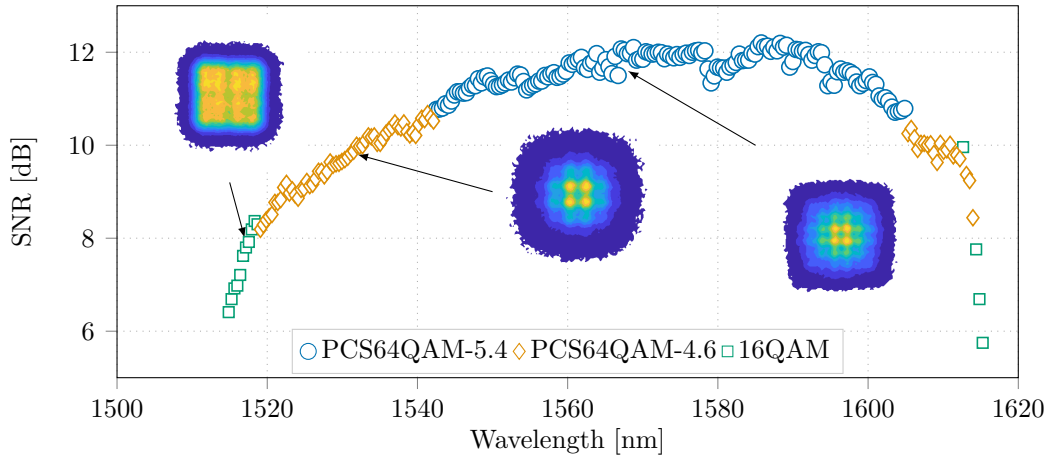
is not achievable and 16QAM is used, without limitation on the FEC code rate but with a bigger gap to Shannon’s capacity. For SNR values between 8.2 and 10.8 dB, PCS64QAM-4.6 is a suitable candidate to optimize the channel rate as its GMI is very close to Shannon’s capacity. For SNR values above 10.8 dB, the entropy of PCS64QAM can be increased to 5.4 b/symb/pol, providing close-to-capacity operation up to high SNR values: when the SNR is equal to 15 dB, still considering ideal FEC decoding, PCS64QAM-5.4 shows only 0.2 b/symb/pol penalty in terms of GMI compared to Shannon’s capacity whereas PCS64QAM-4.6 starts saturating and exhibits 0.6 b/symb/pol penalty.

### 5.5.c) Experimental results

After coherent detection and offline DSP applied to each 49 GBd channel, as shown by Fig. 5.21 the per channel SNR measured from the processed waveforms varies between 5.8 and 12.2 dB. The SNR profile is predominantly impacted by the OSNR variation across the 100 nm bandwidth, with additional penalties at the extreme wavelengths, due to transceiver impairments and the SOA bandwidth limitation. Following the allocation strategy discussed above, the modulation formats are chosen (as depicted by the different markers) in order to reduce the information gap to Shannon capacity as much as possible considering the operating SNR range.

For wavelengths comprised between 1519 nm and 1614 nm, the SNR is above 8.2 dB and the channels are modulated either with PCS64QAM-5.4 (152 channels between 1542.5 and 1605 nm) or with PCS64QAM-4.6 (80 channels). For wavelengths below 1519 nm and wavelengths above 1614 nm, only 16QAM is suitable for the transmission of the 14 corresponding channels. Note that for the channel at 1612.62 nm, the experimental waveforms recorded using PCS64QAM-4.6 are not exploitable due to an excessive detuning ( $>4$  GHz) between the transmitter laser and the LO that occurred when switching the test group wavelength. Therefore, for this channel we show the 16QAM results whereas its neighbours belong to the PCS64QAM-4.6 group.

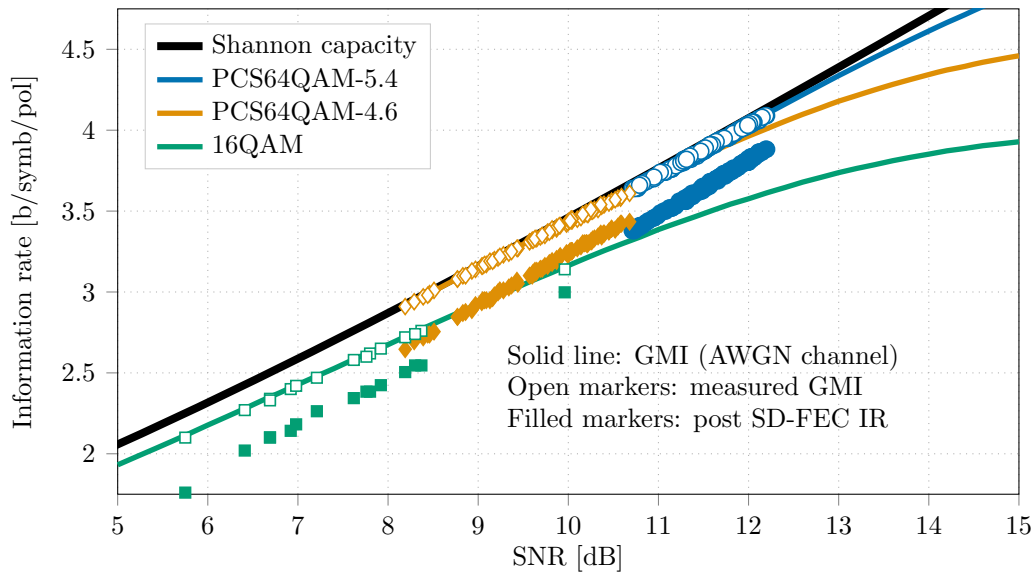
For each channel, in order to maximize the net bit rate for each processed waveform, the code from the SC-LDPC family with the highest code rate ensuring error



**Figure 5.21:** SNR evolution for the 247 channels using 16QAM and PCS64QAM with entropies 4.6 or 5.4 b/symb/pol

free transmission is selected. The post SD-FEC IR is then computed from the code rate value  $r_c$  as

$$IR = H - (1 - r_c) \cdot m. \quad (5.2)$$



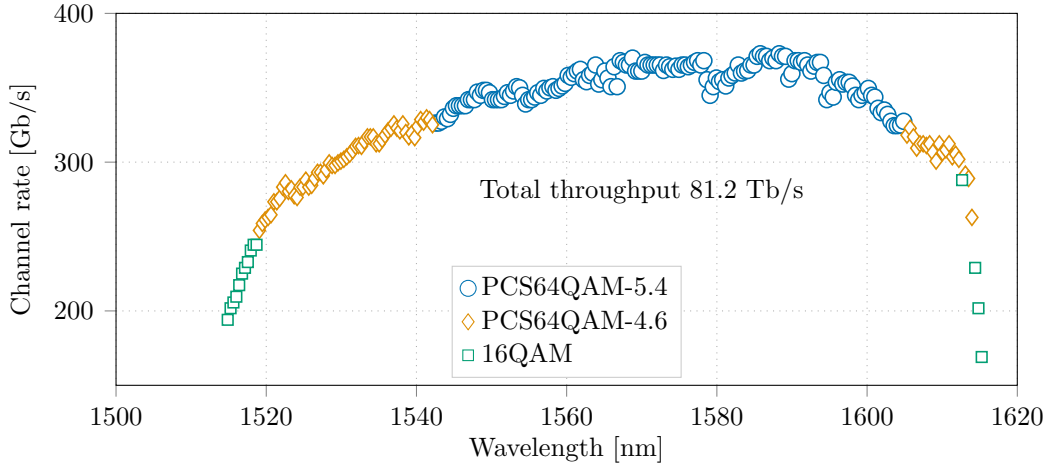
**Figure 5.22:** GMI and post SD-FEC IR evolution versus channel SNR for the 247 channels

Fig. 5.22 shows the evolution of the GMI and the post-SD FEC IR of the 247 channels, as a function of the SNR. For the 16QAM channels the GMI ranges from 2.1 to 3.14 b/symb/pol, with a corresponding code rate between 0.44 and 0.75, leading to IR between 1.76 and 3.00 b/symb/pol. When using PCS64QAM, the capacity-approaching GMI rises almost continuously between 2.91 and 4.09 b/symb/pol, leading to AIR between 2.65 and 3.89 b/symb/pol with optimal code rates between 0.67 and 0.81. The 16QAM channel with SNR close to 10 dB corresponds to the 1612.62 nm channel with missing data for PCS64QAM-4.6. Our adaptive strategy using 3 different modulation formats enables us to cope with the high SNR variations arising from the challenging design of this unrepeated link, where the WDM channels are inequitably impaired by linear and NL noise contributions.

Considering the post SD-FEC IR obtained after optimization, the net bit rate  $R_b$  carried by each channel is obtained through the formula

$$R_b = 2 \cdot IR \cdot R_s \cdot r_p \quad (5.3)$$

where 2 stands for the two polarizations of the signal,  $r_s = 49$  GBd is the symbol rate and  $r_p = 0.98$  accounts for the rate reduction due to DSP pilot symbol insertion. The resulting net channel rate for all channels is given in Fig. 5.23. The net channel rate ranges from 169 to 372 Gb/s, with a total net rate of 81.2 Tb/s. The capacity-distance product of 20.9 Pb/s·km corresponds to a 143% improvement compared to the previous record [133].



**Figure 5.23:** Net bit rate evolution for the 247 channels using 16QAM and PCS64QAM with entropies 4.6 or 5.4 b/symb/pol

## Conclusions on UWB unrepeated transmission

With this record transmission experiment demonstrating both the highest capacity and the highest capacity-distance product ever achieved on a single-mode fiber unrepeated system, we show the potential of S+C+L continuous amplification with UWB SOA to scale the capacity of unrepeated systems. Without utilizing ROPAs, a simplified design based on UWB SOAs at the transmitter and receiver ends and distributed Raman amplification has been proposed. The result of 20.9 Pb/s·km presented herein brings a 143% improvement compared to the previous record for a similar distance [133]. This record was achieved through, on one hand, the interplay between the 100 nm optical bandwidth enabled by the SOAs and, on the other hand, the high net-rates obtained from the utilization of advanced modulation formats and adaptive SD-FEC codes tailored to each channel.

## 5.6 Summary

In this chapter, we investigated the potential of UWB amplification with SOAs for capacity upgrade of optical fiber networks. After a decade of extensive progress in C-band system capacity with advanced modulation, coding and DSP schemes, SOAs appear as one of the possible technologies to extend the optical system bandwidth and harness the capacity offered by the low-loss window of the fiber. As the use of SOAs as inline amplifiers has been ruled out for decades because of their worse performance compared to EDFAs, we have experimentally shown that our UWB SOA device can be suited for UWB WDM amplification at high power regime, as the nonlinear impairments are reduced by increasing the number of WDM channels.

We then reported experimental demonstrations showing the potential of UWB SOAs for capacity upgrade in two different configurations. First, we demonstrated a 107 Tb/s transmission over 300 km, using 254 capacity-approaching channels over a 103 nm spectrum. We combined distributed Raman backward pumping with UWB SOAs to fit the typical power loss constraints of 100 km SSMF spans of legacy terrestrial networks, and we highlighted the impact of nonlinear SRS power transfer in the transmission system design. This result paves the way for capacity upgrades of metropolitan optical networks. In a second experiment, we demonstrated a record throughput on an unrepeated fiber link, a transmission system configuration with a very long single span and without inline amplifiers. To cope with the large variations of the performance over the 100 nm bandwidth, we used an adaptive modulation format strategy able to maximize the total system throughput. Leveraging UWB amplification provided by the Raman/SOA scheme, we demonstrated a 143% improvement of the capacity distance product compared to the previous record, showing the potential of UWB SOA for upgrade of capacity-approaching systems.

# Conclusions and perspectives

Over the past two decades, continuous progress in optical fiber transmission systems enabled the development of a global high capacity infrastructure at the core of the Internet communication network. First, optimization of the optical path elements together with digital compensation of propagation impairments using coherent DSP has allowed to considerably increase the end-of-link SNR, which is ultimately limited by the physical limits defined by optical amplification noise and NL fiber impairments. Besides, advanced modulation schemes such as PCS modulation, together with powerful SD-FEC coding techniques, now enable the SE to approach the Shannon's capacity limit.

To further scale the capacity of optical fiber links, alternative paradigms are now being considered. SDM (including MCF and MMF) aims at scaling the number of optical paths while UWB systems rely on the optical bandwidth extension beyond 4.5 THz of C-band systems. As leveraging these physical dimensions generally reduces the system SNR due to multiplexing constraints or impairments, research efforts must focus on limiting the SE degradation or the system complexity to keep these methods attractive for throughput scaling of optical links.

Furthermore, the constant progress in D/A and A/D converter technology has fostered the scaling of transponder symbol rate, towards high speed transmitters able to cope with the evolution of client rates, from 100 GbE up to 400 GbE now, and even 800 GbE and 1.6 TbE in the future. This is mainly encouraged for cost and integration reason, not only for short reach applications but this appears also as a key enabling factor for future cost-efficient systems based on SDM or UWB systems.

## Thesis summary

The chapter 1 of this thesis was dedicated to an overview of fundamental concepts of digital communication systems and the specificities of optical coherent transmissions. In particular, the modeling of the optical communication channel (which includes TX, propagation and RX) has been presented, as well as the corresponding DSP to compensate for propagation impairments.

In chapter 2, we studied the performance characterization of the communication system. From an information theory point of view, we presented the suitable metrics to quantify the impairments caused by the optical communication channel on the transmitted symbols. We detailed the impact of modulation and coding on the information rate using QAM and PCS-QAM modulations, and reviewed the interest for PCS-QAM as a capacity-approaching modulation scheme with attractive flexibility.

Chapter 3 was devoted to the experimental demonstration of high symbol rate transmitters in various transmission use cases. We presented the architecture and characterization of a 80 to 100 GBd transmitter, based on CMOS technology and using a single DAC per modulated dimension. We introduced an electro-optical

bandwidth compensation scheme, required to assess the performance of future high symbol rate transmitters with improved characteristics. In a first experiment, we demonstrated the capabilities of 99.5 GBd DP-64QAM signals to address 800 Gb/s net channel rate over a 605 km. This shows the possibility to address future 800 GbE demand in future regional networks with 8 b/s/Hz SE thanks to high performance transmission using ultra low-loss fibers. Then, we reported a record 20570 km transmission of 300 Gb/s channel rate for all 41 channels in the C-band, using 99 GBd DP-QPSK and without NLC techniques. We showed in our experiment that the transmission power efficiency could be increased by 76% when halving the fiber input power, which is compatible with the current trend in the industry towards SDM systems. Since the increase of fiber counts in submerged cables inevitably scales the number of required transponders to operate the cable, high symbol rate transceivers are attractive solutions for the design of cost-efficient systems. Finally, we conducted a field trial over a live traffic network to study the compatibility of 80 to 95 GBd signals with real-world network architectures, based on 100 GHz grid nodes. Leveraging symbol rate and constellation shaping, we have demonstrated the successful transmission of 400 Gb/s over 3400 km ultra long-haul distance, as well as 600 Gb/s over 1100 km using 90 GBd signals. In particular, we highlighted the 95 GBd signal penalties coming from implementation and transmission in the 100 GHz grid network, showing potential limits of close to 100 GBd transmissions over legacy network architectures.

We presented in chapter 4 a study of equalization enhanced phase noise (EPPN), which is a potentially dominant impairment at high symbol rates. As symbol rates of 100 GBd and more are now practical, and analytical studies predict a linear scaling of EPPN variance with the accumulated CD (hence with the transmission distance), the symbol rate and the LO laser linewidth, the EPPN impact could be detrimental for high symbol rate transmissions over ultra long subsea distances. We started with numerical simulations to isolate EPPN contributions and we highlighted through the studies of EPPN temporal and statistical characteristics that the CPE algorithm must be taken into account in EPPN impact analysis. In particular, we showed that not taking into account the CPE can lead to the overestimation of EPPN impact, which can rule out the use of high symbol rate transmitters with the current specifications of laser sources. Owing to the lack of satisfying model to assess EPPN impact on high symbol rate subsea communications, through an experimental characterization campaign over a 10476 km straight line testbed we showed that the EPPN impact when using a standard ECL source with 100 kHz linewidth specification was negligible compared to a sub-kHz ULPNS reference laser. These investigations temper the industry concerns EPPN impact in the design of high symbol rate subsea communications. As EPPN arises from the interaction of the transponder laser PN with the electronic CDC, it bonds the transmission line properties to the transponder characteristics. Further analysis is still required to accurately quantify EPPN impact in future transoceanic systems, especially in the open cable context that imposes a disaggregated analysis of the transmission penalties.

Chapter 5 was dedicated to investigations on UWB transmission systems based on SOA. For the past decades, the use of SOAs as inline amplifiers has been ruled out because of their polarization-dependence, worse performance and nonlinear behaviour compared to EDFAs. We have first reviewed the main characteristics of

a UWB SOA module with polarization diversity architecture, able to provide high power and dual polarization gain over a 100 nm bandwidth over S, C and L bands. Second, we experimentally assessed the nonlinear behaviour of the UWB SOA in WDM configuration, and we showed that UWB SOA can enable UWB WDM amplification at high power regime, as the nonlinear impairments are reduced by increasing the number of WDM channels. Finally, we demonstrated experimental transmissions using hybrid Raman/SOA amplifiers and showed that UWB SOAs are potential candidates for capacity upgrades of optical links. We demonstrated the compatibility of this UWB amplification scheme with a 100 Tb/s transmission over a regional 300 km link based on SSMF legacy architecture, as well as a record throughput over a 257 km unrepeated link, thanks to the transmissions of circa 250 channels using capacity-approaching PCS modulation.

## Perspectives

Coherent optical communications have enabled the development of flexible high capacity links at the core of the global communications networks. In the near future, capacity-approaching solutions will soon become available from DCI to subsea transmissions, as key technological breakthroughs are increasingly maturing. To further scale the capacity of optical links, new paradigms are now emerging. Whereas the per-fiber throughput has been for years the main design criterion, global optimization of optical system throughput and cost-efficiency will presumably require better utilization of fiber available capacity through bandwidth extension and optical path multiplicity.

We have reported on the use of UWB SOAs as potential candidates for bandwidth extension up to 100 nm. Together with hybrid Raman/SOA amplification schemes, we have demonstrated potential upgrades of optical capacity on legacy regional link architecture and unrepeated transmission. Further improvement of UWB SOA module performance, custom optical path design with innovative techniques leveraging artificial intelligence, together with flexible, adaptive and capacity-approaching transponders, will undoubtedly encourage capacity upgrades beyond the C-band current systems.

The continuous increase of transponder symbol rate has been driven in recent years by cost-efficiency and footprint optimization concerns. We have highlighted the flexibility provided by high symbol rate transmitters and leveraged by adaptive PCS modulation to optimize the rate versus reach trade-off from regional transmissions up to transoceanic distances. EEPN is considered to be a potentially detrimental impairment for high symbol rate systems with large accumulated chromatic dispersion and has raised concerns for future subsea communication systems, that we have tempered through numerical and experimental investigations. In the context of open cables, optical vendors are encouraged to provide disaggregated specifications of transmission lines, transponder technology and other additional impairments. Further optimization of transceiver bandwidth and thorough characterization of impairments such as EEPN, crosstalk and filtering penalties, that bond the optical path design and transceiver equipments, will be required to optimize the design of next-generation high capacity and cost-efficient optical transport networks.



# Acknowledgements

As a final addition to this manuscript, I would like to express my deepest gratitude to all the persons that supported me in many different ways during this exciting and challenging experience.

My journey in the world of optical communications started with an internship in the Transmission department at Nokia Bell Labs in 2017, and I would like to thank Amir, Jeremie and Gabriel for their support and guidance and for transmitting me their passion for optical communications.

I am grateful to Amir and Jeremie, Yann and then Badr-Eddine for the supervision of this thesis work, as well as to all the members of the jury for accepting to take part in the evaluation of this work, and especially the reviewers of the manuscript for their insightful comments that helped me to finalize this work.

The work presented in this thesis would not have been achieved without the invaluable contributions, advice and support of all the colleagues and external co-authors I had the opportunity and privilege to work with. I am indebted to all of them for providing me the material conditions to obtain results in a high-quality environment, as well as sharing their knowledge and experience with generosity.

During these almost 4 years, I also had the chance to work in a unique atmosphere within the optical communication research teams in Nokia Bell Labs Paris-Saclay. Besides the stimulating work environment, I will not forget all the laughs in the lab, the countless coffee-breaks and never-ending passionate debates at lunch or in the office. Special thanks to my team mates for all these good memories in Nozay, in conferences, all along the RER B for our social events and also later with remote "teams coffee". Especially during the lockdown periods, working with friends and not only colleagues was an invaluable asset.

Finally, I would like to thank my colleagues, my family and my friends, for their unwavering support all along the path towards the end of this challenge. I am truly grateful for all your advice, affectionate backing and encouragement, during these years and especially during the period of PhD redaction and defense, as well as helping me in many ways to move forward with a new stimulating experience.



# List of acronyms

<b>A/D</b> analog-to-digital	<b>FFT</b> fast Fourier transform
<b>ADC</b> analog-to-digital converter	<b>FWM</b> four wave mixing
<b>ASE</b> amplified spontaneous emission	<b>FWHM</b> full width at half maximum
<b>AWGN</b> additive white Gaussian noise	<b>GAWBS</b> guided acoustic Brillouin scattering
<b>BER</b> bit error rate	<b>GFF</b> gain flattening filter
<b>BMD</b> bit metric decoding	<b>GMI</b> generalized mutual information
<b>BPS</b> blind phase search	<b>GNM</b> Gaussian noise model
<b>CD</b> chromatic dispersion	<b>GVD</b> group velocity dispersion
<b>CDC</b> chromatic dispersion compensation	<b>HD</b> hard decision
<b>CM</b> coded modulation	<b>IMDD</b> intensity modulation direct detection
<b>CMOS</b> complementary metal oxide semiconductor	<b>I/Q</b> in-phase and quadrature
<b>COI</b> channel of interest	<b>IR</b> information rate
<b>CFE</b> carrier frequency estimation	<b>ITU</b> International Telecommunication Union
<b>CMA</b> constant modulus algorithm	<b>LCOS</b> liquid crystal on silicon
<b>CPE</b> carrier phase estimation	<b>LO</b> local oscillator
<b>D/A</b> digital-to-analog	<b>LMS</b> least mean squares
<b>DAC</b> digital-to-analog converter	<b>MCF</b> multi-core fiber
<b>DBP</b> digital back propagation	<b>MCI</b> multi-channel interference
<b>DCI</b> datacenter interconnect	<b>MI</b> mutual information
<b>DFB</b> distributed feedback	<b>MIMO</b> multiple-input multiple-output
<b>DP</b> dual polarization	<b>MMA</b> multi-modulus algorithm
<b>DSP</b> digital signal processing	<b>MMF</b> multi-mode fiber
<b>DU</b> dispersion-unmanaged	<b>MZM</b> Mach-Zehnder modulator
<b>EDFA</b> erbium doped fiber amplifier	<b>NF</b> noise figure
<b>EEPN</b> equalization enhanced phase noise	<b>NGMI</b> normalized generalized mutual information
<b>ENOB</b> effective number of bits	<b>NL</b> nonlinear
<b>FEC</b> forward error correction	

<b>NLT</b> nonlinear threshold	<b>TRX</b> transceiver (transmitter/receiver)
<b>NLSE</b> nonlinear Schrödinger equation	<b>TX</b> transmitter
<b>PCS</b> probabilistic constellation shaping	<b>UWB</b> ultra-wideband
<b>PDG</b> polarization dependent gain	<b>VOA</b> variable optical attenuator
<b>PDL</b> polarization dependent loss	<b>WDM</b> wavelength division multiplexing
<b>PMD</b> polarization mode dispersion	<b>WSS</b> wavelength selective switch
<b>PMF</b> probability mass function	<b>XCI</b> cross-channel interference
<b>PN</b> phase noise	
<b>PSCF</b> pure silica core fiber	
<b>PSD</b> power spectral density	
<b>QAM</b> quadrature and amplitude modulation	
<b>QPSK</b> quadrature phase shift keying	
<b>RC</b> raised cosine	
<b>RF</b> radio frequency	
<b>ROADM</b> reconfigurable optical add/drop multiplexer	
<b>ROPA</b> remote optically pumped amplifier	
<b>RRC</b> root raised cosine	
<b>RX</b> receiver	
<b>SC-LDPC</b> spatially-coupled low density parity check	
<b>SCI</b> single channel interference	
<b>SD</b> soft decision	
<b>SDM</b> space-division multiplexing	
<b>SE</b> spectral efficiency	
<b>SOA</b> semiconductor optical amplifier	
<b>SMF</b> single mode fiber	
<b>SNR</b> signal to noise ratio	
<b>SRS</b> stimulated Raman scattering	
<b>SSMF</b> standard single mode fiber	
<b>SSFM</b> split-step Fourier method	
<b>TLS</b> tunable laser source	

# List of symbols

$B_{ref}$ reference bandwidth (12.5 GHz or 0.1 nm around $\lambda_0$ )	$SE$ spectral efficiency
$c$ speed of light	$SNR$ signal to noise ratio
$D$ dispersion coefficient	$t$ time
$F$ noise factor	$T_s$ symbol period
$f$ frequency	$W$ optical bandwidth
$GMI$ generalized mutual information	$z$ distance
$\hbar$ reduced Planck constant	
$H$ entropy	$\alpha$ fiber attenuation
$IR$ (post SD-FEC) information rate	$\beta$ propagation constant
$j$ imaginary unit	$\beta_i$ $i$ -th derivative of $\beta(\omega)$ , evaluated at $\omega_0$
$L$ transmission length	$\gamma$ nonlinearity coefficient
$M$ number of optical paths (modes, cores)	$\Delta\nu$ laser linewidth
$MI$ mutual information	$\lambda$ wavelength
$m$ number of bits per symbol ( $2^m$ QAM constellation)	$\lambda_0$ reference wavelength (1550 nm)
$n$ refractive index	$\rho$ roll-off (RC or RRC pulse-shaping)
$NF$ noise figure (in dB)	$\omega$ angular frequency
$NGMI$ normalized generalized mutual information	$\omega_0$ reference angular frequency $2\pi c/\lambda_0$
$OSNR$ optical signal to noise ratio	
$p_X$ prior probability of $X$	
$p_{X Y}$ posterior probability of $X$ given observation $Y$	
$p_{Y X}$ likelihood of observation $Y$ given $X$	
$r_c$ code rate	
$r_p$ pilot rate	
$R_b$ (post SD-FEC) bit rate	
$R_s$ symbol rate	



# Bibliography

- [1] “Cisco Annual Internet Report (2018–2023) White Paper,” Mar. 2020. [Online] <https://www.cisco.com/c/en/us/solutions/collateral/executive-perspectives/annual-internet-report/white-paper-c11-741490.pdf>.
- [2] “Telegeography Global Internet Map 2021,” 2021. [Online] <https://global-internet-map-2021.telegeography.com/>.
- [3] G. P. Agrawal, *Fiber-Optic Communications Systems, Third Edition*. Wiley & Sons, 2002.
- [4] P. J. Winzer, D. T. Neilson, and A. R. Chraplyvy, “Fiber-optic transmission and networking: the previous 20 and the next 20 years [Invited],” *Optics Express*, vol. 26, pp. 24190–24239, Sept. 2018.
- [5] S. Zhang, F. Yaman, Y.-K. Huang, J. D. Downie, D. Zou, W. A. Wood, A. Zakharian, R. Khrapko, S. Mishra, V. Nazarov, J. Hurley, I. B. Djordjevic, E. Mateo, and Y. Inada, “Capacity-approaching transmission over 6375 km at spectral efficiency of 8.3 bit/s/Hz,” in *2016 Optical Fiber Communications Conference and Exhibition (OFC)*, pp. 1–3, Mar. 2016.
- [6] A. Ghazisaeidi, I. F. de Jauregui Ruiz, R. Rios-Muller, L. Schmalen, P. Tran, P. Brindel, A. C. Meseguer, Q. Hu, F. Buchali, G. Charlet, and J. Renaudier, “65Tb/s transoceanic transmission using probabilistically-shaped PDM-64QAM,” in *European Conference on Optical Communication*, pp. 1–3, 2016.
- [7] J.-X. Cai, H. G. Batshon, M. Mazurczyk, O. V. Sinkin, D. Wang, M. Paskov, W. Patterson, C. Davidson, P. Corbett, G. Wolter, T. Hammon, M. A. Bolshtyansky, D. Foursa, and A. Pilipetskii, “70.4 Tb/s Capacity over 7,600 km in C+L Band Using Coded Modulation with Hybrid Constellation Shaping and Nonlinearity Compensation,” in *2017 Optical Fiber Communications Conference and Exhibition (OFC)*, p. Th5B.2, 2017.
- [8] T. Drenski and J. C. Rasmussen, “ADC/DAC and ASIC technology trends,” in *24th OptoElectronics and Communications Conference (OECC) and International Conference on Photonics in Switching and Computing (PSC)*, pp. 1–3, July 2019.
- [9] “The 2020 Ethernet roadmap,” 2020. [Online] <https://ethernetalliance.org/technology/2020-roadmap/>.
- [10] “OIF Implementation Agreement 400ZR,” 2020. [Online] [https://www.oiforum.com/wp-content/uploads/OIF-400ZR-01.0\\_reduced2.pdf](https://www.oiforum.com/wp-content/uploads/OIF-400ZR-01.0_reduced2.pdf).
- [11] “OMDIA Optical Networks Analyst Call - 4Q20,” 2020. [Online] <https://omdia.tech.informa.com/OM018722/Optical-Networks-Analyst-Call-4Q20>.
- [12] C. E. Shannon, “A Mathematical Theory of Communication,” *The Bell System Technical Journal*, vol. 27, no. 3, pp. 379–423, 1948.
- [13] J. Proakis, *Digital Communications*. McGraw-Hill, 2001.
- [14] ITU-T, “G.652 - Characteristics of a single-mode optical fibre and cable,” Nov. 2016.

- [15] ITU-T, “G.654 - Characteristics of a cut-off shifted single-mode optical fibre and cable,” Mar. 2020.
- [16] ITU-T, “G.651.1 - Characteristics of a 50/125  $\mu\text{m}$  multimode graded index optical fibre cable for the optical access network,” Nov. 2018.
- [17] M. C. Fugihara and A. Nolasco Pinto, “Attenuation fitting functions,” *Microwave and Optical Technology Letters*, 2009.
- [18] G. P. Agrawal, *Nonlinear fiber optics, Third Edition*. Academic press, 2002.
- [19] A. Splett, C. Kurtzke, and K. Petermann, “Ultimate Transmission Capacity of Amplified Optical Fiber Communication Systems taking into Account Fiber Nonlinearities,” in *European Conference on Optical Communication*, p. MoC2.4, 1993.
- [20] J. Tang, “The Channel Capacity of a Multispan DWDM System Employing Dispersive Nonlinear Optical Fibers and an Ideal Coherent Optical Receiver,” *Journal of Lightwave Technology*, vol. 20, no. 7, pp. 1095–1101, 2002.
- [21] X. Chen and W. Shieh, “Closed-form expressions for nonlinear transmission performance of densely spaced coherent optical OFDM systems,” *Optics Express*, vol. 18, no. 18, 2010.
- [22] P. Poggiolini, A. Carena, V. Curri, G. Bosco, and F. Forghieri, “Analytical Modeling of Nonlinear Propagation in Uncompensated Optical Transmission Links,” *IEEE Photonics Technology Letters*, vol. 23, no. 11, pp. 472–744, 2011.
- [23] A. Carena, V. Curri, G. Bosco, P. Poggiolini, and F. Forghieri, “Modeling of the Impact of Nonlinear Propagation Effects in Uncompensated Optical Coherent Transmission Links,” *Journal of Lightwave Technology*, vol. 30, no. 10, pp. 1524–1539, 2012.
- [24] P. Poggiolini, G. Bosco, A. Carena, V. Curri, Y. Jiang, and F. Forghieri, “The GN-model of fiber non-linear propagation and its applications,” *Journal of Lightwave Technology*, vol. 32, no. 4, pp. 694–721, 2014.
- [25] A. Mecozzi and R.-J. Essiambre, “Nonlinear Shannon Limit in Pseudolinear Coherent Systems,” *Journal of Lightwave Technology*, vol. 30, no. 12, pp. 2011–2024, 2012.
- [26] R. Dar, M. Feder, A. Mecozzi, and M. Shtaif, “Properties of nonlinear noise in long, dispersion-uncompensated fiber links,” *Optics Express*, vol. 21, pp. 25685–25699, Nov. 2013.
- [27] A. Carena, G. Bosco, V. Curri, Y. Jiang, P. Poggiolini, and F. Forghieri, “EGN model of non-linear fiber propagation,” *Optics Express*, vol. 22, pp. 16335–16362, June 2014.
- [28] L. Beygi, N. V. Irukulapati, E. Agrell, P. Johannisson, M. Karlsson, H. Wymeersch, P. Serena, and A. Bononi, “On nonlinearly-induced noise in single-channel optical links with digital backpropagation,” *Optics Express*, vol. 21, pp. 26376–26386, Nov. 2013.
- [29] P. Serena, “Nonlinear Signal–Noise Interaction in Optical Links With Nonlinear Equalization,” *Journal of Lightwave Technology*, vol. 34, pp. 1476–1483, Mar. 2016.
- [30] A. Ghazisaeidi, “A Theory of Nonlinear Interactions Between Signal and Amplified Spontaneous Emission Noise in Coherent Wavelength Division Multiplexed Systems,” *Journal of Lightwave Technology*, vol. 35, pp. 5150–5175, Dec. 2017.

- 
- [31] R. H. Stolen, E. P. Ippen, and A. R. Tynes, "Raman Oscillation in Glass Optical Waveguide," *Applied Physics Letters*, vol. 20, no. 2, p. 62, 1972.
- [32] G. Saavedra, D. Semrau, M. Tan, M. A. Iqbal, D. J. Elson, L. Galdino, P. Harper, R. I. Killely, and P. Bayvel, "Inter-channel Stimulated Raman Scattering and its Impact in Wideband Transmission Systems," in *2018 Optical Fiber Communications Conference and Exposition (OFC)*, p. Th1C.3, Mar. 2018.
- [33] K. Minoguchi, S. Okamoto, F. Hamaoka, A. Matsushita, M. Nakamura, E. Yamazaki, and Y. Kisaka, "Experiments on Stimulated Raman Scattering in S- and L-bands 16-QAM Signals for Ultra-Wideband Coherent WDM Systems," in *2018 Optical Fiber Communications Conference and Exposition (OFC)*, pp. 1–3, Mar. 2018.
- [34] A. Chraplyvy, "Limitations on lightwave communications imposed by optical-fiber nonlinearities," *Journal of Lightwave Technology*, vol. 8, pp. 1548–1557, Oct. 1990.
- [35] D. Semrau, R. I. Killely, and P. Bayvel, "The Gaussian Noise Model in the Presence of Inter-Channel Stimulated Raman Scattering," *Journal of Lightwave Technology*, vol. 36, pp. 3046–3055, July 2018.
- [36] A. R. Chraplyvy, J. A. Nagel, and R. W. Tkach, "Equalization in amplified WDM lightwave transmission systems," *IEEE Photonics Technology Letters*, vol. 4, pp. 920–922, Aug. 1992.
- [37] J. P. Gordon and H. Kogelnik, "PMD fundamentals: Polarization mode dispersion in optical fibers," *Proceedings of the National Academy of Sciences of the United States of America*, vol. 97, no. 9, pp. 4541–4550, 2000.
- [38] G. V. d. Faria, M. R. Jimenez, and J. P. v. d. Weid, "PMD variations from factory to field in OPGW cabled fibers," *IEEE Photonics Technology Letters*, vol. 18, pp. 250–252, Jan. 2006.
- [39] S. Abbott, "Review of 20 years of undersea optical fiber transmission system development and deployment since TAT-8," in *2008 34th European Conference on Optical Communication*, pp. 1–4, Sept. 2008.
- [40] R. J. Mears, L. Reekie, I. M. Jauncey, and D. N. Payne, "Low-noise erbium-doped fibre amplifier operating at 1.54 $\mu\text{m}$ ," *Electronics Letters*, vol. 23, no. 19, pp. 1026–1028, 1987.
- [41] E. Desurvire, J. R. Simpson, and P. C. Becker, "High-gain erbium-doped traveling-wave fiber amplifier," *Optics Letters*, vol. 12, pp. 888–890, Nov. 1987.
- [42] E. Desurvire, D. Bayart, B. Desthieux, and S. Bigo, *Erbium-Doped Fiber Amplifiers - Device and System Developments*. Wiley & Sons, 2002.
- [43] H. T. Friis, "Noise Figures of Radio Receivers," *Proceedings of the IRE*, vol. 32, pp. 419–422, July 1944.
- [44] H. A. Haus, "The noise figure of optical amplifiers," *IEEE Photonics Technology Letters*, vol. 10, pp. 1602–1604, Nov. 1998.
- [45] J. Bromage, "Raman amplification for fiber communications systems," *Journal of Lightwave Technology*, vol. 22, pp. 79–93, Jan. 2004.
- [46] C. Headley and G. P. Agrawal, *Raman Amplification in Fiber Optical Communication Systems*. Elsevier Academic Press, 2005.

- [47] K. Kikuchi, "Fundamentals of coherent optical fiber communications," *Journal of Lightwave Technology*, vol. 34, no. 1, pp. 157–179, 2016.
- [48] R.-J. Essiambre, G. Kramer, P. J. Winzer, G. J. Foschini, and B. Goebel, "Capacity limits of optical fiber networks," *Journal of Lightwave Technology*, vol. 28, no. 4, pp. 662–701, 2010.
- [49] S. J. Savory, "Digital filters for coherent optical receivers," *Optics Express*, vol. 16, no. 2, pp. 804–817, 2008.
- [50] T. Xu, G. Jacobsen, S. Popov, M. Forzati, J. Martensson, J. Li, K. Wang, Y. Zhang, and A. T. Friberg, "Frequency-Domain Chromatic Dispersion Equalization Using Overlap-Add Methods in Coherent Optical System," *Journal of Optical Communications*, vol. 32, no. 2, pp. 131–135, 2011.
- [51] F. N. Hauske, M. Kuschnerov, B. Spinnler, and B. Lankl, "Optical performance monitoring in digital coherent receivers," *Journal of Lightwave Technology*, vol. 27, no. 16, pp. 3623–3631, 2009.
- [52] D. Godard, "Self-recovering equalization and carrier tracking in two-dimensional data communication systems," *IEEE Transactions on Communications*, vol. 28, no. 11, pp. 1867–1875, 1980.
- [53] W. Sethares, G. Rey, and C. Johnson, "Approaches to blind equalization of signals with multiple modulus," in *International Conference on Acoustics, Speech, and Signal Processing*, pp. 972–975 vol.2, 1989.
- [54] M. Selmi, C. Gosset, M. Noelle, P. Ciblat, and Y. Jaouen, "Block-Wise Digital Signal Processing for PolMux QAM/PSK Optical Coherent Systems," *Journal of Lightwave Technology*, vol. 29, pp. 3070–3082, Oct. 2011.
- [55] T. Pfau, S. Hoffmann, and R. Noé, "Hardware-efficient coherent digital receiver concept with feedforward carrier recovery for M-QAM constellations," *Journal of Lightwave Technology*, vol. 27, no. 8, pp. 989–999, 2009.
- [56] E. Ip and J. M. Kahn, "Compensation of Dispersion and Nonlinear Impairments Using Digital Backpropagation," *Journal of Lightwave Technology*, vol. 26, pp. 3416–3425, Oct. 2008.
- [57] K. Roberts, C. Li, L. Strawczynski, M. O'Sullivan, and I. Hardcastle, "Electronic precompensation of optical nonlinearity," *IEEE Photonics Technology Letters*, vol. 18, pp. 403–405, Jan. 2006.
- [58] D. Lavery, D. Ives, G. Liga, A. Alvarado, S. J. Savory, and P. Bayvel, "The Benefit of Split Nonlinearity Compensation for Single-Channel Optical Fiber Communications," *IEEE Photonics Technology Letters*, vol. 28, pp. 1803–1806, Sept. 2016.
- [59] L. B. Du and A. J. Lowery, "Improved single channel backpropagation for intra-channel fiber nonlinearity compensation in long-haul optical communication systems," *Optics Express*, vol. 18, pp. 17075–17088, Aug. 2010.
- [60] A. Ghazisaeidi and R.-J. Essiambre, "Calculation of Coefficients of Perturbative Nonlinear Pre-Compensation for Nyquist Pulses," in *European Conference on Optical Communication*, p. We.1.3.3, 2014.
- [61] I. Fernandez de Jauregui Ruiz, A. Ghazisaeidi, O. A. Sab, P. Plantady, A. Calsat, S. Dubost, L. Schmalen, V. Letellier, and J. Renaudier, "25.4-Tb/s Transmission Over Transpacific Distances Using Truncated Probabilistically Shaped PDM-64QAM," *Journal of Lightwave Technology*, vol. 36, pp. 1354–1361, Mar. 2018.

- 
- [62] T. Mizuochi, "Next Generation FEC for Optical Communication," in *OFC/NFOEC*, p. OTuE5, Feb. 2008.
- [63] A. Leven and L. Schmalen, "Status and Recent Advances on Forward Error Correction Technologies for Lightwave Systems," *Journal of Lightwave Technology*, vol. 32, pp. 2735–2750, Aug. 2014.
- [64] A. Alvarado and E. Agrell, "Four-Dimensional Coded Modulation with Bit-Wise Decoders for Future Optical Communications," *Journal of Lightwave Technology*, vol. 33, pp. 1993–2003, May 2015.
- [65] ITU-T, "G.975 - Forward error correction for submarine systems," Oct. 2000.
- [66] ITU-T, "G.975.1 - Forward error correction for high bit-rate DWDM submarine systems," Feb. 2004.
- [67] O. Ait Sab and V. Lemaire, "Block Turbo Code Performance for long-haul DWDM optical transmission systems," in *Optical Fiber Communication Conference*, p. ThS5, Mar. 2000.
- [68] L. Schmalen, V. Aref, J. Cho, D. Suikat, D. Rösener, and A. Leven, "Spatially Coupled Soft-Decision Error Correction for Future Lightwave Systems," *Journal of Lightwave Technology*, vol. 33, pp. 1109–1116, Mar. 2015.
- [69] A. Alvarado, E. Agrell, D. Lavery, R. Maher, and P. Bayvel, "Replacing the Soft-Decision FEC Limit Paradigm in the Design of Optical Communication Systems," *Journal of Lightwave Technology*, vol. 34, pp. 707–721, Jan. 2016.
- [70] J. Cho, L. Schmalen, and P. J. Winzer, "Normalized Generalized Mutual Information as a Forward Error Correction Threshold for Probabilistically Shaped QAM," in *2017 European Conference on Optical Communication (ECOC)*, pp. 1–3, Sept. 2017.
- [71] G. Böcherer, P. Schulte, and F. Steiner, "Probabilistic Shaping and Forward Error Correction for Fiber-Optic Communication Systems," *Journal of Lightwave Technology*, vol. 37, no. 2, pp. 230–244, 2019.
- [72] J. Cho and P. J. Winzer, "Probabilistic Constellation Shaping for Optical Fiber Communications," *Journal of Lightwave Technology*, vol. 37, pp. 1590–1607, Mar. 2019.
- [73] G. Böcherer, F. Steiner, and P. Schulte, "Bandwidth Efficient and Rate-Matched Low-Density Parity-Check Coded Modulation," *IEEE Transactions on Communications*, vol. 63, pp. 4651–4665, Dec. 2015.
- [74] F. Buchali, F. Steiner, G. Böcherer, L. Schmalen, P. Schulte, and W. Idler, "Rate Adaptation and Reach Increase by Probabilistically Shaped 64-QAM: An Experimental Demonstration," *Journal of Lightwave Technology*, vol. 34, pp. 1599–1609, Apr. 2016.
- [75] G. Charlet, M. Salsi, P. Tran, M. Bertolini, H. Mardoyan, J. Renaudier, O. Bertran-Pardo, and S. Bigo, "72×100Gb/s transmission over transoceanic distance, using large effective area fiber, hybrid Raman-Erbium amplification and coherent detection," in *Optical Fiber Communication Conference and National Fiber Optic Engineers Conference (2009)*, p. PDPB6, Optical Society of America, Mar. 2009.
- [76] T. Zami, B. Lavigne, O. B. Pardo, S. Weisser, J. David, M. L. Monnier, and J.-P. Faure, "31.2-Tb/s real time bidirectional transmission of 78x400 Gb/s interleaved channels over C band of one 90-km SMF span," in *2018 Optical Fiber Communications Conference and Exposition (OFC)*, p. W1B.5, Optical Society of America, Mar. 2018.

- [77] H.-C. Chien, J. Yu, B. Zhu, J. Shi, Y. Cai, X. Xiao, Y. Xia, X. Wei, and Y. Chen, "Probabilistically Shaped DP-64QAM Coherent Optics at 105 Gbd Achieving 900 Gbps Net Bit Rate per Carrier over 800 km Transmission," in *2018 European Conference on Optical Communication (ECOC)*, pp. 1–3, Sept. 2018.
- [78] F. Pittalà, M. Schaedler, C. Bluemm, G. Goeger, S. Calabrò, M. Kuschnerov, and C. Xie, "800ZR+ DWDM Demonstration over 600km G.654D Fiber Enabled by Adaptive Nonlinear TripleX Equalization," in *2020 Optical Fiber Communications Conference and Exhibition (OFC)*, p. M4K.5, Mar. 2020.
- [79] H. Sun, M. Torbatian, M. Karimi, R. Maher, S. Thomson, M. Tehrani, Y. Gao, A. Kumpera, G. Soliman, A. Kakkar, M. Osman, Z. A. El-Sahn, C. Doggart, W. Hou, S. Sutarwala, Y. Wu, M. R. Chitgarha, V. Lal, H.-S. Tsai, S. Corzine, J. Zhang, J. Osenbach, S. Buggaveeti, Z. Morbi, M. I. Olmedo, I. Leung, X. Xu, P. Samra, V. Dominic, S. Sanders, M. Ziari, A. Napoli, B. Spinnler, K.-T. Wu, and P. Kandappan, "800G DSP ASIC Design Using Probabilistic Shaping and Digital Sub-Carrier Multiplexing," *Journal of Lightwave Technology*, vol. 38, pp. 4744–4756, Sept. 2020.
- [80] F. Buchali, V. Lauinger, M. Chagnon, K. Schuh, and V. Aref, "1.1 Tb/s/ $\lambda$  at 9.8 bit/s/Hz DWDM transmission over DCI distances supported by CMOS DACs," in *2020 Optical Fiber Communications Conference and Exhibition (OFC)*, p. Th3E.2, Optical Society of America, Mar. 2020.
- [81] G. Raybon, S. Randel, A. Adamiecki, P. J. Winzer, L. Salamanca, R. Urbanke, S. Chandrasekhar, A. Konczykowska, F. Jorge, J. Dupuy, L. L. Buhl, S. Draving, M. Grove, and K. Rush, "1-Tb/s dual-carrier 80-GBaud PDM-16QAM WDM transmission at 5.2 b/s/Hz over 3200 km," in *IEEE Photonics Conference 2012*, pp. 1–2, Sept. 2012.
- [82] J. Renaudier, R. Rios-Muller, L. Schmalen, M. Salsi, P. Tran, G. Charlet, and S. Bigo, "1-Tb/s transceiver spanning over just three 50-GHz frequency slots for long-haul systems," in *39th European Conference and Exhibition on Optical Communication (ECOC 2013)*, pp. 1–3, Sept. 2013.
- [83] M. Yoshida, T. Hirooka, and M. Nakazawa, "Ultrahigh-Speed Nyquist Pulse Transmission Beyond 10 Tbit/s," *IEEE Journal of Selected Topics in Quantum Electronics*, vol. 27, pp. 1–12, Mar. 2021.
- [84] R. Rios-Müller, J. Renaudier, P. Brindel, H. Mardoyan, P. Jennevé, L. Schmalen, and G. Charlet, "1-Terabit/s Net Data-Rate Transceiver Based on Single-Carrier Nyquist-Shaped 124 GBaud PDM-32QAM," in *2015 Optical Fiber Communications Conference and Exhibition (OFC)*, p. Th5B.1, Mar. 2015.
- [85] G. Raybon, A. Adamiecki, J. Cho, P. Winzer, A. Konczykowska, F. Jorge, J. Dupuy, M. Riet, B. Duval, K. Kim, S. Randel, D. Pileri, B. Guan, N. Fontaine, and E. C. Burrows, "Single-carrier all-ETDM 1.08-Terabit/s line rate PDM-64-QAM transmitter using a high-speed 3-bit multiplexing DAC," in *2015 IEEE Photonics Conference (IPC)*, pp. 1–2, Oct. 2015.
- [86] J. Zhang, J. Zhang, J. Yu, J. Yu, B. Zhu, Z. Jia, F. Li, X. Li, H.-C. Chien, S. Shi, C. Ge, Y. Xia, and Y. Chen, "WDM Transmission of Twelve 960 Gb/s Channels based on 120-GBaud ETDM PDM-16QAM over 1200-km TeraWave™ Fiber Link," in *2016 Optical Fiber Communications Conference and Exhibition (OFC)*, p. Tu3A.2, Mar. 2016.
- [87] X. Chen, S. Chandrasekhar, G. Raybon, S. Olsson, J. Cho, A. Adamiecki, and P. Winzer, "Generation and Intradyne Detection of Single-Wavelength 1.61-Tb/s

- Using an All-Electronic Digital Band Interleaved Transmitter,” in *2018 Optical Fiber Communications Conference and Exposition (OFC)*, p. Th4C.1, Mar. 2018.
- [88] M. Nakamura, F. Hamaoka, M. Nagatani, H. Yamazaki, T. Kobayashi, A. Matsushita, S. Okamoto, H. Wakita, H. Nosaka, and Y. Miyamoto, “1.04 Tbps/Carrier Probabilistically Shaped PDM-64QAM WDM Transmission Over 240 km Based on Electrical Spectrum Synthesis,” in *2019 Optical Fiber Communications Conference and Exhibition (OFC)*, pp. 1–3, Mar. 2019.
- [89] M. Nakamura, F. Hamaoka, M. Nagatani, Y. Ogiso, H. Wakita, H. Yamazaki, T. Kobayashi, M. Ida, H. Nosaka, and Y. Miyamoto, “192-Gbaud Signal Generation using Ultra-Broadband Optical Frontend Module Integrated with Bandwidth Multiplexing Function,” in *2019 Optical Fiber Communications Conference and Exhibition (OFC)*, pp. 1–3, Mar. 2019.
- [90] X. Chen, J. Cho, G. Raybon, D. Che, K. W. Kim, E. Burrows, P. Kharel, C. Reimer, K. Luke, L. He, and M. Zhang, “Single-Wavelength and Single-Photodiode 700 Gb/s Entropy-Loaded PS-256-QAM and 200-GBaud PS-PAM-16 Transmission over 10-km SMF,” in *2020 European Conference on Optical Communications (ECOC)*, pp. 1–4, Dec. 2020.
- [91] F. Pittalà, M. Schaedler, G. Khanna, S. Calabrò, M. Kushnerov, C. Xie, Z. Ye, Q. Wang, and B. Zheng, “220 GBaud Signal Generation Enabled by a Two-channel 256 GSa/s Arbitrary Waveform Generator and Advanced DSP,” in *2020 European Conference on Optical Communications (ECOC)*, pp. 1–4, Dec. 2020.
- [92] K. Schuh, F. Buchali, W. Idler, T. A. Eriksson, L. Schmalen, W. Templ, L. Altenhain, U. Dümmler, R. Schmid, M. Möller, and K. Engenhardt, “Single Carrier 1.2 Tbit/s Transmission over 300 km with PM-64 QAM at 100 GBaud,” in *2017 Optical Fiber Communications Conference and Exhibition (OFC)*, p. Th5B.5, Mar. 2017.
- [93] V. Bajaj, F. Buchali, M. Chagnon, S. Wahls, and V. Aref, “Single-channel 1.61 Tb/s Optical Coherent Transmission Enabled by Neural Network-Based Digital Pre-Distortion,” in *2020 European Conference on Optical Communications (ECOC)*, pp. 1–4, Dec. 2020.
- [94] M. Nakamura, A. Matsushita, S. Okamoto, F. Hamaoka, and Y. Kisaka, “Spectrally Efficient 800 Gbps/Carrier WDM Transmission with 100-GHz Spacing Using Probabilistically Shaped PDM-256QAM,” in *2018 European Conference on Optical Communication (ECOC)*, pp. 1–3, Sept. 2018.
- [95] A. Matsushita, M. Nakamura, F. Hamaoka, and Y. Kisaka, “41-Tbps C-band transmission with 10-bps/Hz spectral efficiency using 1-Tbps 96-GBd PS-256QAM for DCI,” in *45th European Conference on Optical Communication (ECOC 2019)*, pp. 1–3, Sept. 2019.
- [96] A. Matsushita, M. Nakamura, K. Horikoshi, S. Okamoto, F. Hamaoka, and Y. Kisaka, “64-GBd PDM-256QAM and 92-GBd PDM-64QAM Signal Generation using Precise-Digital-Calibration aided by Optical-Equalization,” in *2019 Optical Fiber Communications Conference and Exhibition (OFC)*, p. W4B.2, Mar. 2019.
- [97] J. Lin, H. Sepehrian, L. A. Rusch, and W. Shi, “Single-carrier 72 GBaud 32QAM and 84 GBaud 16QAM transmission using a SiP IQ modulator with joint digital-optical pre-compensation,” *Optics Express*, vol. 27, pp. 5610–5619, Feb. 2019. Publisher: Optical Society of America.

- [98] R. Rios-Müller, J. Renaudier, P. Brindel, A. Ghazisaeidi, I. Fernandez, P. Tran, C. Simonneau, L. Schmalen, and G. Charlet, “Spectrally-Efficient 400-Gb/s Single Carrier Transport Over 7 200 km,” *Journal of Lightwave Technology*, vol. 33, pp. 1402–1407, Apr. 2015. Publisher: IEEE.
- [99] F. Buchali, M. Chagnon, K. Schuh, and V. Lauinger, “Beyond 100 GBaud transmission supported by a 120 GSa/s CMOS digital to analog converter,” in *European Conference and Exhibition on Optical Communications (ECOC)*, Jan. 2019.
- [100] A. Ghazisaeidi, I. Fernandez de Jauregui Ruiz, R. Rios-Müller, L. Schmalen, P. Tran, P. Brindel, A. Carbo Meseguer, Q. Hu, F. Buchali, G. Charlet, and J. Renaudier, “Advanced C+L-Band Transoceanic Transmission Systems Based on Probabilistically Shaped PDM-64QAM,” *Journal of Lightwave Technology*, vol. 35, pp. 1291–1299, Apr. 2017.
- [101] J. Cho, X. Chen, S. Chandrasekhar, G. Raybon, R. Dar, L. Schmalen, E. Burrows, A. Adamiecki, S. Corteselli, Y. Pan, D. Correa, B. McKay, S. Zsigmond, P. Winzer, and S. Grubb, “Trans-Atlantic field trial using probabilistically shaped 64-QAM at high spectral efficiencies and single-carrier real-time 250-Gb/s 16-QAM,” in *2017 Optical Fiber Communications Conference and Exhibition (OFC)*, pp. 1–3, Mar. 2017.
- [102] V. Kamalov, L. Jovanovski, V. Vusirikala, S. Zhang, F. Yaman, K. Nakamura, T. Inoue, E. Mateo, and Y. Inada, “Evolution from 8QAM live traffic to PS 64-QAM with Neural-Network Based Nonlinearity Compensation on 11000 km Open Subsea Cable,” in *2018 Optical Fiber Communications Conference and Exposition (OFC)*, pp. 1–3, Mar. 2018.
- [103] R. Dar, P. J. Winzer, A. R. Chraplyvy, S. Zsigmond, K. Huang, H. Fevrier, and S. Grubb, “Cost-Optimized Submarine Cables Using Massive Spatial Parallelism,” *Journal of Lightwave Technology*, vol. 36, pp. 3855–3865, Sept. 2018.
- [104] O. V. Sinkin, A. V. Turukhin, Y. Sun, H. G. Batshon, M. V. Mazurczyk, C. R. Davidson, J. Cai, W. W. Patterson, M. A. Bolshtyansky, D. G. Foursa, and A. N. Pilipetskii, “SDM for Power-Efficient Undersea Transmission,” *Journal of Lightwave Technology*, vol. 36, pp. 361–371, Jan. 2018.
- [105] P. Pecci, L. Jovanovski, M. Barezani, V. Kamalov, J. F. Marcerou, M. Cantono, M. Grumier, O. Courtois, and V. Vusirikala, “Pump farming as enabling factor to increase subsea cable capacity,” in *SubOptic*, 2019.
- [106] “Nokia 1830 PSS,” 2020. [Online] <https://www.nokia.com/networks/products/1830-photonic-service-switch/>.
- [107] E. Rivera Hartling, A. Pilipetskii, D. Evans, E. Mateo, M. Salsi, P. Pecci, and P. Mehta, “Design, Acceptance and Capacity of Subsea Open Cables,” *Journal of Lightwave Technology*, vol. 39, pp. 742–756, Feb. 2021.
- [108] W. Shieh and K.-P. Ho, “Equalization-enhanced phase noise for coherent-detection systems using electronic digital signal processing,” *Optics Express*, vol. 16, no. 20, pp. 15718–15727, 2008.
- [109] A. Kakkar, J. R. Navarro, R. Schatz, H. Louchet, X. Pang, O. Ozolins, G. Jacobsen, and S. Popov, “Comprehensive Study of Equalization-Enhanced Phase Noise in Coherent Optical Systems,” *Journal of Lightwave Technology*, vol. 33, pp. 4834–4841, Dec. 2015.

- [110] C. Xie, "Local oscillator phase noise induced penalties in optical coherent detection systems using electronic chromatic dispersion compensation," in *2009 Conference on Optical Fiber Communication*, pp. 1–3, 2009.
- [111] I. Fatadin and S. J. Savory, "Impact of phase to amplitude noise conversion in coherent optical systems with digital dispersion compensation," *Optics Express*, vol. 18, pp. 16273–16278, July 2010.
- [112] R. Farhodi, A. Ghazisaeidi, and L. A. Rusch, "Performance of carrier phase recovery for electronically dispersion compensated coherent systems," *Optics Express*, vol. 20, pp. 26568–26582, Nov. 2012.
- [113] X. Zhou and L. Nelson, "Advanced DSP for 400 Gb/s and Beyond Optical Networks," *Journal of Lightwave Technology*, vol. 32, pp. 2716–2725, Aug. 2014.
- [114] A. Kakkar, R. Schatz, X. Pang, J. R. Navarro, H. Louchet, O. Ozolins, G. Jacobsen, and S. Popov, "Impact of local oscillator frequency noise on coherent optical systems with electronic dispersion compensation," *Optics Express*, vol. 23, pp. 11221–11226, May 2015.
- [115] A. Kakkar, J. R. Navarro, R. Schatz, X. Pang, O. Ozolins, H. Louchet, G. Jacobsen, and S. Popov, "Mitigation of EEPN in Coherent Optical Systems With Low-Speed Digital Coherence Enhancement," *IEEE Photonics Technology Letters*, vol. 27, pp. 1942–1945, Sept. 2015.
- [116] G. Colavolpe, T. Foggi, E. Forestieri, and M. Secondini, "Impact of Phase Noise and Compensation Techniques in Coherent Optical Systems," *Journal of Lightwave Technology*, vol. 29, pp. 2790–2800, Sept. 2011.
- [117] O. Ait Sab, A. Ghazisaeidi, P. Plantady, A. Calsat, I. F. d. J. Ruiz, S. Dubost, P. Pecci, J. Renaudier, and V. Letellier, "376 Pb/s×km Transmission Record over 13,419km Using TPCS-64QAM and C-Band EDFA-Only," in *Asia Communications and Photonics Conference*, p. Su2B.2, Nov. 2017.
- [118] F. Buchali, K. Schuh, R. Dischler, M. Chagnon, V. Aref, H. Buelow, Q. Hu, F. Pulka, M. Frascolla, E. Alhammedi, A. Samhan, I. Younis, M. El-Zonkoli, and P. Winzer, "1.3-Tb/s single-channel and 50.8-Tb/s WDM transmission over field-deployed fiber," in *45th European Conference on Optical Communication (ECOC)*, pp. 1–4, Sept. 2019.
- [119] A. Sano, T. Kobayashi, S. Yamanaka, A. Matsuura, H. Kawakami, Y. Miyamoto, K. Ishihara, and H. Masuda, "102.3-Tb/s ( $224 \times 548$ -Gb/s) C- and Extended L-band All-Raman Transmission over 240 km Using PDM-64QAM Single Carrier FDM with Digital Pilot Tone," in *OFC/NFOEC*, p. PDP5C.3, Mar. 2012.
- [120] M. Ionescu, L. Galdino, A. Edwards, J. James, W. Pelouch, E. Sillekens, D. Semrau, D. Lavery, R. I. Killey, S. Barnes, P. Bayvel, and S. Desbruslais, "91 nm C+L Hybrid Distributed Raman–Erbium-Doped Fibre Amplifier for High Capacity Subsea Transmission," in *2018 European Conference on Optical Communication (ECOC)*, pp. 1–3, Sept. 2018.
- [121] M. Ionescu, D. Lavery, A. Edwards, E. Sillekens, L. Galdino, D. Semrau, R. I. Killey, W. Pelouch, S. Barnes, and P. Bayvel, "74.38 Tb/s Transmission Over 6300 km Single Mode Fiber with Hybrid EDFA/Raman Amplifiers," in *2019 Optical Fiber Communications Conference and Exhibition (OFC)*, p. Tu3F.3, Mar. 2019.

- [122] J. Renaudier, A. C. Meseguer, A. Ghazisaeidi, P. Tran, R. R. Muller, R. Brenot, A. Verdier, F. Blache, K. Mekhazni, B. Duval, and others, "First 100-nm continuous-band WDM transmission system with 115Tb/s transport over 100km using novel ultra-wideband semiconductor optical amplifiers," in *2017 European Conference on Optical Communication (ECOC)*, pp. 1–3, 2017.
- [123] J. Renaudier, A. C. Meseguer, A. Ghazisaeidi, P. Brindel, P. Tran, A. Verdier, F. Blache, M. Makhsian, K. Mekhazni, C. Calo, H. Debregeas, F. Pulka, J. Suignard, A. Boutin, N. Fontaine, D. Neilson, R. Ryf, H. Chen, R. Dellinger, S. Grubb, M. Achouche, and G. Charlet, "Field Trial of 100nm Ultra-Wideband Optical Transport with 42GBd 16QAM Real-Time and 64GBd PCS64QAM Channels," in *2018 European Conference on Optical Communication (ECOC)*, pp. 1–3, Sept. 2018.
- [124] T. Akiyama, M. Ekawa, M. Sugawara, H. Sudo, K. Kawaguchi, A. Kuramata, H. Ebe, K. Morito, H. Imai, and Y. Arakawa, "An ultrawide-band (120 nm) semiconductor optical amplifier having an extremely-high penalty-free output power of 23 dBm realized with quantum-dot active layers," in *Optical Fiber Communication Conference, 2004*, Feb. 2004.
- [125] "SOA1117S - C-Band Semiconductor Optical Amplifier." [Online] <https://www.thorlabs.com/thorproduct.cfm?partnumber=SOA1117S>.
- [126] G. Agrawal and N. Olsson, "Self-phase modulation and spectral broadening of optical pulses in semiconductor laser amplifiers," *IEEE Journal of Quantum Electronics*, vol. 25, pp. 2297–2306, Nov. 1989.
- [127] A. Ghazisaeidi, "Theory of Coherent WDM Systems Using In-Line Semiconductor Optical Amplifiers," *Journal of Lightwave Technology*, vol. 37, pp. 4188–4200, Sept. 2019.
- [128] J. Renaudier and A. Ghazisaeidi, "Scaling Capacity Growth of Fiber-Optic Transmission Systems Using 100+nm Ultra-Wideband Semiconductor Optical Amplifiers," *Journal of Lightwave Technology*, vol. 37, pp. 1831–1838, Apr. 2019.
- [129] J. Renaudier, A. Arnould, A. Ghazisaeidi, D. L. Gac, P. Brindel, E. Awwad, M. Makhsian, K. Mekhazni, F. Blache, A. Boutin, L. Letteron, Y. Frignac, N. Fontaine, D. Neilson, and M. Achouche, "Recent Advances in 100+nm Ultra-Wideband Fiber-Optic Transmission Systems Using Semiconductor Optical Amplifiers," *Journal of Lightwave Technology*, vol. 38, pp. 1071–1079, Mar. 2020.
- [130] N. K. Fontaine, R. Ryf, D. T. Neilson, and H. Chen, "Low Loss Wavelength Selective Switch with 15-THz Bandwidth," in *2018 European Conference on Optical Communication (ECOC)*, pp. 1–3, Sept. 2018.
- [131] F. Boubal, E. Brandon, L. Buet, S. Chernikov, V. Havard, C. Heerdt, A. Hugbart, W. Idler, L. Labrunie, P. Le Roux, S. Lewis, A. Pham, L. Piriou, R. Uhel, and J.-P. Blondel, "4.16 Tbit/s (104 × 40 Gbit/s) unrepeated transmission over 135 km in S+C+L bands with 104 nm total bandwidth," in *27th European Conference on Optical Communication (ECOC)*, pp. 58–59 vol.1, Sept. 2001.
- [132] D.-i. Chang, W. Pelouch, P. Perrier, H. Fevrier, S. Ten, C. Towery, and S. Makovejs, "15 Tb/s Unrepeated Transmission over 409.6 km using Distributed Raman Amplification and ROPA," in *Asia Communications and Photonics Conference*, p. AF4B.4, Nov. 2014.
- [133] H. Bissessur, C. Bastide, S. Dubost, A. Calsat, F. Hedaraly, P. Plantady, and A. Ghazisaeidi, "Unrepeated Transmission of 29.2 Tb/s over 295 km with Probabilistically Shaped 64 QAM," in *2018 European Conference on Optical Communication (ECOC)*, pp. 1–3, Sept. 2018.

# Publications

## As first author

- [P1] A. Arnould, D. Le Gac, A. Ghazisaeidi, P. Brindel, M. Makhsiyani, K. Mekhazni, F. Blache, H. Debregeas, M. Achouche, G. Charlet and J. Renaudier, "Impact of the Number of Channels on the Induced Nonlinear Distortions in Ultra-Wideband SOAs", in Proc. OFC, paper Tu3F.1, 2019.
- [P2] A. Arnould, J. Renaudier, A. Ghazisaeidi, D. Le Gac, P. Brindel, M. Makhsiyani, F. Blache and M. Achouche, "Ultra-Wideband Transmission Systems based on Semiconductor Optical Amplifiers", in Proc. ICTON, paper We.B7.4, July 2019.
- [P3] A. Arnould and A. Ghazisaeidi, "Equalization Enhanced Phase Noise in Coherent Receivers: DSP-Aware Analysis and Shaped Constellations", in Journal of Lightwave Technology, 37(20), pp. 5282-5290, October 2019.
- [P4] A. Arnould, A. Ghazisaeidi, D. Le Gac, E. Awwad, P. Brindel, J. Renaudier, "Net 800 Gbit/s Transmission over 605 km using 99.5 Gbaud PDM-64QAM with CMOS Digital-to-Analog Converters", in Proc. ECOC, paper Tu2.D.2, 2019.
- [P5] A. Arnould, A. Ghazisaeidi, D. Le Gac, P. Brindel, M. Makhsiyani, K. Mekhazni, F. Blache, N. Fontaine, D. Neilson, R. Ryf, H. Chen, M. Achouche and J. Renaudier, "103 nm Ultra-Wideband Hybrid Raman/SOA Transmission over 3x100 km SSMF", in Journal of Lightwave Technology, 38 (2), pp. 504-508, January 2020.
- [P6] A. Arnould, A. Ghazisaeidi, D. Le Gac, P. Brindel, M. Makhsiyani, K. Mekhazni, F. Blache, M. Achouche and J. Renaudier, "Experimental Characterization of Non-linear Distortions of Semiconductor Optical Amplifiers in the WDM Regime", in Journal of Lightwave Technology, 38 (2), pp. 509-513, January 2020.
- [P7] A. Arnould, A. Ghazisaeidi, D. Le Gac, M. Ionescu, P. Brindel and J. Renaudier, "Record 300 Gb/s per Channel 99 GBd PDM-QPSK Full C-Band Transmission over 20570 km Using CMOS DACs", in Proc. OFC, paper M3G.1, 2020.
- [P8] A. Arnould, A. Ghazisaeidi, H. Mardoyan, P. Brindel, M. Ionescu and J. Renaudier, "High-Speed and Ultra-Wideband Devices for Coherent Transmission: Challenges and Opportunities", in Proc. ICTON, paper We.C2.3, July 2020.
- [P9] A. Arnould, H. Mardoyan, F. Pulka, A. Ghazisaeidi, V. Aref, B. Bordez, P. Tondo, L. Dalle Cort, E. Pincemin, N. Brochier, F. Chatter, V. Guillot-Common, O. Bertran-Pardo, M. Frascolla, L. Luchesini and J. Renaudier, "Field Trial Demonstration over Live Traffic Network of 400 Gb/s Ultra-Long Haul and 600 Gb/s Regional Transmission", in Proc. ECOC, paper TU2E.4, December 2020.

## As co-author

- [P10] J. Renaudier, A. Arnould, D. Le Gac, A. Ghazisaeidi, P. Brindel, M. Makhsiyani, A. Verdier, K. Mekhazni, F. Blache, H. Debregeas, A. Boutin, N. Fontaine, D. Neilson, R. Ryf, H. Chen, M. Achouche, G. Charlet, "107 Tb/s Transmission of 103-nm Bandwidth over 3x100 km SSMF using Ultra-Wideband Hybrid Raman/SOA Repeaters", in Proc. OFC, paper Tu3F.2, 2019.
- [P11] A. Ghazisaeidi, A. Arnould, D. Le Gac, E. Awwad, P. Brindel, P. Pecci, O. Courtois, A. Leroy and J. Renaudier, "Power-efficient Transmission of 320 Gb/s over 17545 km, and 560 Gb/s over 6050 km using 98 GBd QPSK and 64QAM and CMOS technology", in Proc. ECOC, paper Tu2D.4, 2019.
- [P12] A. Carbo Meseguer, A. Arnould, J.-C. Antona, A. Ghazisaeidi, P. Plantady, S. Dubost, A. Calsat, E. Awwad, J. Renaudier and V. Letellier, "Experimental Characterization of Equalization-Enhanced Phase Noise in Transoceanic Transmission Systems", in Proc. ECOC, paper We1A.2, 2019.
- [P13] X. Ye, A. Arnould, A. Ghazisaeidi, D. Le Gac and J. Renaudier, "Experimental Prediction and Design of Ultra-Wideband Raman Amplifiers Using Neural Networks", in Proc. OFC, paper W1K.3, 2020.
- [P14] J. Renaudier, A. Arnould, A. Ghazisaeidi, D. Le Gac, P. Brindel, E. Awwad, M. Makhsiyani, K. Mekhazni, F. Blache, B. Duval, D. Lanteri, A. Boutin, L. Letteron, Y. Frignac, N. Fontaine, D. Neilson and M. Achouche, "Recent Advances in 100+nm Ultra-Wideband Fiber-Optic Transmission Systems Using Semiconductor Optical Amplifiers", in Journal of Lightwave Technology, 38 (5), pp. 1071-1079, March 2020.
- [P15] M. Ionescu, A. Arnould, D. Le Gac, S. Etienne, A. Ghazisaeidi, M. Duval, C. Bastide, H. Bissessur and J. Renaudier, "20.6 Pb/s.km Unrepeated Transmission without ROPA: UWB SOA Booster and Backward Raman Amplification", in Proc. ECOC, paper WE2E.1, December 2020.
- [P16] T. Zami, K. Benyahya, A. Arnould, H. Mardoyan, J. Renaudier and B. Lavigne, "Impact of crosstalk on 800 Gb/s 90 GBaud 64QAM channel", in Proc. OFC, paper M5C.3, June 2021.
- [P17] K. Benyahya, A. Ghazisaeidi, V. Aref, M. Chagnon, A. Arnould, S. Ranzini, H. Mardoyan, F. Buchali and J. Renaudier, "On the Comparison of Single-Carrier vs. Digital Multi-Carrier Signaling for Long-Haul Transmission of Probabilistically Shaped Constellation Formats", in Proc. OFC, paper M3H.6, June 2021.



**Titre :** Systèmes de transmission ultra large bande et à haut débit symbole pour communications par fibre optique de prochaine génération

**Mots clés :** communications à fibre optique, transmissions à haut débit symbole, amplificateurs optiques à semi-conducteurs

**Résumé :** Les transmissions par fibre optique ont permis le développement de réseaux robustes et performants constituant la base du système mondial de télécommunications. Alors que les fibres à faibles pertes et les amplificateurs à fibre dopée à l'erbium (EDFA) ont ouvert la voie au multiplexage en longueur d'onde (WDM), la détection cohérente permet l'utilisation de techniques de modulation et de codage avancées et le traitement du signal numérique (DSP) est utilisé pour compenser les effets physiques de propagation.

Dans cette thèse, nous nous intéressons à des solutions pour la prochaine génération de systèmes WDM à détection cohérente. Des amplificateurs optiques à semi-conducteurs (SOA) sont utilisés pour fournir une amplification ultra large bande (UWB) sur plus de 100 nm, permettant un plus large débit en comparaison aux systèmes à EDFA avec une largeur de bande inférieure à 40 nm. Nous montrons que des UWB SOA spécifiques permettent une transmission WDM à haute puissance, et nous démontrons expérimentalement des transmissions UWB WDM mettant à profit la bande passante des SOA. En par-

ticulier, nous détaillons la conception de schémas d'amplifications et la caractérisation des effets non-linéaires spécifiques aux transmissions UWB.

Par ailleurs, le développement de transmetteurs à haut débit symbole est encouragé par l'industrie afin de limiter le coût des systèmes optiques WDM, en réduisant le nombre de transmetteurs par fibre. Cette thèse étudie la capacité et les limites de transmetteurs de prochaine génération avec des débits symboles jusqu'à 100 GBd. Nous examinons l'impact du phénomène de bruit de phase augmenté par l'égalisation, une dégradation potentiellement dominante à haut débit symbole. Nous démontrons des transmissions à haut débit symbole, pour des configurations en laboratoire allant jusqu'à des distances transocéaniques, ainsi que dans un essai terrain conduit sur un réseau commercial. En utilisant la mise en forme probabiliste de constellation et des codes correcteurs d'erreur performants, nous mettons en évidence la flexibilité permise par les transmetteurs à haut débit symbole pour répondre aux différents scénarios de transmission qui composent le coeur du réseau des communications Internet.

**Title :** Ultra-wideband and high symbol rate transmission systems for next-generation optical fiber communications

**Keywords :** fiber-optic communications, high symbol rate transmissions, semiconductor optical amplifier

**Abstract :** Optical fiber transmissions have enabled the development of the high capacity and resilient networks that form the backbone of the modern-day global telecommunication system. Whereas low-loss fibers and erbium doped fiber amplifiers (EDFA) allow wavelength division multiplexing (WDM), coherent detection enables advanced modulation and coding schemes, and digital signal processing (DSP) is used to compensate for physical propagation effects.

In this thesis, we address possible solutions for the next generation coherent WDM systems. Semiconductor optical amplifiers (SOA) are used to provide ultra-wideband (UWB) seamless amplification over more than 100 nm, a promising way to scale the throughput compared to conventional systems using EDFA with bandwidth less than 40 nm. We show that custom UWB SOA can enable WDM transmission in high power regime, and we demonstrate UWB WDM experimental transmissions leveraging the SOA bandwidth. In particular, the design of specific amplification

schemes is presented, and the nonlinear impairments arising from UWB spectrum transmission are characterized.

Furthermore, the industry fosters the development of high symbol rate transceivers to provide cost-efficient optical WDM systems with reduced number of transceivers per fiber link. This work studies the capacity and limitations of next-generation coherent transceivers, operating at symbol-rates up to 100 GBd. We investigate the impact of equalization enhanced phase noise, which is a potentially dominant impairment at high symbol rates. We demonstrate high symbol rate transmissions, from regional distances to ultra-long-haul subsea distances in laboratory conditions, as well as in a field trial over a live commercial traffic network. Using probabilistic constellation shaping and powerful forward error correcting codes, we show the flexibility provided by high symbol rate transceivers to address the different transmission cases that constitute the core of the Internet communication network.